

**THERMAL EMISSION SPECTROSCOPY OF SILICATE GLASSES AND MELTS:
APPLICATIONS TO REMOTE SENSING OF GLASSY VOLCANIC ENVIRONMENTS**

by

Rachel Jennifer Lee

B.S. Geosciences, Trinity University, 2004

Submitted to the Graduate Faculty of
Arts and Sciences in partial fulfillment
of the requirements for the degree of
Doctor of Philosophy

University of Pittsburgh

2011

UNIVERSITY OF PITTSBURGH

ARTS AND SCIENCES

This dissertation was presented

by

Rachel Jennifer Lee

It was defended on

April 1, 2011

and approved by

William Harbert, Professor, University of Pittsburgh

Penelope King, Senior Research Scientist, University of New Mexico

Ian Skilling, Assistant Professor, University of Pittsburgh

Brian Stewart, Associate Professor, University of Pittsburgh

Dissertation Advisor: Michael Ramsey, Associate Professor, University of Pittsburgh

Copyright © by Rachel Jennifer Lee

2011

THERMAL EMISSION SPECTROSCOPY OF SILICATE GLASSES AND MELTS: APPLICATIONS TO REMOTE SENSING OF GLASSY VOLCANIC ENVIRONMENTS

Rachel Jennifer Lee, PhD

University of Pittsburgh, 2011

Thermal infrared (TIR) remote sensing is a useful tool for the detection and analysis of volcanic surfaces. The data have been used to determine heat flux, eruption rates, surface petrology, geochemistry, and textures, for example. The majority of past studies using TIR spectroscopy for compositional determination have focused primarily on crystalline minerals, as minerals possess high-order molecular structure, and unique and identifiable TIR spectral features. Although ubiquitous in both hazardous and non-hazardous volcanic terranes, silicate glasses are poorly studied spectrally. This is primarily due to the amorphous and structurally-disordered nature of glasses, which causes them to display very similar spectral features regardless of composition. Because of this, glasses are difficult to distinguish spectrally in the TIR, especially at lower spectral resolutions. Furthermore, spectral features change with the changing physical state of the glass. For example, as a silicate glass transitions from a solid to a molten state, the glass structure becomes less polymerized, bond angles within the O-Si-O structure decrease, and the number of non-bridging oxygens (NBO) increase. These structural changes are reflected in thermal emission spectra as a broadening of the main Si-O spectral feature, and an increase in its wavelength position.

A micro glass-melting furnace has been developed specifically for use with a Nexus 670 FTIR spectrometer in order to collect *in-situ* thermal emission spectra of actively melting and

cooling synthetic silicate glasses of dacitic and rhyolitic composition. Changes in the wavelength position, the emissivity, and the width of the laboratory emission spectra have been observed as the glasses transition from a fully molten to a completely solid state. Differences in spectral behavior and morphology are observed between a glass in a solid state, and its molten counterpart. Furthermore, the approximate temperature range over which the glass transition takes place is also identified. This growing library of laboratory-acquired solid glass and melt spectra will be used in conjunction with TIR airborne and field-based remote sensing instrumentation to more definitively characterize the ever-changing composition and physical state of active silicic lava domes and flows. This, in turn, will contribute to improvement of mapping and hazard assessment of volcanic environments.

TABLE OF CONTENTS

PREFACE.....	XXXIV
1.0 INTRODUCTION.....	1
2.0 SPECTRAL ANALYSIS OF SYNTHETIC QUARTZO-FELDSPATHIC GLASSES USING LABORATORY THERMAL INFRARED SPECTROSCOPY	6
2.1 INTRODUCTION	6
2.2 METHODOLOGY	9
2.2.1 Experimental Procedures.....	9
2.2.2 Analytical Procedures.....	10
2.2.2.1 Electron Microprobe Analysis	10
2.3 RESULTS	12
2.3.1 Glass Composition	12
2.3.2 Infrared Reflectance and Thermal Emission Spectra	13
2.3.3 Spectral Characteristics With Varying Composition.....	16
2.4 DISCUSSION.....	16
2.4.1 Reflectance and Emission Spectra.....	16
2.5 CONCLUSIONS	26
3.0 CONSTRUCTION, CALIBRATION AND TESTING OF THE HIGH-TEMPERATURE MICRO-FURNACE	28

3.1	INTRODUCTION	28
3.2	INSTRUMENT DESIGN	31
3.2.1	Heating Elements	32
3.2.2	Power Supply and Temperature Control	36
3.2.3	Furnace Chamber	38
3.2.3.1	Insulation	38
3.2.3.2	Sample Containment.....	40
3.2.3.3	Water Jacket.....	40
3.2.3.4	Spectrometer and Glove Box	41
3.3	METHODOLOGY	42
3.3.1	Initial Testing	42
3.3.2	Sample Temperature	45
3.3.3	Calibration.....	46
3.3.4	Spectrum Acquisition of Glasses and Melts	49
3.3.5	Comparison of Quenched and Slowly-Cooled Oligoclase Feldspar	50
3.4	RESULTS	51
3.4.1	Furnace Testing.....	51
3.4.2	Sample Temperature	53
3.4.3	Calibration.....	53
3.4.4	Micro-furnace Spectra of Quartz Sand	58
3.4.5	Synthetic Glass Melt	59
3.4.6	Quenched vs. Slowly-Cooled Oligoclase Glass	61
3.5	DISCUSSION.....	62

3.5.1	Sample Temperature and Calibration	67
3.5.2	Relative Emissivity Spectra of Minerals and Glass	70
3.6	CONCLUSIONS	72
4.0	HIGH-TEMPERATURE THERMAL EMISSION SPECTROSCOPY OF SILICATES	74
4.1	INTRODUCTION	74
4.2	METHODOLOGY	78
4.3	RESULTS	80
4.3.1	Thermal Emission Spectra	80
4.3.2	Quenched vs. Slowly Cooled Glasses	97
4.3.3	Wt % SiO ₂ , Al / [Al+Si], and [Na+Ca] / Si	99
4.3.4	Half Width and Spectral Shape with Temperature	111
4.3.5	Total Emitted Energy with Temperature	112
4.4	DISCUSSION	113
4.4.1	Calibration	113
4.4.2	Relative Emissivity Spectra: 7 to 14 microns	116
4.4.3	Relative Emissivity Spectra: 14 to 20 microns	119
4.4.4	Heat-Up vs. Cool-Down Spectra	122
4.5	CONCLUSIONS	123
5.0	DERIVING SILICATE LAVA COMPOSITION FROM IMAGE AND FIELD- BASED THERMAL EMISSION SPECTRA	125
5.1	INTRODUCTION	125
5.1.1	Geology of Medicine Lake Volcano	127

5.1.2	Glass Mountain Rhyodacite Flow.....	129
5.1.3	MODIS/ASTER (MASTER) Airborne Simulator	131
5.1.4	The Forward Looking Infrared Radiometer (FLIR)	131
5.2	METHODOLOGY	134
5.3	RESULTS	135
5.3.1	Synthetic Glass Spectra	135
5.3.2	Natural Glassy Sample Spectra	136
5.3.3	FLIR and MASTER Image Spectra.....	139
5.4	DISCUSSION.....	149
5.5	CONCLUSIONS	157
APPENDIX A		162
APPENDIX B		188
BIBLIOGRAPHY.....		204

LIST OF TABLES

Table 2-1 Compositional and Spectral Data For Glasses	22
Table 4-1 Glass Compositions, Liquidus Temperatures and Maximum Furnace Temperatures	82
Table 5-1 Half Width and Wt. % SiO ₂ for Un-degraded Natural Samples	151
Table 5-2 Half Width and Wt. % SiO ₂ for MASTER-degraded Natural Samples	151
Table 5-3 Half Width and Wt. % SiO ₂ for FLIR-degraded Natural Samples.....	151
Table 5-4 Half Width and Wt. % SiO ₂ values for MASTER image-based spectra.....	154
Table 5-5 Half Width and Wt. % SiO ₂ for FLIR image-based spectra in Figure 5-13B	157
Table 5-6 Half Width and Wt. % SiO ₂ for FLIR image-based spectra in Figure 5-14B	157

LIST OF FIGURES

Figure 2-1 Ab-An-Q ternary diagram of the entire synthetic glass suite, from this study and from that of Byrnes et al. (2007). Glass sample numbers match those listed in Table 1. Glasses are grouped by molar Al / [Al+Si] concentration. Solid lines indicate constant Al / [Al+Si]. Dashed lines denote feldspar-quartz groups (labeled in italic).....	14
Figure 2-2 (A) Infrared micro-reflectance (% R) spectra of six glasses in the compositional suite. Both the reflectance maxima (~1100 cm ⁻¹) and the shoulders (~1200 – 1300 cm ⁻¹) shift to higher wavenumbers with decreasing molar Al / [Al+Si]. (B) Thermal emission spectra of the same six glasses as in (A). Emission minima (~1000 - 1100 cm ⁻¹) and shoulders (~1150 – 1250 cm ⁻¹) also shift to higher wavenumbers with decreasing molar Al / [Al+Si]......	15
Figure 2-3 Infrared micro-reflectance (% R) band maximum position versus emission band minimum position for all the samples, showing a strong degree of correlation.	17
Figure 2-4 Weight % SiO ₂ versus %R maximum position (A), emission minimum position (B) and %R shoulder position (C). Data are grouped by molar Al / [Al+Si] concentration. Maxima, minima and shoulder positions increase in wavenumber with increasing wt. % SiO ₂ and decreasing molar Al / [Al+Si]......	18
Figure 2-5 Molar Al / [Al+Si] versus %R maximum position (A), emission minimum position (B) and %R shoulder position (C). A decrease in molar Al / [Al+Si] is associated with an increase in the maxima, minima and shoulder positions.	19

Figure 2-6 Molar [Na+Ca] / Si versus %R maximum position (A), emission minimum position (B) and %R shoulder position (C). An increase in molar [Na+Ca] / Si causes a decrease in the maxima, minima, and shoulder positions. 21

Figure 3-1 (A) Side view of the micro-furnace assembly, without the cooled cover in place. Medium grey-colored areas are insulation, heating elements are shown in dark grey, and the stainless steel shell and water jacket are shown in black. The dense alumina tube and sample support post (very light grey) house the platinum crucible. The heating elements hang downwards into an airspace inside the furnace, and are connected to the power supply via the ~3/4" section of shank above the heating element holders. Two B-type thermocouples (white tubes) measure the temperature of the sample and the heating elements, and connect to the power supply through plugs at the bottom of the furnace. (B) Top view of the furnace, without the cooled cover in place. The heating elements (black circles) and their holders surround the sample port hole on three sides. The baffle slides outward to expose the sample to the spectrometer..... 33

Figure 3-2 The micro-furnace set-up. The micro-furnace is 8.5" in total height, and 11" in diameter at the base. The aluminum and stainless steel square cover on top of the furnace assembly, and the plastic and copper tubing, are part of the water cooling system. Power is provided to the heating elements via the 120A black cables in the foreground. 34

Figure 3-3 (A) MoSi₂ hairpin heating element. (B) The micro-furnace consists of three MoSi₂ heating elements. The elements surround the sample port on three sides, and are connected to the power supply in series via insulated aluminum-nickel braiding..... 35

Figure 3-4 (A) Front panel of the power supply, showing the power switch (bottom right) and the voltmeter and ammeter (center). Furnace temperature is controlled via an Omega CN8201 single

output PID temperature controller (top left), and heating element temperature is monitored by an Omega DPi32 panel meter. (B) Internal view of the power box, showing the SCR, the transformer, and the Omega units. 37

Figure 3-5 IVIS Laboratory spectrometer setup. The spectrometer (left) and Plexiglas glove box (right) sit atop a Melles Griot optical bench, and are continuously purged of CO₂ and H₂O. Red silicone hand-ports on the glove box allow for access to the inside of the glove box for sample preparation and operation of the furnace baffle. The glove box is open to the external port of the spectrometer via a hole in the Plexiglas, which allows for the spectrometer signal to pass into and out of the glove box for spectrum acquisition. The power supply for the furnace sits beneath the spectrometer, and is fully shielded to prevent electromagnetic interference with the spectrometer. 43

Figure 3-6 (A) Testing the air temperature over the furnace port from 500 °C to 1500 °C using a series of three K-type thermocouples attached to a ring stand at 3” increments. (B) Thermocouple temperatures over the furnace port for each of the three thermocouples. Each point represents the average temperature measured by the thermocouple over a 10 second time period in which the furnace port was open at each set point. TC1 is closest to the furnace port, and TC3 is the furthest. Temperature steadily rises with increasing set point, but none of the thermocouples ever exceed 55 °C. 54

Figure 3-7 Change in cooled cover temperature with increasing set point. The temperature of the cover steadily increased with increasing set point, but never exceeded 35 °C. 55

Figure 3-8 (A) Element temperature vs. sample temperature for an empty Pt crucible (grey lines) and a quartz sand sample (black lines). Element temperature remains virtually the same, as is expected; however the quartz sand has a consistently larger temperature difference from the

heating elements, and is also lower in temperature than the platinum crucible. This can be attributed to a difference in thermal conductivity between the bare crucible and quartz sand. (B) The calculated difference between element and sample temperature over time. In both cases, the temperature difference is sharp as the heating elements initially heat up much faster than the sample. Eventually, the sample temperature stabilizes at ~200 °C - 250 °C lower than the heating elements..... 56

Figure 3-9 (A) Example FLIR image of a glass sample in the furnace, taken at a sample temperature of approximately 1500 °C. The black 0.4”-diameter circle represents the spot size of the spectrometer. (B) Glass sample temperature over a 10 second time period (1 FLIR image/second) for the same glass sample as in A. Sample temperature was analyzed at three furnace set points: 500 °C, 800 °C and 1200 °C. The higher the set point, the more sharply the sample temperature decreases over the 10 second time period. This is illustrated by the more negative slope of the temperature line with increasing set point temperature..... 57

Figure 3-10 Original ceria pellet signal intensity data from 500 °C to 1500 °C. At temperatures below 1200 °C, signal intensity rises systematically with increasing temperature. Above 1200 °C, the intensity spectra become more variable in intensity. Black lines at 7.5, 9.5, and 14 microns indicate the signal intensity values plotted against the third-order polynomial curves shown in Figure 3-11. 59

Figure 3-11 (A) The third-order polynomial curve-fitting process for the signal intensity data at 7.5 μm. Each point on the Measured Data curve represents the signal intensity value of the ceria pellets at 7.5 μm, from 500 °C to 1400 °C. At 1200 °C and above, the data deviates from the third order polynomial curves (Calculated Data), due to a drop-off in signal intensity of the ceria pellets at temperatures higher than 1200 °C. To correct for this, the Measured Data points were

scaled to the Calculated Data polynomial curve, using a calculated scaling factor. Data at (B) 9.5 μm and (C) 14 μm are also shown..... 60

Figure 3-12 Corrected ceria pellet signal intensity from 500 $^{\circ}\text{C}$ to 1600 $^{\circ}\text{C}$. The reference spectra from 1300 $^{\circ}\text{C}$ to 1600 $^{\circ}\text{C}$ were extended using polynomial curve fitting and a scaling factor, to maintain a Stefan-Boltzmann curve shape above 1200 $^{\circ}\text{C}$ 61

Figure 3-13 Quartz Sand Emissivity Spectra from 80 $^{\circ}\text{C}$ to 1000 $^{\circ}\text{C}$. (A) 80 $^{\circ}\text{C}$ spectrum was acquired in the low-temperature spectrometer setup, and 300 $^{\circ}\text{C}$ -1000 $^{\circ}\text{C}$ spectra were acquired in the furnace. As the sample heats to 600 $^{\circ}\text{C}$, the quartz doublet feature between 8 and 9 μm disappears. This is attributed to a phase change in quartz from α -quartz to β -quartz at approximately 573 $^{\circ}\text{C}$ (Gervais and Piriou, 1975). (B) A close-up view of the quartz doublet feature, showing the changes and eventual disappearance of the doublet between 300 $^{\circ}\text{C}$ and 600 $^{\circ}\text{C}$ 63

Figure 3-14 The values of the quartz emissivity minima increase steadily with increasing temperature. 64

Figure 3-15 Relative emissivity spectra of glass 2 from 80 $^{\circ}\text{C}$ to 900 $^{\circ}\text{C}$ (A) and from 1000 $^{\circ}\text{C}$ to 1400 $^{\circ}\text{C}$ (B). The spectra show changes in emissivity minimum value and minimum position with increasing temperature. Beyond the liquidus of glass 2 (1250 $^{\circ}\text{C}$), the emissivity minimum values drop sharply. 65

Figure 3-16 Wavelength position of emissivity minima vs. set point (A) and emissivity minimum value vs. set point (B) for glass 2. The minimum position decreases steadily with decreasing temperature. Emissivity minimum values rise sharply from 1400 $^{\circ}\text{C}$ to 1200 $^{\circ}\text{C}$, and this rise indicates the glass transition from a fully molten material to a more solid material. At

temperatures below 1200 °C, emissivity minimum values decrease more linearly with decreasing temperature. 66

Figure 3-17 (A) Emission spectra of unfused oligoclase feldspar from Ramsey (1996), from this study, and from the ASU spectral library. Slight differences in the spectra are due to differences in particle size of the samples. (B) Emission spectrum of oligoclase feldspar quenched at 1130 °C (Ramsey, 1996) vs. a micro-furnace spectrum of oligoclase at 1100 °C. (C) Emission spectrum of oligoclase feldspar quenched at 1220 °C (Ramsey, 1996) vs. a micro-furnace spectrum of oligoclase at 1200 °C. (D) Emission spectrum of oligoclase feldspar quenched at 1490 °C (Ramsey, 1996) vs. a micro-furnace spectrum of oligoclase at 1500 °C. In B, C, and D the emissivity minimum value of the quenched oligoclase is higher than that of the non-quenched oligoclase analyzed in the furnace. 68

Figure 3-18 Low-temperature (80 °C) spectra of quenched glass 2, and glass 2 slowly cooled to room temperature in the micro-furnace. The emissivity minimum of the quenched glass is higher than that of the slowly-cooled glass. 69

Figure 4-1 Relative emissivity spectra of Glass 1 shown from 7 to 14 μm, (A) 80 °C to 1000 °C; (B) 1100 °C to 1200 °C; (C) 1220 °C to 1300 °C; and (D) 1320 °C to 1400 °C. The 80 °C spectrum is absolute emissivity acquired from the low-temperature laboratory setup, but is included here as a comparison to the micro-furnace spectra. Emissivity minima values increase with increasing temperature from 500 °C to 1000 °C. At temperatures higher than 1000 °C, the minima values and wavelength positions are more variable. Arrows denote locations of shoulder features at ~11.5 and 12.5 μm. 83

Figure 4-2 Relative emissivity spectra of Glass 1a shown from 7 to 14 μm, (A) 80 °C to 1000 °C; (B) 1100 °C to 1200 °C; (C) 1220 °C to 1300 °C; and (D) 1320 °C to 1400 °C. The 80 °C

spectrum is absolute emissivity acquired from the low-temperature laboratory setup, but is included here as a comparison to the micro-furnace spectra. Emissivity minima values increase with increasing temperature from 500 °C to 1000 °C. At temperatures higher than 1000 °C, the minima values and wavelength positions are more variable. Arrows denote locations of shoulder features at ~11.5 and 12.5 μm..... 84

Figure 4-3 Relative emissivity spectra of Glass 7 shown from 7 to 14 μm, (A) 80 °C to 1000 °C; (B) 1100 °C to 1200 °C; (C) 1220 °C to 1300 °C; and (D) 1320 °C to 1500 °C. The 80 °C spectrum is absolute emissivity acquired from the low-temperature laboratory setup, but is included here as a comparison to the micro-furnace spectra. Emissivity minima values increase with increasing temperature from 500 °C to 1000 °C. At temperatures higher than 1000 °C, the minima values and wavelength positions are more variable. Arrows denote locations of shoulder features at ~11.5 and 12.5 μm..... 85

Figure 4-4 Relative emissivity spectra of Glass 8 shown from 7 to 14 μm, (A) 80 °C to 1000 °C; (B) 1100 °C to 1200 °C; (C) 1220 °C to 1300 °C; and (D) 1320 °C to 1500 °C. The 80 °C spectrum is absolute emissivity acquired from the low-temperature laboratory setup, but is included here as a comparison to the micro-furnace spectra. Emissivity minima values increase with increasing temperature from 500 °C to 1000 °C. At temperatures higher than 1000 °C, the minima values and wavelength positions are more variable. Arrows denote locations of shoulder features at ~11.5 and 12.5 μm..... 86

Figure 4-5 Relative emissivity spectra of Glass 21 shown from 7 to 14 μm, (A) 80 °C to 1000 °C; (B) 1100 °C to 1200 °C; (C) 1220 °C to 1300 °C; and (D) 1320 °C to 1500 °C. The 80 °C spectrum is absolute emissivity acquired from the low-temperature laboratory setup, but is included here as a comparison to the micro-furnace spectra. Emissivity minima values increase

with increasing temperature from 500 °C to 1000 °C. At temperatures higher than 1000 °C, the minima values and wavelength positions are more variable. Arrows denote locations of shoulder features at ~11.5 and 12.5 μm..... 87

Figure 4-6 Relative emissivity spectra of Glass 21a shown from 7 to 14 μm, (A) 80 °C to 1000 °C; (B) 1100 °C to 1200 °C; (C) 1220 °C to 1300 °C; and (D) 1320 °C to 1400 °C. The 80 °C spectrum is absolute emissivity acquired from the low-temperature laboratory setup, but is included here as a comparison to the micro-furnace spectra. Emissivity minima values increase with increasing temperature from 500 °C to 1000 °C. At temperatures higher than 1000 °C, the minima values and wavelength positions are more variable. Arrows denote locations of shoulder features at ~11.5 and 12.5 μm..... 88

Figure 4-7 Relative emissivity spectra of Glass 24 shown from 7 to 14 μm, (A) 80 °C to 1000 °C; (B) 1100 °C to 1200 °C; (C) 1220 °C to 1300 °C; and (D) 1320 °C to 1400 °C. The 80 °C spectrum is absolute emissivity acquired from the low-temperature laboratory setup, but is included here as a comparison to the micro-furnace spectra. Emissivity minima values increase with increasing temperature from 500 °C to 1000 °C. At temperatures higher than 1000 °C, the minima values and wavelength positions are more variable. Arrows denote locations of shoulder features at ~11.5 and 12.5 μm..... 89

Figure 4-8 Variation in spectral features for glass 1. (A) Emissivity minimum position vs. set point temperature and (B) emissivity minimum value vs. set point temperature. At temperatures lower than ~1120 °C, minimum positions and emissivity values decrease linearly with decreasing set point temperature to 500 °C. Above 1120 °C, the minimum positions and emissivity values are more variable with temperature. Plots are divided into melt, Tg, and solid

regions. The temperature range within which the T_g occurs is denoted by the grey box, and the dotted line marks the liquidus temperature of the glass..... 90

Figure 4-9 Variation in spectral features for glass 1a. (A) Emissivity minimum position vs. set point temperature and (B) emissivity minimum value vs. set point temperature. At temperatures lower than ~1120 °C, minimum positions and emissivity values decrease linearly with decreasing set point temperature to 500 °C. Above 1120 °C, the minimum positions and emissivity values are more variable with temperature. Plots are divided into melt, T_g, and solid regions. The temperature range within which the T_g occurs is denoted by the grey box, and the dotted line marks the liquidus temperature of the glass..... 91

Figure 4-10 Variation in spectral features for glass 7. (A) Emissivity minimum position vs. set point temperature and (B) emissivity minimum value vs. set point temperature. At temperatures lower than 1200 °C, minimum positions and emissivity values decrease linearly with decreasing set point temperature to 500 °C. Above 1200 °C, the minimum positions and emissivity values are more variable with temperature. Plots are divided into melt, T_g, and solid regions. The temperature range within which the T_g occurs is denoted by the grey box, and the dotted line marks the liquidus temperature of the glass..... 92

Figure 4-11 Variation in spectral features for glass 8. (A) Emissivity minimum position vs. set point temperature and (B) emissivity minimum value vs. set point temperature. At temperatures lower than 1200 °C, minimum positions and emissivity values decrease linearly with decreasing set point temperature to 500 °C. Above 1200 °C, the minimum positions and emissivity values are more variable with temperature. Plots are divided into melt, T_g, and solid regions. The temperature range within which the T_g occurs is denoted by the grey box, and the dotted line marks the liquidus temperature of the glass..... 93

Figure 4-12 Variation in spectral features for glass 21. (A) Emissivity minimum position vs. set point temperature and (B) emissivity minimum value vs. set point temperature. At temperatures lower than ~ 1180 °C, minimum positions and emissivity values decrease linearly with decreasing set point temperature to 500 °C. Above 1180 °C, the minimum positions and emissivity values are more variable with temperature. Plots are divided into melt, Tg, and solid regions. The temperature range within which the Tg occurs is denoted by the grey box, and the dotted line marks the liquidus temperature of the glass..... 94

Figure 4-13 Variation in spectral features for glass 21a. (A) Emissivity minimum position vs. set point temperature and (B) emissivity minimum value vs. set point temperature. At temperatures lower than 1160 °C, minimum positions and emissivity values decrease linearly with decreasing set point temperature to 500 °C. Above 1160 °C, the minimum positions and emissivity values are more variable with temperature. Plots are divided into melt, Tg, and solid regions. The temperature range within which the Tg occurs is denoted by the grey box, and the dotted line marks the liquidus temperature of the glass..... 95

Figure 4-14 Variation in spectral features for glass 24. (A) Emissivity minimum position vs. set point temperature and (B) emissivity minimum value vs. set point temperature. At temperatures lower than 1200 °C, minimum positions and emissivity values decrease linearly with decreasing set point temperature to 500 °C. Above 1200 °C, the minimum positions and emissivity values are more variable with temperature. Plots are divided into melt, Tg, and solid regions. The temperature range within which the Tg occurs is denoted by the grey box, and the dotted line marks the liquidus temperature of the glass..... 96

Figure 4-15 Change in spectral shape with temperature. The spectrum at 1200 °C is representative of the spectral shape at temperatures 1200 °C and below. Above 1200 °C, a

significant shoulder is introduced into the spectra from ~14 to 20 μm . The change in shape of the shoulder does not behave in a linear manner with temperature. All glass spectra in this study were scaled to an emissivity of 1 at 7.5 and 14 μm in order to eliminate this shoulder feature... 98

Figure 4-16 Comparison of 80 $^{\circ}\text{C}$ quenched glass spectra to 80 $^{\circ}\text{C}$ slowly-cooled glass spectra for (A) glass 1, (C), glass 7, and (E) glass 21. Slowly-cooled spectra (grey lines) have deeper emission minima than their quenched counterparts (black lines). The quenched spectrum was divided by the slowly-cooled spectrum for (B) glass 1, (D) glass 7 and (F) glass 21. In each case, a muted spectral feature with some spectral morphology is apparent at ~9 μm 100

Figure 4-17 Glass 8 heat-up vs. cool-down spectra from (A) 500 $^{\circ}\text{C}$ to 700 $^{\circ}\text{C}$, (B) 800 $^{\circ}\text{C}$ to 1100 $^{\circ}\text{C}$, and (C) 1200 $^{\circ}\text{C}$ to 1500 $^{\circ}\text{C}$. At temperatures 1100 $^{\circ}\text{C}$ and below, the cool-down spectrum at a given temperature is more muted than the corresponding heat-up spectrum. During heat-up, the emissivity minimum values increase and emissivity minimum positions shift to longer wavelengths with increasing temperature. During cool-down, emissivity minimum values decrease and emissivity minimum positions shift to shorter wavelengths with decreasing temperature. The difference in minimum value between heat-up and cool-down spectra is shown in (D). At temperatures above 1200 $^{\circ}\text{C}$, the minimum values of the heat-up and cool-down spectra are more variable and non-linear with temperature..... 101

Figure 4-18 Glass 21 heat-up vs. cool-down spectra from (A) 500 $^{\circ}\text{C}$ to 700 $^{\circ}\text{C}$, (B) 800 $^{\circ}\text{C}$ to 1100 $^{\circ}\text{C}$, and (C) 1200 $^{\circ}\text{C}$ to 1500 $^{\circ}\text{C}$. At temperatures 1100 $^{\circ}\text{C}$ and below, the cool-down spectrum at a given temperature is more muted than the corresponding heat-up spectrum. During heat-up, the emissivity minimum values increase and emissivity minimum positions shift to longer wavelengths with increasing temperature. During cool-down, emissivity minimum values decrease and emissivity minimum positions shift to shorter wavelengths with decreasing

temperature. The difference in minimum value between heat-up and cool-down spectra is shown in (D). At temperatures above 1200 °C, the minimum values of the heat-up and cool-down spectra are more variable and non-linear with temperature..... 102

Figure 4-19 Change in emissivity minimum position with wt. % SiO₂ for all glass spectra at (A) 80 °C, (B) 500 °C, (C) 600 °C, (D) 700 °C, (E) 800 °C, and (F) 900 °C. The minimum position for each of the glasses increases slightly with increasing temperature. Wt. % SiO₂ values remain the same for each temperature, as the wt. % SiO₂ of the glasses is not expected to change with increasing temperature..... 104

Figure 4-20 Change in emissivity minimum position with wt. % SiO₂ for all glass spectra at (A) 1000 °C, (B) 1100 °C, (C) 1200 °C, (D) 1300 °C, (E) 1400 °C, and (F) 1500 °C. Open circles denote data outliers. Overall, the minimum position for each of the glasses increases slightly with increasing temperature. Wt. % SiO₂ values remain the same for each temperature, as the wt. % SiO₂ of the glasses is not expected to change with increasing temperature..... 105

Figure 4-21 Change in emissivity minimum position with Al / [Al+Si] for all glass spectra at (A) 80 °C, (B) 500 °C, (C) 600 °C, (D) 700 °C, (E) 800 °C, and (F) 900 °C. Overall, the minimum position for each of the glasses increases slightly with increasing temperature. Al / [Al+Si] values remain the same for each temperature, as the Al / [Al+Si] of the glasses is not expected to change with increasing temperature..... 106

Figure 4-22 Change in emissivity minimum position with Al / [Al+Si] for all glass spectra at (A) 1000 °C, (B) 1100 °C, (C) 1200 °C, (D) 1300 °C, (E) 1400 °C, and (F) 1500 °C. Open circles denote data outliers. Overall, the minimum position for each of the glasses increases slightly with increasing temperature. Al / [Al+Si] values remain the same for each temperature, as the Al / [Al+Si] of the glasses is not expected to change with increasing temperature..... 107

Figure 4-23 Change in emissivity minimum position with [Na+Ca] / Si for all glass spectra at (A) 80 °C, (B) 500 °C, (C) 600 °C, (D) 700 °C, (E) 800 °C, and (F) 900 °C. Overall, the minimum position for each of the glasses increases slightly with increasing temperature. [Na+Ca] / Si values remain the same for each temperature, as the [Na+Ca] / Si of the glasses is not expected to change with increasing temperature. 108

Figure 4-24 Change in emissivity minimum position with [Na+Ca] / Si for all glass spectra at (A) 1000 °C, (B) 1100 °C, (C) 1200 °C, (D) 1300 °C, (E) 1400 °C, and (F) 1500 °C. Open circles denote data outliers. Overall, the minimum position for each of the glasses increases slightly with increasing temperature. [Na+Ca] / Si values remain the same for each temperature, as the [Na+Ca] / Si of the glasses is not expected to change with increasing temperature. 109

Figure 4-25 Change in (A) slope and (B) R^2 value with temperature for the wt. % SiO_2 vs. emissivity minimum position plots in Figures 4-19 and 4-20. Slope and R^2 values are variable above 1200 °C. The low point at 1300 °C is attributed to the greater degree of variability in the data at this temperature as compared to the other temperatures. The low point at 1500 °C is due to the lack of data at this temperature, as only 5 of the glasses needed to reach a temperature of 1500 °C in order to fully melt. Both slope and R^2 values are near-linear from 1100 °C to 80 °C. 110

Figure 4-26 (A) Graphical representation of the half width calculation. ϵ_{min} is the emissivity minimum value of the spectrum. λ_1 and λ_2 are the wavelengths at which the half depth falls on the spectrum. The difference between λ_1 and λ_2 is the half width of the spectrum. (B) Change in half width with increasing set point temperature for 4 of the glasses. Half width remains relatively linear at temperatures up to ~1200 °C. At temperatures above 1200 °C, the half width

becomes much more variable with temperature. This is consistent with the variation in emissivity minimum at higher temperatures..... 114

Figure 4-27 Emitted energy with decreasing temperature for (A) glass 1, (B) glass 1a, (C) glass 7, (D) glass 8, (E) glass 21, and (F) glass 24. Grey points denote the calculated emitted energy at each set point temperature. As each glass cools from its maximum temperature, the emitted energy is variable, but an overall decrease in energy occurs. From ~1200 °C to 500 °C, the emitted energy data for each glass takes on an exponential shape (thick black line), which has a consistently high R^2 value of 0.99. 115

Figure 5-1 Topographic map of Glass Mountain flow and vicinity at Medicine Lake volcano. Major lava flows are shown in pink. The dotted line denotes the location of the caldera rim (Donnelly-Nolan, 1988)..... 128

Figure 5-2 The multi-spectral field-based spectrometer. (A) FLIR thermal camera with one of the filters in the fore optics. Each filter currently fits onto the fore optics individually for image acquisition. (B) Band-passes for each of the 6 filters. The wavelength centers of the filters are 8.05, 8.69, 9.32, 10.08, 10.87 and 11.53 μm 133

Figure 5-3 (A) MASTER-degraded emission spectra of glass 1 at 80 °C, 500 °C, 1000 °C, and 1300 °C. (B) FLIR-degraded emission spectra of glass 1 at 80 °C, 500 °C, 1000 °C, and 1300 °C. 137

Figure 5-4 Calculated half width vs. wt. % SiO_2 for all un-degraded synthetic glass spectra at (A) 80 °C, (B) 500 °C, (C) 1000 °C, and (D) 1300 °C. Glasses at 80 °C, 500 °C, and 1000 °C show excellent fits and R^2 values. The fit for glasses at 1300 °C is much poorer, and suggests that calculation of the half width needs to be modified for glasses within the melt region..... 140

Figure 5-5 Calculated half width vs. wt. % SiO₂ for all MASTER-degraded synthetic glass spectra at (A) 80 °C, (B) 500 °C, (C) 1000 °C, and (D) 1300 °C. Glasses at 80 °C, 500 °C, and 1000 °C show good fits and R² values. The fit for glasses at 1300 °C is much poorer, and suggests that calculation of the half width needs to be modified for glasses within the melt region. 141

Figure 5-6 Calculated half width vs. wt. % SiO₂ for all FLIR-degraded synthetic glass spectra at (A) 80 °C, (B) 500 °C, (C) 1000 °C, and (D) 1300 °C. R² values at each temperature are poorer than that of the un-degraded and MASTER-degraded spectra. This confirms that spectral resolution is important to the accurate calculation of half width..... 142

Figure 5-7 (A) Un-degraded, (B) MASTER-degraded and (C) FLIR-degraded spectra of obsidian. The spectral shoulder at ~8.5 μm is resolved in all three spectra. 143

Figure 5-8 (A) Un-degraded, (B) MASTER-degraded and (C) FLIR-degraded spectra of fine vesicular pumice (FVP). The spectral shoulder at ~8.5 μm is resolved in the MASTER spectrum..... 144

Figure 5-9 (A) Undegraded, (B) MASTER-degraded and (C) FLIR-degraded spectra of a dacite with basaltic andesite inclusions. The slight spectral feature at ~10 μm is resolved in the MASTER spectrum..... 145

Figure 5-10 (A) Undegraded, (B) MASTER-degraded and (C) FLIR-degraded spectra of vesicular dacite. The slight spectral shoulder at ~8.5 μm is resolved in the MASTER spectrum. 146

Figure 5-11 (A) Undegraded, (B) MASTER-degraded and (C) FLIR-degraded spectra of an altered breccia. The significant spectral shoulder at ~8.5 μm is resolved in both the MASTER and FLIR spectra..... 147

Figure 5-12 (A) Half width vs. wt. % SiO₂ plots for un-degraded synthetic glass spectra with calculated half widths and wt. % SiO₂ values for the 5 natural samples plotted on the trend line. (B) Half width vs. wt. % SiO₂ plots for MASTER-degraded synthetic glass spectra with calculated half widths and wt. % SiO₂ values for the 5 natural samples plotted on the trend line. (C) Half width vs. wt. % SiO₂ plots for FLIR-degraded synthetic glass spectra with calculated half widths and wt. % SiO₂ values for the 5 natural samples plotted on the trend line. Wt. % SiO₂ and half width values of natural samples in (A) and (B) are slightly different than the synthetic glasses. Natural samples in (C) have much different half widths and wt. % SiO₂ values than expected. 150

Figure 5-13 MASTER images of Glass Mountain flow, Medicine Lake Volcano. (A) Visible color image (source: Google Earth). (B) False color image. Dark and light purple colors depict the widespread compositional mixing of the flow. The image is distorted in the E-W direction due to the scanning motion of the MASTER instrument. The two long lobes to the east of the main body of the flow are 67 wt. % SiO₂ dacite, and a zone of compositionally-mixed material lies between the two lobes. The large lobe extending from the top-center of the flow to the northeast is 74 wt. % SiO₂ rhyolite. White dots denote areas where image-based emission spectra were acquired..... 152

Figure 5-14 Half width vs. wt. % SiO₂ values for MASTER-degraded synthetic glass spectra, with data from MASTER image-based spectra plotted on the trend line. Half width values of the image-based spectra are within the range of the lab spectra; however, the calculated wt. % SiO₂ value for each spectrum is slightly higher than the inferred wt. % SiO₂ value for the spectrum. 153

Figure 5-15 (A) Field image of an obsidian boulder ejected from an explosion pit, and (B) an RGB 6-3-1 (11.53 μ m – 9.32 μ m – 8.05 μ m) FLIR decorrelation stretch image of the same field site. Pink and purple colors represent areas of high silica. Green and blue colors denote areas behaving as blackbody-like material. Black dots denote points at which emission spectra were acquired from the FLIR image..... 155

Figure 5-16 (A) Field image of a compositionally-mixed area on Glass Mountain and (B) an RGB 5-3-1 (10.87 μ m – 9.32 μ m – 8.05 μ m)FLIR decorrelation stretch image of the same field site. Pink and purple colors represent areas of high silica. Green and blue colors denote areas behaving as blackbody-like material. Black dots denote points at which emission spectra were acquired from the FLIR image..... 156

Figure 5-17 Half width vs. wt. % SiO₂ values for MASTER-degraded synthetic glass spectra, with data from MASTER image-based spectra plotted on the trend line. Half width values of the image-based spectra are within the range of the lab spectra; however, the calculated wt. % SiO₂ value for each spectrum is slightly higher than the inferred wt. % SiO₂ value for the spectrum. 158

Figure A-1 Relative emissivity spectra for glass 2 from (A) 80 °C to 900 °C and (B) 1000 °C to 1400 °C. 163

Figure A-2 Change in (A) emissivity minimum position and (B) emissivity minimum value with temperature for glass 2..... 164

Figure A-3 Relative emissivity spectra for glass 2a from (A) 80 °C to 900 °C and (B) 1000 °C to 1400 °C. 165

Figure A-4 Change in (A) emissivity minimum position and (B) emissivity minimum value with temperature for glass 2a..... 166

Figure A-5 Relative emissivity spectra for glass 3 from (A) 80 °C to 900 °C and (B) 1000 °C to 1300 °C.	167
Figure A-6 Change in (A) emissivity minimum position and (B) emissivity minimum value with temperature for glass 3.....	168
Figure A-7 Relative emissivity spectra for glass 6 from (A) 80 °C to 900 °C and (B) 1000 °C to 1400 °C.	169
Figure A-8 Change in (A) emissivity minimum position and (B) emissivity minimum value with temperature for glass 6.....	170
Figure A-9 Relative emissivity spectra for glass 19 from (A) 80 °C to 900 °C and (B) 1000 °C to 1300 °C.	171
Figure A-10 Change in (A) emissivity minimum position and (B) emissivity minimum value with temperature for glass 19.....	172
Figure A-11 Relative emissivity spectra for glass 19a from (A) 80 °C to 900 °C and (B) 1000 °C to 1275 °C.	173
Figure A-12 Change in (A) emissivity minimum position and (B) emissivity minimum value with temperature for glass 19a.....	174
Figure A-13 Relative emissivity spectra for glass 20a from (A) 80 °C to 900 °C and (B) 1000 °C to 1375 °C.	175
Figure A-14 Change in (A) emissivity minimum position and (B) emissivity minimum value with temperature for glass 20a.....	176
Figure A-15 Relative emissivity spectra for glass 27 from (A) 80 °C to 900 °C and (B) 1000 °C to 1400 °C.	177

Figure A-16 Change in (A) emissivity minimum position and (B) emissivity minimum value with temperature for glass 27..... 178

Figure A-17 Relative emissivity spectra for glass 28 from (A) 80 °C to 1000 °C and (B) 1100 °C to 1500 °C..... 179

Figure A-18 Change in (A) emissivity minimum position and (B) emissivity minimum value with temperature for glass 28..... 180

Figure A-19 Comparison of 80 °C quenched glass spectra to 80 °C slowly-cooled glass spectra for (A) glass 2, (C), glass 2a, and (E) glass 3. Slowly-cooled spectra (dotted lines) have deeper emissivity minima than their quenched counterparts (solid lines). The quenched spectrum was divided by the slowly-cooled spectrum for (B) glass 2, (D) glass 2a, and (F) glass 3. In each case, a muted spectral feature with some spectral morphology is apparent at ~9 μm..... 181

Figure A-20 Comparison of 80 °C quenched glass spectra to 80 °C slowly-cooled glass spectra for (A) glass 6, (C), glass 19, and (E) glass 19a. Slowly-cooled spectra (dotted lines) have deeper emissivity minima than their quenched counterparts (solid lines). The quenched spectrum was divided by the slowly-cooled spectrum for (B) glass 6 (D) glass 19 and (F) glass 19a. In each case, a muted spectral feature with some spectral morphology is apparent at ~9 μm..... 182

Figure A-21 Comparison of 80 °C quenched glass spectra to 80 °C slowly-cooled glass spectra for (A) glass 20a, (C), glass 27, and (E) glass 28. Slowly-cooled spectra (dotted lines) have deeper emissivity minima than their quenched counterparts (solid lines). The quenched spectrum was divided by the slowly-cooled spectrum for (B) glass 20a, (D) glass 27 and (F) glass 28. In each case, a muted spectral feature with some spectral morphology is apparent at ~9 μm..... 183

Figure A-22 Glass 21a heat-up vs. cool-down spectra from (A) 500 °C to 700 °C, (B) 800 °C to 1100 °C, and (C) 1200 °C to 1500 °C. At temperatures 1100 °C and below, the cool-down

spectrum at a given temperature is more muted than the corresponding heat-up spectrum. During heat-up, the emissivity minimum values increase and emissivity minimum positions shift to longer wavelengths with increasing temperature. During cool-down, emissivity minimum values decrease and emissivity minimum positions shift to shorter wavelengths with decreasing temperature. The difference in emissivity minimum value between heat-up and cool-down spectra is shown in (D). At temperatures above 1200 °C, the emissivity minimum values of the heat-up and cool-down spectra are more variable and non-linear with temperature. 184

Figure A-23 Glass 24 heat-up vs. cool-down spectra from (A) 500 °C to 700 °C, (B) 800 °C to 1100 °C, and (C) 1200 °C to 1500 °C. At temperatures 1100 °C and below, the cool-down spectrum at a given temperature is more muted than the corresponding heat-up spectrum. During heat-up, the emissivity minimum values increase and emissivity minimum positions shift to longer wavelengths with increasing temperature. During cool-down, emissivity minimum values decrease and emissivity minimum positions shift to shorter wavelengths with decreasing temperature. The difference in emissivity minimum value between heat-up and cool-down spectra is shown in (D). At temperatures above 1200 °C, the emissivity minimum values of the heat-up and cool-down spectra are more variable and non-linear with temperature. 185

Figure A-24 Change in slope and R^2 value with temperature for the Al / [Al+Si] vs. emissivity minimum position plots in Figures 4-23 and 4-24. Slope and R^2 values are variable above 1200 °C. The low point at 1300 °C is attributed to the greater degree of variability in the data at this temperature as compared to the other temperatures. The low point at 1500 °C is due to the lack of data at this temperature, as only 5 of the glasses needed to reach a temperature of 1500 °C in order to fully melt. Both slope and R^2 values are near-linear from 1100 °C to 80 °C. 186

Figure A-25 Change in slope and R^2 value with temperature for the [Na+Ca] / Si vs. emissivity minimum position plots in Figures 4-25 and 4-26. Slope and R^2 values are variable above 1200 °C. The low point at 1300 °C is attributed to the greater degree of variability in the data at this temperature as compared to the other temperatures. The low point at 1500 °C is due to the lack of data at this temperature, as only 5 of the glasses needed to reach a temperature of 1500 °C in order to fully melt. Both slope and R^2 values are near-linear from 1100 °C to 80 °C. 187

Figure B-1 (A) MASTER-degraded emission spectra of glass 1a at 80 °C, 500 °C, 1000 °C, and 1300 °C. (B) FLIR-degraded emission spectra of glass 1a at 80 °C, 500 °C, 1000 °C, and 1300 °C. 189

Figure B-2 (A) MASTER-degraded emission spectra of glass 2 at 80 °C, 500 °C, 1000 °C, and 1300 °C. (B) FLIR-degraded emission spectra of glass 2 at 80 °C, 500 °C, 1000 °C, and 1300 °C. 190

Figure B-3 (A) MASTER-degraded emission spectra of glass 2a at 80 °C, 500 °C, 1000 °C, and 1300 °C. (B) FLIR-degraded emission spectra of glass 2a at 80 °C, 500 °C, 1000 °C, and 1300 °C. 191

Figure B-4 (A) MASTER-degraded emission spectra of glass 3 at 80 °C, 500 °C, 1000 °C, and 1300 °C. (B) FLIR-degraded emission spectra of glass 3 at 80 °C, 500 °C, 1000 °C, and 1300 °C. 192

Figure B-5 (A) MASTER-degraded emission spectra of glass 6 at 80 °C, 500 °C, 1000 °C, and 1300 °C. (B) FLIR-degraded emission spectra of glass 6 at 80 °C, 500 °C, 1000 °C, and 1300 °C. 193

Figure B-6 (A) MASTER-degraded emission spectra of glass 7 at 80 °C, 500 °C, 1000 °C, and 1300 °C. (B) FLIR-degraded emission spectra of glass 7 at 80 °C, 500 °C, 1000 °C, and 1300 °C. 194

Figure B-7 (A) MASTER-degraded emission spectra of glass 8 at 80 °C, 500 °C, 1000 °C, and 1300 °C. (B) FLIR-degraded emission spectra of glass 8 at 80 °C, 500 °C, 1000 °C, and 1300 °C. 195

Figure B-8 (A) MASTER-degraded emission spectra of glass 19 at 80 °C, 500 °C, 1000 °C, and 1300 °C. (B) FLIR-degraded emission spectra of glass 19 at 80 °C, 500 °C, 1000 °C, and 1300 °C. 196

Figure B-9 (A) MASTER-degraded emission spectra of glass 19a at 80 °C, 500 °C, 1000 °C, and 1300 °C. (B) FLIR-degraded emission spectra of glass 19a at 80 °C, 500 °C, 1000 °C, and 1300 °C. 197

Figure B-10 (A) MASTER-degraded emission spectra of glass 20a at 80 °C, 500 °C, 1000 °C, and 1300 °C. (B) FLIR-degraded emission spectra of glass 20a at 80 °C, 500 °C, 1000 °C, and 1300 °C. 198

Figure B-11 (A) MASTER-degraded emission spectra of glass 21 at 80 °C, 500 °C, 1000 °C, and 1300 °C. (B) FLIR-degraded emission spectra of glass 21 at 80 °C, 500 °C, 1000 °C, and 1300 °C. 199

Figure B-12 (A) MASTER-degraded emission spectra of glass 21a at 80 °C, 500 °C, 1000 °C, and 1300 °C. (B) FLIR-degraded emission spectra of glass 21a at 80 °C, 500 °C, 1000 °C, and 1300 °C. 200

Figure B-13 (A) MASTER-degraded emission spectra of glass 24 at 80 °C, 500 °C, 1000 °C, and 1300 °C. (B) FLIR-degraded emission spectra of glass 24 at 80 °C, 500 °C, 1000 °C, and 1300 °C. 201

Figure B-14 (A) MASTER-degraded emission spectra of glass 27 at 80 °C, 500 °C, 1000 °C, and 1300 °C. (B) FLIR-degraded emission spectra of glass 27 at 80 °C, 500 °C, 1000 °C, and 1300 °C. 202

Figure B-15 (A) MASTER-degraded emission spectra of glass 28 at 80 °C, 500 °C, 1000 °C, and 1300 °C. (B) FLIR-degraded emission spectra of glass 28 at 80 °C, 500 °C, 1000 °C, and 1300 °C. 203

PREFACE

"If I find 10,000 ways something won't work, I haven't failed. I am not discouraged, because every wrong attempt discarded is another step forward". - Thomas A. Edison

To Dr. Michael Ramsey: When we first started talking about doing this project, my first thought was “he must be insane”. My second thought was “I can barely operate the furnace at my apartment. What makes him think I can build one?!?” Well, after about \$25,000+ of grant money, many ups and downs, a good deal the world’s platinum supply, and what seems like a hundred different design iterations, I actually did it! I cannot thank you enough your guidance and support, and thank you for believing in me and encouraging me to keep moving forward.

To Dr. Penny King: I remember how nervous and apprehensive I was when I first visited your lab to make glass. How far I have come! Without a doubt, this project could not have been accomplished without your help and guidance. Thank you for patiently and tirelessly showing me the ropes, and for all your support and encouragement throughout my graduate school years. Here’s to many more years of great science!

To My Committee - Dr. Ian Skilling, Dr. Brian Stewart and Dr. Bill Harbert: Each of you have contributed greatly to my graduate education, and have made me a well-rounded and well-

educated geologist. Thank you for your help and encouragement as I jumped through all the “hoops” of graduate school!

To my family – Robin, Jacqueline and Andrew Lee: Well, it’s the end of another era! The end of this tunnel has been reached, the light is right in front of me, and now it’s time to move on to the next tunnel. Throughout my life you have all held my hand and tirelessly supported me through all that I’ve done. From my first school science fair to my first scientific publication, you’ve helped guide me in the right direction. Dad, during these grad school years, there have been many debates, many late night talks, and a whole lot of ups and downs. But through it all, because of you, I have become a better person and a better scientist. A girl could not have asked for a more fantastic father. Mom, ever since I took my first steps, I have strived to follow in yours. Your compassion, integrity, talent and strength of character are an inspiration to me every day. Thank you for making all of this possible for me! Andrew, I have always looked up to you, and your many successes have been the driving force for my own. You are the ultimate big brother....always right behind me, with words of encouragement, good advice, and unwavering support. There is no doubt how lucky I am to have such a fantastic brother!

To Dr. Adam Carter: You were one of the first people I met when I first arrived at grad school, and I remember thinking “wow, he’s a Brit! Like me! But his accent is cooler.” Who knew that we would become such close friends, and make such fantastic memories? Thank you for always being there with a hug, a beer, and a listening ear whenever I needed it. You’re one of the people I’ve looked up to most during grad school.

To Dr. Christopher Hughes: When I walked into the IVIS lab for our very first lab group meeting, I remember listening to you talk about computer issues, and thinking “wow, that computer tech guy sure knows what he’s talking about. Maybe he’ll fix my computer.” Then I realized you were one of Mike’s students as well. Yet that still did not, and does not to this day, stop me from asking you to fix my computer! I am so very glad that I met you, and we shared our grad school experience. What seemed so far away has now been achieved! Thank you for being a great friend and confidant, making me a better person, and for always supporting me and giving me a shoulder to cry on, no matter how rocky the road got.

To Dr. Shellie Rose: On our first day at Pitt, I remember a girl with long blonde hair, wearing jeans and an oversized Harley Davidson shirt, walking into the room, sitting down, and quietly introducing herself as Shellie. We’ve been through a whole lot over the years, and through all of it I am happy to call you my sister. I will never forget “chicken finger Fridays”, impromptu shopping trips when we were too stressed to function, or our special office language and humor that probably only the two of us ever understood!

To Dr. Stephen Scheidt: One of the smartest and most amazing scientists I have ever met, grillmaster extraordinaire, and 1/3 of the most amazing cornhole team in the city of Pittsburgh! Thank you for always being there with a helping hand, and spending more time than you probably had available to help me with problems. And thank you for re-instilling my confidence during the times I thought all was lost. You are my other big brother!

To Sarah Morealli: You arrived at Pitt a shy and quiet masters student, who kept mostly to herself. And all of us were convinced that you just didn't like us very much! However, you eventually broke out of your shell, and have become one of the best friends I've ever had. I can't thank you enough for being there for me through all the good and bad times, grad school and otherwise. Those bad days always got better when you walked into our office to say hello, and graced us with your hilariously abrasive humor! There are far more awesome memories than can be written here, and I will truly treasure them, and your friendship, forever.

To all the amazing friends who have taken this journey with me: Jeffrey Byrnes, Kim Dalby, Ashley Denny, James Gardiner, Alison Graettinger, Jefferson Hungerford, Holly Kagy, Bobby Karimi, Kristen LaMoreaux, Eric Manalo, Emily Mercurio, Tamara Misner, Redha Mohammad, Kevin Reath, Katie Redling, Celeste Schofield, Marion Sikora, Elizabeth Simoneau, Veronica Peet, Lindsay Williams, Amy Wolfe, and so many more. Some of you are old friends, and some are newer. But each of you has influenced and inspired me in some way, and for that, I thank you!

1.0 INTRODUCTION

Thermal infrared (TIR) remote sensing has become a useful tool in the mapping and analysis of volcanic environments. It is an advantageous technique that allows for remote analysis and observation of geochemistry and eruptive activity. In the TIR wavelength range ($\sim 5\text{-}50\ \mu\text{m}$ or ~ 2000 to $200\ \text{cm}^{-1}$), silicon-oxygen bonds within a silicate material undergo stretching and bending vibrations, which create distinct absorptions at particular wavelengths in the material's spectrum (e.g. King et al., 2004). The specific wavelength location, morphology and depth of these absorptions are all dependent on a variety of factors including composition, vesicularity, crystallinity and temperature. TIR data have been widely used both in the laboratory and in the field to derive information about geologic samples such as the relative age (e.g. Kahle et al., 1988; Crisp et al., 1990; Realmuto et al., 1992), texture (e.g. Byrnes et al., 2004; Ramsey and Dehn, 2004; Carter et al., 2009), composition (e.g. Salisbury et al., 1991; Clark 1999; Wright and Ramsey, 2006), physical properties (e.g. Walter and Salisbury, 1989; Christensen et al., 2000), and temperature (e.g. Vaughan et al., 2005; Carter et al., 2007).

The majority of geologic studies using TIR methods have focused primarily on minerals, however, which possess high-order molecular structure and have unique and identifiable spectral features. Amorphous and structurally-disordered materials such as silicate glasses show only a broad spectral feature at $\sim 9.1\ \mu\text{m}$ ($\sim 1100\ \text{cm}^{-1}$) and an additional feature at $\sim 22\ \mu\text{m}$ ($\sim 450\ \text{cm}^{-1}$).

The broad feature is common to all silicate glasses regardless of composition, making them difficult to distinguish spectrally. Natural silicate glasses occur most commonly in volcanic environments, but can also form as a result of impact-related shock metamorphism (e.g. Johnson et al., 2003, 2006), alteration, and disordering of the crystal structure of a mineral. They are ubiquitous in potentially hazardous volcanic environments. A variety of studies have examined glass spectra as a function of composition (e.g. Sweet and White, 1969; Byrnes et al., 2004, 2007; Dalby et al., 2006; Dalby and King, 2006; Minitti et al., 2006, 2007; Dufresne et al., 2009), texture (e.g. Ondrusek et al., 1993; Ramsey and Fink, 1999), and alteration (e.g. Crisp et al., 1990; Minitti et al., 2002). Most of these studies have focused on glasses in either a quenched or solid state, however, and no studies yet exist which comprehensively examine the effects that partially or fully molten silicate materials have on emitted energy.

The first phase of this research, presented in Chapter 2, involves the synthesis and spectral analysis of a suite of synthetic glasses, composed of simplistic, bi-modal mineral mixtures. These glasses are representative of rhyolitic and dacitic lava compositions. Laboratory micro-reflectance and thermal emission spectra gathered of each glass showed that the spectral signature of the glasses is highly dependent on the wt % SiO₂ content, the Si-O bond distance, and the presence (or absence) of network modifying cations. Each of these components has a bearing on the degree of polymerization of the glass, which in turn affects spectral morphology. For example, the wavelength positions of the emissivity minima and reflectance maxima consistently shift to lower wavelengths with increasing wt % SiO₂ and decreasing amounts of network modifying cations. These observations are consistent with previous studies, and provide further insight into the effects of structure and composition on TIR glass spectra.

A custom laboratory micro-furnace was then constructed to work in conjunction with the FTIR emission spectroscopy laboratory at University of Pittsburgh. The micro-furnace is a novel piece of equipment that allows for the very first *in-situ* emission spectra of partially and fully molten silicates to be collected in the laboratory, as they melt and cool through the glass transition. Chapter 3 describes the process of constructing, calibrating and testing this micro-furnace. The micro-furnace was modeled after laboratory box furnaces and industrial glass melting furnaces, and can currently reach temperatures of up to 1500 °C. Each of the major components of the furnace, as well as some of the initial test data, are presented and discussed. The specialized procedure developed to calibrate the micro-furnace data, and derive relative emissivity spectra, is also presented. Relative emissivity spectra from the first synthetic glass melt show changes in spectral behavior with changing temperature, and also with transition from a solid to a molten state. These initial data validate the micro-furnace as an effective laboratory tool for spectral analysis of solid and molten materials at varying temperatures.

Analysis and interpretations of the thermal emission spectra collected of the remainder of the synthetic glass suite are presented in Chapter 4. The overall spectral behavior with changing temperature is consistent among all glass compositions. Emissivity minima values and the wavelength positions of the minima both shift to higher values and increasing wavelengths, respectively, with increasing temperature. When a glass nears its liquidus temperature, and begins the transition from a solid to a molten state, however, the minima behave much more variably and melt spectra exhibit subtle changes in morphology. The emissivity minimum value of a rapidly quenched glass is higher than that of glass of the same composition allowed to cool slowly to room temperature. Furthermore, emission spectra of glasses upon heat-up in the

furnace display much more muted features relative to spectra of glasses during cool-down. Significant differences in the behavior of emitted energy between solid and molten silicates are particularly apparent. Use of the micro-furnace in characterizing the change in spectral behavior of glasses as they melt and cool has been extremely successful, and the data gathered will make a significant contribution to the understanding of glass and melt spectral behavior in the TIR.

The energy emitted from actively cooling lava surface is complex, with constantly varying compositions, temperatures, vesicularities, and glass percentages. For the purposes of hazard mitigation and assessment it is vital to understand how the aforementioned petrologic properties contribute to, and affect, the emitted energy from a silicic volcanic surface. However, accurate determination of emissivity in the field is a potentially complex and dangerous process. Chapter 5 presents a field method being developed that uses the half width of emissivity spectra to derive wt % SiO₂ compositions from volcanic surfaces in real-time. Half width calculations were performed on laboratory-acquired spectra of synthetic glasses, natural samples collected from Glass Mountain at Medicine Lake Volcano in northern California, and image-based and field-based emissivity data of Glass Mountain. Half width values derived from emissivity spectra were used to calculate the wt % SiO₂ of the sample. Although improvements need to be made to the method, it does show promise for deriving accurate wt % SiO₂ contents in the field, and can possibly be expanded to characterize other physical properties of a volcanic surface, such as vesicularity, surface roughness, and glassy crust formation.

Gaining a better understanding of the spectral effects of glassy material at a variety of temperatures and physical states, and the relationship between glasses and crystalline solids of the same composition, is of particular importance due to the growing popularity of using TIR instrumentation to map and monitor active and inactive volcanic environments. Spectral information attained from both synthetic glasses and field samples will allow for more accurate characterization of glassy surfaces by both current and future TIR instruments and real-time monitoring equipment.

2.0 SPECTRAL ANALYSIS OF SYNTHETIC QUARTZO-FELDSPATHIC GLASSES USING LABORATORY THERMAL INFRARED SPECTROSCOPY

2.1 INTRODUCTION

Thermal infrared (TIR) remote sensing and laboratory-based spectroscopy are useful tools for non-destructively analyzing planetary surfaces and small-scale samples, respectively. In the TIR wavelength range ($\sim 5 - 50 \mu\text{m}$ or $\sim 2000 - 200 \text{ cm}^{-1}$), Si-O-Si and Si-O-Al bonds (referred to as Si-O bonds henceforth) within a silicate material undergo stretching and bending vibrations, which create absorptions at discrete wavelengths in the spectrum of the material (King et al., 2004, and references therein). Most geologic studies using emission or reflectance TIR methods have focused primarily on crystalline minerals (i.e. those which possess high-order molecular structure) that have unique and identifiable spectral features. However, amorphous and structurally-disordered silicate glasses show only a very broad Reststrahlen feature in the $\sim 1100 - 800 \text{ cm}^{-1}$ ($\sim 8 - 12 \mu\text{m}$) region due to Si-O asymmetric stretching vibrations, and a feature between $500 - 400 \text{ cm}^{-1}$ ($20 - 25 \mu\text{m}$) due to bending vibrations (Bell et al., 1968; Dowty, 1987; Salisbury et al., 1991; Poe et al., 1992; McMillan and Wolf, 1995; Agarwal and Tomozawa, 1997; McMillan et al., 1998). An additional spectral shoulder feature exists at $\sim 1200 \text{ cm}^{-1}$ ($\sim 8.3 \mu\text{m}$) region. These features are common to all silicate glasses regardless of composition, making them especially problematic to distinguish using TIR spectra. Furthermore, the specific

wavelength location, morphology and depth of these absorptions in glassy silicate materials depend on a variety of factors, including composition, degree of crystallinity, micron-scale surface roughness, and temperature. It would be useful to better understand these complexities of TIR spectra, so that silicate glass composition may be more accurately determined.

TIR data have been used extensively to derive information about silicate materials, either remotely or on the hand sample scale. For example, TIR can be used to determine silicate composition (Salisbury et al., 1991; Clark, 1999; Wyatt et al., 2001; Eisinger, 2002; Minitti et al., 2002; Wright and Ramsey, 2006), relative age (Kahle et al., 1988; Crisp et al., 1990; Realmuto et al., 1992), surface textures (Ondrusek et al., 1993; Ramsey and Fink, 1999; Byrnes et al., 2004; Ramsey and Dehn, 2004), physical properties (Walter and Salisbury, 1989; Christensen et al., 2000), and temperature (Vaughan et al., 2005; Carter et al., 2007).

Natural silicate glasses can form as a result of impact-related shock metamorphism (Johnson et al., 2003, 2006), alteration, and disordering of the crystal structure of a crystalline mineral or melt (McMillan and Wolf, 1995; Stebbins, 1995; Henderson, 2005; Henderson et al., 2006). However, they occur most commonly in volcanic environments on planetary surfaces. Active silicic domes are steep-sided masses of volatile-rich, glassy lava that may explode or collapse catastrophically, posing a potential hazard to populated areas. As they grow and collapse, these domes can undergo changes in both composition and surface texture (Fink and Anderson, 2000). The study of lava dome composition and behavior is of great importance, because even subtle transitions in composition, temperature and texture can indicate an increase in the explosive potential of the dome. The energy emitted from an actively cooling dome

surface is complex, with constantly varying compositions, temperatures, vesicularities, and glass percentages as the dome grows and collapses. For the purposes of volcanic hazard mitigation and assessment it is vital to understand how these petrologic properties contribute to, and affect, the emitted energy from a silicic volcanic dome.

Due to their prevalence in potentially hazardous volcanic environments on Earth and their ubiquitous presence on other planetary bodies (e.g. the Moon and Mars), there have been a variety of studies that have systematically examined infrared (IR) reflectance and emission spectra of glasses as a function of composition (Sweet and White, 1969; Wyatt et al., 2001, Byrnes et al., 2004, 2005, 2007; Dalby et al., 2006; Dalby and King, 2006; Minitti et al., 2006, 2007; Dufresne et al., 2009). The goal of this investigation is to expand upon the work of Byrnes et al. (2007), using a similar systematic experimental approach to identify and characterize distinctive spectral features in a suite of compositionally diverse synthetic high-SiO₂ glasses. A better understanding of how the silicate structure of glass affects spectral signatures in the TIR will improve the detection and characterization of glasses, particularly those associated with volcanic environments, and will contribute to the accuracy and mapping capabilities of TIR remote sensing on Earth and other planetary bodies.

2.2 METHODOLOGY

2.2.1 Experimental Procedures

Glasses were synthesized at the University of Western Ontario (UWO), and consist of mixtures of albite/quartz, oligoclase/quartz, and andesine/quartz, as well as albite, andesine, and oligoclase end-members. Mixtures were chosen to represent a range of compositions found in dacite/rhyolite glassy volcanic domes and flows. Each mineral was ground to a powder (~20 - 80 μm) in an agate mortar and pestle under ethanol, dried in a 110 °C oven for several hours, and then mixed in various proportions to create the suite of glasses. For the albite-quartz glasses, Na_2CO_3 , SiO_2 , and Al_2O_3 powders were used as starting materials for albite, because most natural albites contain alteration minerals which affect their bulk composition.

The starting materials were packed tightly into platinum crucibles, covered with lids, and melted in a Thermolyne box furnace for six hours. Melting temperatures varied between 1475 °C and 1600 °C, and were at least 200 °C higher than the liquidus temperature from an Ab - An - Q phase diagram (Schairer, 1957). After melting, each glass was rapidly quenched in an ice-water bath, and removed from the platinum crucible. A polarized petrographic microscope was used to examine each glass for the presence of microlite crystals. If crystals were present, the glass was re-ground and re-melted for < 2 hours at a slightly higher temperature.

2.2.2 Analytical Procedures

2.2.2.1 Electron Microprobe Analysis

Each glass was characterized with a JEOL 8200 electron microprobe at the University of New Mexico (UNM) using a 15 kV, 5 nA, 20 μm beam, wavelength dispersive spectroscopy, and ZAF corrections. Although glass compositions could be calculated using the mineral mixture compositions, the measured compositions did not precisely agree with the calculations because 1) the original minerals contained inclusions; 2) the minerals were not pure end-members; and 3) alkali loss may have occurred during synthesis. Therefore, the electron microprobe – determined compositions were used in all subsequent data analysis.

2.2.2.2. Micro-Reflectance Fourier Transform Infrared Spectroscopy

Micro-specular reflectance measurements were collected at UWO, using a Nexus 670 FTIR spectrometer with a Continuum micro-FTIR microscope attachment. A collimated Global source, an extended range potassium bromide (XT-KBr) beamsplitter, and a mercury cadmium telluride (MCT-A) detector with a spectral range of 4000 - 650 cm^{-1} (2.5 - 15.4 μm) were used. Two to three small grains of each glass (1 - 2 mm in size) were mounted in epoxy, and polished flat. Glasses were placed in a purged chamber in the microscope, and four individual infrared micro-reflectance (% R) spectra (at 400 scans each) were collected at different locations on each glass at a resolution of 4 cm^{-1} . A background spectrum of a gold standard was collected prior to

the glass analysis. Finally, the four spectra for each glass were averaged, and the wavenumber position of the % R maximum for each was recorded. The % R shoulder position was found by taking the second derivative of each averaged spectrum.

2.2.2.3. Fourier Transform Thermal Emission Spectroscopy

Thermal emission spectra were collected in the Image Visualization and Infrared Spectroscopy (IVIS) Laboratory, at the University of Pittsburgh (UP). The IVIS Nexus 870 spectrometer uses a KBr beamsplitter, and a deuterated triglycerine sulfate (DTGS) detector with a spectral range of 2000 - 400 cm^{-1} (5.0 - 25.0 μm). Glasses were sieved into small (< 125 μm), medium (< 500 μm), and large (2 - 4 mm) size fractions. Medium and large size fractions were placed in an ultrasonic machine to remove clinging fine-grained particles, which can cause diffraction effects that change the intensity and shape of spectral features (Lyon, 1965; Salisbury and Wald, 1992; Moersch and Christensen, 1995; Ramsey and Christensen, 1998).

Approximately 2 grams of the medium and large size fraction of each glass were heated to 80 °C for 24 hours, which allowed the samples to serve as the TIR source. Prior to the glass analysis, spectra were acquired from two blackbody sources that are precision controlled to 70 °C and 100 °C. The spectra of the blackbody targets allow for the instrument and environmental emission to be quantified and removed (Ruff et al., 1997). Copper sample cups painted with high-emissivity paint and containing each glass were removed from the oven and placed on a heating stage within the H₂O and CO₂ purged glove box. The temperature of the sample cups was allowed to re-equilibrate prior to the collection of the spectra, which is an important factor in

attaining accurate emissivity spectra (Ramsey, 2004). The entire heating stage/sample cup assembly was raised into a temperature-controlled blackbody chamber that eliminated downwelling radiation.

Emission spectra were collected over 250 scans, at a spectral resolution of 4 cm^{-1} , and averaged. Raw data were converted to absolute emissivity as described in Ruff et al. (1997) and the wavenumber position of the emissivity minimum was found for each glass spectrum. Shoulder positions were not identified for the emission spectra because they are more difficult to precisely locate on emission spectra due to the lower signal to noise ratio (SNR) of this technique. Furthermore, % R and emission spectra are well-correlated in this study; therefore, only the % R shoulder positions were required.

2.3 RESULTS

2.3.1 Glass Composition

Electron microprobe data verified that the glasses were homogenous and crystal-free. Overall, the compositions were close to the intended compositions, although some glasses showed evidence of alkali loss during melting. The concentrations of albite, anorthite and quartz components were derived from the microprobe data, normalized, and plotted as individual glass compositions on an Ab-An-Q ternary diagram (Figure 2-1). Compositions are grouped by Al /

[Al+Si] concentration because Al and Si content influences glass structure, which in turn affects spectral morphology (Sweet and White, 1969; Neuville and Mysen, 1996; Angeli et al., 2000; Dufresne et al., 2009).

2.3.2 Infrared Reflectance and Thermal Emission Spectra

Figures 2-2A and 2-2B show % R and thermal emission spectra, respectively, of six representative glass compositions. Each of the six glasses has a different composition, including different molar Al / [Al+Si] concentration. Both the Restsrahlen feature ($\sim 1100 \text{ cm}^{-1}$) and the $\sim 1200 \text{ cm}^{-1}$ shoulder feature shift to higher wavenumbers with increasing wt % SiO_2 and decreasing molar Al / [Al+Si] content. This is consistent with previous studies involving the correlation of spectral feature position with glass composition and also holds true for silicate mineral spectra. Spectral morphology is also affected by the composition of the glass. The shoulder becomes more distinct with increasing SiO_2 content.

The reflectance (R) spectra and emission (ϵ) spectra are generally related to each other through Kirchhoff's Law ($\epsilon = 1 - R$) (Nicodemus, 1965). Also, both spectral types show comparable changes in spectral band position and shape for the six compositions (Figures 2-2A and 2-2B). The % R maxima positions versus emission minima positions are strongly correlated (Figure 2-3). Thus, for the purposes of this study, % R spectra and thermal emission spectra are comparable.

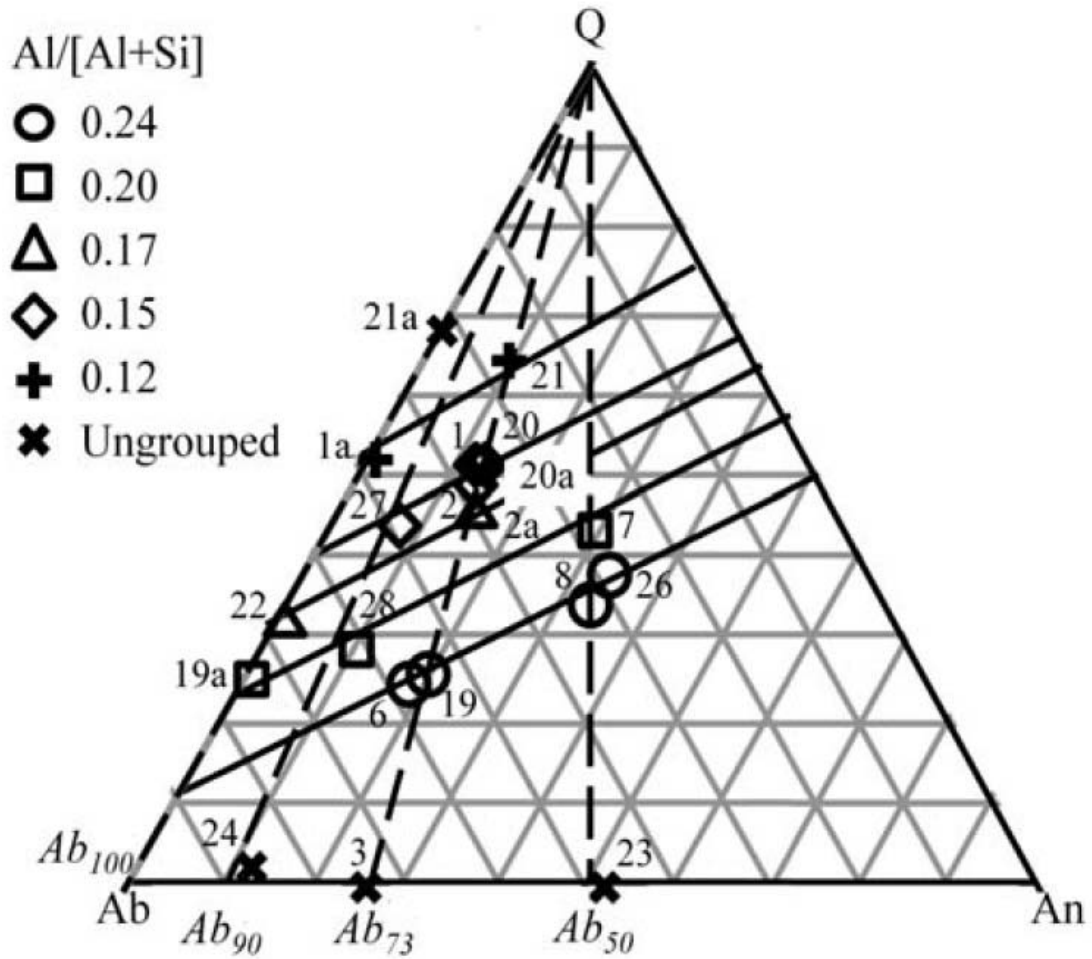


Figure 2-1 Ab-An-Q ternary diagram of the entire synthetic glass suite, from this study and from that of Byrnes et al. (2007). Glass sample numbers match those listed in Table 1. Glasses are grouped by molar Al / [Al+Si] concentration. Solid lines indicate constant Al / [Al+Si]. Dashed lines denote feldspar-quartz groups (labeled in *italic*).

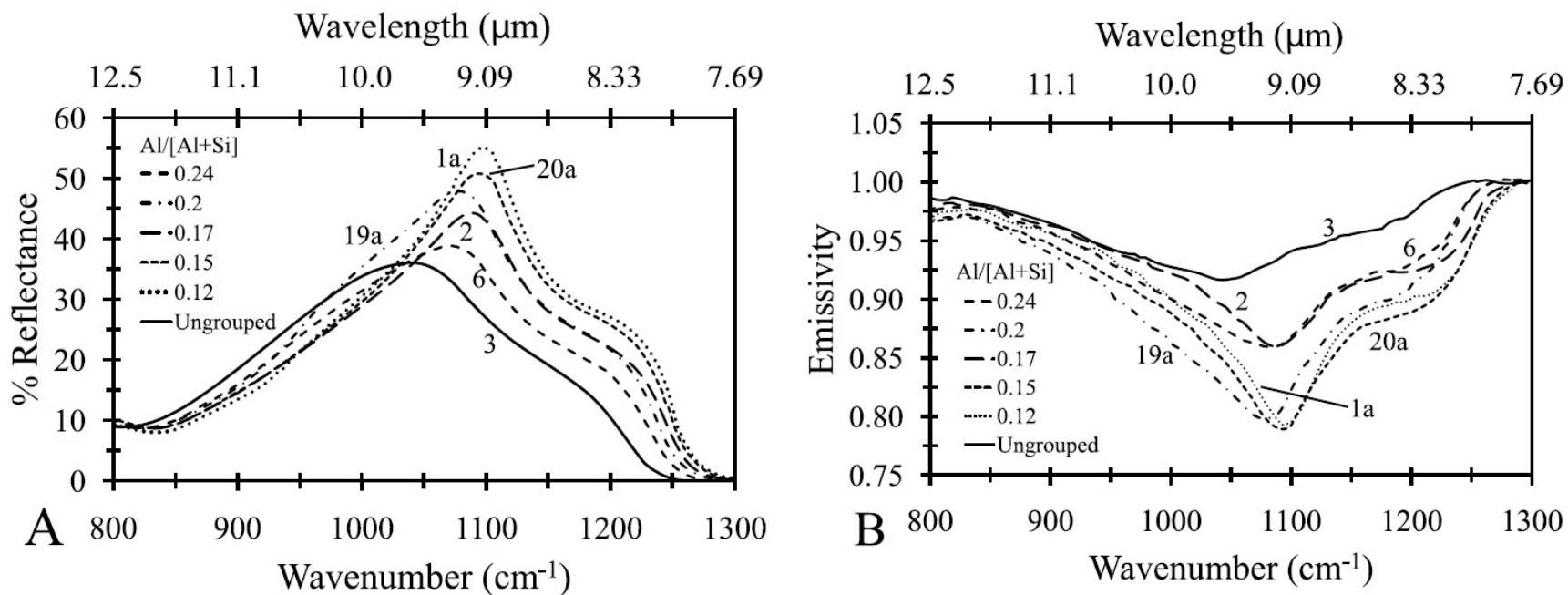


Figure 2-2 (A) Infrared micro-reflectance (% R) spectra of six glasses in the compositional suite. Both the reflectance maxima (~1100 cm⁻¹) and the shoulders (~1200 – 1300 cm⁻¹) shift to higher wavenumbers with decreasing molar Al / [Al+Si]. (B) Thermal emission spectra of the same six glasses as in (A). Emission minima (~1000 - 1100 cm⁻¹) and shoulders (~1150 – 1250 cm⁻¹) also shift to higher wavenumbers with decreasing molar Al / [Al+Si].

2.3.3 Spectral Characteristics With Varying Composition

Figures 2-4A and 2-4B show the wavenumber position of the % R maximum and the emission minimum, respectively, versus wt % SiO₂. Maxima and minima are grouped by molar Al / [Al+Si]. The % R maxima and emission minima shift to higher wavenumbers with increasing wt. % SiO₂, and decreasing amounts of Al. The position of the ~1200 cm⁻¹ shoulder in % R spectra also increases in wavenumber with increasing SiO₂ and decreasing Al (Figure 2-4C). Figures 2-5A – 2-5C show % R maxima, emission minima, and % R shoulder positions plotted against molar Al / [Al+Si]. These band locations shift to higher wavenumbers with decreasing molar Al / [Al+Si] content, as expected. Conversely, an increase in molar [Na+Ca] / Si in the glasses causes a shift in the % R maxima, emission minima, and % R shoulder positions to lower wavenumbers (Figures 2-6A – 2-6C). Although K is also present in most of the glasses, it was not included in the alkali analyses, because it occurs only in trace amounts (Table 2-1).

2.4 DISCUSSION

2.4.1 Reflectance and Emission Spectra

Kirchhoff's Law ($\epsilon = 1 - R$) is valid only if emission spectra are directional, and reflectance spectra are either hemispherical-directional or directional-hemispherical (Hapke, 1993; Korb et al,

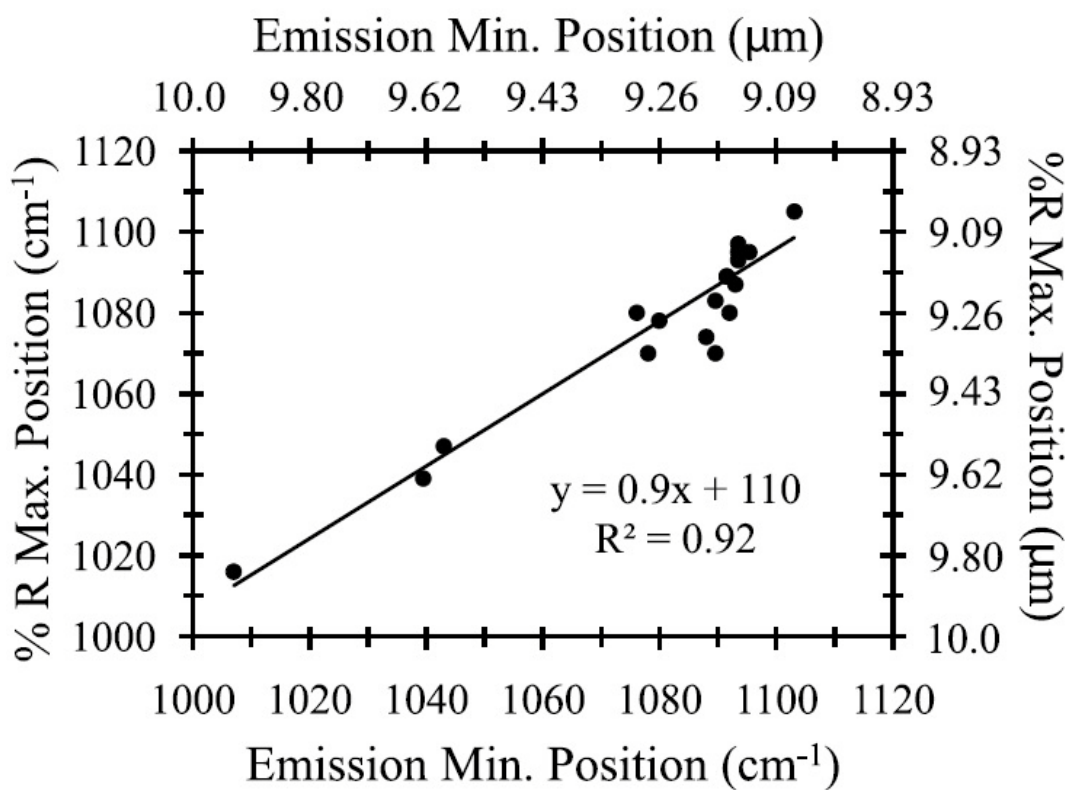


Figure 2-3 Infrared micro-reflectance (% R) band maximum position versus emission band minimum position for all the samples, showing a strong degree of correlation.

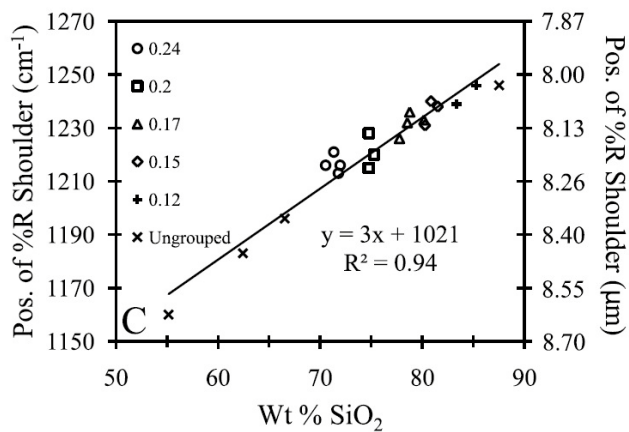
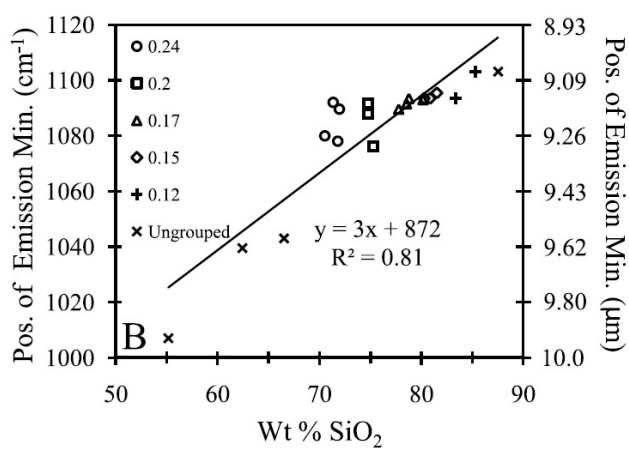
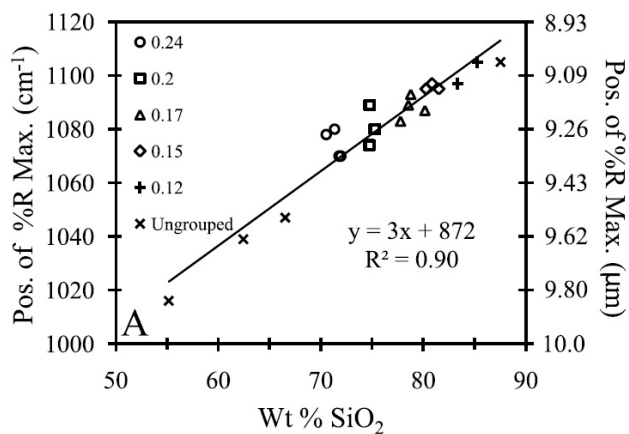


Figure 2-4 Weight % SiO₂ versus %R maximum position (A), emission minimum position (B) and %R shoulder position (C). Data are grouped by molar Al / [Al+Si] concentration. Maxima, minima and shoulder positions increase in wavenumber with increasing wt. % SiO₂ and decreasing molar Al / [Al+Si].

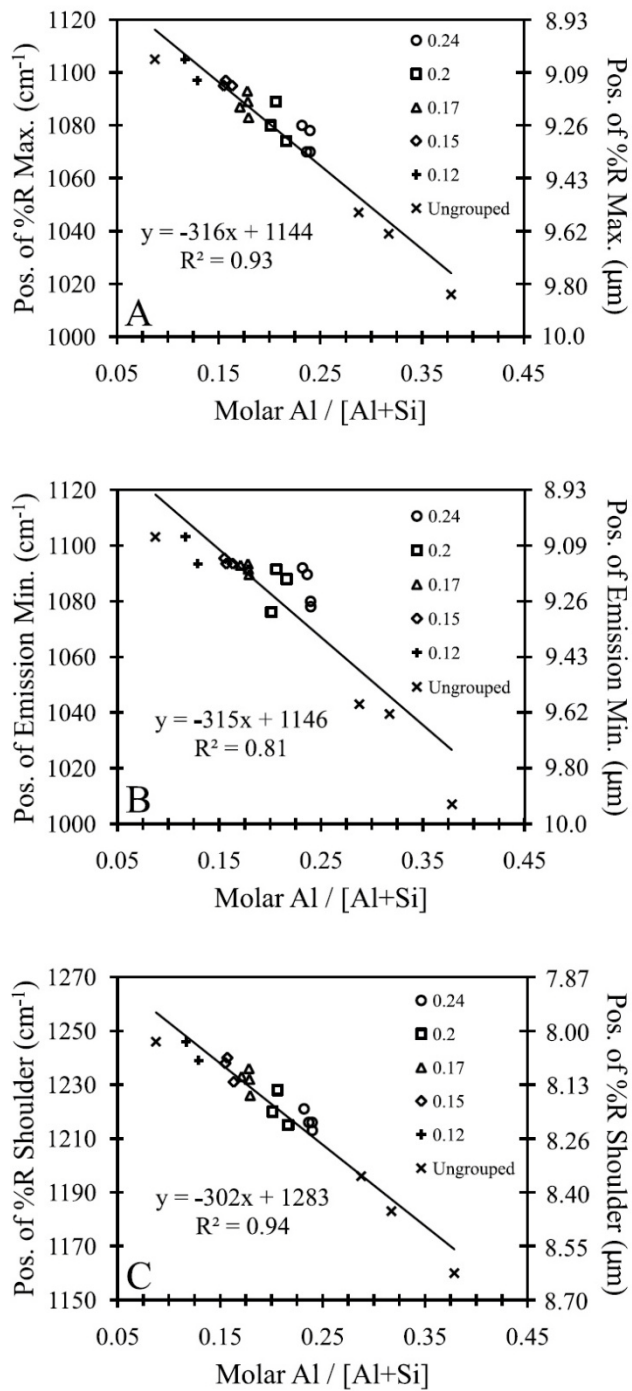


Figure 2-5 Molar Al / [Al+Si] versus %R maximum position (A), emission minimum position (B) and %R shoulder position (C). A decrease in molar Al / [Al+Si] is associated with an increase in the maxima, minima and shoulder positions.

1999). For this study, specular micro-reflectance measurements were acquired. However, glasses are amorphous and single polished glass grains were analyzed; thus, the diffusely-scattered component from each sample is considered negligible and Kirchhoff's Law remains valid. In contrast, emission spectra of numerous large glass particles per sample were acquired. This results in spectra with slightly shallowed and more muted spectral features relative to the reflectance spectra, because multiple emission and reflection events between each of the particles have the effect of adding a reflected component to the spectra (Ramsey and Fink, 1999). Despite the differences between emissivity spectra and reflectance spectra, a strong correlation still exists between the band shape, minima, and maxima positions. The spectra acquired from each technique are therefore directly comparable to one another. A Kramers-Kronig (KK) transform is commonly performed on reflectance spectra in order to remove optical constant effects (McMillan and Hoffmeister, 1988), and to compare spectral features with compositional parameters (e.g., Sweet and White, 1969; Dufresne et al., 2009). However, KK transforms were not applied to the reflectance spectra in this study, because the transformed data would no longer be equivalent to thermal emission spectra.

2.4.2. Compositional Controls on TIR Spectral Features

Silicate glasses are made of oxygens bonded to 1) cations that form the glass network (T; four-fold network formers like $^{[4]}\text{Si}^{4+}$, $^{[4]}\text{Al}^{3+}$ and $^{[4]}\text{Ti}^{4+}$); 2) network modifiers (M; e.g., Na^+ , K^+ , Mg^{2+} and Ca^{2+}) that break up the silicate network, and; 3) charge compensators (e.g., Na^+ , K^+ and Ca^{2+}) that compensate for charge deficiencies (e.g., excess Al^{3+} relative to Si^{4+} in alumino -

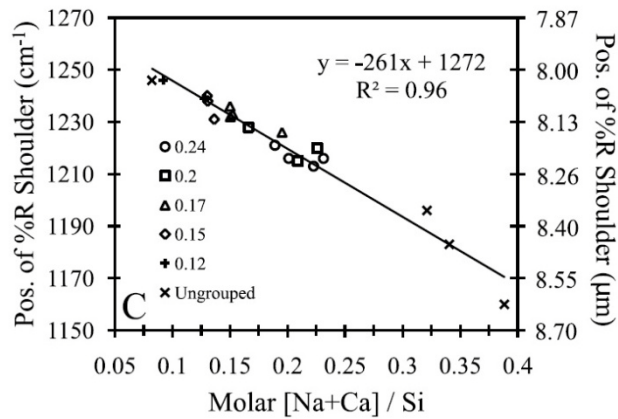
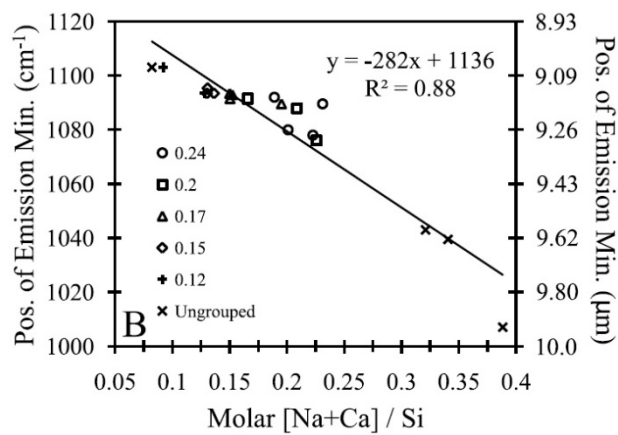
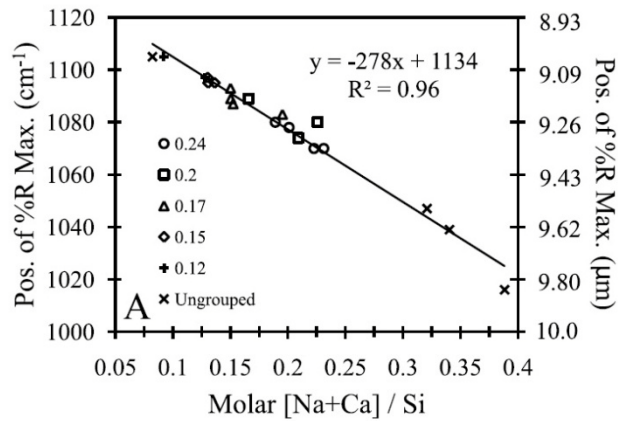


Figure 2-6 Molar [Na+Ca] / Si versus %R maximum position (A), emission minimum position (B) and %R shoulder position (C). An increase in molar [Na+Ca] / Si causes a decrease in the maxima, minima, and shoulder positions.

Table 2-1 Compositional and Spectral Data For Glasses

Symbol ^a	Glass	Starting Group	Ab (wt %)	An (wt %)	Q (wt %)	SiO ₂ (wt %)	Si (mol)	Al (mol)	Na (mol)	Ca (mol)	K (mol)	Percent R Maximum (cm ⁻¹)	Emission Minima (cm ⁻¹)	Percent R Shoulder (cm ⁻¹)
Square	19a	Ab100 – Q	75.31	0.10	24.60	75.27	1.25	0.32	0.28	0.00	0.00	1080	1076	1220
Triangle	22	Ab100 – Q	67.35	0.04	32.61	77.77	1.29	0.28	0.25	0.00	0.00	1083	1090	1226
Plus	1a	Ab100 – Q	47.52	0.03	52.45	83.36	1.39	0.21	0.18	0.00	0.00	1097	1093	1239
Cross	21a	Ab100 – Q	32.21	0.05	67.74	87.54	1.46	0.14	0.12	0.00	0.00	1105	1103	1246
Cross	24 ^b	Ab90An10 – Q	86.11	11.38	2.50	66.53	1.11	0.45	0.32	0.04	0.01	1047	1043	1196
Square	28 ^b	Ab90An10 – Q	61.37	9.54	29.09	74.76	1.24	0.34	0.23	0.03	0.01	1074	1088	1215
Triangle	27 ^b	Ab90An10 – Q	48.65	6.72	44.64	80.17	1.33	0.28	0.18	0.02	0.01	1087	1093	1233
Cross	3	Ab73An27 – Q	74.03	25.97	0.00	62.44	1.04	0.48	0.27	0.09	0.02	1039	1039	1183
Circle	6	Ab73An27 – Q	58.03	17.64	24.33	71.96	1.20	0.37	0.22	0.06	0.01	1070	1090	1216
Circle	19	Ab73An27 – Q	54.88	19.37	25.75	71.79	1.19	0.38	0.20	0.07	0.02	1070	1078	1213
Triangle	2	Ab73An27 – Q	40.23	14.21	45.57	78.78	1.31	0.28	0.15	0.05	0.01	1093	1093	1236
Triangle	2a	Ab73An27 – Q	40.04	14.48	45.48	78.55	1.31	0.28	0.15	0.05	0.01	1089	1092	1232
Diamond	20a	Ab73An27 – Q	37.04	13.22	49.74	80.27	1.34	0.26	0.14	0.05	0.01	1095	1093	1231
Diamond	20	Ab73An27 – Q	36.40	12.21	51.38	81.52	1.36	0.25	0.13	0.04	0.01	1095	1095	1238
Diamond	1	Ab73An27 – Q	36.01	12.41	51.58	80.85	1.35	0.25	0.13	0.04	0.01	1097	1093	1240
Plus	21	Ab73An27 – Q	26.28	9.62	64.11	85.29	1.42	0.19	0.10	0.03	0.01	1105	1103	1246
Cross	23 ^b	Ab50 – Q	48.63	51.37	0.00	55.16	0.92	0.10	0.18	0.18	0.01	1016	1007	1160
Circle	8	Ab50 – Q	32.27	33.23	34.50	70.53	1.17	0.37	0.12	0.12	0.01	1078	1080	1216
Circle	26 ^b	Ab50 – Q	28.93	33.38	37.69	71.34	1.19	0.36	0.11	0.12	0.01	1080	1092	1221
Square	7	Ab50 – Q	28.11	28.69	43.21	74.75	1.24	0.32	0.11	0.10	0.01	1089	1092	1228

^a Symbols represent those in Figure 2.1

^b From Byrnes et al. (2007)

silicate glasses) (e.g., Neuville et al., 2004). The network formers bond to either bridging oxygens that are bound to another network former (T-O-T bonds) or non-bridging oxygens where there is a network modifier (T-O-M bonds).

2.4.3. Effect of SiO₂ on TIR Spectral Features

The results showing that the R% maximum and emission minimum band locations increase as SiO₂ increases (Figures 2-4A, 2-4B) agree with other studies (e.g., Sweet and White, 1969; Domine and Piriou, 1983; Poe et al., 1992; McMillan et al., 1998; Angeli et al., 2000; De Maeyer et al., 2002; Dufresne et al., 2009). These studies showed that the IR peak location is related to the average bond length of the bulk glass: as SiO₂ increases, the average bond in the glass is shorter. The average bond distance decreases because there is an increase in the number of T-O bonds (more polymerized) that have a shorter bond distance (~1.6-1.7 Å) relative to M-O bonds (less polymerized) that have longer bond distances (~2-3 Å) and higher co-ordination numbers (e.g., De Maeyer et al., 2002; Guillot and Sator, 2007).

Similarly, the position of the %R shoulder location increases as SiO₂ increases (Figure 2-4C). This observation is consistent with previous workers (e.g. Dalby et al., 2006; King et al., 2008; Dufresne et al., 2009). Because the position of the %R shoulder location is highly correlated with wt. % SiO₂ ($R^2 = 0.94$) with little scatter (Figure 2-4C) it is probable that the average bonds contributing to this vibrational feature are highly polymerized, shorter bonds (e.g., like those in SiO₂ glass).

2.4.4. Effect of Molar Al / [Al+Si] and [Na+Ca]/Si on TIR Spectral Features

If the local charge-balance is disrupted (e.g. by adding excess Na⁺, K⁺, or Ca²⁺), then Al may become a network modifier with either five- or six-fold coordination (^[5]Al or ^[6]Al). The influence of Al coordination, Al content, alkali and alkaline earth content on glass structure have all been extensively examined using Raman spectroscopy (e.g. Neuvillle and Mysen, 1996; Neuvillle et al., 2004; Neuvillle et al., 2006). Those studies found that the addition of ^[4]Al to silicate glasses results in Raman silicate stretching bands at 900 – 1300 cm⁻¹ that show a progressive decrease to lower wavenumbers. However, this spectral effect is not observed with ^[5]Al or ^[6]Al. This study examined the effect of adding ^[4]Al, because Al was added to the glasses via feldspars, without adding excess charge. The addition of ^[4]Al, examined in terms of molar Al / [Al+Si], causes the Si-O band position to shift to lower wavenumbers in % R spectra (Figure 2-5A, 2-5C) and emission spectra (Figure 2-5B). These findings are supported by observations in other glasses, where increasing Al / [Al+Si] results in longer average bond distances (e.g., alkali aluminosilicate glasses; Neuvillle and Mysen, 1996).

Because alkali and alkaline earth oxides strongly affect glass structure and bond lengths, the effect on spectral features of adding molar [Na+Ca] relative to Si (i.e. increasing molar [Na+Ca] / Si, but charge balancing with ^[4]Al³⁺) was also examined. Due to the large effect of Si, increasing molar [Na+Ca] / Si causes the Si-O band positions to decrease in wavenumber and intensity, and broaden, as the Si-O bond angle decreases and the average bond length decrease

(e.g. Sweet and White, 1969; McMillan et al., 1998; de Maeyer et al., 2002) (Figures 2-6a – 2-6C). In general, the correlations between the % R spectral features and molar [Na+Ca] / Si are excellent (i.e., high R^2 and little scatter).

It is hypothesized that Na+Ca have a stronger control on the average bond length of the glass than Al. Support for this hypothesis comes from calculations for rhyolitic glasses where $^{18}\text{Na-O}$ bond distances are $\sim 2.5 \text{ \AA}$ and $^{7}\text{Ca-O}$ bond distances are $\sim 2.4 \text{ \AA}$; whereas, $^{4}\text{Si-O}$ bond distances are $\sim 1.6 \text{ \AA}$ and $^{4}\text{Al-O}$ bond distances are $\sim 1.7 \text{ \AA}$ (Guillot and Sator, 2007). In other words, one mole of Na+Ca will have a greater effect than one mole of Al on increasing the average bond length of a silicate glass. Therefore, the factor Na+Ca / Si shows an excellent correlation with the TIR spectra because increasing Na+Ca tends to increase the average bond length and increasing Si tends to decrease the average bond length. In sum, Na+Ca / Si is a good proxy for the average bond length of these felsic glasses and therefore there is an excellent correlation between Na+Ca / Si and TIR spectral features.

2.4.5. Comparison of Spectra At Atmospheric Pressure With Spectra At High Pressure

The glasses in this study were prepared at atmospheric pressure; however, felsic silicate glasses commonly form at high pressure in impact events, particularly in extraterrestrial environments. Laboratory modeling of pressure shocked plagioclase feldspars (Johnson et al., 2003) and the study of shocked feldspars using Thermal Emission Spectrometer (TES) data from Mars (Johnson et al., 2006) have shown that plagioclase undergoes structural changes with increasing pressures, which affect the position and morphology of spectral features. Compression of the

silica tetrahedral structure causes the average bond length (and perhaps angle) to decrease, affecting the bending and stretching motions. Spectral features thus become more muted and band depths decrease. The plagioclase Reststrahlen feature also coalesces into a single broad band near 9 μm , making the spectra more glass-like. The features of the glass spectra in Johnson et al. (2003, 2006) shift to lower wavenumbers with increasing Al content and the average bond distances increases. These findings are consistent with the data presented here, and further validate spectral features as accurate indicators of composition and structure in silicate glasses.

2.5 CONCLUSIONS

The results of this study show that the general spectral morphology and the individual positions of the reflectance maxima and emission minima (cm^{-1}) are highly dependent on glass composition. Both reflectance maxima and emission minima show a systematic shift to higher wavenumber with increasing wt. % SiO_2 and decreasing molar $\text{Al} / [\text{Al}+\text{Si}]$ and $[\text{Na}+\text{Ca}] / \text{Si}$ within the glass. These observations are consistent with previous glass compositional studies and with average bond lengths of glasses. This study expands upon the suite of high - SiO_2 glass compositions presented by Byrnes et al. (2007), and further validates the thermal emission spectroscopy technique through comparison to other analytical techniques. The findings presented here may be applied to future TIR remote sensing measurements of surfaces containing a glass fraction. For example, if the spectral shape is consistent with that of glass and the wavenumber position is determined, then the wt. % SiO_2 and molar $[\text{Na}+\text{Ca}] / \text{Si}$ could be

determined. The glass suite presented here provides further insight into the behavior of silicate glass spectra in relation to composition and structure. However, the focus of this study is on laboratory-scale glasses of synthetic compositions. The study of natural glasses using remote sensing techniques introduces a number of variables that were not constrained in the laboratory study. For example, natural glasses are often glass/crystal mixes, and are commonly vesicular. Although the data in this study cannot be directly applied to remote sensing of volcanoes, it does validate thermal emission as a technique for studying glass composition.

This work is the initial facet of examining the effects of short to medium- range Si - O bonding on the infrared spectra of synthetic and natural high - SiO₂ glasses, as the glasses transition from solid to molten states. A better understanding of how the silicate structure of glass directly affects TIR emission during melting and cooling through the glass transition temperature will help improve the ability of current and future remote sensing instrumentation to accurately detect and verify all volcanic glass compositions and physical states, especially during active lava emplacement.

3.0 CONSTRUCTION, CALIBRATION AND TESTING OF THE HIGH-TEMPERATURE MICRO-FURNACE

3.1 INTRODUCTION

Thermal infrared (TIR) emission spectroscopy has proven to be a practical tool for the non-destructive analysis of silicate minerals and rocks. Silicates are a prime focus of spectroscopic studies in geology, because they are the most common rock-forming materials on Earth and other planets. Additionally, vibrational processes of Si-O-Si and Al-O-Al(Si) bonds within silicate materials create prominent, unique and identifiable absorption features in its spectrum (e.g. King et al., 2004 and references therein). However, in an amorphous glassy state, a silicate material undergoes structural changes that in turn alter its spectral signature. All silicate glasses, regardless of composition, display two broad spectral features in the 7 to 25 μm region: one in the $\sim 1100 - 800 \text{ cm}^{-1}$ ($\sim 8 - 12 \mu\text{m}$) region due to Si-O-Si asymmetric stretching vibrations, and another between $500 - 400 \text{ cm}^{-1}$ ($20 - 25 \mu\text{m}$) due to bending vibrations (Bell et al., 1968; Dowty, 1987; Poe et al., 1992; Salisbury et al., 1991; McMillan and Wolf, 1995; Agarwal and Tomozawa, 1997; McMillan et al., 1998). The wavelength location, morphology and depth of these absorptions are also dependent on composition, crystallinity, surface roughness, and

temperature of the glass. Thus, silicate glasses are difficult to distinguish from one another in the TIR, particularly at the lower spectral resolutions commonly encountered with remote sensing TIR data.

Silicate glasses are prominent on the Earth's surface, and occur most commonly in volcanic environments. They form the steep sides of lava domes, occur as glassy crusts on lava flows, and are a significant component in ash plumes and pyroclastic flow deposits. The energy emitted from the surface of an active volcano is complex, variable and unpredictable. Impending volcanic activity is commonly marked by subtle changes in lava composition, temperature, physical state, texture and glass percentage. Thus, the study of active glassy volcanic surfaces, and the ways in which they change over time, is of great importance to volcanic hazard mitigation and assessment.

Glasses are ubiquitous in hazardous volcanic environments on Earth, and on other planetary bodies, and variety of studies have examined the thermal infrared spectra of glasses as a function of composition (e.g. Wyatt et al., 2001; Minitti et al., 2006, 2007; Sweet and White, 1969; Byrnes et al., 2004, 2007; Dalby 2007; Dalby and King, 2006; Dufresne et al., 2009, Lee et al., 2010; Minitti and Hamilton, 2010). Laboratory studies have shown that the morphology and wavelength positions of absorption features are both highly dependent on glass composition and structure. For example, absorption positions shift to lower wavelengths with increasing SiO₂ content, and to higher wavelengths with greater amounts of network-modifying cations, longer Si-O bond distances, and decreased polymerization (Neuville and Mysen, 1996; Dalby et al., 2006; Dalby, 2007; King et al., 2008; Byrnes et al., 2007; Lee et al., 2010; Minitti and Hamilton,

2010; King et al, 2011). Temperature also has a major role in controlling the IR spectra of glasses (e.g. King et al., 2004; McMillan and Wolf, 1995; Agarwal and Tomozawa, 1997). However, no studies yet exist that measure the thermal emission of molten silicate glasses in a well-controlled laboratory environment, as they actively melt and cool through the glass transition temperature, which is defined as the temperature at which a glass transitions from a molten to a solid state.

A micro-furnace has been constructed in order to perform *in-situ* laboratory thermal emission analysis of silicate glasses. The design, construction, implementation, and calibration of the micro-furnace are presented here. In addition, preliminary thermal emission spectra of a quartz sand, an oligoclase feldspar mineral, and glassy melt of rhyolitic composition are discussed. With this novel equipment and technique, the ways in which thermal emission spectra are affected by the melting and cooling of silicate glasses through their glass transition temperature will be more accurately understood. This work, along with the accompanying low-temperature work by Byrnes et al (2007) and Lee et al (2010), will help improve the ability to accurately detect and characterize volcanic glass compositions and physical states on active lava flows as well as glass-rich surfaces on the Earth, moon and Mars, using current remote sensing instrumentation. It should also help contribute to the design capabilities of future TIR remote sensing instruments.

3.2 INSTRUMENT DESIGN

The overall design of the micro-furnace is shown in Figure 3-1 A-B and Figure 3-2. The furnace has been modeled after larger laboratory box furnaces. The heating elements hang downwards into the furnace chamber, and are supported by insulation and connected in series via nickel-aluminum braiding. The micro-furnace is rated at 900 W. It is cylindrical in shape, and the inside is composed of nested cylinders of insulating material. The sample sits within a cylindrical tube, surrounded by the heating elements. This acts to more effectively focus radiation from the heating elements onto the sample, making the micro-furnace thermally efficient for its size.

In order to acquire sample spectra, another important design consideration was having the ability to open the micro-furnace via a small sliding door. This exposes the sample to the spectrometer mirror, which is situated directly above the micro-furnace port, and allows for a sample's emission to be focused into the spectrometer port for acquisition. Because the micro-furnace is in such close proximity to other temperature-sensitive equipment, including the glove box itself, it was vital to ensure that the micro-furnace top and sides never exceeded a temperature of 100 °C. A water cooling system was incorporated into the design in order to regulate the exterior temperature. The heating elements, insulating material, water cooling system, and power supply are all modular, which allows for simple removal and replacement of parts. Each component of the micro-furnace is discussed below in detail.

3.2.1 Heating Elements

In order to completely melt glass samples of dacite-rhyolite mineralogy, a maximum sample temperature of 1500 °C is required, as determined by initial synthesis of a suite of synthetic glasses in this compositional range (Byrnes et al., 2007; Lee et al 2010). Heating elements within the micro-furnace must be capable of reaching a temperature of approximately 1800 °C, allowing the target maximum sample temperature to be achieved and also accounting for expected heat losses through the air, the insulation and the power supply. Heating elements capable of reaching this temperature in air include those composed of noble metals such as platinum, and compounds such as molybdenum disilicide (MoSi_2). Platinum is too expensive to be a viable choice. Commercially available metallic (Fe/Cr) and silicon carbide heating elements are limited to maximum temperatures of 1400 °C and 1600 °C, respectively. Tungsten and graphite heating elements can operate at 1800 °C (and much higher) but, due to rapid oxidation, can do so only in a vacuum or an inert atmosphere. MoSi_2 heating elements have a long-running and proven capability for use in industrial and laboratory sintering, heating, glass and metal melting operations.

The micro-furnace utilizes three Sentrotech 4/9 MoSi_2 heating elements each with a hot zone length of 3" and a shank length of 3" (Figure 3-3A). Each is rated at 300 W, providing up to 900 W of power. The micro-furnace easily reaches a temperature of 1500 °C with the elements reaching a temperature of approximately 1700 °C. The heating elements are situated around three sides of the micro-furnace furnace sample holder (Figure 3-3B), and are connected in series with aluminum-nickel braided straps, using a custom mini bus bar system on

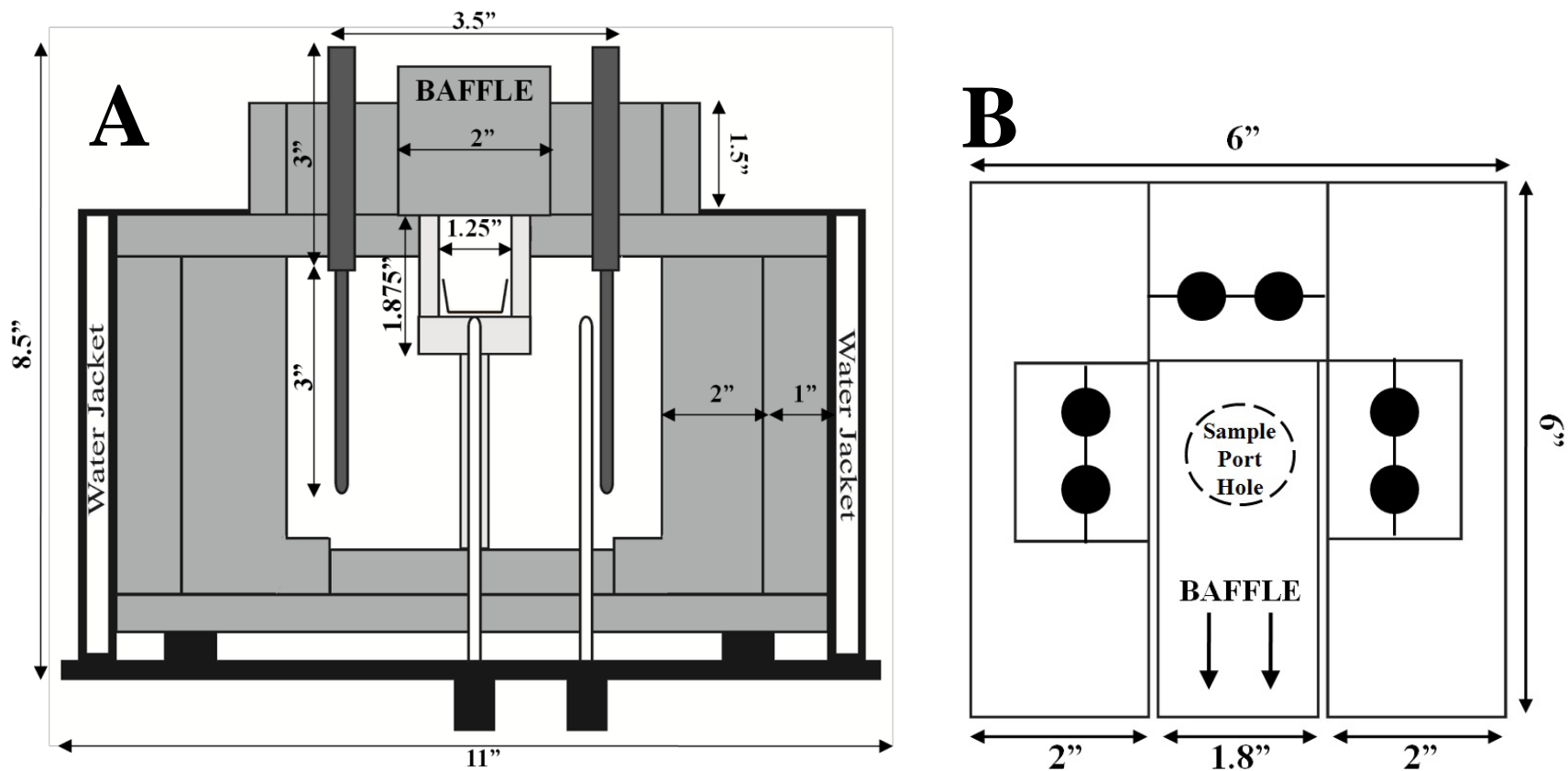


Figure 3-1 (A) Side view of the micro-furnace assembly, without the cooled cover in place. Medium grey-colored areas are insulation, heating elements are shown in dark grey, and the stainless steel shell and water jacket are shown in black. The dense alumina tube and sample support post (very light grey) house the platinum crucible. The heating elements hang downwards into an airspace inside the furnace, and are connected to the power supply via the $\sim 3/4$ " section of shank above the heating element holders. Two B-type thermocouples (white tubes) measure the temperature of the sample and the heating elements, and connect to the power supply through plugs at the bottom of the furnace. (B) Top view of the furnace, without the cooled cover in place. The heating elements (black circles) and their holders surround the sample port hole on three sides. The baffle slides outward to expose the sample to the spectrometer.

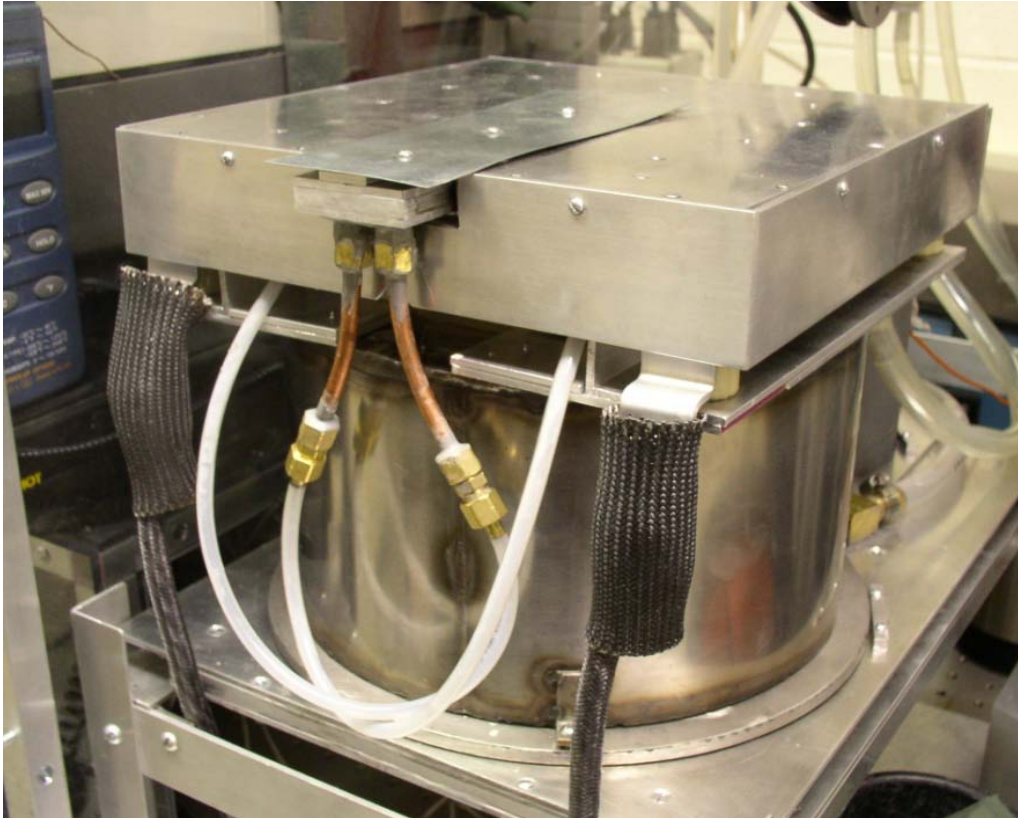


Figure 3-2 The micro-furnace set-up. The micro-furnace is 8.5" in total height, and 11" in diameter at the base. The aluminum and stainless steel square cover on top of the furnace assembly, and the plastic and copper tubing, are part of the water cooling system. Power is provided to the heating elements via the 120A black cables in the foreground.

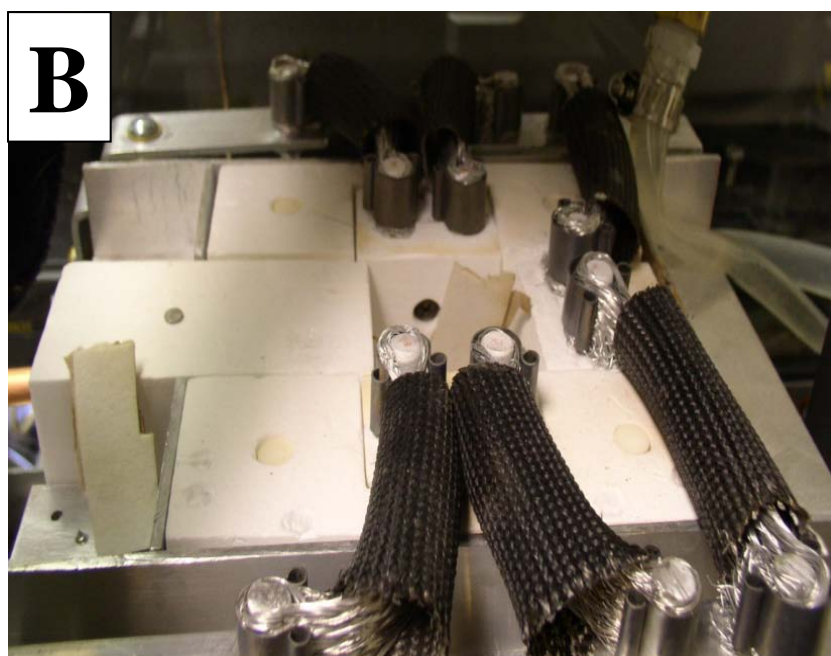
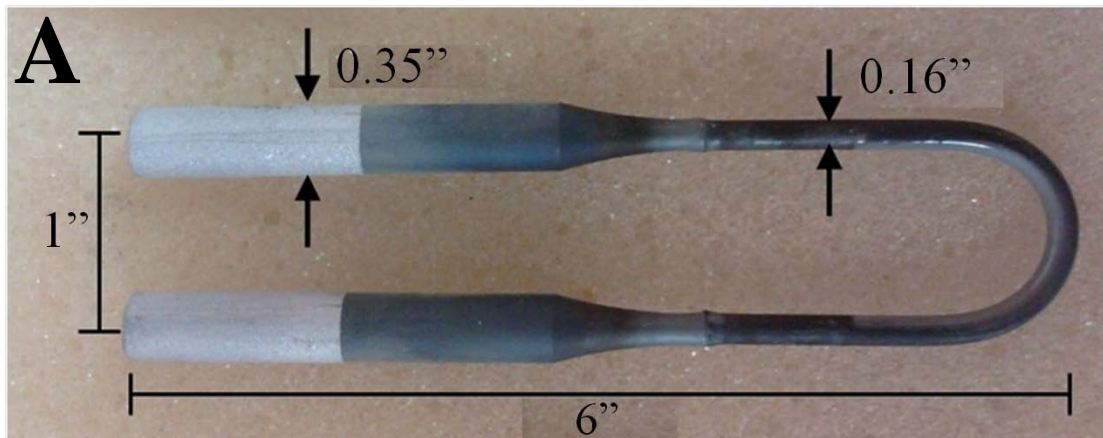


Figure 3-3 (A) MoSi₂ hairpin heating element. (B) The micro-furnace consists of three MoSi₂ heating elements. The elements surround the sample port on three sides, and are connected to the power supply in series via insulated aluminum-nickel braiding.

top the micro-furnace enclosure. The top 3/4" of the element shanks are aluminized to provide good contact with the braided straps at temperatures up to approximately 300 °C. Each element is held in place using a custom, two-part, alumina element holder that allows for easy element removal and replacement.

3.2.2 Power Supply and Temperature Control

The MoSi₂ heating elements require a current and voltage of approximately 90 A at 14 V to reach an element temperature of 1700 °C. An MHI Powerphase ST9001 single phase silicon-controlled rectifier (SCR) power controller, and an ACME T-1-13074 120V/16V 1500VA rated transformer are used to power the heating elements. This transformer is capable of delivering up to 100A at 16V. The SCR is equipped with variable output voltage and current limits and a variable soft-start to control the initial in-rush current to the heating elements, whose cold resistance is approximately one eighth of their hot resistance. The power output from the SCR is controlled by a 4-20 mA current signal.

The power box (Figure 3-4), containing the SCR and transformer, is equipped with an ammeter and voltmeter, and a small internal power supply with a 10 turn potentiometer to provide the 4-20 mA signal when used under manual control. When used under automatic control, this signal is supplied by an Omega CN8201 single output PID temperature controller, with an RS232 connection to the laboratory computer for remote setup and monitoring. The input from a B-type (platinum-rhodium) thermocouple, located directly beneath the sample, is used along with the Omega controller to control the sample temperature. The controller can also

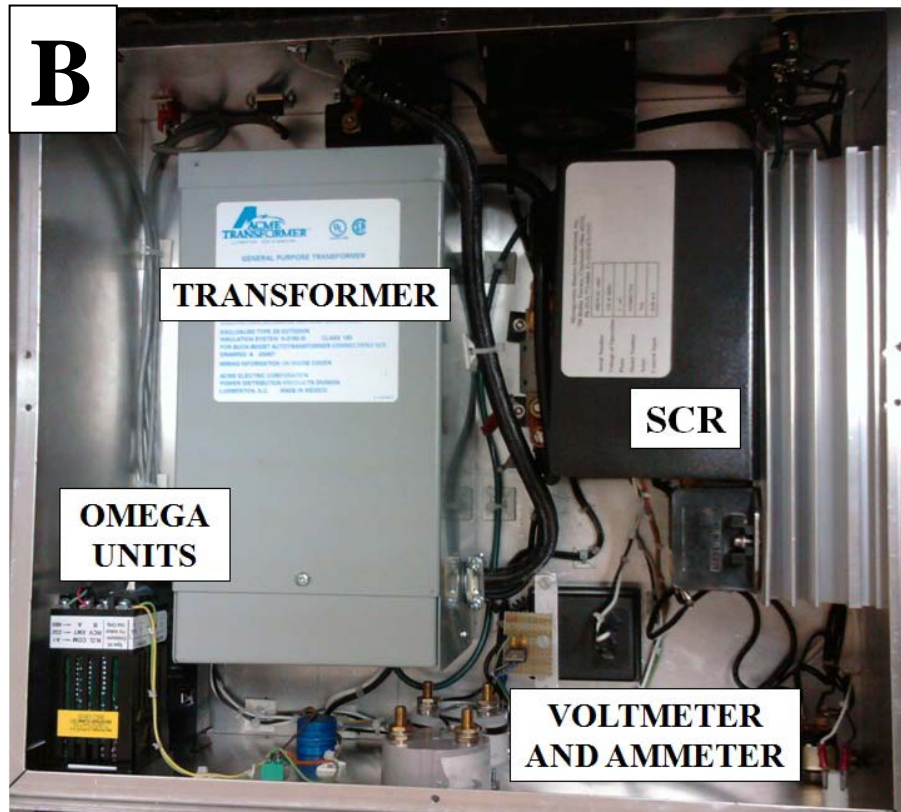


Figure 3-4 (A) Front panel of the power supply, showing the power switch (bottom right) and the voltmeter and ammeter (center). Furnace temperature is controlled via an Omega CN8201 single output PID temperature controller (top left), and heating element temperature is monitored by an Omega DPi32 panel meter. (B) Internal view of the power box, showing the SCR, the transformer, and the Omega units.

be programmed to provide multi-step ramp/soak recipes for the sample. Heating element temperature is monitored using an Omega DPi32 panel meter and an additional B-type thermocouple situated proximal to one of the heating elements. The power supply is connected to the micro-furnace via two 120 A power cables. These cables, as well as the thermocouple and RS232 power cables, are shielded with braided metal cable to help minimize any electromagnetic interference with the internal components of the spectrometer.

3.2.3 Furnace Chamber

3.2.3.1 Insulation

The near-cylindrical internal micro-furnace chamber is composed of SALI alumina insulation from Zircar Ceramics. Alumina insulation is a widely-used refractory insulation material in the furnace industry, due to its high melting point (~2015 °C), high strength, low density, and rigidity. It exhibits superior hot strength and stability at temperatures up to 1825 °C, is non-reactive with most materials, undergoes minimal expansion upon heating, and can be easily cut into various shapes. The micro-furnace consists of two nested 4” tall cylindrical pieces of SALI insulation, with notches cut out for the three heating elements (Figure 3-1). These cylinders sit atop a circular, 1” thick SALI insulation base, which forms the “floor” of the micro-furnace. Another 5/8” thick piece sits above the cylinders. This piece supports the three heating element holders. A 1.5” hole in the center of the top piece houses the sample support post, and the three holes surrounding the sample support post allow for the hairpin heating elements to pass through to the center of the micro-furnace (Figure 3-1).

The sample crucible support post consists of a 1.5" diameter, 0.5" thick dense alumina disk upon which the crucible is situated. The disk has a pass-through hole for the sample temperature thermocouple. A 1.25" ID, 1 3/8" long furnace tube sits on the dense alumina disk, and surrounds the sample crucible (Figure 3-1A). The furnace tube is lined with platinum foil, and acts as a shield for the sample crucible from downwelling radiation of the heating elements and micro-furnace chamber insulation. The entire assembly is supported from underneath by a 3/8" OD, 1/4" ID, 2.52" - long alumina tube, which positions the sample support post at the height necessary to provide a 0.4" spot size from the spectrometer.

The holders, furnace tube, sample support post, and all surrounding insulation exposed to the spectrometer beam path upon opening the micro-furnace port are painted with cerium oxide high-temperature, high-emissivity paint. This paint is water-based, non-reactive, and non-corrosive. The paint provides coating with near-featureless TIR spectra, which prevents the spectral features of alumina from contaminating the sample spectrum. This paint is one of the few cost-effective options for high-emissivity paint that can withstand very high operating temperatures, and do so in an oxidizing environment, without reacting with any materials within the micro-furnace.

The sample chamber is covered with a 2"x 4" baffle (Figure 3-1). This baffle is composed of Fractalin refractory alumina insulation, and acts as a heat shield to protect the spectrometer and surrounding equipment from excess heat as the micro-furnace heats to the desired temperature. When a spectrum is to be acquired, the user slides the baffle to the side using an alumina handle. The baffle slides back into place once the spectrum has been collected.

The baffle is also painted with cerium oxide, in order to keep all internal surfaces of the micro-furnace a consistent composition, and create a near-blackbody environment for calibration purposes.

3.2.3.2 Sample Containment

All samples are melted in platinum crucibles within the micro-furnace. Platinum is used because it has a melting point of approximately 1770 °C, is stable at high temperatures, and is the only material capable of withstanding the high temperatures of the furnace in air without oxidizing or reacting with any surrounding materials or the sample itself. The crucibles are ~1” in diameter, and hold up to 2 grams of sample. Crucibles are loaded into and removed from the micro-furnace using long platinum-tipped tongs. Once a cooled sample is removed from the micro-furnace, it is carefully tapped out of the crucible using a small hammer. Then the crucible is filled with sodium carbonate powder, and placed into a muffle furnace at 900 °C for ~20 minutes. The sodium carbonate acts to remove glass residue from the platinum surface. The cooled sodium carbonate is then removed from the crucible, and the crucible is placed into hydrochloric acid for several hours to dissolve any remaining material. This must be performed after each sample analysis in order to avoid contamination from one sample to the next.

3.2.3.3 Water Jacket

In order to control the heat emitted from the micro-furnace and protect surrounding equipment, a cooling system surrounds the micro-furnace on all sides (Figure 3-1A, 3-2B). Water at a

temperature of 10 °C is circulated through the entire system via a VWR temperature-controlled water circulator and a 10.8 psi water pump. There are three components to the system: a bottom cooling plate, a cylindrical water jacket, and a top cooling cover. Each of the components is independently sealed from one another to avoid leaks. Additionally, the top cooling cover has a water-cooled baffle located directly over the alumina insulation baffle. When a sample spectrum is ready to be acquired, this water-cooled baffle slides aside, along with the alumina baffle. All three components have separate water-in and water-out spouts, and are connected to one another, and to the water circulator, via ½" ID Tygon tubing, which allows for water flow through the micro-furnace at ~10.8 psi.

3.2.3.4 Spectrometer and Glove Box

The micro-furnace, low-temperature (80°C) spectrometer setup, and all accompanying accessories are housed in a Plexiglas glove box adjacent to the external port of a Nicolet Nexus 670 FTIR spectrometer (Figure 3-5). The low-temperature setup sits adjacent to the micro-furnace on a sliding shuttle. The user can slide the shuttle from side to side, to align either the low-temperature emissivity acquisition setup or the micro-furnace setup beneath the spectrometer mirror prior to sample analysis. The spectrometer and the glove box are both continuously purged using a Parker-Balston purge system, which removes CO₂ and H₂O from the environment, maintaining a low relative humidity (<5%). It is important to minimize these TIR-active gases in the environment, because they have significant spectral features and can degraded the spectrometer detector and beamsplitter over time (Ruff et al., 1997). The glove box has several hand-ports that allow for access to all equipment within it without compromising the

purged environment. This includes two sealable ports on the front of the glove box for manipulating samples in the low-temperature setup, and a port on the upper left hand side that allows for operation of the micro-furnace baffle. Each panel of the glove box is fully removable, providing easy access to the micro-furnace and low-temperature setups for any needed maintenance or repair. The glove box is open to the external port of the spectrometer via a hole in the Plexiglas, which allows for the emitted energy from the sample to pass out of the glove box for spectrum acquisition.

3.3 METHODOLOGY

3.3.1 Initial Testing

Prior to operating the micro-furnace within the spectrometer setup, the micro-furnace underwent extensive testing within the laboratory fume hood. The purpose of this testing was to study how the micro-furnace operates, and to determine any potential effects it may have on the surrounding laboratory environment. In the first test, the air temperature above the open micro-furnace port was measured in order to determine the height at which laboratory equipment and accessories can be safely situated above the furnace. A series of three K-type thermocouples were attached to a ring stand every 3" above the port. The micro-furnace was heated in 100 °C increments from 100 °C to 1500 °C, and at each temperature, the port was opened for a 10 second time period. This is the maximum time that the port would be open in order to acquire a

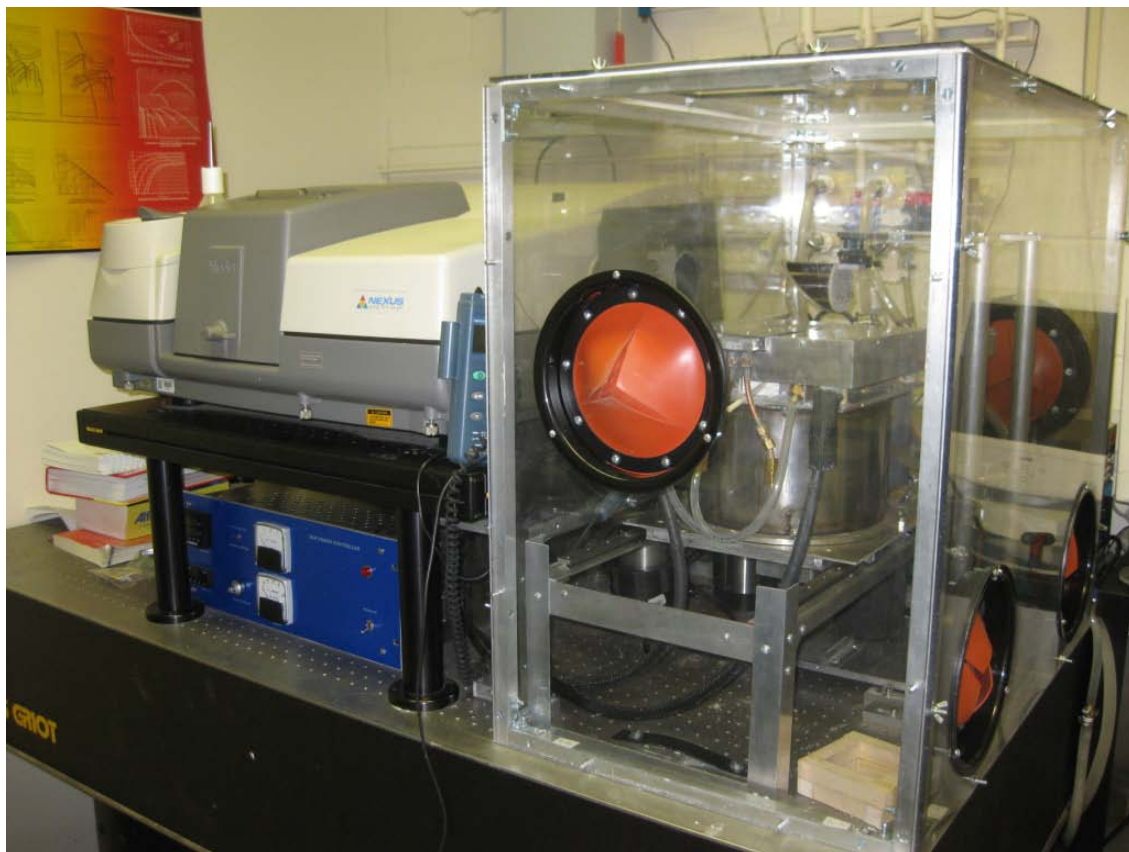


Figure 3-5 IVIS Laboratory spectrometer setup. The spectrometer (left) and Plexiglas glove box (right) sit atop a Melles Griot optical bench, and are continuously purged of CO₂ and H₂O. Red silicone hand-ports on the glove box allow for access to the inside of the glove box for sample preparation and operation of the furnace baffle. The glove box is open to the external port of the spectrometer via a hole in the Plexiglas, which allows for the spectrometer signal to pass into and out of the glove box for spectrum acquisition. The power supply for the furnace sits beneath the spectrometer, and is fully shielded to prevent electromagnetic interference with the spectrometer.

spectrum of a melt. While the micro-furnace was open, temperature data from the thermocouples were digitally collected every second using a Keithley multimeter. An average temperature reading was calculated for each thermocouple at each set point.

To test the efficacy of the water cooling system, the temperatures of the top and sides of the micro-furnace were monitored using a tripod-mounted Forward Looking Infrared (FLIR) camera and a K-type thermocouple surface-mounted to the exterior of the furnace. The micro-furnace was heated in 100 °C increments from 500 °C to 1500 °C, and held at each temperature for 15 minutes. The FLIR camera acquired measurements every 10 minutes. The surface-mounted thermocouple was situated on the top cover near the port, and monitored the change in surface temperature every 50 °C as the micro-furnace heated to temperature.

In an effort to constrain the overall behavior of the heating elements, element temperature and sample temperature data were collected for both an empty platinum crucible and for a quartz sand sample. These data served to document the behavior of the heating elements, the power controller, and the sample temperature as the micro-furnace was heated to given temperatures over time. The difference between sample and element temperature was calculated for an empty crucible and quartz sand, and the overall behavior of this temperature difference was noted. All of these initial test data serve as examples of the performance data gathered for the micro-furnace. If any problems arise, the performance data can be reviewed to determine whether the heating elements, power supply, and other micro-furnace components are performing as expected.

3.3.2 Sample Temperature

In FTIR spectroscopy, measurements are converted into radiance values via the instrument response function (Ruff et al, 1997). The response function is the measure of the spectrometer's voltage output in response to input signal from the sample. For low temperature samples (80 °C), which are measured in the low-temperature setup adjacent to the micro-furnace, the response function is calculated by measuring the emissivity of two known blackbodies at two different known temperatures. The blackbody is a 30° cone painted with high-emissivity blackbody paint, and heated using heating pads at the bottom and top of the cone. The temperature of the blackbody is measured using two platinum resistance thermometers (PRTs). These blackbody measurements are used to calculate the response function of the spectrometer, and ultimately, the emission spectrum of the sample. This method of deriving emissivity is called the one-temperature method, and is described in detail in Ruff et al. (1997).

For the micro-furnace setup, direct temperature measurement of a blackbody material and a sample is not easily done. The sample thermocouple situated beneath the platinum sample crucible measures the temperature of the crucible, and acts as the assumed sample temperature. However, FLIR measurements of samples within the crucible show that the actual sample temperature can vary from that of the crucible, which suggests the temperature at the bottom of the crucible is much hotter than that of the sample surface. The size of this difference is dependent upon the sample and furnace set point temperature. This gradient can be intensified and introduced into the sample spectrum when the micro-furnace is opened for spectrum acquisition, and the sample surface begins to cool with exposure to the air. This temperature

differential between the sample surface and the thermocouple cannot be avoided in the current design and with the high temperatures of the furnace. The sample thermocouple and FLIR camera were therefore used together to assess the general behavior of sample temperature.

At each set point, the micro-furnace port was opened and ten FLIR images were acquired of the sample within the crucible, one image every second, to simulate the ten seconds that the furnace would be open for spectrum acquisition. During post-processing of the FLIR data, a 0.4” diameter annotated circle was added to each FLIR image, to approximate the spot size of the spectrometer. The average sample temperature within the circle was determined, and the ten average sample temperatures for the ten FLIR images at each set point were then averaged together. This provided an overall average sample temperature for the time in which the furnace port would be open under the spectrometer.

3.3.3 Calibration

No material has been found that is perfectly blackbody across the entire temperature range of the furnace, which can also operate within the micro-furnace environment. External blackbody standards which go up to 2500 °C do exist, but they are very expensive, and also would not be situated in the same environment than the sample, which would invalidate the one-temperature calibration approach of Ruff et al. (1997). However, a near-blackbody material was found that allows for an approximation of a blackbody environment. Cerium oxide (CeO_2) is a nearly spectrally featureless, near-blackbody material. It comes in many forms, including paint, woven cloth and pellets. Ceria pellets are ideal for the micro-furnace calibration, as they are similar in

size and shape to the glass samples being melted, and thus allow for an accurate representation of the micro-furnace environment. Because the temperature of the cerium oxide pellets cannot be directly and accurately measured within the micro-furnace, and because the environment temperature within the micro-furnace is dynamic at any given set point, the one-temperature method still cannot be used to derive accurate absolute emissivity spectra for glass melts. However, the pellets do allow for a measure of the blackbody signal intensity vs. wavelength response of the spectrometer detector, from which relative emissivity spectra can be derived. The method devised for doing this is described below.

First, using the low temperature (80 °C) calibrated laboratory setup and the one-temperature method, an absolute emissivity spectrum was collected for each of the glass samples once they were slowly cooled to room temperature in the micro-furnace (as described in the next section). The wavelength location of the Christiansen frequency was then found for each of these absolute emissivity spectra. The Christiansen frequency is defined as the wavelength of maximum sample transparency (maximum emissivity) in a TIR spectrum (Moersch and Christensen, 1995), and over 95% of minerals have been found to have Christiansen frequencies within the 7 to 14 μm range (Salisbury et al., 1991). The Christiansen frequencies for the 80 °C glass spectra in this study occur at 7.5 μm .

Due to a suspected phase change in the ceria pellets above 1200 °C, the signal intensity of the ceria drops off dramatically with increasing temperature. This makes the ceria pellets difficult to use as a spectrometer calibration standard above 1200 °C . To account for this phase change, and provide calibration spectra up to 1600 °C, the signal intensity data at 7.5, 9.5, and 14

μm for all the set points were plotted. These wavelengths were chosen because the Christiansen frequency of absolute emissivity spectra of the glasses occurs at $7.5 \mu\text{m}$, the main absorption feature of glass occurs between 9 and $10 \mu\text{m}$, and the wavelength range for the main absorption feature spans 7 to $14 \mu\text{m}$.

The calibration curves were then extended by fitting a third-order polynomial curve to the data. This was done in order to simulate a Stefan-Boltzmann-like curve shape. The intensity values were then derived for $1300 \text{ }^\circ\text{C}$ – $1600 \text{ }^\circ\text{C}$ at each wavelength, using the polynomial curve. These derived intensity values were divided by the signal intensity value at $1200 \text{ }^\circ\text{C}$ to create a scaling factor. The scaling factor was then applied to the signal intensity values, from 7 to $14 \mu\text{m}$, for each of the four temperatures. This process created a set of high-temperature ceria pellet reference spectra with a similar shape to the $1200 \text{ }^\circ\text{C}$ ceria pellet spectrum, but with signal intensity increasing with temperature as a close approximation to what is expected from the Stefan-Boltzmann law (Rybicki and Lightman, 1979; Jensen, 2007).

It is important to note that this calibration method does not calculate a true response function for the spectrometer, as the temperature of the ceria pellets cannot be determined because of the approximation of the blackbody measurements, temperatures and the environmental temperatures. However the method does account for the normal DTGS detector signal intensity drop-off with increasing wavelength that occurs for both the sample and the ceria pellets without the need for a high temperature blackbody. In other words, this approach avoids the need for a high temperature blackbody by leveraging the micro-furnace spectra off of the

Christiansen frequency to derive relative emission spectra. Furthermore, the scaling of the featureless ceria spectra in this way accounts for the fact that the emissivity of ceria is less slightly less than 1.

3.3.4 Spectrum Acquisition of Glasses and Melts

Thermal emission spectra were collected in the Image Visualization and Infrared Spectroscopy (IVIS) Laboratory, at the University of Pittsburgh, using a Nexus 870 spectrometer. Prior to melting glass samples within the micro-furnace, it was important to first test a sample with a well-known TIR spectrum, that would not melt within the temperature range of the micro-furnace. This would ensure that the spectra acquired from the micro-furnace using the calibration method were accurate, and that spectral features were being properly resolved. Quartz sand was chosen as a first test sample because it has identifiable spectral features, and it has a melting point higher than that of the micro-furnace temperature range. The quartz sand was placed into the platinum crucible, and spectra were acquired at 100 °C intervals from 500 °C to 1000 °C. The sample was soaked at each set point for 5 minutes before acquisition, to ensure that the sample was as isothermal as possible.

One of the synthetic glass samples, glass 2 ($\text{Ab}_{40}\text{An}_{14}\text{Q}_{46}$), was the first glass sample to be melted, and was used to test the melting capacity of the furnace. Approximately 2 grams of glass 2 was crushed into millimeter-sized pieces. The sample was placed into a platinum crucible, and heated to 1400 °C, approximately 200 °C above its liquidus. This was done in order to ensure that all the glass particles were fully melted. Spectra were acquired of the glass

in 100 °C intervals, from 1400 °C down to 500 °C in order to mimic the cooling behavior of a natural glassy lava. The glass was soaked for approximately 5 minutes at each set point. The top port of the micro-furnace was then opened to expose the sample for analysis. Because of the extreme signal intensity associated with the hot sample, and the variable and dynamic environmental temperatures within the micro-furnace, spectra were acquired over only 6 scans (~10 seconds). Once the glass had fully cooled to room temperature, a low-temperature (80 °C) spectrum was acquired again, for comparisons to previous spectra of the cooled sample as well as to the high-temperature spectra.

The signal intensity of the glass at each temperature was then divided by the adjusted signal intensity of the ceria pellets, as described above, to yield a relative emissivity spectrum at each set point. This resulted in data that were directly comparable to each other, as well as to the 80 °C emissivity spectra taken of the glass after it had completely cooled. Emission spectra were assigned an emissivity of 1 at both 7.5 and 14 μm , and linearly scaled based on the difference in emissivity between 1 and the observed emissivity of the spectra at 7.5 and 14 μm . The emissivity minimum value, and the wavelength position of the emissivity minimum, was located for each of the glass spectra.

3.3.5 Comparison of Quenched and Slowly-Cooled Oligoclase Feldspar

The laboratory emission spectra of crystalline and vitrified oligoclase feldspar were studied by Ramsey (1996), in order to determine the spectral changes that occur from a crystalline to a fully glassy physical state. Samples of oligoclase were heated to four different temperatures (unfused,

1130 °C, 1220 °C and 1490 °C) and quickly quenched. TIR emissivity spectra of the four samples were then acquired in order to characterize the spectral changes that occurred as the oligoclase transitioned from a completely crystalline material to a completely glassy material (as well as within the two-phase field of oligoclase). The spectral features inherent in crystalline oligoclase began to disappear at ~1200 °C, and were replaced by the characteristic broad absorption features of a glassy material. At 1490 °C, the spectrum of the sample indicated that the sample was completely glassy.

Emission spectra of an oligoclase powder (~20 to 80 μm) were acquired in the micro-furnace from 1500 °C to 500 °C to ensure that the oligoclase powder underwent a complete transition from crystalline mineral to glass. The 1500 °C, 1200 °C, 1100 °C, and 80 °C spectra acquired in the IVIS laboratory were then compared to the four spectra presented in Ramsey (1996). For ease of comparison, a series of wavelengths was chosen between 7 and 14 μm and the emission value at each wavelength was plotted for each of the spectra.

3.4 RESULTS

3.4.1 Furnace Testing

The arrangement of the three K-type thermocouples used to measure the air temperature above the micro-furnace port is shown in Figure 3-6A, and the change in air temperature is plotted in

Figure 3-6B. At all set points up to 1500 °C, the temperature above the open port did not exceed 55 °C at any of the thermocouples in the 10 second time period that temperature was measured. Therefore it was determined that opening the micro-furnace port to acquire spectra was determined should have no potential adverse effects on surrounding equipment. The surface-mounted thermocouple placed near the port measured the surface temperature of the water-cooled cover every 50 °C. Although the cover temperature increased steadily with increasing micro-furnace temperature, it did not exceed an outer surface temperature of 35 °C at any point during micro-furnace operation (Figure 3-7), even near the edges of the port. This confirmed the efficiency of the water cooling system in drawing excess heat away from the outer surfaces of the micro-furnace.

Because the heating elements are required to heat the sample to a specific temperature while also accounting for heat losses through the air, the furnace parts, and the power supply, it is expected that the heating element temperature will exceed the sample temperature at any given time. Element temperature vs. sample temperature was compared for a bare platinum crucible and a crucible with a quartz sand sample (Figure 3-8A). Whereas heating element temperature remains the same in both cases, as was expected, both the quartz sample and the bare crucible temperatures differ from the element temperature by as much as 250 °C.

There is a consistently larger difference in temperature between the quartz sample and the heating elements, compared to the bare crucible and the heating elements. This indicates that the difference in temperature between the sample and the heating elements is dependent on the thermal conductivity of the sample, quartz having a lower conductivity than that of platinum.

Figure 3-8B represents the calculated difference between sample temperature and heating element temperature for both the bare crucible and the quartz sample. The platinum crucible has a lower overall temperature difference than the quartz; however both behave similarly over the range of set point temperatures.

3.4.2 Sample Temperature

FLIR images were collected of glass samples during furnace operation at a range of set point temperatures in order to visually examine the temperature structure and heat loss within the furnace sample chamber. One example of the 1500 °C set point is shown in Figure 3-9A. The walls of the micro-furnace port appear cooler than the glass sample, and areas of much hotter temperatures can be seen around the edges of the sample crucible. This illustrates the variable temperatures that can exist within the furnace environment at a given set point. Figure 3-9B shows the decrease in FLIR-derived sample temperature over a 10 second time period for the glass sample, at three set point temperatures. As expected, the higher the set point the more sharply the sample temperature decreases during the 10 second time period that the micro-furnace port is opened. This analysis confirms that sample temperature is dynamic over the course of a spectral acquisition, and thus cannot be used to accurately simulate a blackbody in order to derive the instrument response function.

3.4.3 Calibration

A phase change in the cerium oxide pellets at approximately 1200 °C causes the overall shape of the signal intensity to change at temperatures exceeding 1200 °C (Figure 3-10), which in turn

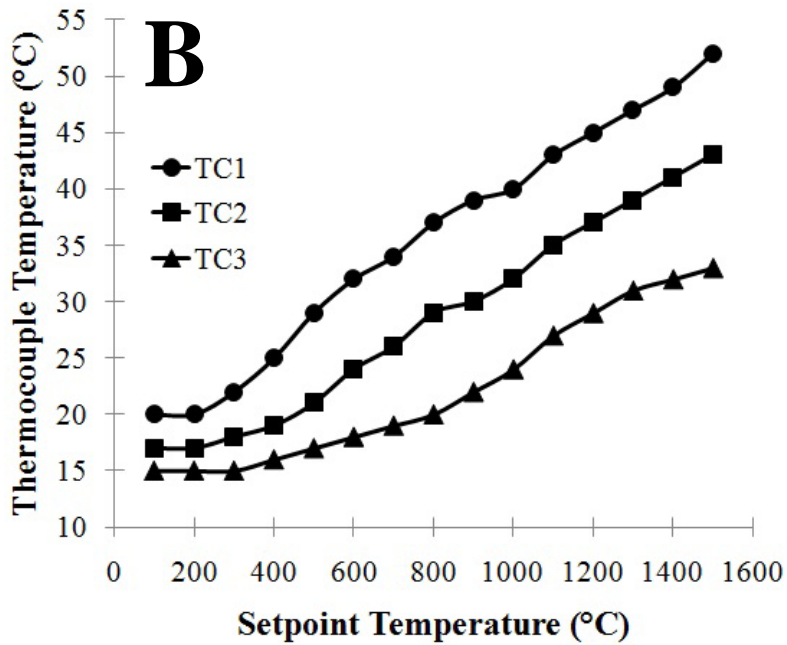
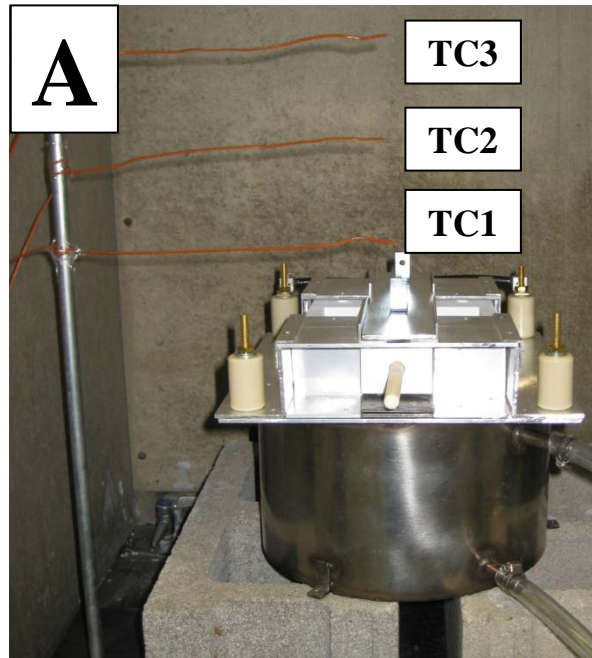


Figure 3-6 (A) Testing the air temperature over the furnace port from 500 °C to 1500 °C using a series of three K-type thermocouples attached to a ring stand at 3” increments. (B) Thermocouple temperatures over the furnace port for each of the three thermocouples. Each point represents the average temperature measured by the thermocouple over a 10 second time period in which the furnace port was open at each set point. TC1 is closest to the furnace port, and TC3 is the furthest. Temperature steadily rises with increasing set point, but none of the thermocouples ever exceed 55 °C.

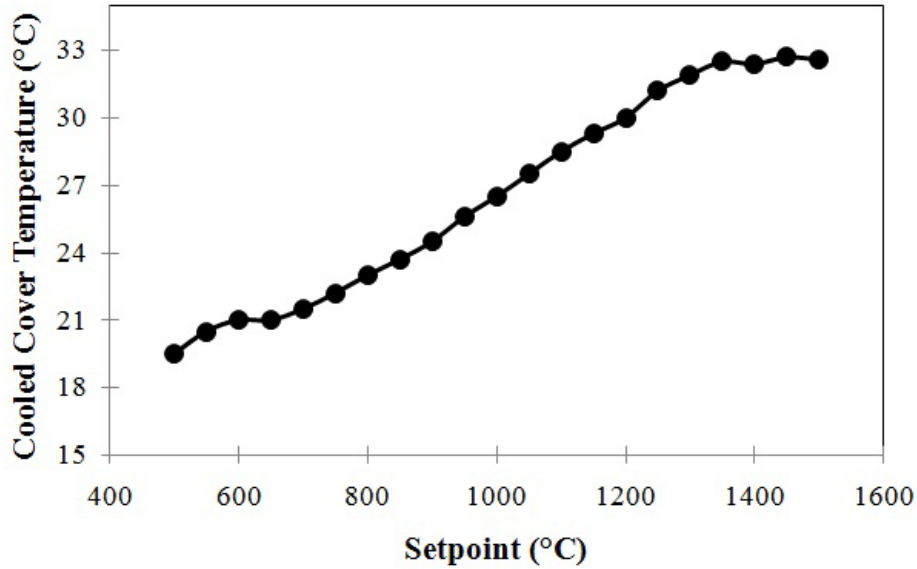


Figure 3-7 Change in cooled cover temperature with increasing set point. The temperature of the cover steadily increased with increasing set point, but never exceeded 35 °C.

affects the shape of the relative emissivity spectra at higher temperatures. In order to correct for this, the original (measured) signal intensity data of the pellets at each set point temperature for three different wavelengths (7.5, 9.5, and 14 microns) were found (Figure 3-10). These data were then plotted against a third-order polynomial curve for each of the three wavelengths (Figure 3-11). The original (measured) intensity data at each wavelength are plotted from 500 °C to ~1500 °C, and show the drop in signal intensity after 1200 °C. The calculated third-order polynomial curve demonstrates how the corrected data from 1300 °C – 1600 °C are derived. Original (measured) signal intensity values are scaled upwards to match those of the third-order polynomial curve, and correct for the drop in signal intensity at temperatures > 1300 °C. The high degree of correlation between the calculated third-order polynomial curves and the measured intensity data illustrates the validity of using this process to derive corrected intensity

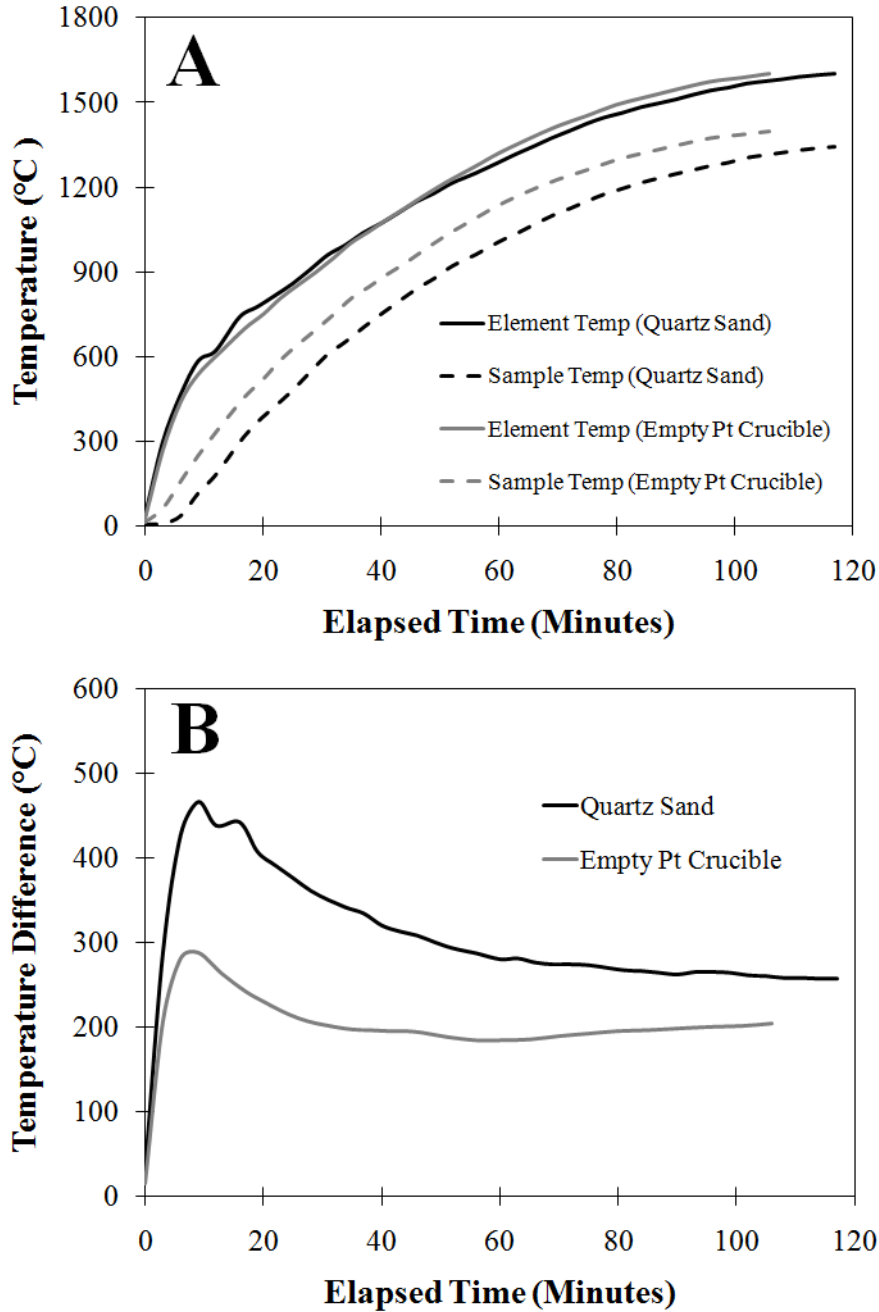


Figure 3-8 (A) Element temperature vs. sample temperature for an empty Pt crucible (grey lines) and a quartz sand sample (black lines). Element temperature remains virtually the same, as is expected; however the quartz sand has a consistently larger temperature difference from the heating elements, and is also lower in temperature than the platinum crucible. This can be attributed to a difference in thermal conductivity between the bare crucible and quartz sand. (B) The calculated difference between element and sample temperature over time. In both cases, the temperature difference is sharp as the heating elements initially heat up much faster than the sample. Eventually, the sample temperature stabilizes at ~200 °C - 250 °C lower than the heating elements.

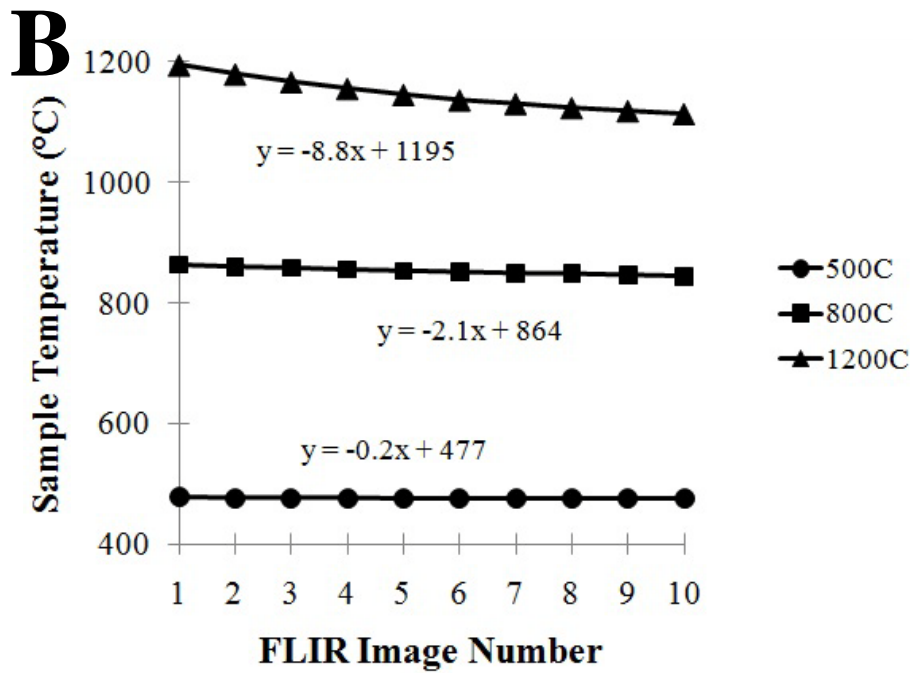
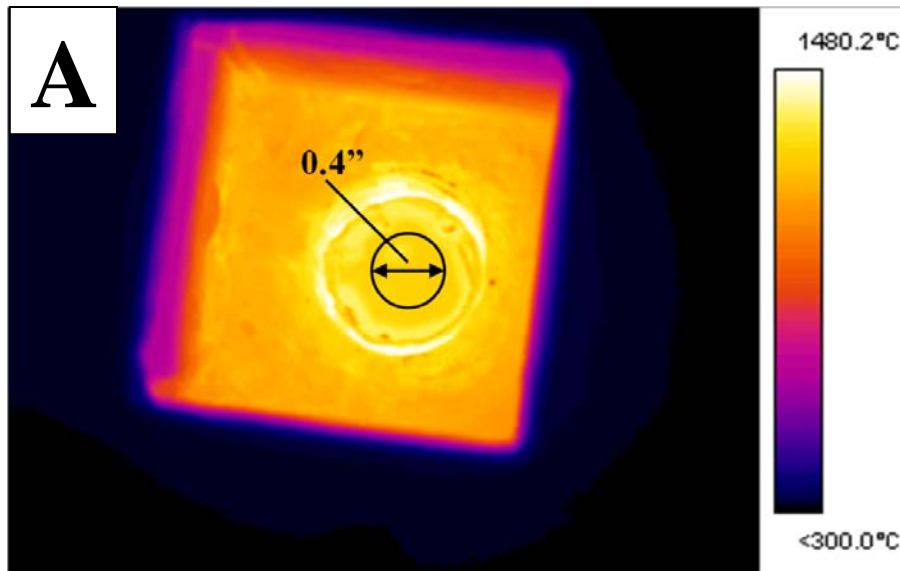


Figure 3-9 (A) Example FLIR image of a glass sample in the furnace, taken at a sample temperature of approximately 1500 °C. The black 0.4"-diameter circle represents the spot size of the spectrometer. (B) Glass sample temperature over a 10 second time period (1 FLIR image/second) for the same glass sample as in A. Sample temperature was analyzed at three furnace set points: 500 °C, 800 °C and 1200 °C. The higher the set point, the more sharply the sample temperature decreases over the 10 second time period. This is illustrated by the more negative slope of the temperature line with increasing set point temperature.

data above 1200 °C. The set of corrected high-temperature ceria reference spectra (Figure 3-12) show signal intensity increasing with temperature as a close approximation to what is expected from the Stefan-Boltzmann law (Rybicki and Lightman, 1979; Jensen, 2007).

3.4.4 Micro-furnace Spectra of Quartz Sand

A series of quartz sand spectra were initially collected using the micro-furnace. These spectra, including a spectrum of the quartz sand at 80 °C using the low-temperature setup, are shown in Figure 3-13. The furnace spectra were calibrated using the previously described methodology. Although somewhat muted compared to the features in the 80 °C quartz spectrum, the Reststrahlen feature of quartz is resolved in the 80 °C, 300 °C, and 400 °C spectra. This muting is likely due to side-welling reflectance in the furnace chamber that is not completely removed with the current calibration. At 500 °C, the characteristic doublet feature of the quartz at 9 microns becomes significantly less prominent, and disappears at temperatures above 600 °C. This change in spectral shape with temperature is attributed to the alpha-to-beta phase transition of quartz (Gervais and Piriou, 1975). Additionally, the average emissivity increases with temperature (Figure 3-14), demonstrating the change in signal intensity and spectral shape with increasing temperature.

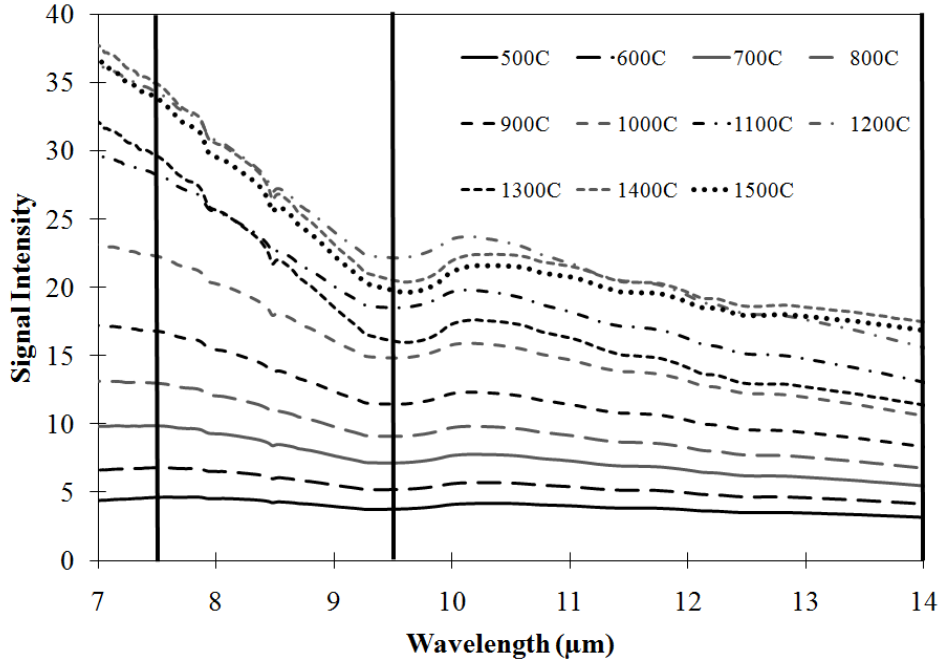


Figure 3-10 Original ceria pellet signal intensity data from 500 °C to 1500 °C. At temperatures below 1200 °C, signal intensity rises systematically with increasing temperature. Above 1200 °C, the intensity spectra become more variable in intensity. Black lines at 7.5, 9.5, and 14 microns indicate the signal intensity values plotted against the third-order polynomial curves shown in Figure 3-11.

3.4.5 Synthetic Glass Melt

Synthetic glass samples were melted within the micro-furnace in order of increasing liquidus temperature. Relative emissivity spectra of glass 2 ($\text{Ab}_{40}\text{An}_{14}\text{Q}_{46}$) from 1400 °C to 500 °C are shown in Figure 3-15. As expected, differences in spectral characteristics can be seen with decreasing temperature. Between 1400 °C and 1200 °C, the emissivity minimum value rises sharply and the minima position shifts towards shorter wavelengths relative to the other spectra. This corresponds with the liquidus of the glass (~1250 °C). Below 1200 °C, both the emissivity

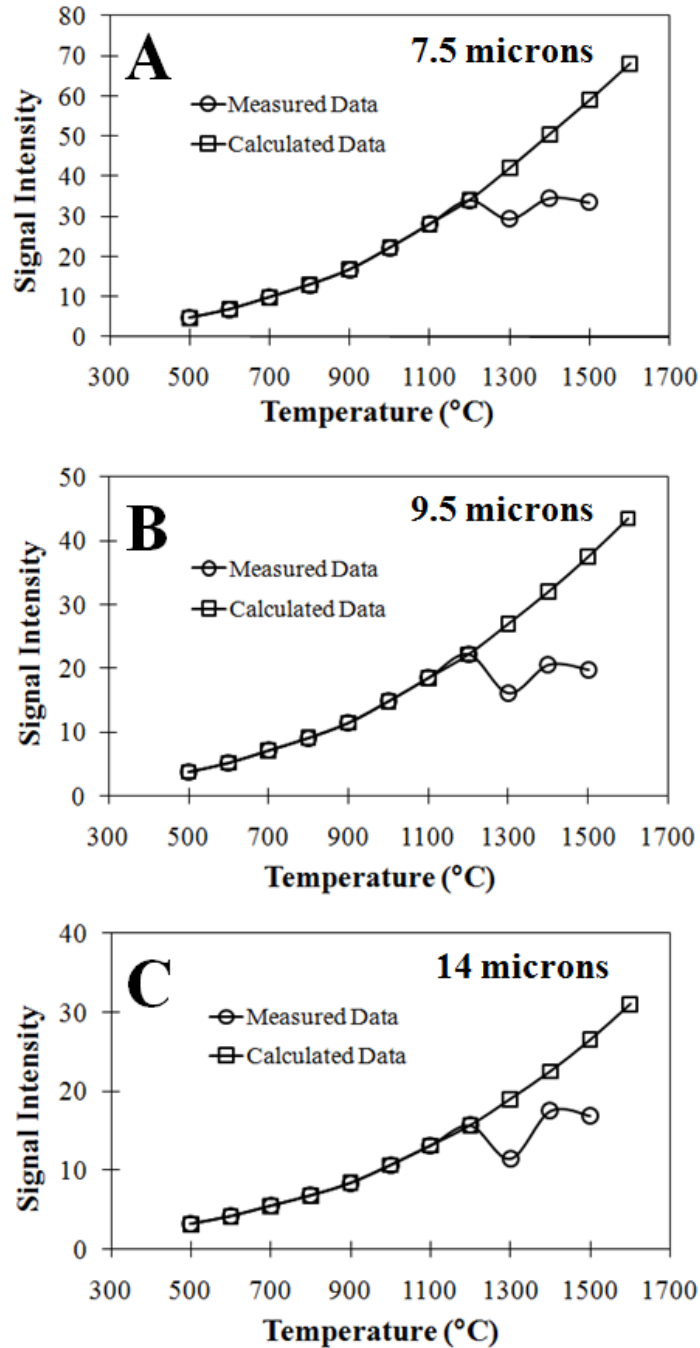


Figure 3-11 (A) The third-order polynomial curve-fitting process for the signal intensity data at 7.5 μm . Each point on the Measured Data curve represents the signal intensity value of the ceria pellets at 7.5 μm , from 500 $^{\circ}\text{C}$ to 1400 $^{\circ}\text{C}$. At 1200 $^{\circ}\text{C}$ and above, the data deviates from the third order polynomial curves (Calculated Data), due to a drop-off in signal intensity of the ceria pellets at temperatures higher than 1200 $^{\circ}\text{C}$. To correct for this, the Measured Data points were scaled to the Calculated Data polynomial curve, using a calculated scaling factor. Data at (B) 9.5 μm and (C) 14 μm are also shown.

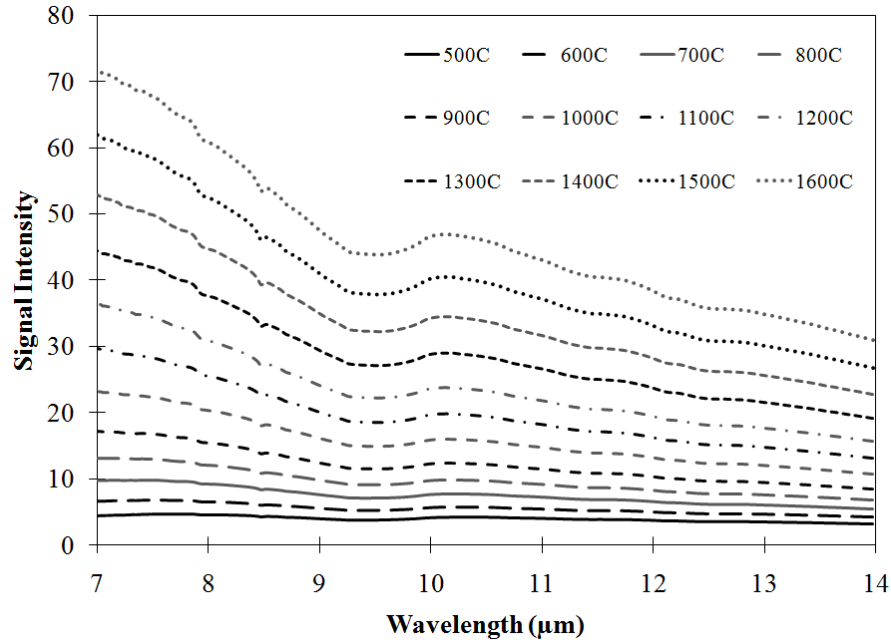


Figure 3-12 Corrected ceria pellet signal intensity from 500 °C to 1600 °C. The reference spectra from 1300 °C to 1600 °C were extended using polynomial curve fitting and a scaling factor, to maintain a Stefan-Boltzmann curve shape above 1200 °C.

minima values and emissivity minima wavelength positions decrease steadily towards 500 °C. These changes in emissivity minimum position and emissivity minimum value with temperature are shown in Figure 3-16.

3.4.6 Quenched vs. Slowly-Cooled Oligoclase Glass

The 1500 °C, 1200 °C, 1100 °C, and 80 °C spectra of a powdered oligoclase mineral acquired in the IVIS laboratory were compared to four oligoclase spectra presented in Ramsey (1996) (Figure 3-17). Both of the low temperature (80 °C) spectra of the unfused oligoclase demonstrate definitive crystalline spectral features, and also match closely with an oligoclase

spectrum from the Arizona State University (ASU) spectral library. The slight differences in emissivity can be attributed to the slight differences in particle size and composition of the oligoclase sample used in each study.

At 1130 °C, 1220 °C, and 1490 °C, however, the quenched glass spectra from Ramsey (1996), although similar in shape to the micro-furnace spectra, all display higher emissivity values from 7 to 14 microns than the spectra of samples slowly cooled in the micro-furnace. This analysis was repeated for the 80 °C spectrum of the quenched glass 2 versus the 80 °C spectrum of glass 2 taken after the glass had slowly cooled to room temperature in the micro-furnace (Figure 3-18). The same result was found, suggesting that the overall emissivity of a rapidly quenched glass is higher than that of a glass slowly-cooled to a solid.

3.5 DISCUSSION

Extensive testing of the micro-furnace has shown that the micro-furnace will be able to safely and efficiently work within the spectrometer setup to acquire emission data. Thermal heterogeneities that exist within the furnace materials surrounding the sample, as well as within the sample itself, cannot be avoided. Specifically, fluctuations in sample temperature at a given set point currently preclude an accurate and direct sample temperature measurement, which in turn makes it impossible to derive absolute emissivity spectra. Therefore, the calibration procedure using ceria reference spectra, as described above, was created in order to account for

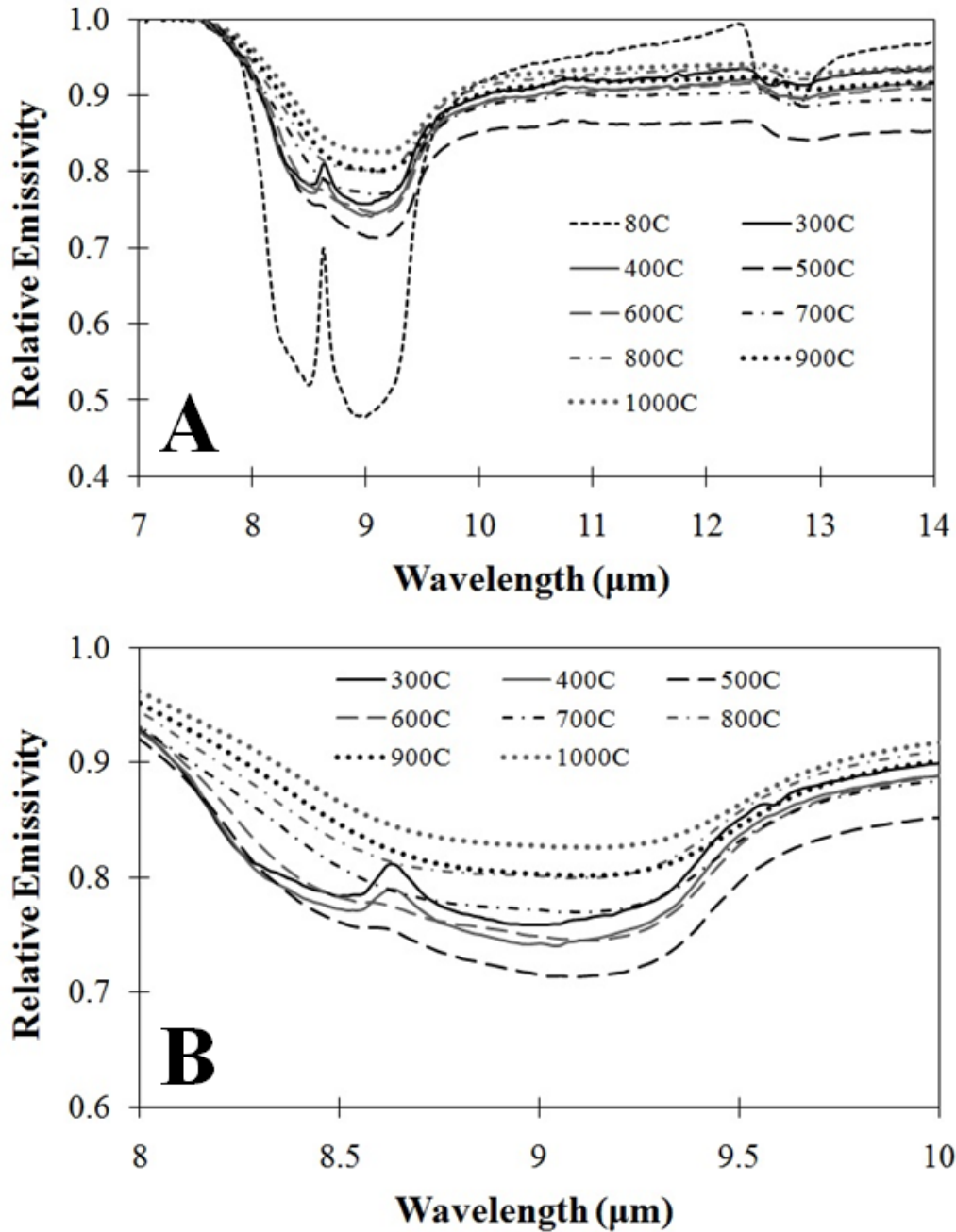


Figure 3-13 Quartz Sand Emissivity Spectra from 80 °C to 1000 °C. (A) 80 °C spectrum was acquired in the low-temperature spectrometer setup, and 300 °C -1000 °C spectra were acquired in the furnace. As the sample heats to 600 °C, the quartz doublet feature between 8 and 9 μm disappears. This is attributed to a phase change in quartz from α -quartz to β -quartz at approximately 573 °C (Gervais and Piriou, 1975). (B) A close-up view of the quartz doublet feature, showing the changes and eventual disappearance of the doublet between 300 °C and 600 °C.

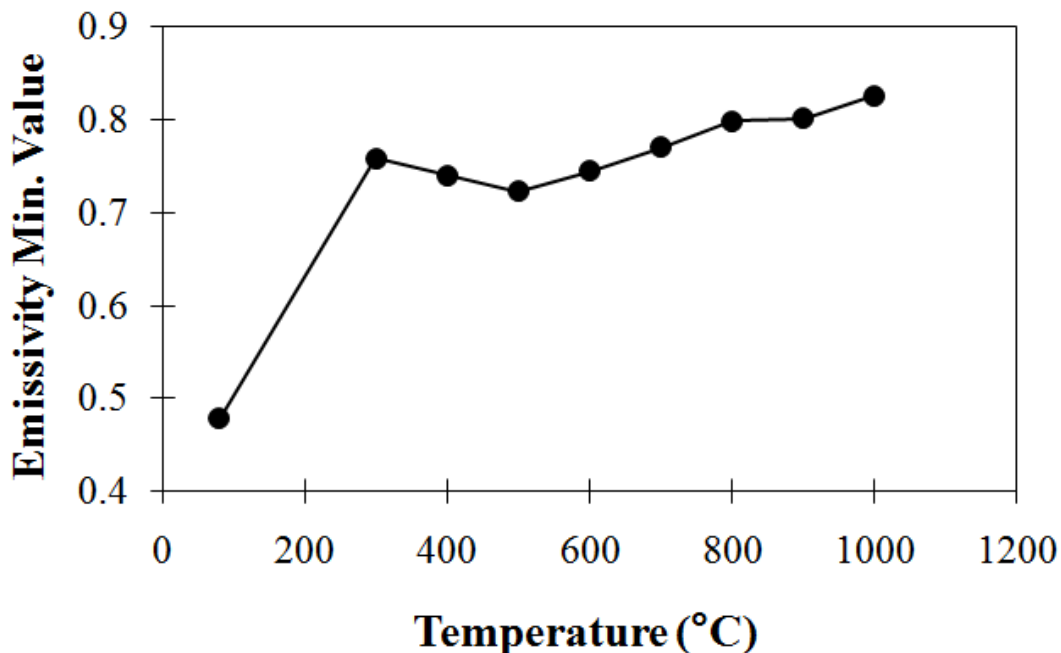


Figure 3-14 The values of the quartz emissivity minima increase steadily with increasing temperature.

this issue, and derive relative emissivity for micro-furnace samples. Meaningful relative emissivity spectra have been produced of solid and melt spectra of one of the synthetic glasses, as well as a quartz sand sample. Significant differences in emissivity minimum positions, emissivity minimum values and spectral shapes can be resolved in the spectra with increasing and decreasing temperature, and differences in emissivity exist between quenched and slowly - cooled glass samples. These data validate the use of thermal emission spectroscopy to study silicate glasses and melts in the laboratory.

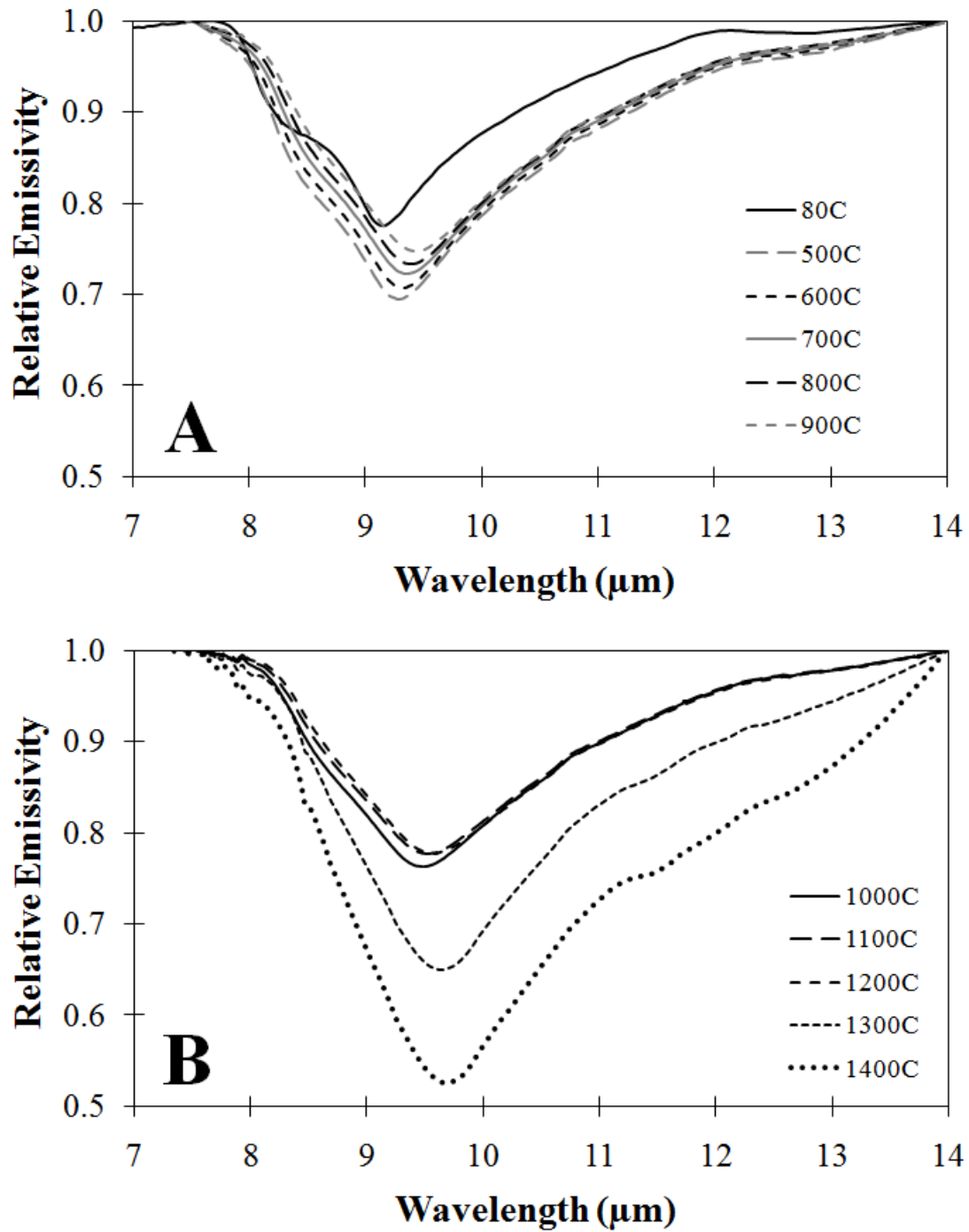


Figure 3-15 Relative emissivity spectra of glass 2 from 80 °C to 900 °C (A) and from 1000 °C to 1400 °C (B). The spectra show changes in emissivity minimum value and minimum position with increasing temperature. Beyond the liquidus of glass 2 (1250 °C), the emissivity minimum values drop sharply.

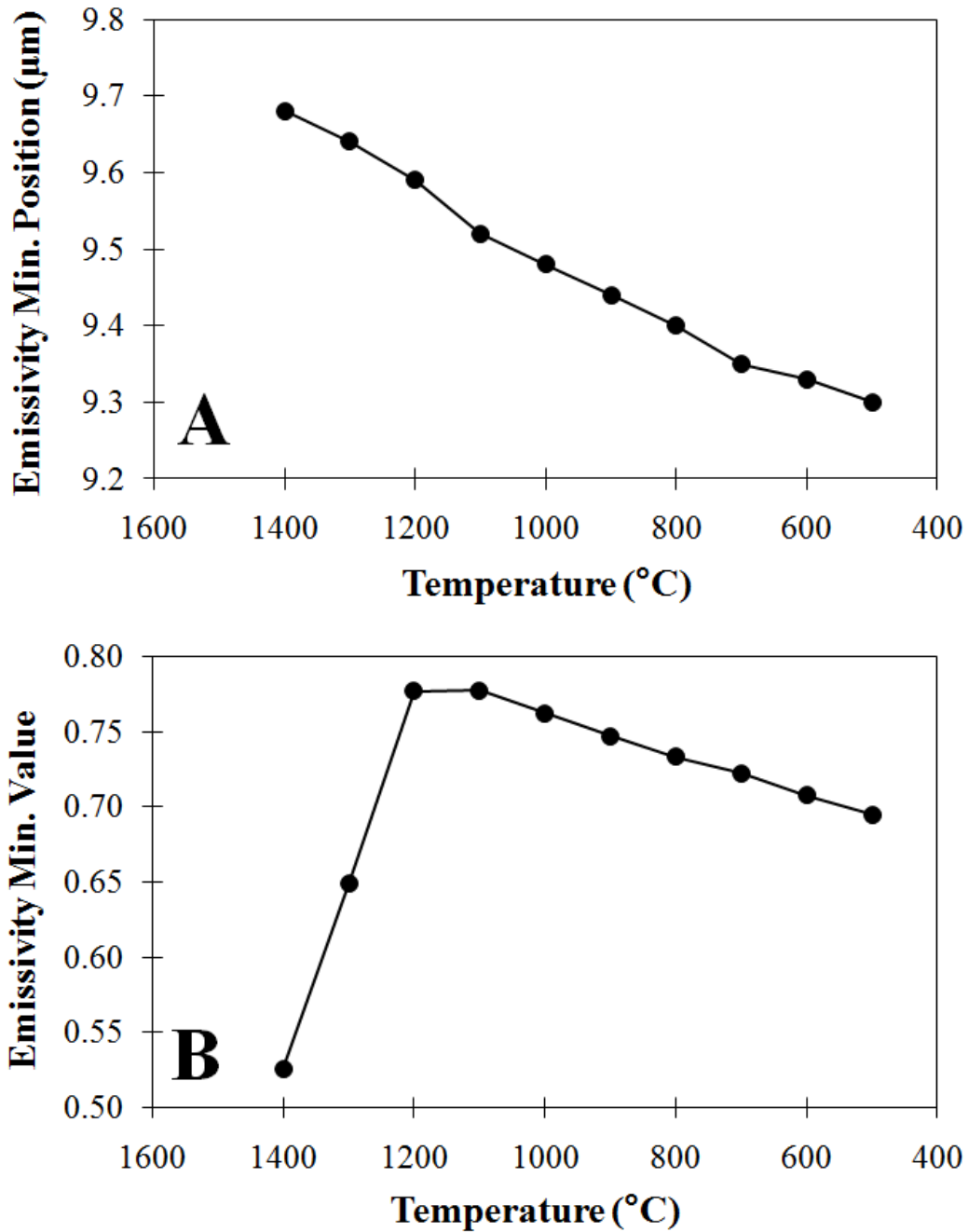


Figure 3-16 Wavelength position of emissivity minima vs. set point (A) and emissivity minimum value vs. set point (B) for glass 2. The minimum position decreases steadily with decreasing temperature. Emissivity minimum values rise sharply from 1400 °C to 1200 °C, and this rise indicates the glass transition from a fully molten material to a more solid material. At temperatures below 1200 °C, emissivity minimum values decrease more linearly with decreasing temperature.

3.5.1 Sample Temperature and Calibration

Conduction is defined as the exchange of kinetic energy from one system to another. According to the second law of thermodynamics, when an object is at a different temperature than its surroundings, heat will transfer from the higher temperature object to the lower temperature objects, until thermal equilibrium is reached. At lower set point temperatures, the temperature difference between the heating elements and the sample is large, as the heating elements begin to heat up significantly faster than the sample. The discrepancy in temperature between the heating elements and the sample temperature is due to changes in heat transfer within the micro-furnace. The input of heat is transferred to the surrounding micro-furnace insulation via conduction. After approximately 20 minutes thermal equilibrium is approached, and the temperature difference between the heating elements and the micro-furnace insulation diminishes. The difference in temperature between the heating elements and the sample begins to stabilize, and the transfer of heat transitions from conductive to radiative. The difference in temperature between the heating element and sample is also sample-dependent. A larger difference in temperature existed between the quartz sample and the heating elements, as compared to the bare platinum crucible, indicating that the thermal conductivity of the sample itself affects the temperature discrepancy, and can also affect the efficiency with which the sample retains heat.

FLIR analysis of the sample and the micro-furnace chamber temperatures indicated that temperatures within the micro-furnace environment at a given set point are both variable and dynamic, and the sample temperature changes significantly over the time the port remains open for spectrum acquisition, especially at higher set point temperatures. This makes an accurate

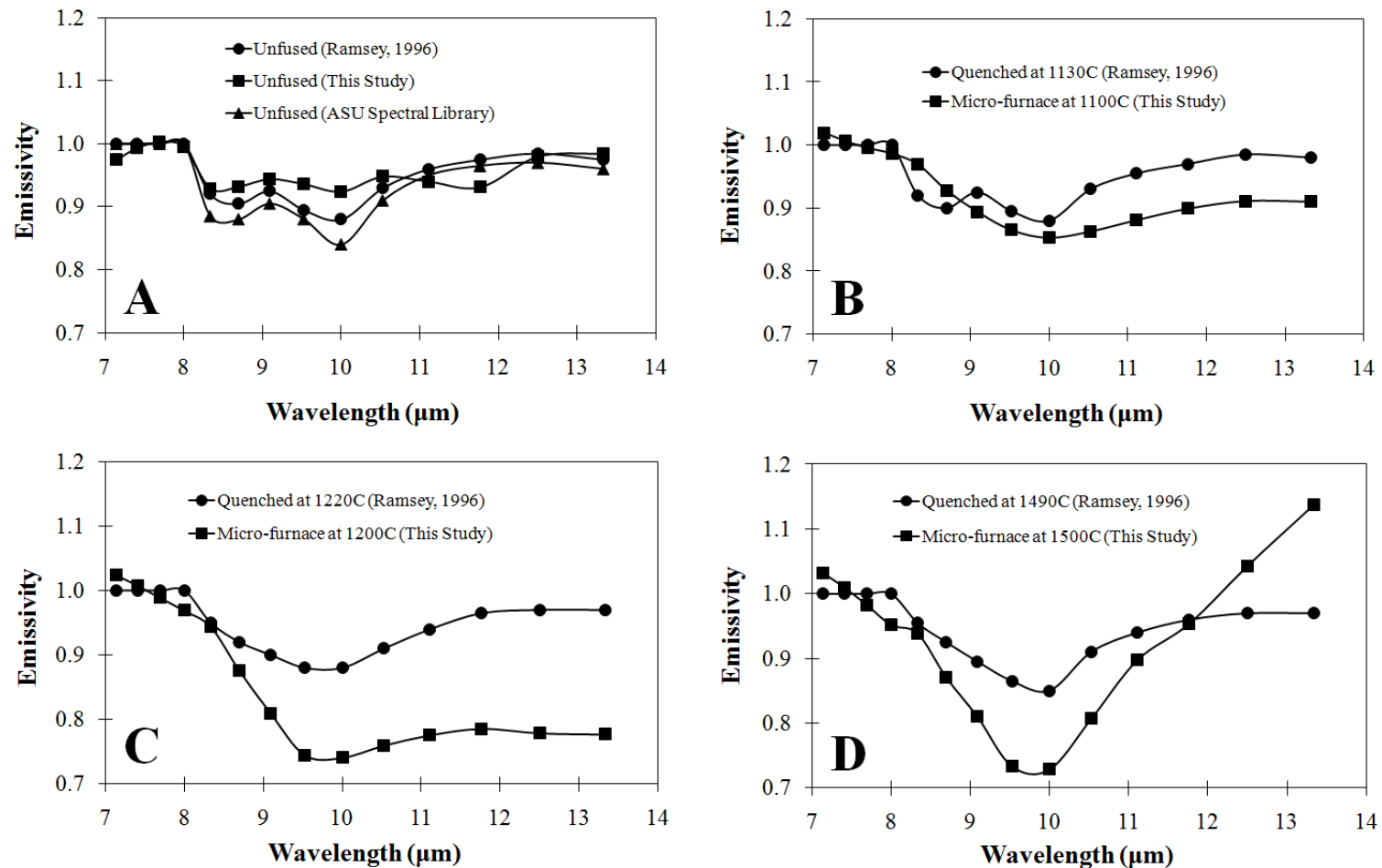


Figure 3-17 (A) Emission spectra of unfused oligoclase feldspar from Ramsey (1996), from this study, and from the ASU spectral library. Slight differences in the spectra are due to differences in particle size of the samples. (B) Emission spectrum of oligoclase feldspar quenched at 1130 °C (Ramsey, 1996) vs. a micro-furnace spectrum of oligoclase at 1100 °C. (C) Emission spectrum of oligoclase feldspar quenched at 1220 °C (Ramsey, 1996) vs. a micro-furnace spectrum of oligoclase at 1200 °C. (D) Emission spectrum of oligoclase feldspar quenched at 1490 °C (Ramsey, 1996) vs. a micro-furnace spectrum of oligoclase at 1500 °C. In B, C, and D the emissivity minimum value of the quenched oligoclase is higher than that of the non-quenched oligoclase analyzed in the furnace.

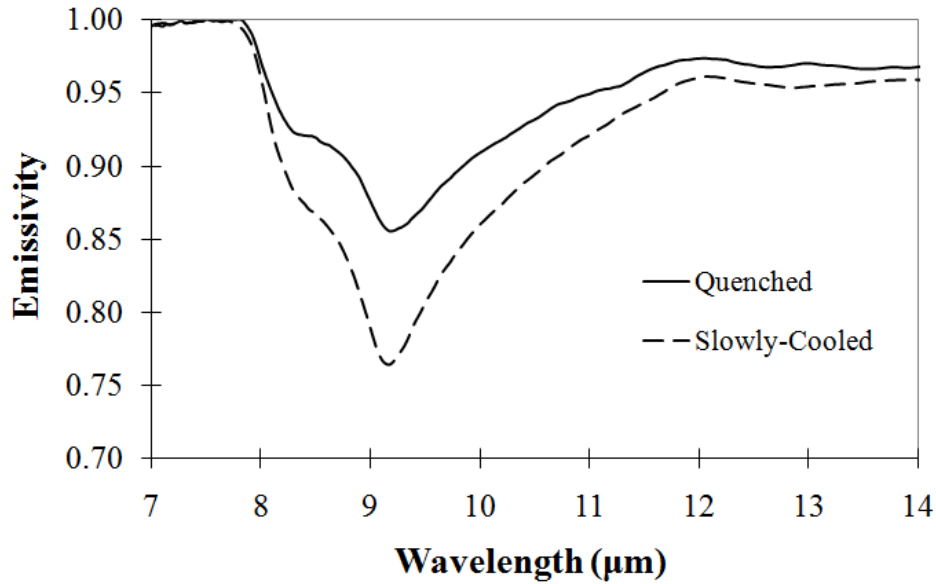


Figure 3-18 Low-temperature (80 °C) spectra of quenched glass 2, and glass 2 slowly cooled to room temperature in the micro-furnace. The emissivity minimum of the quenched glass is higher than that of the slowly-cooled glass.

determination of sample temperature difficult. This is the same situation that arises in the one temperature method described in Ruff et al. (1997) and used for the low-temperature (80 °C) spectra presented here. The sample temperature is never measured directly, but rather calculated at a given wavelength in conjunction with a well-known instrument response function. The instrument response function is derived from the measurement of two blackbody spectra at very precise temperatures. The original strategy for the micro-furnace was to use the hot sample chamber (without a sample) as the blackbody calibration for the instrument response function. However, the fluctuations in the chamber temperature upon exposure to air precluded an accurate sample temperature measurement. This prohibits an absolute emissivity from being derived in a

similar approach to Ruff et al. (1997). Therefore, the calibration procedure and ceria reference spectra described above were created in order to derive relative emissivity for micro-furnace samples.

The procedure used to extend and correctly scale the ceria reference spectra above 1200°C is based on the behavior of signal intensity with temperature according to the Stefan-Boltzmann law. This law states that the radiant flux of a blackbody (i.e. the total energy radiated per unit surface area of the blackbody per unit time, or $W/m^2/s$) is proportional to the fourth power of the blackbody temperature (Jensen, 2007). The accurate fit between the ceria pellet data and the third-order polynomial provides an assurance that the polynomial curve extension to higher temperatures is valid and accurate. This is supported by the fact that, after scaling, the signal intensity of the ceria pellet data behaved in close approximation to the Stefan-Boltzmann law, in that the intensity increased with increasing temperature similar to the lower temperature measurements.

3.5.2 Relative Emissivity Spectra of Minerals and Glass

The relative emissivity spectra of quartz sand confirm that meaningful spectral features can be resolved from the micro-furnace and the calibration procedure. Quartz undergoes several phase changes with increasing temperature, and each phase change is accompanied by a change in the symmetry, volume, and shape of the quartz lattice structure (Le Chatelier, 1889). At standard atmospheric pressure and low temperatures, quartz exists in a stable α -phase. However,

at 573 °C, quartz undergoes a transition to hexagonal β -quartz. The loss of the doublet feature in the quartz spectra above 500 °C suggests that this phase change is being detected in the micro-furnace spectra of the quartz sand sample.

An additional phase change occurs at 870 °C, where hexagonal β -quartz transitions to tridymite. However, tridymite may not form from pure β -quartz. Trace amounts of certain compounds must be added to the quartz in order for the phase transition to take place (Heaney, 1994). The quartz sand does not display any visible spectral changes between 800 °C and 900 °C, suggesting that this phase transition likely did not take place. Quartz undergoes two other phase changes: one at 1470 °C, where quartz transitions to cubic β -cristobalite, and one at 1728 °C where β -cristobalite becomes fully melted (Spearing et al, 1992). The quartz sand was not heated to high enough temperatures in this study to detect any spectral changes associated with these two transitions.

Differences in spectral characteristics with increasing temperature can also be resolved in glass melt spectra. The emissivity minima values and emissivity minima wavelength positions increase steadily up to the liquidus temperature of the glass at 1250 °C. The sharp rise in emissivity value above the liquidus temperature, and the shift of the minima to longer wavelengths, suggests that the transition of the glass from a fully molten material, to a two-phase (crystal and melt) material, and finally to a solid material are being detected in the emission spectra. At 1300 °C and 1400 °C, it is suspected that the spectra are of a material in a fully

molten state. Unlike a solid material, which may only exhibit bending and stretching vibrations within its molecular structure, a fully molten material will exhibit several more degrees of freedom in structural movement, thus changing the spectral character of the material.

A comparison of oligoclase feldspar spectra from Ramsey (1996) with the spectra of an oligoclase feldspar melt in this study show that the emissivity minimum of a glassy material in a quenched, solid state is systematically higher than an material slowly cooled within the micro-furnace. A rapidly quenched melt retains the molecular structure of the temperature at which it was quenched, with almost no crystals forming. It is suspected that some amount of crystal growth occurred in the slowly-cooled glassy melt, which in turn affects the emission minimum value. These concepts, along with the remainder of the glass melts, are discussed in further detail in the next chapter.

3.6 CONCLUSIONS

Initial testing of the micro-furnace within the spectrometer setup has shown that the micro-furnace operates effectively and safely within the laboratory, and can generate significant and meaningful emission data of glasses and melts. Mineral powders and glasses of rhyolitic composition have been melted fully within the micro-furnace up to 1500 °C, and *in-situ* relative

emissivity spectra have been successfully acquired. In the absence of an accurate and true blackbody (and until one is developed), an effective calibration method has been devised, which allows for the derivation of relative emissivity spectra of samples.

The micro-furnace will provide the very first in-situ laboratory thermal emission spectra of glassy melts. This will allow for the spectral morphology of a glass, as it melts and cools through the glass transition, to be characterized. These laboratory measurements will ultimately serve as a well-controlled and calibrated basis for understanding changes in emission spectral features associated with changes in composition and temperature of active lava flows and domes. This will lead to a better understanding of how the formation of glassy crusts and varying textures on cooling lava domes and flows affect emitted energy. The data will have implications for laboratory petrology and spectroscopy of glasses and melts, and will also be used in conjunction with field data to assess potential hazards associated with active lava domes and flows at various spatial scales.

4.0 HIGH-TEMPERATURE THERMAL EMISSION SPECTROSCOPY OF SILICATES

4.1 INTRODUCTION

Thermal emission spectroscopy has been proven as a highly useful technique for compositional studies of glassy materials (e.g. Wyatt et al., 2001; Minitti et al., 2006; Sweet and White, 1969; Byrnes et al., 2004, 2007; Dalby et al., 2006; Dalby and King, 2006; Dufresne et al., 2009; Lee et al., 2010). In comparison to TIR spectra of their crystalline mineral counterparts, silicate glass spectra lack definitive features, and the Reststrahlen feature becomes broadened. Rapid quenching of a liquid affords little time for long-range structural order to be attained, and the resulting glassy solid is amorphous, with muted TIR spectral features. Furthermore, glass spectra are very similar to each other regardless of composition, making the differentiation between spectra of different glass compositions difficult (Bell et al., 1968; Dowty, 1987; Crisp et al., 1990; Poe et al., 1992; Salisbury et al., 1991; McMillan and Wolf, 1995; Agarwal and Tomozawa, 1997; McMillan et al., 1998). Despite this, laboratory studies have shown that the morphology and wavelength positions of silicate spectral features are both highly dependent on wt % SiO₂ content, Si-O bond distance, the presence and abundance of network-

modifying cations, and degree of polymerization (Neuville and Mysen, 1996; Dalby et al., in prep.; Dalby et al., 2006; Byrnes et al., 2007; King et al., 2008; Dufresne et al., 2009; Lee et al., 2010). All of these studies have focused on silicate glasses in a solid or quenched state. No studies yet exist that examine the effects on thermal emission spectra of materials in a partially or fully molten state.

As a glassy material is heated below the glass transition temperature (T_g), the silicate structure may undergo changes in bond length and position that in turn affect the vibrational modes detected in the TIR. These changes depend on the fictive temperature (T_f), which is the temperature at which a liquid structure is “frozen” into a glassy state. For example, IR reflectance studies of quenched silicate glasses have shown that the Si-O-Si bond angles are smaller in glasses quenched at a high T_f compared to the same glass quenched at a low T_f (Tomozawa et al., 2005). At and above the T_g , relaxational modes are introduced as well as vibrational modes, and the structure of the molten material is constantly changing. If the melt is rapidly quenched, the molecular structure at the point of quenching is preserved in the amorphous glass. If the melt is allowed to cool slowly, the structure will continue to change until the viscosity of the material becomes too great to permit structural movement. The constant structural changes that occur in a glass as it melts and cools over time have profound effects on the emission spectrum of the glass, specifically the position, depth, and shape of the main absorption feature (e.g. McMillan and Wolf, 1995). For example, studies of basalt flows using field-based TIR instrumentation have shown that the broadband emissivity of molten basalt flows is significantly lower than their fully-cooled counterparts (Abtahi et al., 2002; Ramsey and

Wessels, 2007). The nature of melt structure coupled with the complexities involved with in-situ laboratory melting experiments at such high temperatures (<1200 °C) and small scales has, until now, precluded laboratory thermal emission spectral analysis of melts.

The use of various spectroscopic techniques to study the behavior of high-temperature and molten materials is not a novel approach, however. Transmission and reflectance IR have been used at a small-scale to analyze glass samples heated to various temperatures (e.g. Grove and Jellyman, 1955; Domine and Piriou, 1983; McMillan et al., 1992; McMillan and Wolf, 1995; Agarwal and Tomozawa, 1997). The atomic absorption of a variety of gaseous and solid species has been studied using vacuum graphite furnaces (e.g. Brown et al, 1973; Woodruff and Ramelow, 1968). X-Ray absorption spectroscopy (XANES) and X-ray diffraction (XRD) have been used to assess changes in the structure of silicate glasses and melts (e.g. Neuville et al., 2004a, 2004b, 2008; Farges and Brown, 1996; Idelfonse et al., 1998; Poe et al, 2001; Magnien et al., 2004, 2006). The presence and nature of magnetic phases in basaltic rocks heated up to 900K has been studied using Mossbauer spectroscopy (Helgason et al., 1994). Raman spectroscopy has been used extensively in the study of the composition and molecular structure of aluminosilicate glasses and their corresponding melts (Daniel et al., 1995; Mysen et al., 1980a, 1981b, 1982a; Siefert et al., 1981, 1982; McMillan 1984; Mysen 1988, 1990; McMillan et al., 1992; Mysen and Franz, 1992, 1993; Richet et al., 1993; McMillan et al., 1994; Neuville and Mysen, 1996; Neuville et al., 2004; Neuville et al., 2006). The local structure and bonding of aluminosilicate materials has been investigated by nuclear magnetic resonance (NMR) both below and above the T_g temperature (e.g. Kirkpatrick, 1988; Stebbins 1988b; Farnan and

Stebbins, 1990; Stebbins and Farnan, 1992; Stebbins et al, 1992; Poe et al., 1992b, 1993; Stebbins and Xu, 1997; Gruener et al, 2001) and these data have been compared to molecular dynamics simulations of the structure and relaxation of aluminosilicate liquids (e.g. Poe et al., 1994).

Laboratory thermal emission analysis of quartzofeldspathic glasses as they melt and cool is a unique and innovative approach, which has important implications for the study and understanding of the behavior of silicate glasses and melts in volcanic environments using remote sensing. Lava flows and domes contain silicate materials with a range of temperatures, compositions and vesicularities, as well as varying thicknesses of glassy crust with cooling. Each of these factors is known to affect the spectral information derived from a silicate volcanic surface (e.g. Salisbury et al., 1991; Clark 1999; Byrnes et al., 2004; Ramsey and Dehn, 2004; Vaughan et al., 2005; Wright and Ramsey, 2006; Carter et al., 2007). It is expected that these observed spectral changes can be used to determine the physical state of a silicate lava, as well as cooling rate and possible flow patterns over time. The spectral characterization of molten lava and glassy surfaces is a potentially dangerous task, and close proximity to areas of glassy material is not commonly possible. Remote sensing instrumentation is therefore a valuable tool for remotely and non-destructively analyzing these surfaces and will allow for a more complete understanding of the structural and physical changes that take place upon cooling, and also improve the understanding of glasses in infrared spectroscopy.

4.2 METHODOLOGY

Thermal emission spectra were collected in the Image Visualization and Infrared Spectroscopy (IVIS) Laboratory, at the University of Pittsburgh, using a Nexus 870 spectrometer. To melt a glass in the micro-furnace for thermal emission analysis, 1 to 2 grams of the glass sample was crushed into millimeter-sized pieces and placed into a platinum crucible. Pieces of this size were used to facilitate the melting process. As the glass was heated, an emission spectrum was acquired at 100 °C increments from 500 °C to the maximum temperature, which was 100 – 250 °C above the glass sample liquidus temperature (calculated during initial synthesis of the glass suite). This was done in order to ensure that the glass was completely molten. The glass sample was held for approximately 5 minutes at each set point to ensure isothermality, before acquiring the spectrum. Then the furnace port was opened, and a spectrum was acquired. Because of the extreme signal intensity associated with the hot glass samples, and the variable and dynamic environmental temperatures within the micro-furnace, each spectrum was acquired over only 6 scans (~10 seconds).

The micro-furnace was then cooled from the maximum temperature downwards, in 100 °C increments, to a temperature of 500 °C. An emission spectrum was acquired at each increment using the same method as described above. Spectra were acquired in this manner in

order to mimic the natural cooling behavior of an erupting glassy lava. After all spectra were acquired, the sample was then allowed to cool completely from 500 °C to room temperature. The room-temperature glass sample was placed into a copper sample cup, and heated in an 80 °C oven for 24 hours. An emission spectrum was taken of the glass using the low-temperature setup, as described in Lee et al., 2010. This process was repeated for all of the glasses in the synthetic suite. For seven of the glasses, additional thermal emission spectra were acquired in 20 °C increments as the glass cooled from its maximum temperature to 1100 °C. This was done in an attempt to determine the approximate glass transition temperature from the emission spectra, and also to determine the effects of glass temperature and physical state on the emission spectra at a smaller temperature scale. These seven glasses are presented here, and the remainder of the glass suite is presented in Appendix A (Figures A-1 through A-18).

The signal intensity of the glass at each temperature was then divided by the adjusted signal intensity of the ceria pellets, as described in Chapter 3 of this work, to yield relative emissivity spectra. Micro-furnace spectra were assigned an emissivity of 1 at both 7.5 and 14 μm, and linearly scaled based on the difference in emissivity between 1 and the observed emissivity of the spectra at 7.5 and 14 μm. Scaling to these two wavelengths was based on ASU Spectral Library spectra of albite, anorthite, and quartz, which all have a Christiansen Feature (CF) at 7.5 μm and an additional near-unit emissivity 14 μm. This scaling process eliminates the slope that occurs in the micro-furnace spectra due to a minor calibration issue (discussed in Chapter 3 of this work), highlights the main absorption feature, and makes the micro-furnace spectra more comparable to the low-temperature (80 °C) spectrum.

4.3 RESULTS

4.3.1 Thermal Emission Spectra

Relative emissivity spectra from 7-14 μm for the seven glass samples analyzed in 20 $^{\circ}\text{C}$ increments above 1100 $^{\circ}\text{C}$, and their corresponding low temperature (80 $^{\circ}\text{C}$) absolute emissivity spectra are shown in Figures 4-1 to 4-7. The approximate liquidus temperatures (derived from Hibbard, 1995 and Hall, 1996) and maximum furnace temperatures for each of the glasses are shown in Table 4.1. For any given glass sample, the spectrum acquired at 80 $^{\circ}\text{C}$ has a shorter emissivity minimum wavelength position, in comparison to the data from the micro-furnace.

The micro-furnace spectra between the maximum temperature and ~ 1250 $^{\circ}\text{C}$ - 1200 $^{\circ}\text{C}$ (depending on glass composition) show no systematic variation with decreasing temperature. For example, for glasses 1 and 7, the emission minimum at 1400 $^{\circ}\text{C}$ is higher than that of 1320 $^{\circ}\text{C}$, whereas in glasses 1a and 24, it is lower. Additionally, two small shoulder features appear in several of the spectra at ~ 11.5 and ~ 12.5 μm , and are only present in above-liquidus spectra. The shoulder features are more pronounced in some spectra than in others, and could be related to structural changes associated with the molten material. Spectra between ~ 1200 $^{\circ}\text{C}$ and 1100 $^{\circ}\text{C}$ were acquired in 20 $^{\circ}\text{C}$ increments, and the spectral shapes are very similar. However

the emissivity minima either rise somewhat linearly with temperature, or rise and slightly fall again with decreasing temperature. In each glass, a sharp and noticeable rise in emissivity occurs between ~ 1280 °C and 1180 °C. The slope of this rise, and the temperature at which it occurs, is dependent upon the glass composition. This sharp rise is representative of the glass transition (T_g), during which the glass undergoes a transition in physical state from a molten material to a brittle solid as it cools. Spectra between 1000 °C to 500 °C have emission minima values which decrease linearly with decreasing temperature for each of the glasses. The change in emissivity minimum values and wavelength positions with decreasing set point temperature are graphically represented in Figures 4-8 to 4-14. The sharp increase in emissivity between 1200 °C and 1250 °C representative of T_g , is clearly illustrated for each glass. Material properties such as viscosity and specific heat are often employed to calculate the glass transition. However, micro-furnace data show that T_g can also be detected spectrally.

The emissivity minimum position (wavelength) of micro-furnace spectra decreases somewhat systematically with decreasing set point temperature at temperatures < 1200 °C. Above 1200 °C, the positions are less linear with temperature, and several of the glasses show a sharp increase in emissivity minimum position and a drop in emission minimum value around the liquidus temperature. For example, glass 7 has a liquidus of approximately 1325 °C. Between 1360 °C and 1380 °C, there is a drop in the emissivity minimum value, and a corresponding spike in emissivity minimum position. A similar condition exists for glass 21a, which has a liquidus of approximately 1400 °C, and experiences a spike in emissivity minimum position and a lowering of emissivity value at a temperature of 1300 °C. These phenomena were not observed in all glasses, however.

Table 4-1 Glass Compositions, Liquidus Temperatures and Maximum Furnace Temperatures

Glass #	Ab (wt. %)	An (wt. %)	Q (wt. %)	SiO ₂ (wt. %)	Liquidus (°C) ¹	Max. Temperature (°C)
19	54.88	19.37	25.75	71.79	1075	1300
19a	75.31	0.10	24.60	75.27	1075	1200
3	74.03	25.97	0.00	62.44	1125	1300
20a	37.04	13.22	49.74	80.27	1175	1300
2	40.23	14.21	45.57	78.78	1200	1400
2a	40.04	14.48	45.48	78.55	1200	1400
27	48.65	6.72	44.64	80.17	1225	1400
1*	36.01	12.41	51.58	80.85	1250	1400
1a*	47.52	0.03	52.45	83.36	1250	1400
28	61.37	9.54	29.09	74.76	1250	1400
6	58.03	17.64	24.33	71.96	1275	1450
7*	28.11	28.69	43.21	74.75	1325	1450
24*	86.11	11.38	2.50	66.53	1325	1450
8*	32.27	33.23	34.50	70.53	1350	1500
21*	26.28	9.62	64.11	85.29	1400	1500
21a*	32.21	0.05	67.74	87.54	1400	1500
26	28.93	33.38	37.69	71.34	1400	1500

*denotes that the glass is discussed in this chapter

¹liquidus temperatures calculated from Hibbard (1995) and Hall (1996)

Un-starred denotes that the glass data is presented in Appendix A

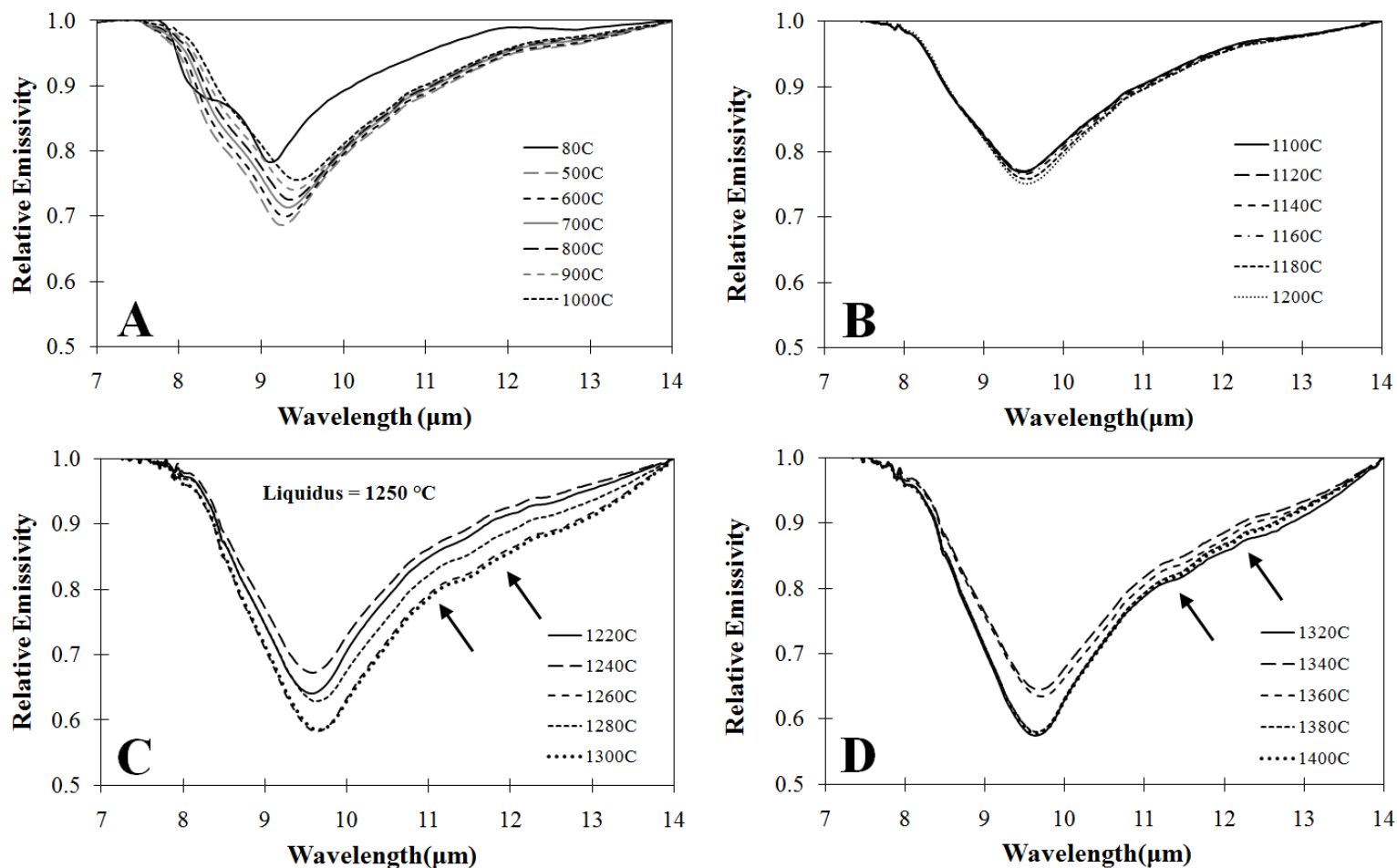


Figure 4-1 Relative emissivity spectra of Glass 1 shown from 7 to 14 μm, (A) 80 °C to 1000 °C; (B) 1100 °C to 1200 °C; (C) 1220 °C to 1300 °C; and (D) 1320 °C to 1400 °C. The 80 °C spectrum is absolute emissivity acquired from the low-temperature laboratory setup, but is included here as a comparison to the micro-furnace spectra. Emissivity minima values increase with increasing temperature from 500 °C to 1000 °C. At temperatures higher than 1000 °C, the minima values and wavelength positions are more variable. Arrows denote locations of shoulder features at ~11.5 and 12.5 μm.

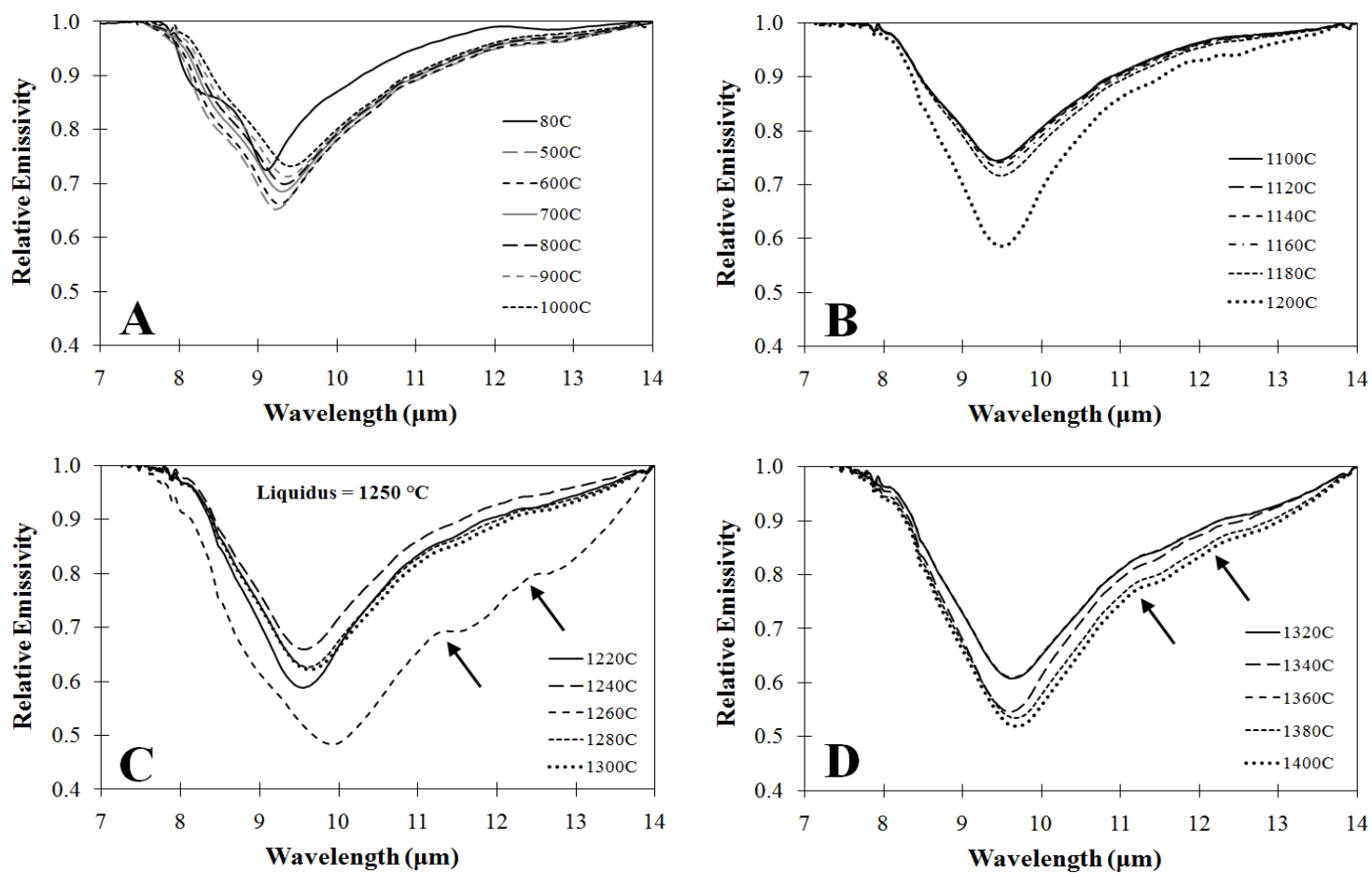


Figure 4-2 Relative emissivity spectra of Glass 1a shown from 7 to 14 μm , (A) 80 $^{\circ}\text{C}$ to 1000 $^{\circ}\text{C}$; (B) 1100 $^{\circ}\text{C}$ to 1200 $^{\circ}\text{C}$; (C) 1220 $^{\circ}\text{C}$ to 1300 $^{\circ}\text{C}$; and (D) 1320 $^{\circ}\text{C}$ to 1400 $^{\circ}\text{C}$. The 80 $^{\circ}\text{C}$ spectrum is absolute emissivity acquired from the low-temperature laboratory setup, but is included here as a comparison to the micro-furnace spectra. Emissivity minima values increase with increasing temperature from 500 $^{\circ}\text{C}$ to 1000 $^{\circ}\text{C}$. At temperatures higher than 1000 $^{\circ}\text{C}$, the minima values and wavelength positions are more variable. Arrows denote locations of shoulder features at ~ 11.5 and 12.5 μm .

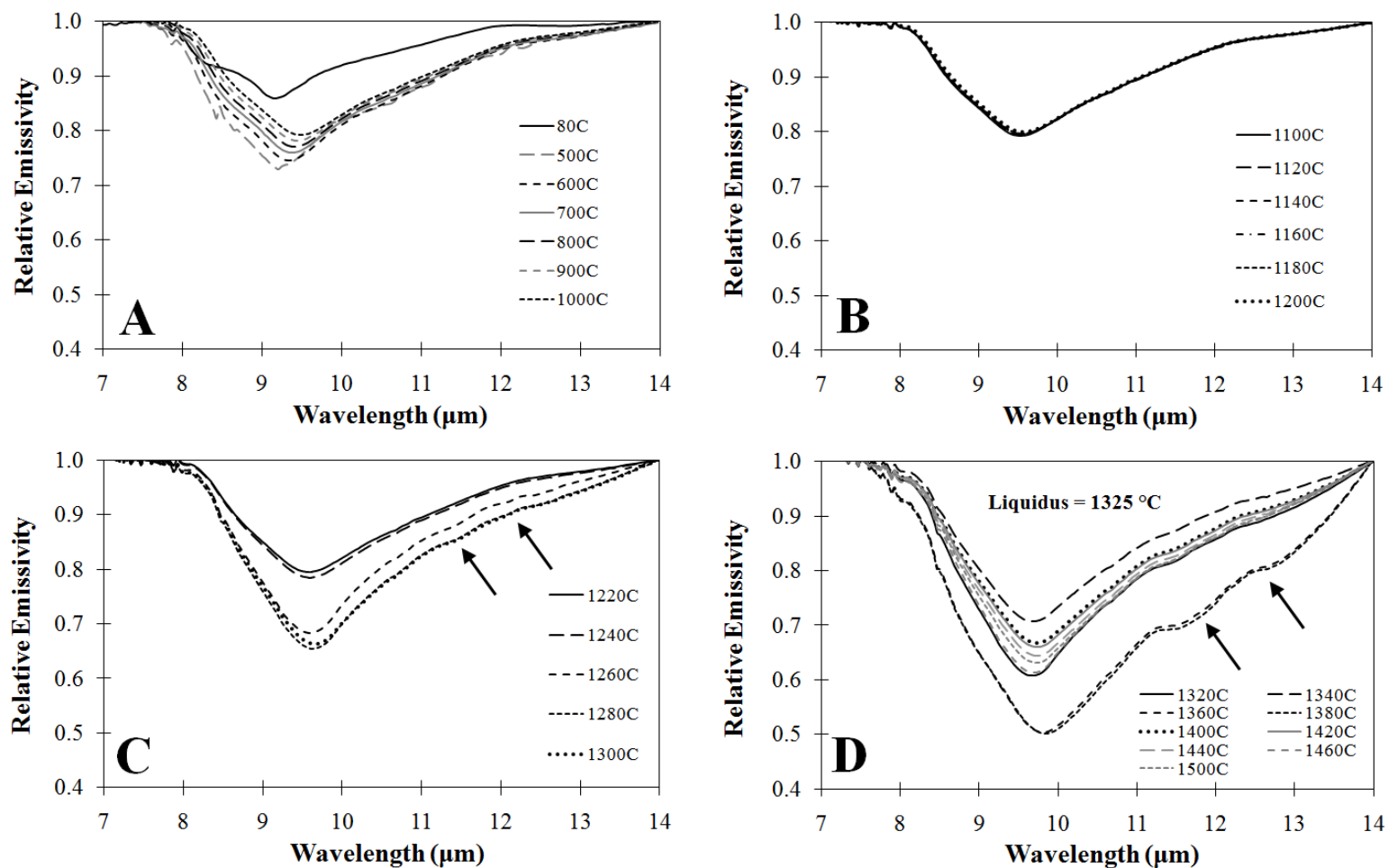


Figure 4-3 Relative emissivity spectra of Glass 7 shown from 7 to 14 μm , (A) 80 $^{\circ}\text{C}$ to 1000 $^{\circ}\text{C}$; (B) 1100 $^{\circ}\text{C}$ to 1200 $^{\circ}\text{C}$; (C) 1220 $^{\circ}\text{C}$ to 1300 $^{\circ}\text{C}$; and (D) 1320 $^{\circ}\text{C}$ to 1500 $^{\circ}\text{C}$. The 80 $^{\circ}\text{C}$ spectrum is absolute emissivity acquired from the low-temperature laboratory setup, but is included here as a comparison to the micro-furnace spectra. Emissivity minima values increase with increasing temperature from 500 $^{\circ}\text{C}$ to 1000 $^{\circ}\text{C}$. At temperatures higher than 1000 $^{\circ}\text{C}$, the minima values and wavelength positions are more variable. Arrows denote locations of shoulder features at ~ 11.5 and 12.5 μm .

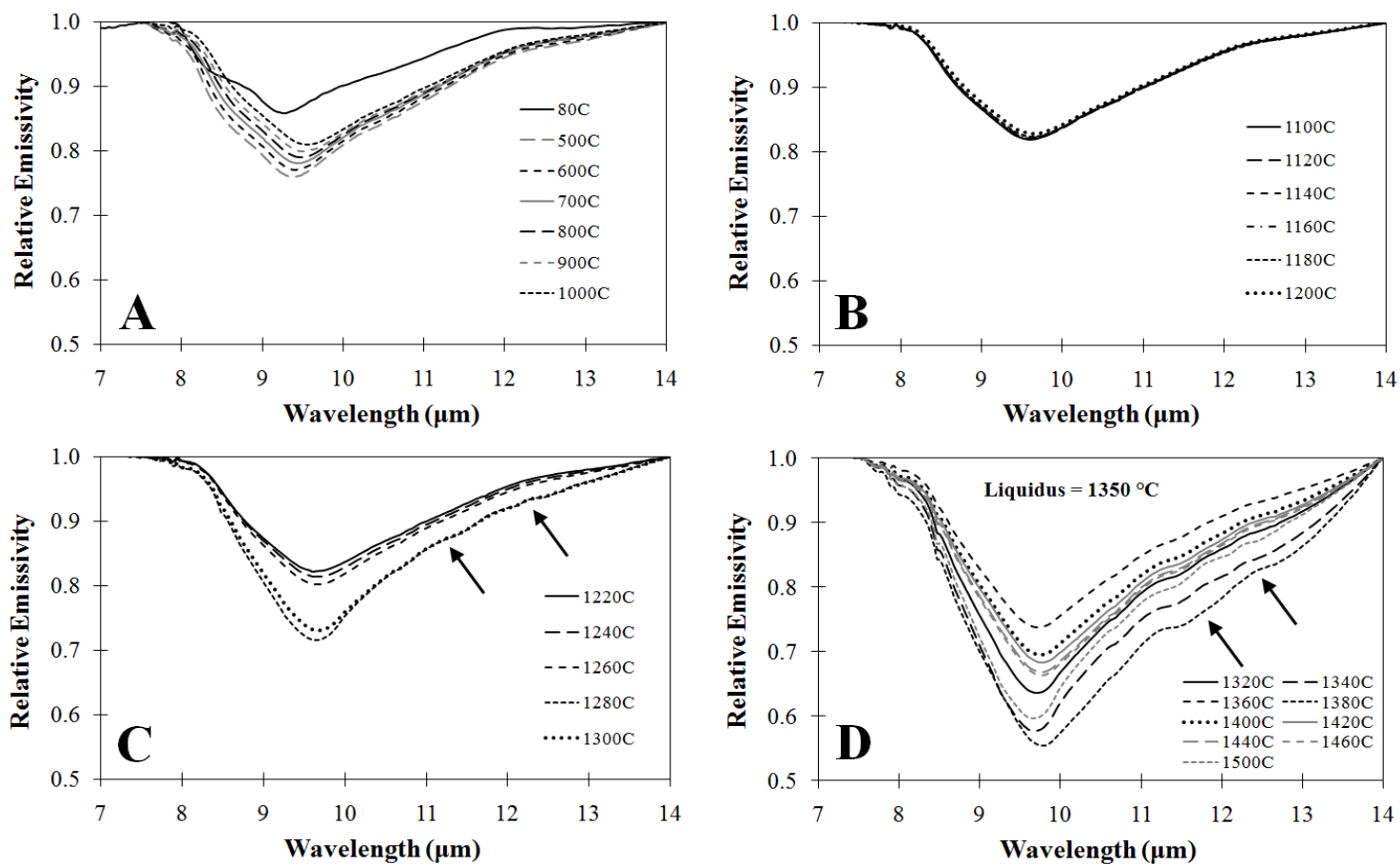


Figure 4-4 Relative emissivity spectra of Glass 8 shown from 7 to 14 μm , (A) 80 $^{\circ}\text{C}$ to 1000 $^{\circ}\text{C}$; (B) 1100 $^{\circ}\text{C}$ to 1200 $^{\circ}\text{C}$; (C) 1220 $^{\circ}\text{C}$ to 1300 $^{\circ}\text{C}$; and (D) 1320 $^{\circ}\text{C}$ to 1500 $^{\circ}\text{C}$. The 80 $^{\circ}\text{C}$ spectrum is absolute emissivity acquired from the low-temperature laboratory setup, but is included here as a comparison to the micro-furnace spectra. Emissivity minima values increase with increasing temperature from 500 $^{\circ}\text{C}$ to 1000 $^{\circ}\text{C}$. At temperatures higher than 1000 $^{\circ}\text{C}$, the minima values and wavelength positions are more variable. Arrows denote locations of shoulder features at ~ 11.5 and 12.5 μm .

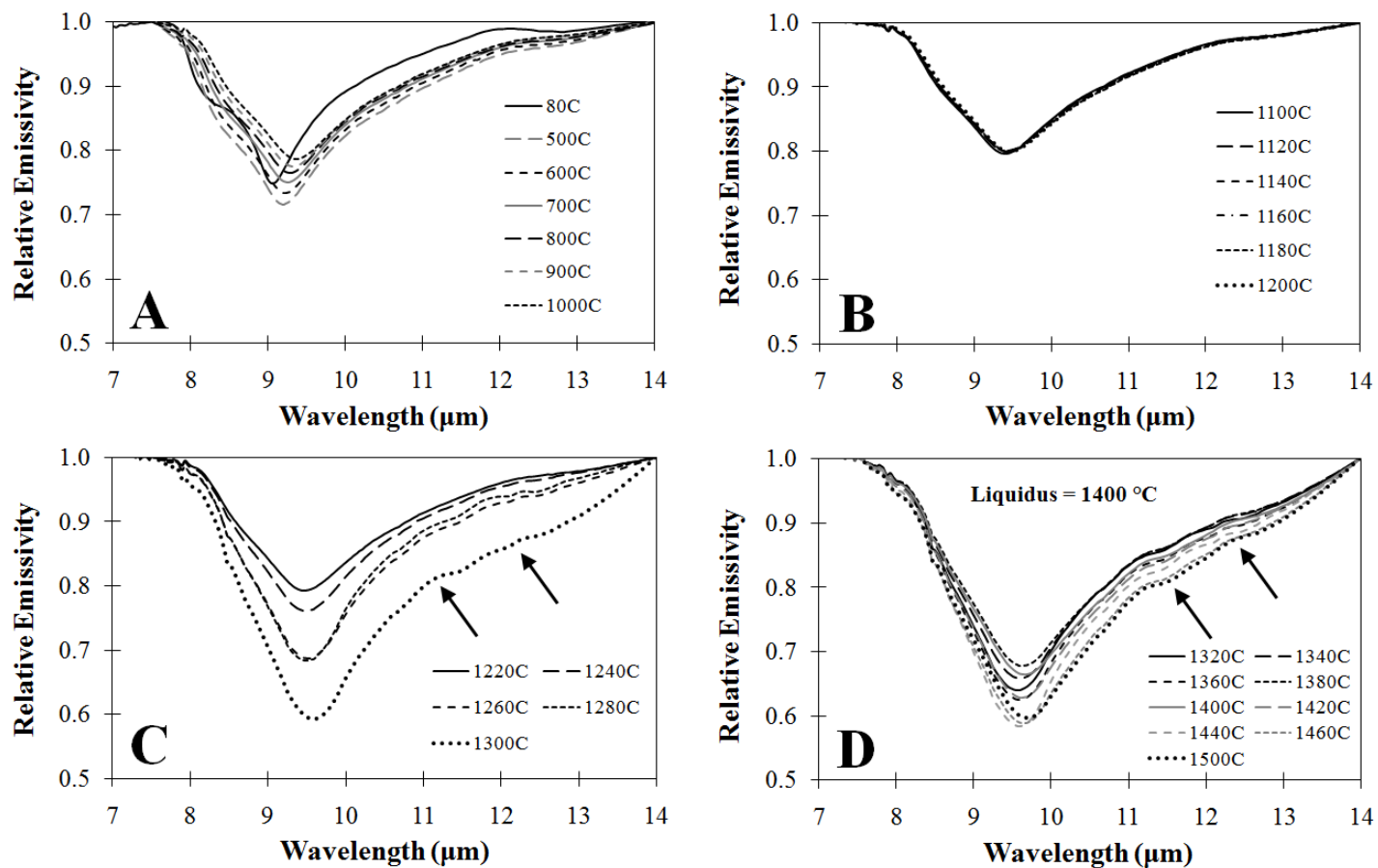


Figure 4-5 Relative emissivity spectra of Glass 21 shown from 7 to 14 μm , (A) 80 $^{\circ}\text{C}$ to 1000 $^{\circ}\text{C}$; (B) 1100 $^{\circ}\text{C}$ to 1200 $^{\circ}\text{C}$; (C) 1220 $^{\circ}\text{C}$ to 1300 $^{\circ}\text{C}$; and (D) 1320 $^{\circ}\text{C}$ to 1500 $^{\circ}\text{C}$. The 80 $^{\circ}\text{C}$ spectrum is absolute emissivity acquired from the low-temperature laboratory setup, but is included here as a comparison to the micro-furnace spectra. Emissivity minima values increase with increasing temperature from 500 $^{\circ}\text{C}$ to 1000 $^{\circ}\text{C}$. At temperatures higher than 1000 $^{\circ}\text{C}$, the minima values and wavelength positions are more variable. Arrows denote locations of shoulder features at ~ 11.5 and 12.5 μm .

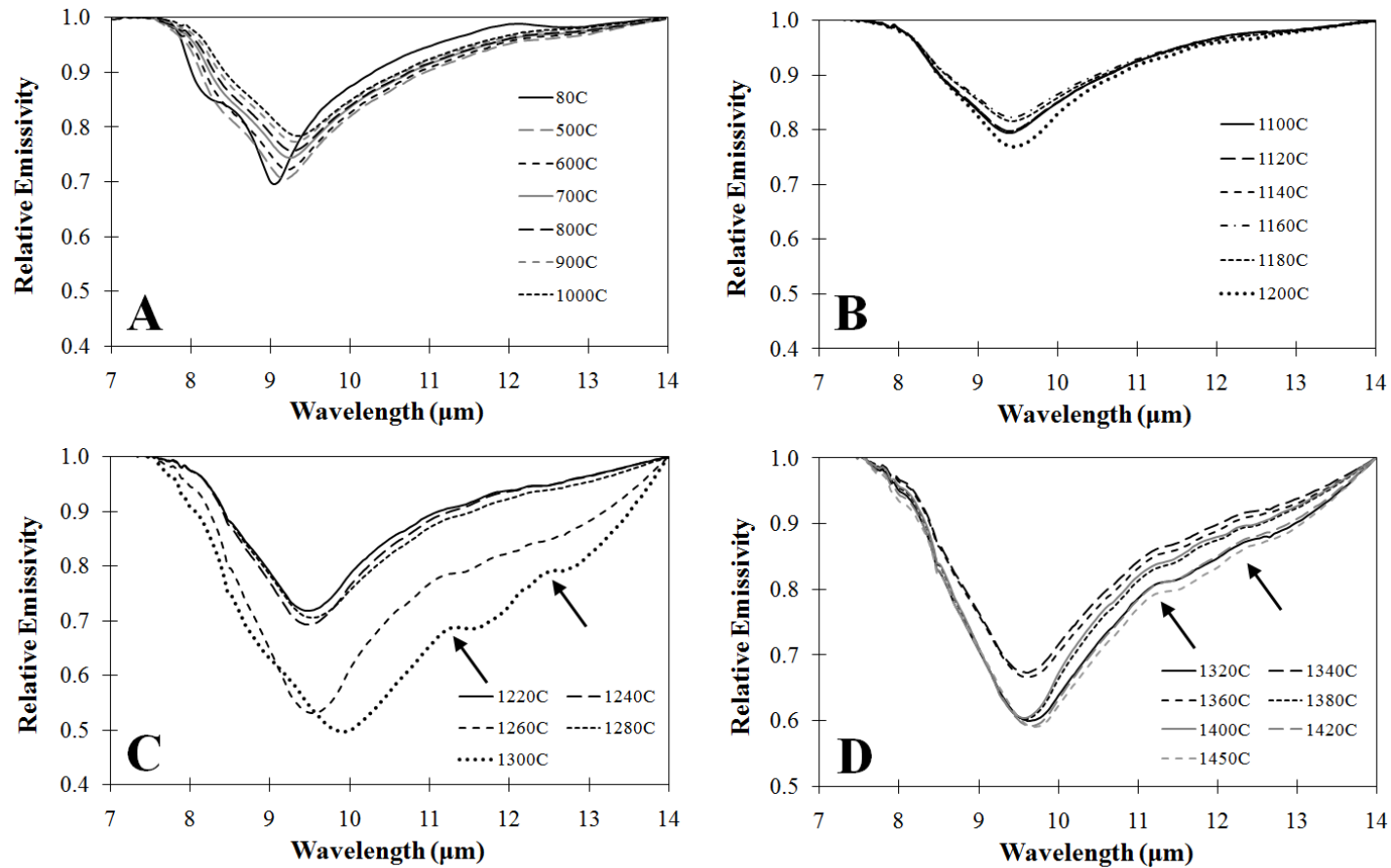


Figure 4-6 Relative emissivity spectra of Glass 21a shown from 7 to 14 μm , (A) 80 $^{\circ}\text{C}$ to 1000 $^{\circ}\text{C}$; (B) 1100 $^{\circ}\text{C}$ to 1200 $^{\circ}\text{C}$; (C) 1220 $^{\circ}\text{C}$ to 1300 $^{\circ}\text{C}$; and (D) 1320 $^{\circ}\text{C}$ to 1400 $^{\circ}\text{C}$. The 80 $^{\circ}\text{C}$ spectrum is absolute emissivity acquired from the low-temperature laboratory setup, but is included here as a comparison to the micro-furnace spectra. Emissivity minima values increase with increasing temperature from 500 $^{\circ}\text{C}$ to 1000 $^{\circ}\text{C}$. At temperatures higher than 1000 $^{\circ}\text{C}$, the minima values and wavelength positions are more variable. Arrows denote locations of shoulder features at ~ 11.5 and 12.5 μm .

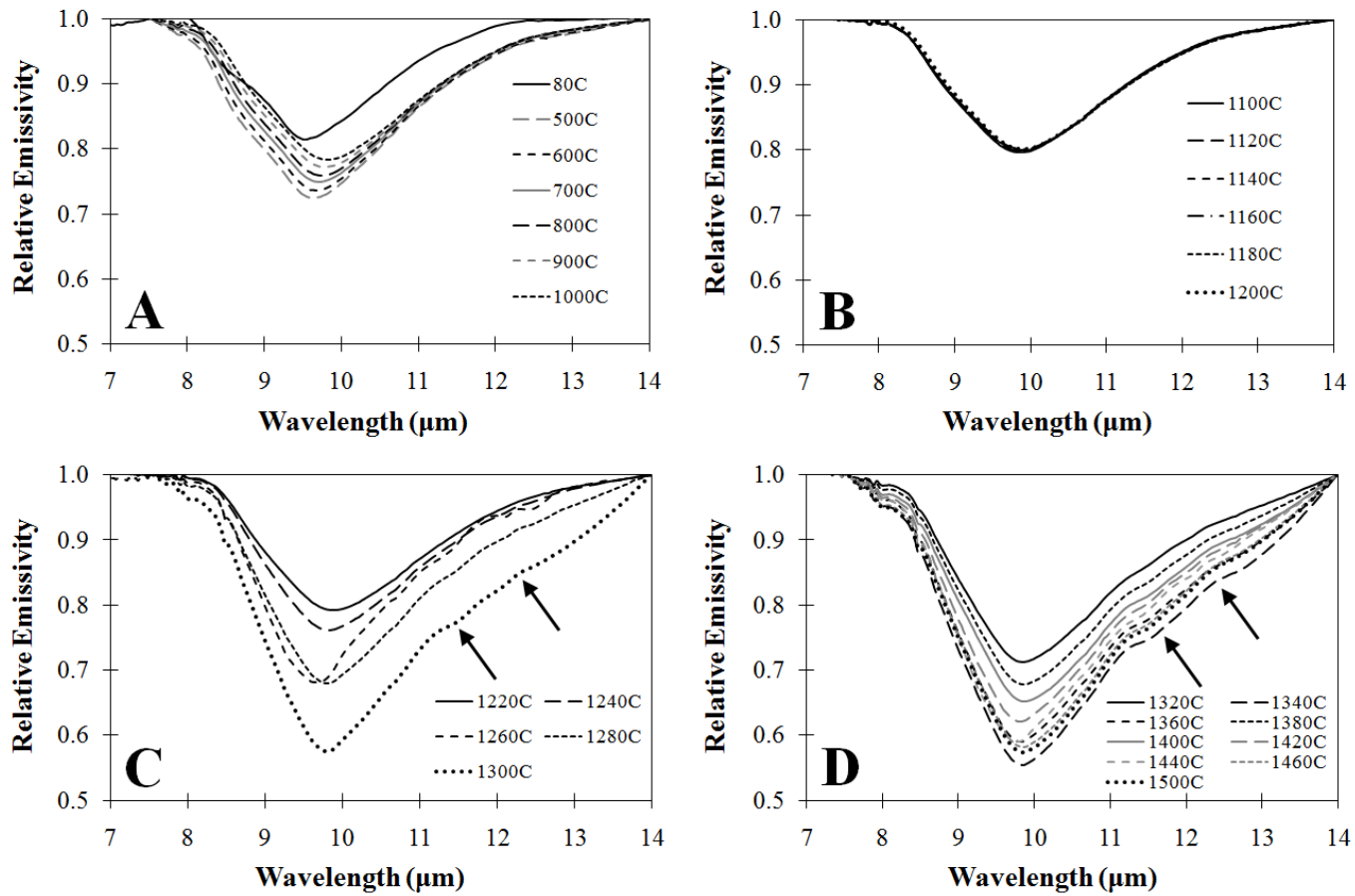


Figure 4-7 Relative emissivity spectra of Glass 24 shown from 7 to 14 μm , (A) 80 $^{\circ}\text{C}$ to 1000 $^{\circ}\text{C}$; (B) 1100 $^{\circ}\text{C}$ to 1200 $^{\circ}\text{C}$; (C) 1220 $^{\circ}\text{C}$ to 1300 $^{\circ}\text{C}$; and (D) 1320 $^{\circ}\text{C}$ to 1400 $^{\circ}\text{C}$. The 80 $^{\circ}\text{C}$ spectrum is absolute emissivity acquired from the low-temperature laboratory setup, but is included here as a comparison to the micro-furnace spectra. Emissivity minima values increase with increasing temperature from 500 $^{\circ}\text{C}$ to 1000 $^{\circ}\text{C}$. At temperatures higher than 1000 $^{\circ}\text{C}$, the minima values and wavelength positions are more variable. Arrows denote locations of shoulder features at ~ 11.5 and 12.5 μm .

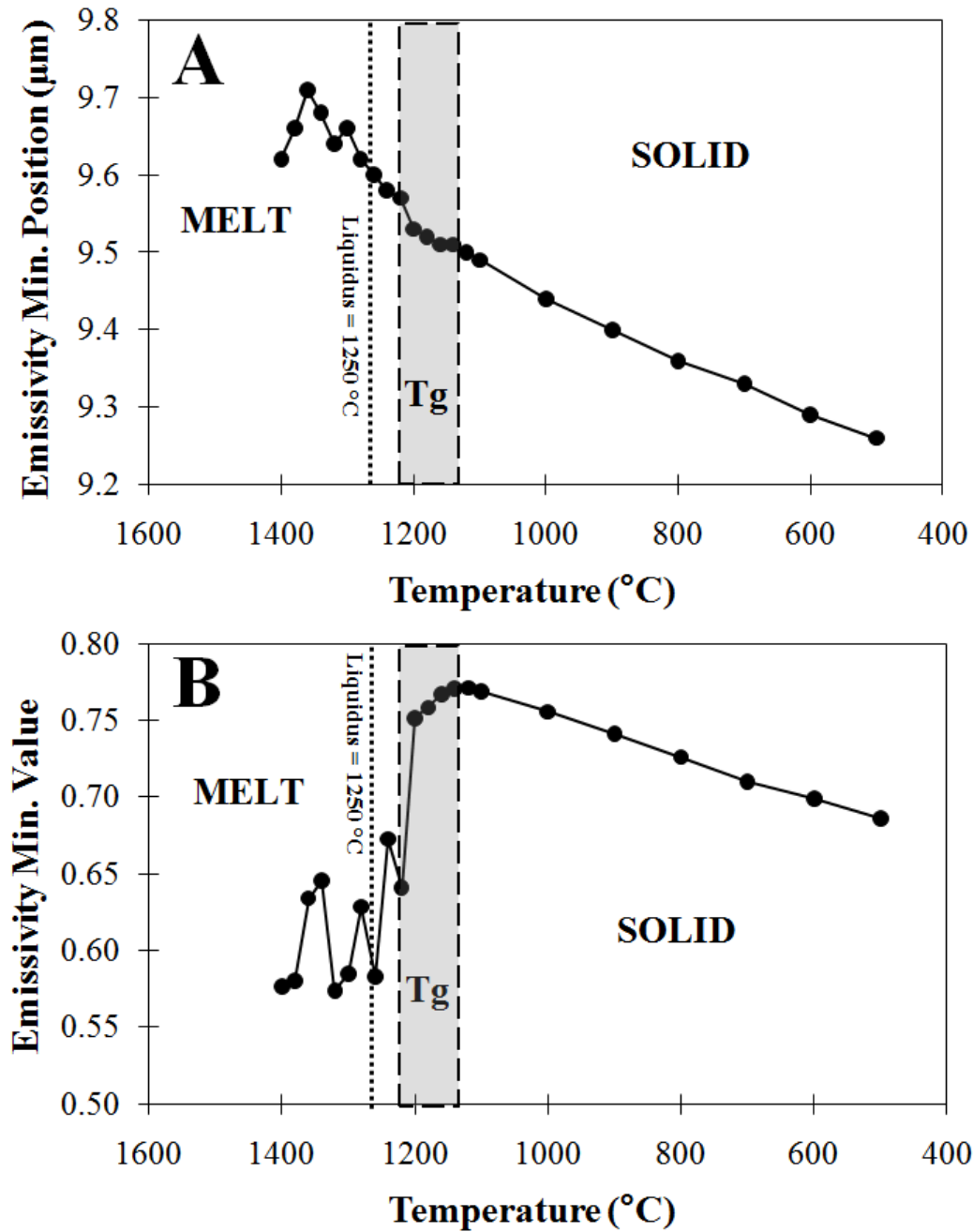


Figure 4-8 Variation in spectral features for glass 1. (A) Emissivity minimum position vs. set point temperature and (B) emissivity minimum value vs. set point temperature. At temperatures lower than ~1120 °C, minimum positions and emissivity values decrease linearly with decreasing set point temperature to 500 °C. Above 1120 °C, the minimum positions and emissivity values are more variable with temperature. Plots are divided into melt, Tg, and solid regions. The temperature range within which the Tg occurs is denoted by the grey box, and the dotted line marks the liquidus temperature of the glass.

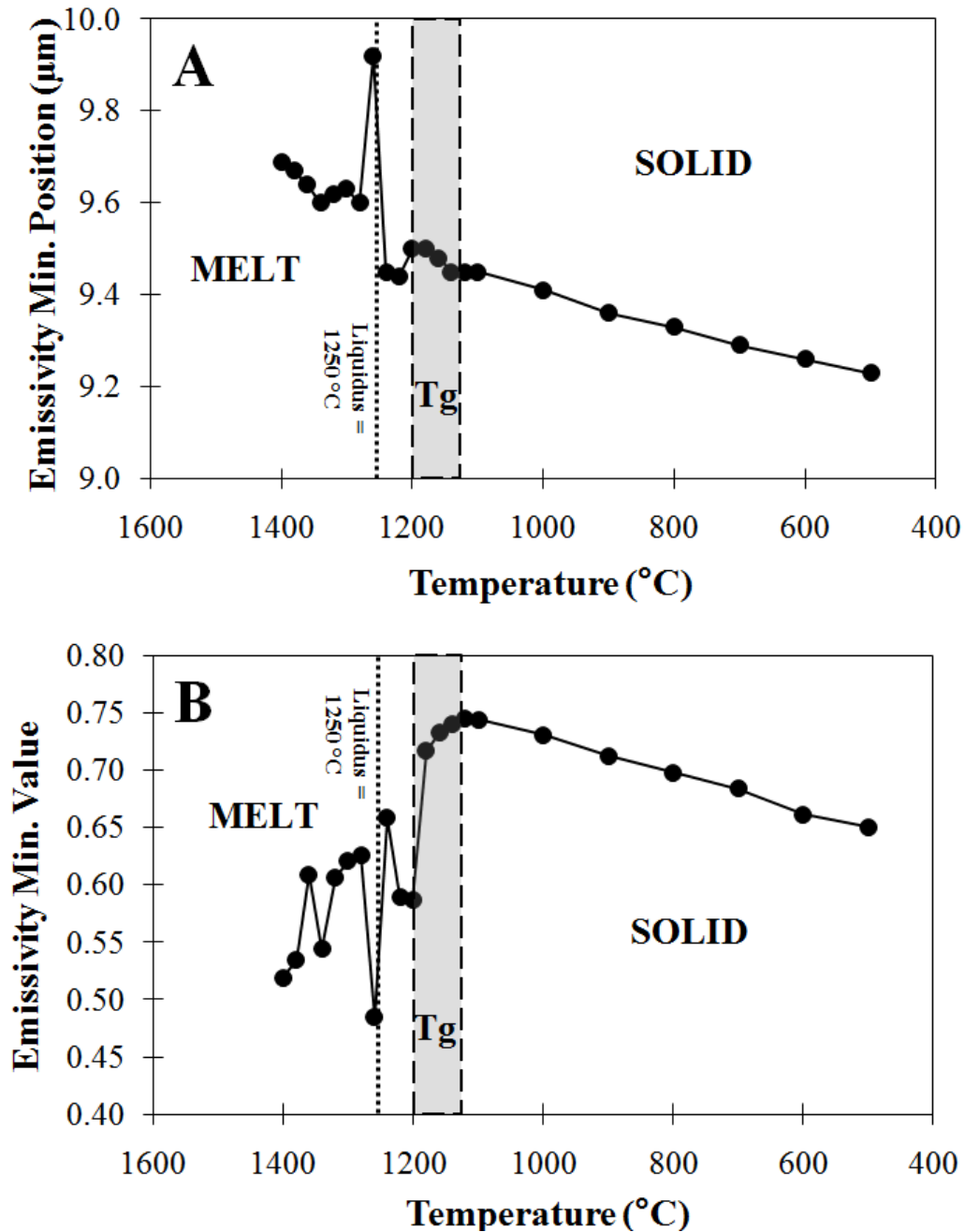


Figure 4-9 Variation in spectral features for glass 1a. (A) Emissivity minimum position vs. set point temperature and (B) emissivity minimum value vs. set point temperature. At temperatures lower than ~1120 °C, minimum positions and emissivity values decrease linearly with decreasing set point temperature to 500 °C. Above 1120 °C, the minimum positions and emissivity values are more variable with temperature. Plots are divided into melt, Tg, and solid regions. The temperature range within which the Tg occurs is denoted by the grey box, and the dotted line marks the liquidus temperature of the glass.

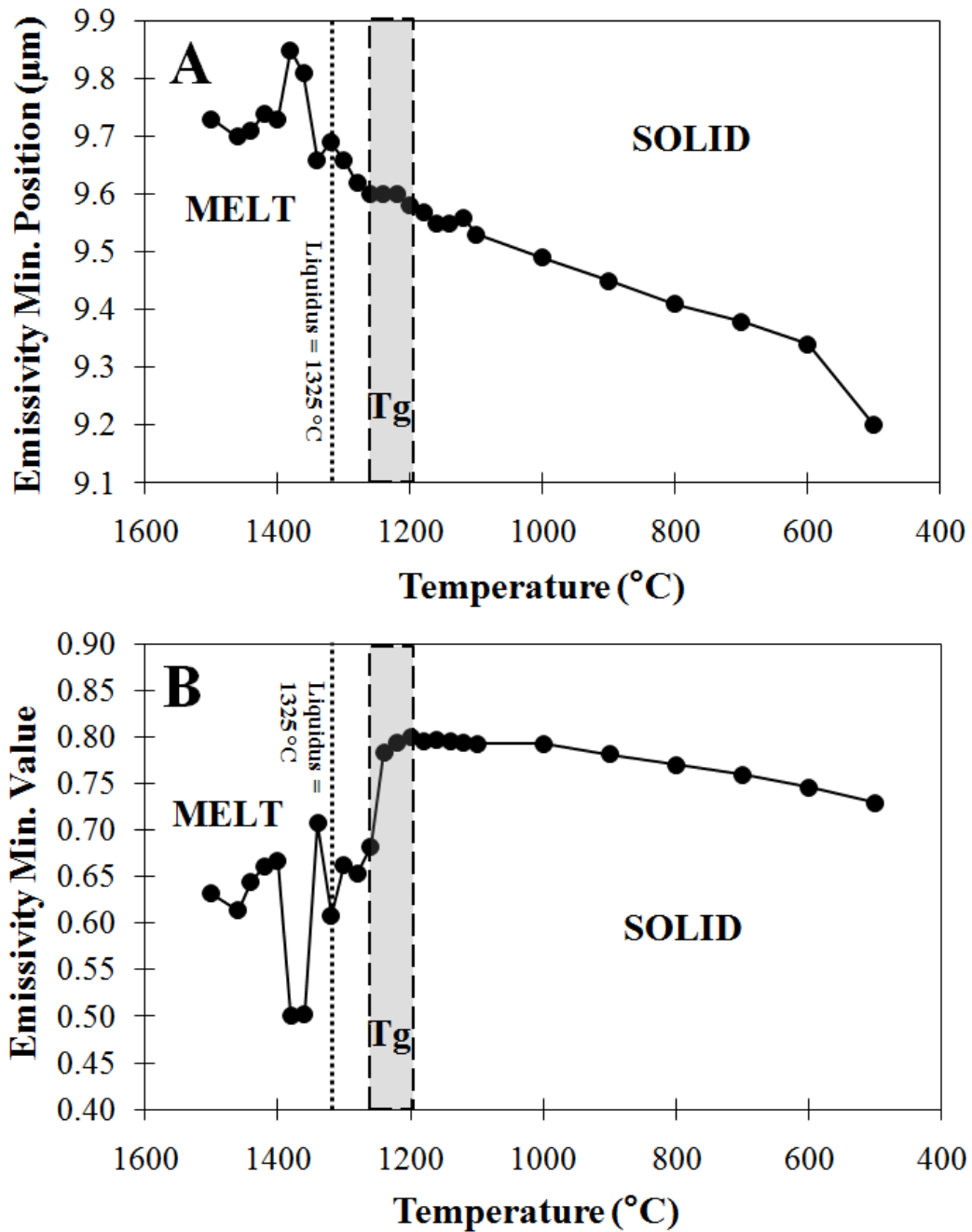


Figure 4-10 Variation in spectral features for glass 7. (A) Emissivity minimum position vs. set point temperature and (B) emissivity minimum value vs. set point temperature. At temperatures lower than 1200 °C, minimum positions and emissivity values decrease linearly with decreasing set point temperature to 500 °C. Above 1200 °C, the minimum positions and emissivity values are more variable with temperature. Plots are divided into melt, Tg, and solid regions. The temperature range within which the Tg occurs is denoted by the grey box, and the dotted line marks the liquidus temperature of the glass.

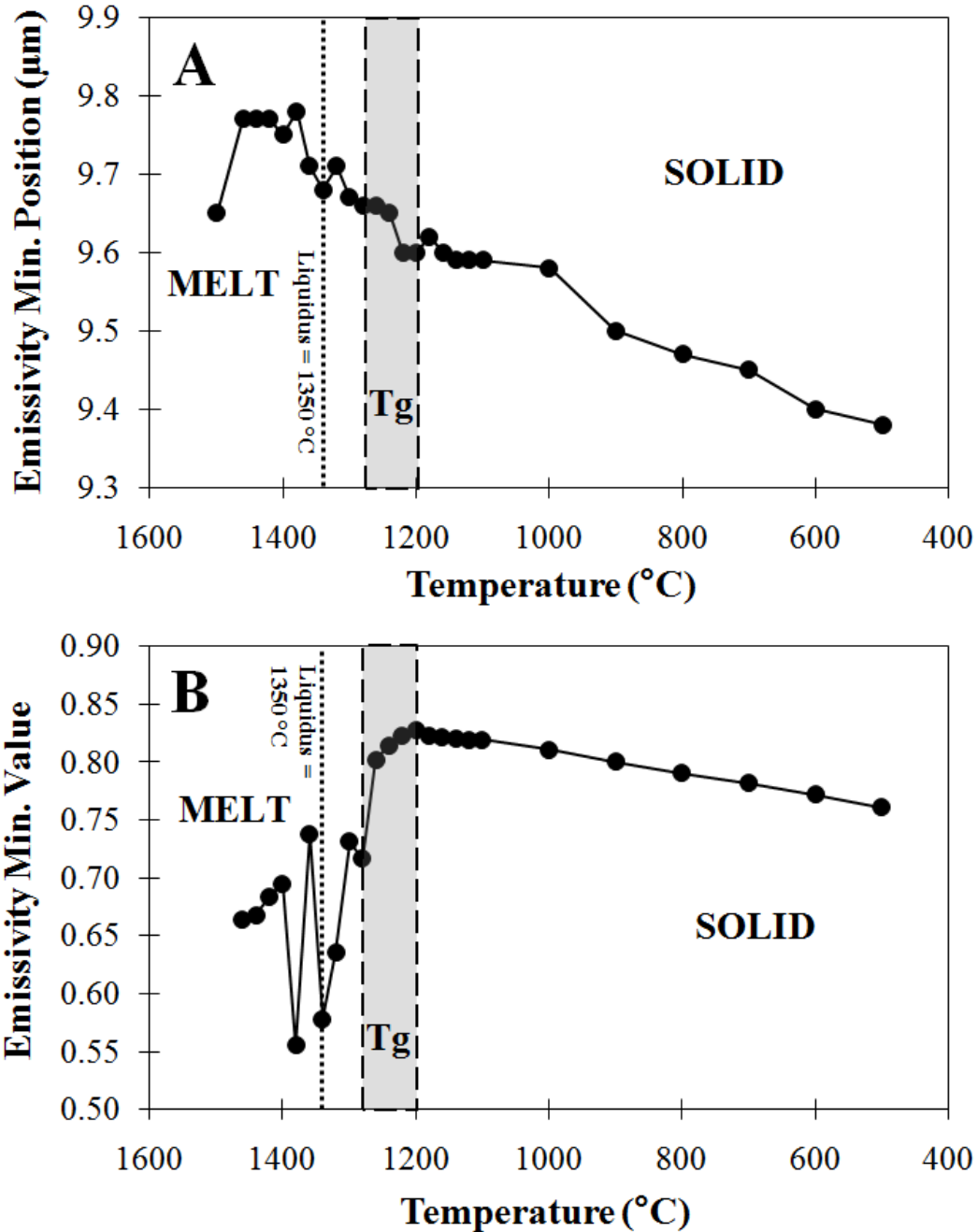


Figure 4-11 Variation in spectral features for glass 8. (A) Emissivity minimum position vs. set point temperature and (B) emissivity minimum value vs. set point temperature. At temperatures lower than 1200 °C, minimum positions and emissivity values decrease linearly with decreasing set point temperature to 500 °C. Above 1200 °C, the minimum positions and emissivity values are more variable with temperature. Plots are divided into melt, T_g, and solid regions. The temperature range within which the T_g occurs is denoted by the grey box, and the dotted line marks the liquidus temperature of the glass.

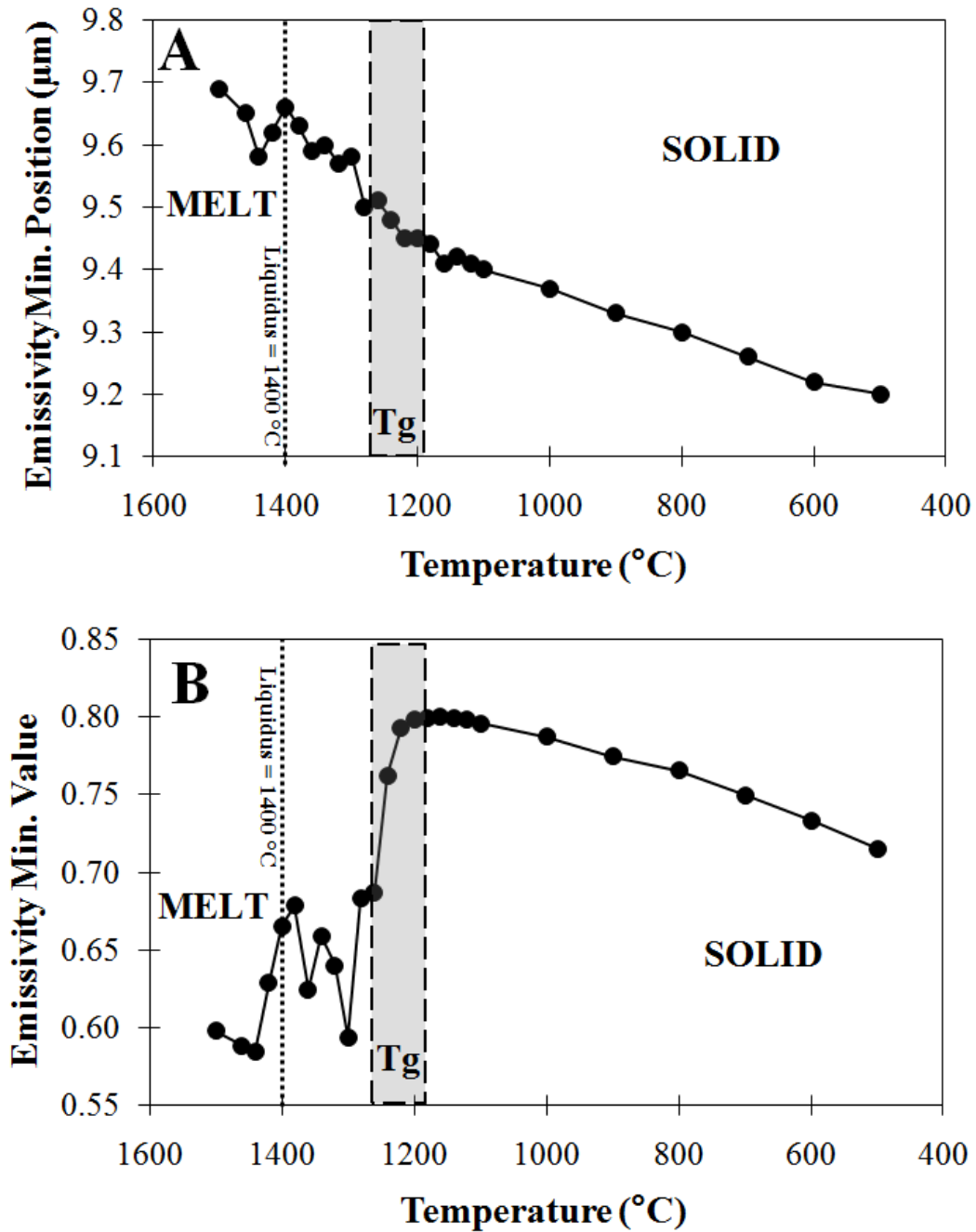


Figure 4-12 Variation in spectral features for glass 21. (A) Emissivity minimum position vs. set point temperature and (B) emissivity minimum value vs. set point temperature. At temperatures lower than ~1180 °C, minimum positions and emissivity values decrease linearly with decreasing set point temperature to 500 °C. Above 1180 °C, the minimum positions and emissivity values are more variable with temperature. Plots are divided into melt, Tg, and solid regions. The temperature range within which the Tg occurs is denoted by the grey box, and the dotted line marks the liquidus temperature of the glass.

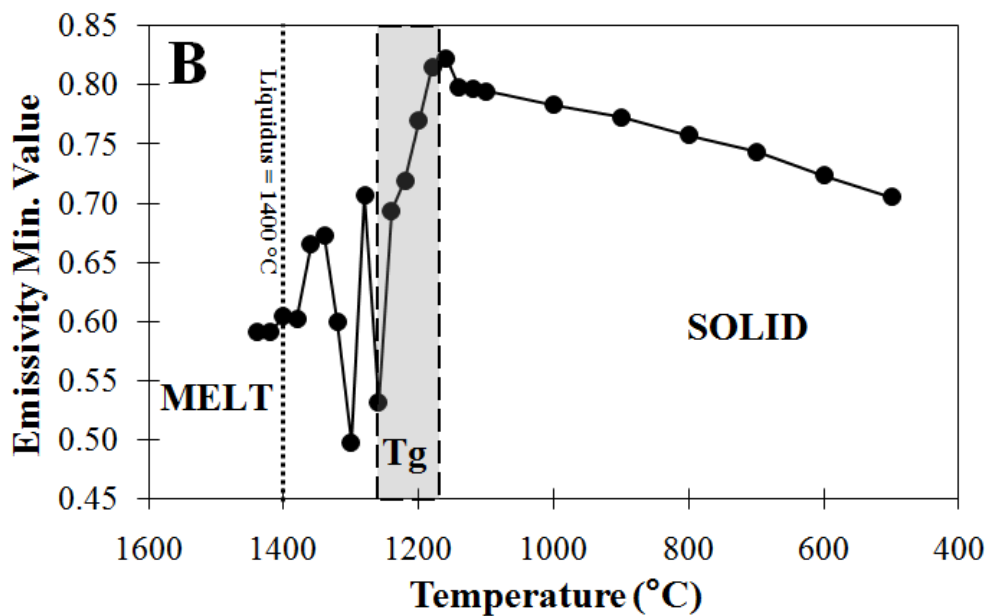
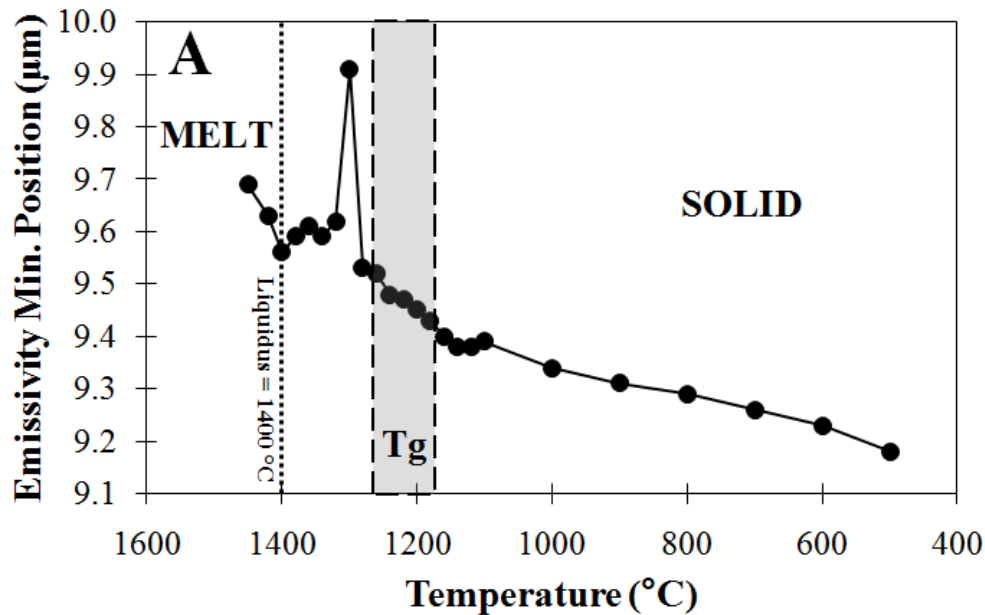


Figure 4-13 Variation in spectral features for glass 21a. (A) Emissivity minimum position vs. set point temperature and (B) emissivity minimum value vs. set point temperature. At temperatures lower than 1160 °C, minimum positions and emissivity values decrease linearly with decreasing set point temperature to 500 °C. Above 1160 °C, the minimum positions and emissivity values are more variable with temperature. Plots are divided into melt, Tg, and solid regions. The temperature range within which the Tg occurs is denoted by the grey box, and the dotted line marks the liquidus temperature of the glass.

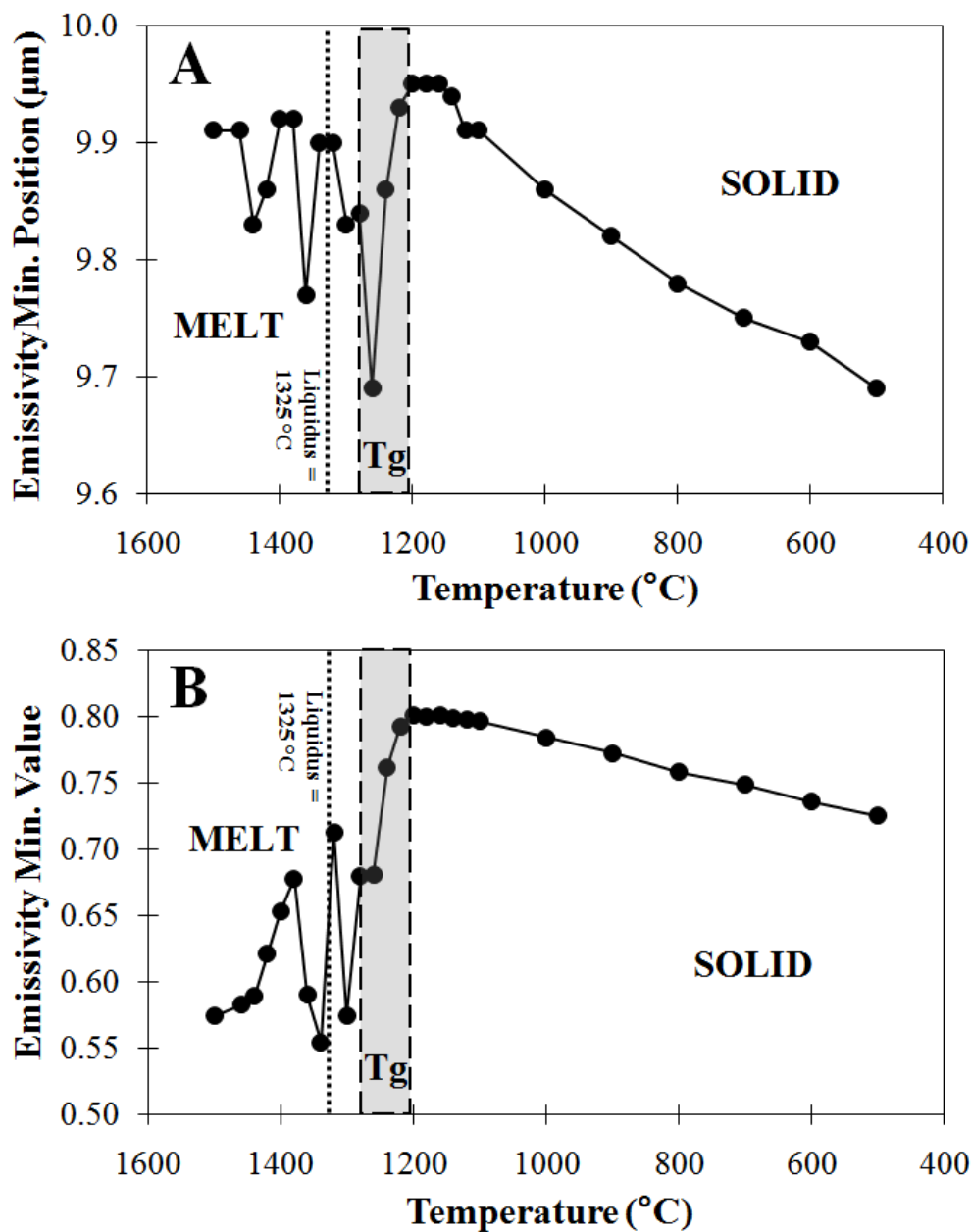


Figure 4-14 Variation in spectral features for glass 24. (A) Emissivity minimum position vs. set point temperature and (B) emissivity minimum value vs. set point temperature. At temperatures lower than 1200 °C, minimum positions and emissivity values decrease linearly with decreasing set point temperature to 500 °C. Above 1200 °C, the minimum positions and emissivity values are more variable with temperature. Plots are divided into melt, T_g, and solid regions. The temperature range within which the T_g occurs is denoted by the grey box, and the dotted line marks the liquidus temperature of the glass.

Emissivity minimum positions and minimum values at above - liquidus temperatures for glass 24 display much more variation than those of the other glasses (Figure 4-14). Glass 24 is the oligoclase end member glass, and thus contains a lower amount of overall SiO₂ compared to the other glass samples. The behavior of glass 24 spectra relative to those of the other glasses further supports the observation that SiO₂ content in a glass directly affects the behavior of the emission spectrum. The spectra of glass 3, another low-quartz end member glass in the suite, display similar behavior to that of glass 24. However, spectra were not collected every 20 °C for glass 3; therefore, there is not yet enough spectral data to allow for a direct comparison of glass 3 and glass 24.

Many of the higher temperature spectra taken in 20 °C increments exhibit a significant spectral shoulder longward of 14 μm, particularly at high temperatures (>1200 °C). An example of glass spectra from 7 to 20 μm at several temperatures is shown in Figure 4-15. The variability in emissivity and spectral shoulder with changing temperature is apparent from 14 to 20 μm. The change in shoulder shape is not linearly correlated with rising temperature, and the size of the shoulder varies with glass composition.

4.3.2 Quenched vs. Slowly Cooled Glasses

During initial glass synthesis, each of the samples was melted from crystalline material and then rapidly quenched to achieve a glassy state (as described in Chapter 2 of this work). Glasses melted in the micro-furnace were not quenched, but rather allowed to cool slowly to room

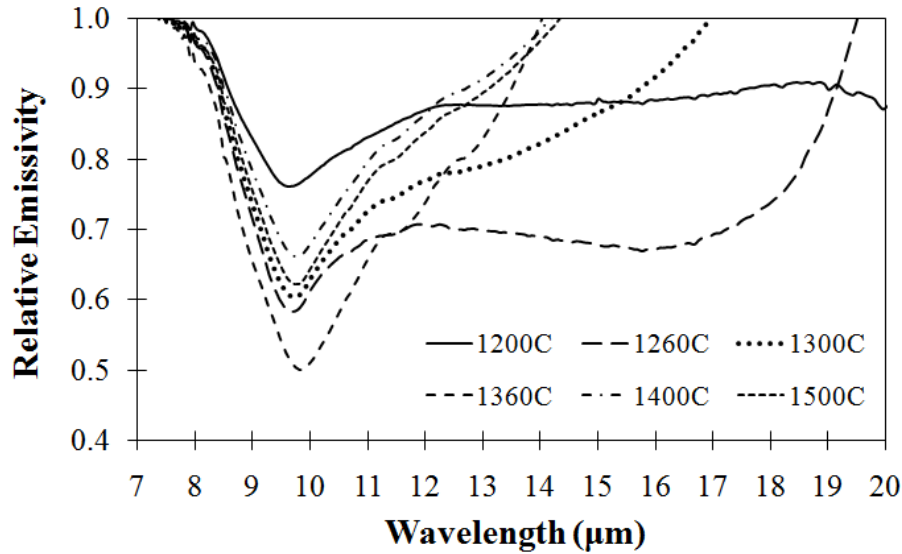


Figure 4-15 Change in spectral shape with temperature. The spectrum at 1200 °C is representative of the spectral shape at temperatures 1200 °C and below. Above 1200 °C, a significant shoulder is introduced into the spectra from ~14 to 20 µm. The change in shape of the shoulder does not behave in a linear manner with temperature. All glass spectra in this study were scaled to an emissivity of 1 at 7.5 and 14 µm in order to eliminate this shoulder feature.

temperature, in order to mimic the natural behavior of lava. Low-temperature (80 °C) emission spectra of several the quenched glasses are compared to that of the slowly-cooled glasses (Figure 4-16). Spectra for the remainder of the glasses are shown in Appendix A (Figures A-19 through A-21). For a given glass, the overall spectral shape remains similar; however, in each case, the quenched glass has a higher emission minimum value than the slowly-cooled glass. For each glass the quenched spectrum was divided by the slowly-cooled spectrum to determine the difference between the two spectra (Figure 4-16). Although some noise is apparent, a possible spectral feature does exist at approximately 9 µm. This spectral feature is muted as compared to the quenched and slowly-cooled spectra, but there appears to be some spectral morphology.

A comparison of spectra acquired during sample heat-up to those acquired during sample cool-down is presented for glasses 8 and 21 (Figures 4-17 and 4-18). Data for two other glasses are shown in Appendix A (A-22 and A-23) For clarity, only spectra at 100 °C increments are plotted, and plot scales have been adjusted to 8-12 μm to better highlight the behavior of the emissivity minimum. At temperatures below 1100 °C, the cool-down spectrum at a given temperature is more muted than the corresponding heat-up spectrum, and the emissivity minimum value of the cool-down spectrum is thus higher than that of the heat-up spectrum. Additionally, during heat-up the emissivity minimum values increase and minimum positions shift to longer wavelengths with increasing temperature. During cool-down, emissivity minimum values decrease and emissivity minimum positions shift to shorter wavelengths with decreasing temperature. This is graphically represented in part D of figures 4-17 and 4-18. The difference in emissivity minimum value between heat-up and cool-down spectra is also apparent. At temperatures above 1200 °C in each glass, the emissivity minimum values of the heat-up and cool-down spectra are more variable and non-linear with temperature.

4.3.3 Wt % SiO₂, Al / [Al+Si], and [Na+Ca] / Si

The change in emissivity minimum position with increasing wt. % SiO₂, Al / [Al+Si], and [Na+Ca] / Si for each of the quenched glasses were presented in Chapter 2. These data showed an increase in emissivity minimum position with increasing wt. % SiO₂, decreasing Al / [Al+Si] and decreasing [Na+Ca] / Si. Emissivity minimum position has proven to change markedly with increasing temperature in this study; therefore, the emissivity minimum position

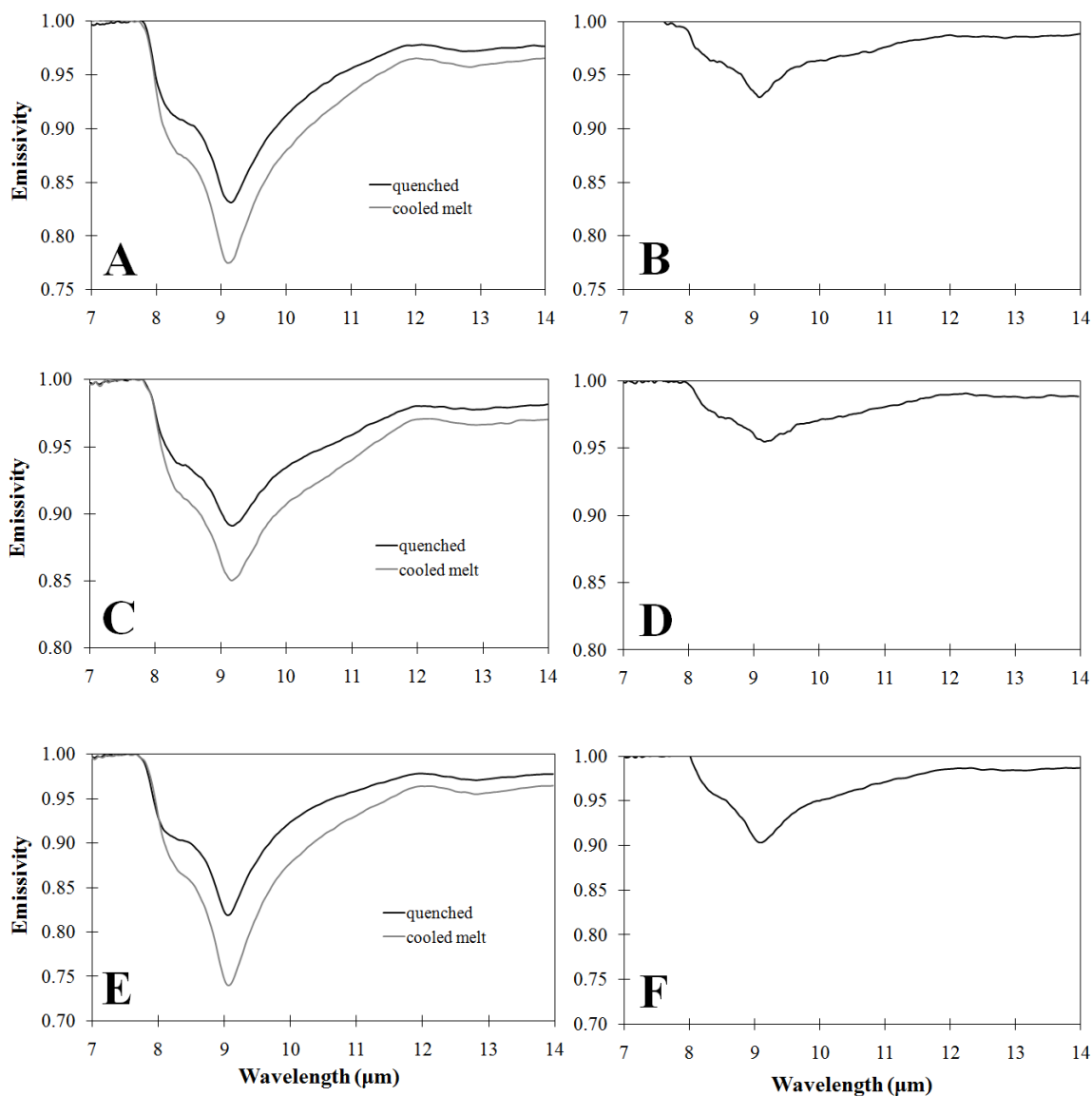


Figure 4-16 Comparison of 80 °C quenched glass spectra to 80 °C slowly-cooled glass spectra for (A) glass 1, (C), glass 7, and (E) glass 21. Slowly-cooled spectra (grey lines) have deeper emission minima than their quenched counterparts (black lines). The quenched spectrum was divided by the slowly-cooled spectrum for (B) glass 1, (D) glass 7 and (F) glass 21. In each case, a muted spectral feature with some spectral morphology is apparent at ~9 μm .

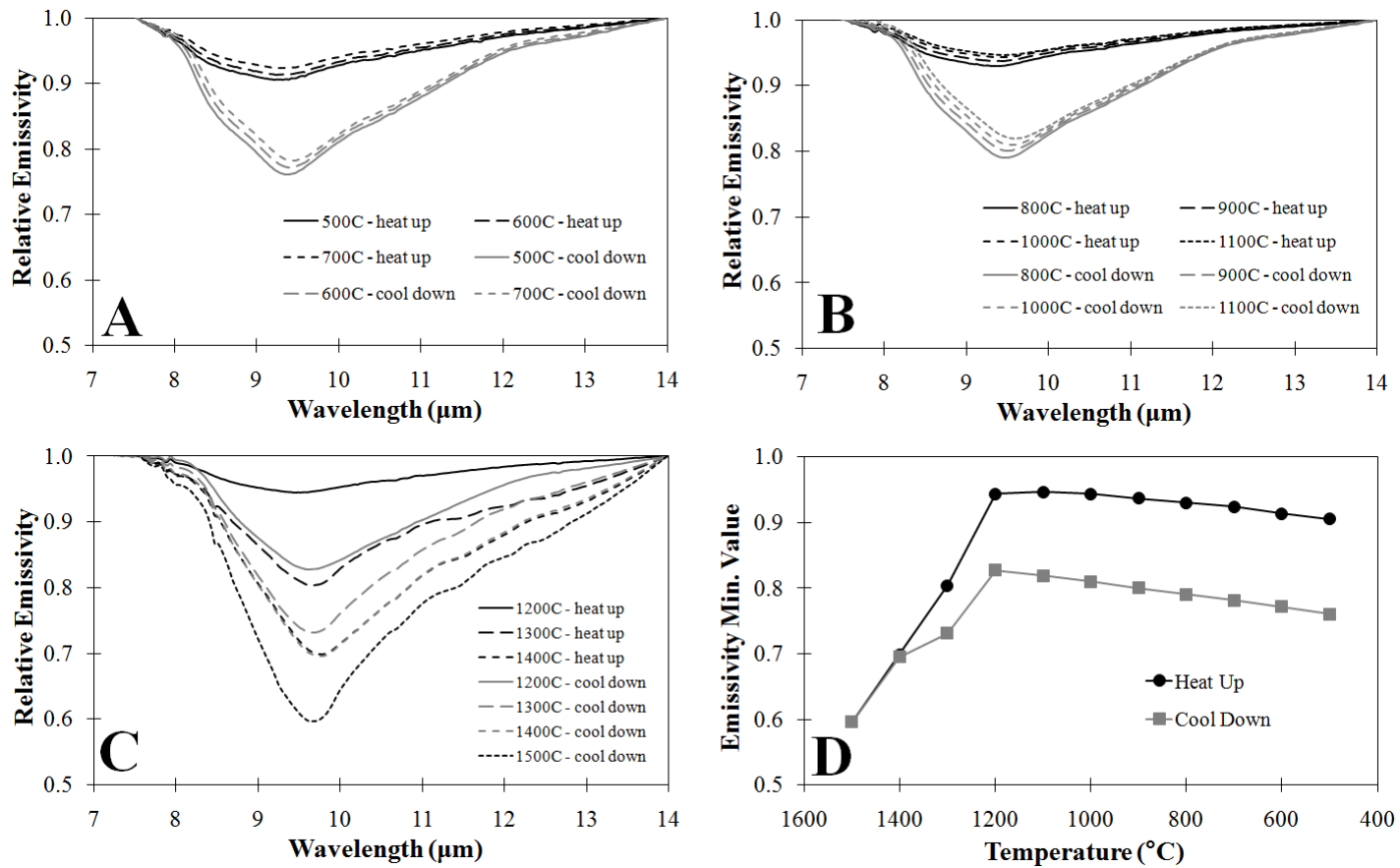


Figure 4-17 Glass 8 heat-up vs. cool-down spectra from (A) 500 °C to 700 °C, (B) 800 °C to 1100 °C, and (C) 1200 °C to 1500 °C. At temperatures 1100 °C and below, the cool-down spectrum at a given temperature is more muted than the corresponding heat-up spectrum. During heat-up, the emissivity minimum values increase and emissivity minimum positions shift to longer wavelengths with increasing temperature. During cool-down, emissivity minimum values decrease and emissivity minimum positions shift to shorter wavelengths with decreasing temperature. The difference in minimum value between heat-up and cool-down spectra is shown in (D). At temperatures above 1200 °C, the minimum values of the heat-up and cool-down spectra are more variable and non-linear with temperature.

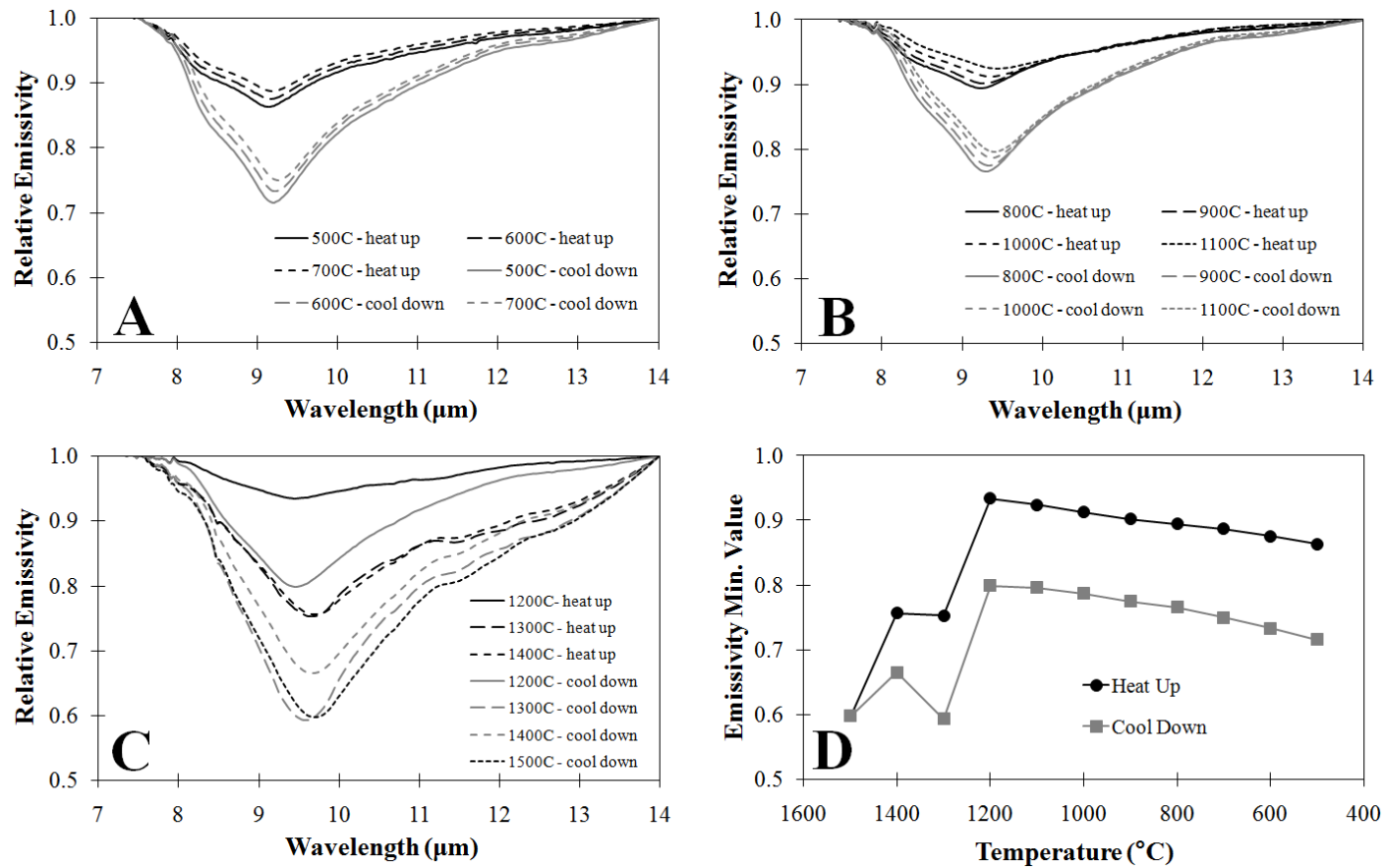


Figure 4-18 Glass 21 heat-up vs. cool-down spectra from (A) 500 °C to 700 °C, (B) 800 °C to 1100 °C, and (C) 1200 °C to 1500 °C. At temperatures 1100 °C and below, the cool-down spectrum at a given temperature is more muted than the corresponding heat-up spectrum. During heat-up, the emissivity minimum values increase and emissivity minimum positions shift to longer wavelengths with increasing temperature. During cool-down, emissivity minimum values decrease and emissivity minimum positions shift to shorter wavelengths with decreasing temperature. The difference in minimum value between heat-up and cool-down spectra is shown in (D). At temperatures above 1200 °C, the minimum values of the heat-up and cool-down spectra are more variable and non-linear with temperature.

data for all glass samples cooled from their maximum temperature to 500 °C, as well as the data acquired at 80 °C, were plotted against wt. % SiO₂, Al / [Al+Si], and [Na+Ca] / Si (Figures 4-19 to 4-24).

Although detailed compositional data has not yet been acquired for the glasses re-melted and slowly-cooled in the micro-furnace, it is not expected that any significant changes in composition would take place during re-melting. The change in the emissivity minimum positions of the glasses with changing temperature, and the effect on the molar ratio data, is consistent regardless of composition. Figure 4-25 shows the change in R² value and linear trend line slope with decreasing temperature for wt. % SiO₂. The change in R² and slope with decreasing temperature for Al / [Al+Si] and [Na+Ca] / Si are shown in Appendix A (Figures A-24 and A-25, respectively). It is important to note that spectra were not acquired for all of the glasses at all temperatures, due to the differences in liquidus temperature and melting requirements among the glass samples. For example, four of the glasses (3, 19, 19a, and 20a) do not have data points at 1400 °C, because they were only heated to temperatures of 1300 °C and below for analysis. Al / [Al+Si], and [Na+Ca] / Si have similar slope and R² behavior to wt. % SiO₂. All of the molar ratios have high R² values and relatively consistent slopes at temperatures below 1200 °C. From 1200 °C to 1500 °C, however, R² and slope values change dramatically with temperature. This is expected, because 1) fewer glasses are plotted at 1400 °C and 1500 °C, and 2) emissivity minimum positions and emissivity minimum values show the most variability

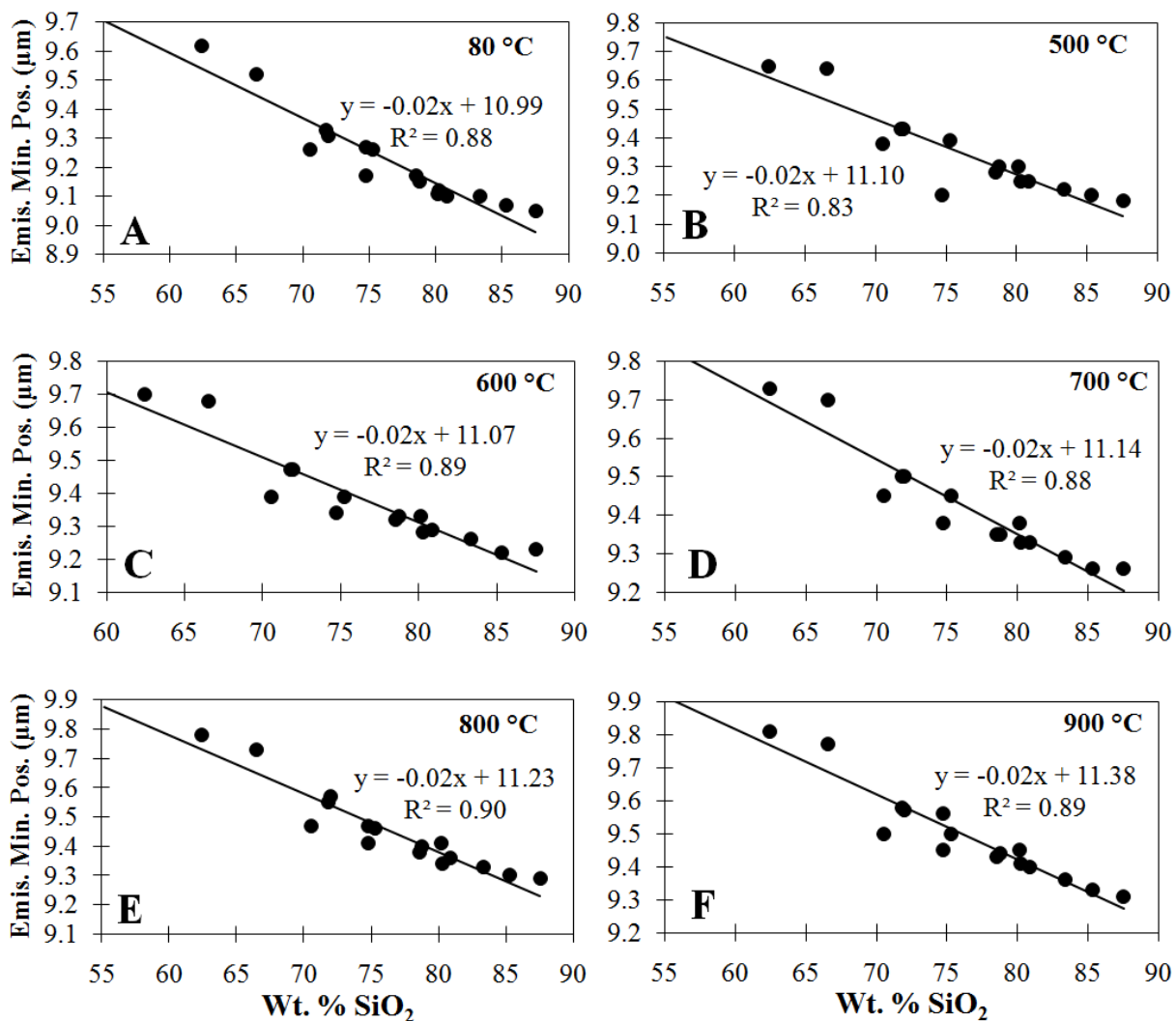


Figure 4-19 Change in emissivity minimum position with wt. % SiO₂ for all glass spectra at (A) 80 °C, (B) 500 °C, (C) 600 °C, (D) 700 °C, (E) 800 °C, and (F) 900 °C. The minimum position for each of the glasses increases slightly with increasing temperature. Wt. % SiO₂ values remain the same for each temperature, as the wt. % SiO₂ of the glasses is not expected to change with increasing temperature.

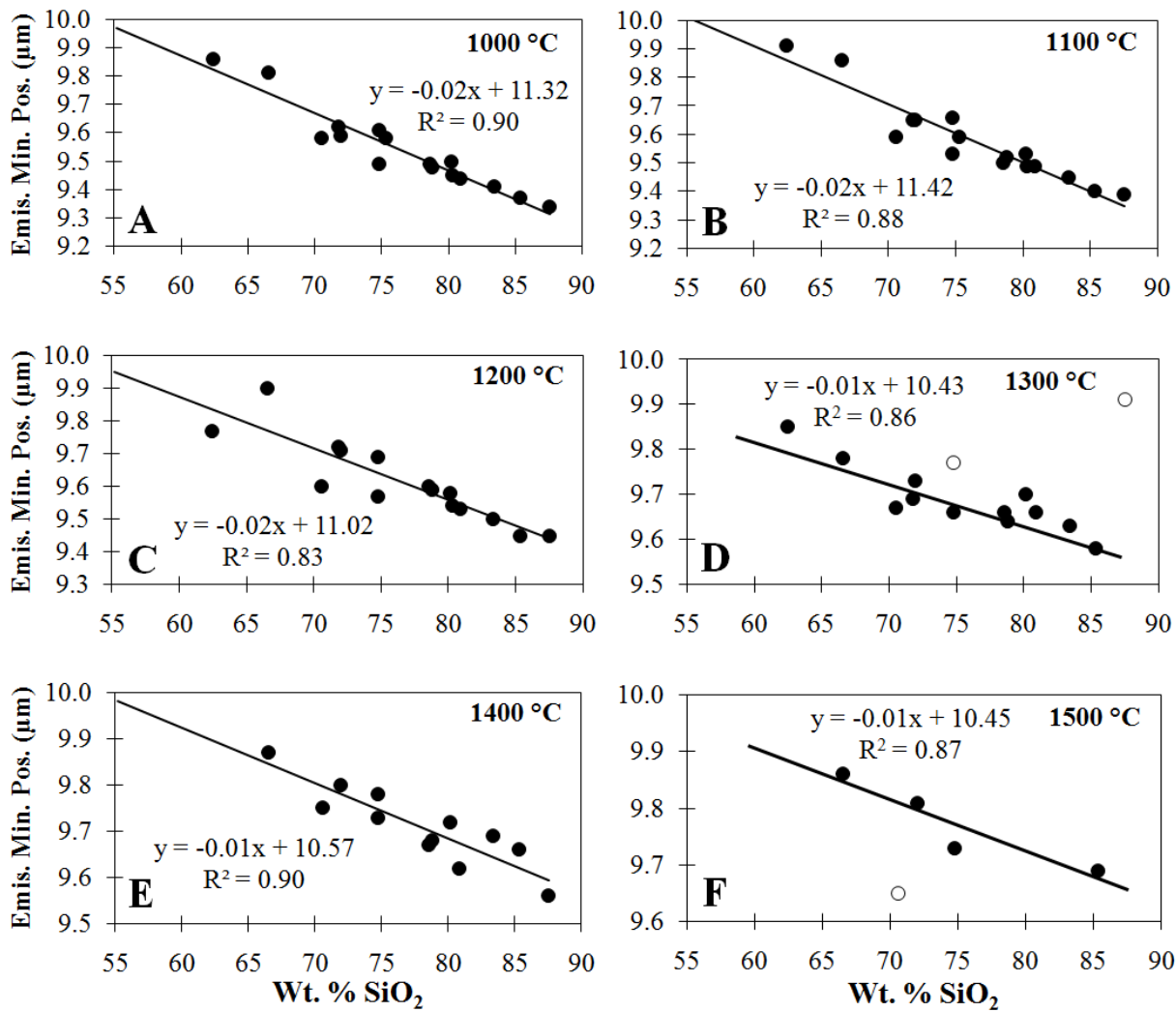


Figure 4-20 Change in emissivity minimum position with wt. % SiO₂ for all glass spectra at (A) 1000 °C, (B) 1100 °C, (C) 1200 °C, (D) 1300 °C, (E) 1400 °C, and (F) 1500 °C. Open circles denote data outliers. Overall, the minimum position for each of the glasses increases slightly with increasing temperature. Wt. % SiO₂ values remain the same for each temperature, as the wt. % SiO₂ of the glasses is not expected to change with increasing temperature.

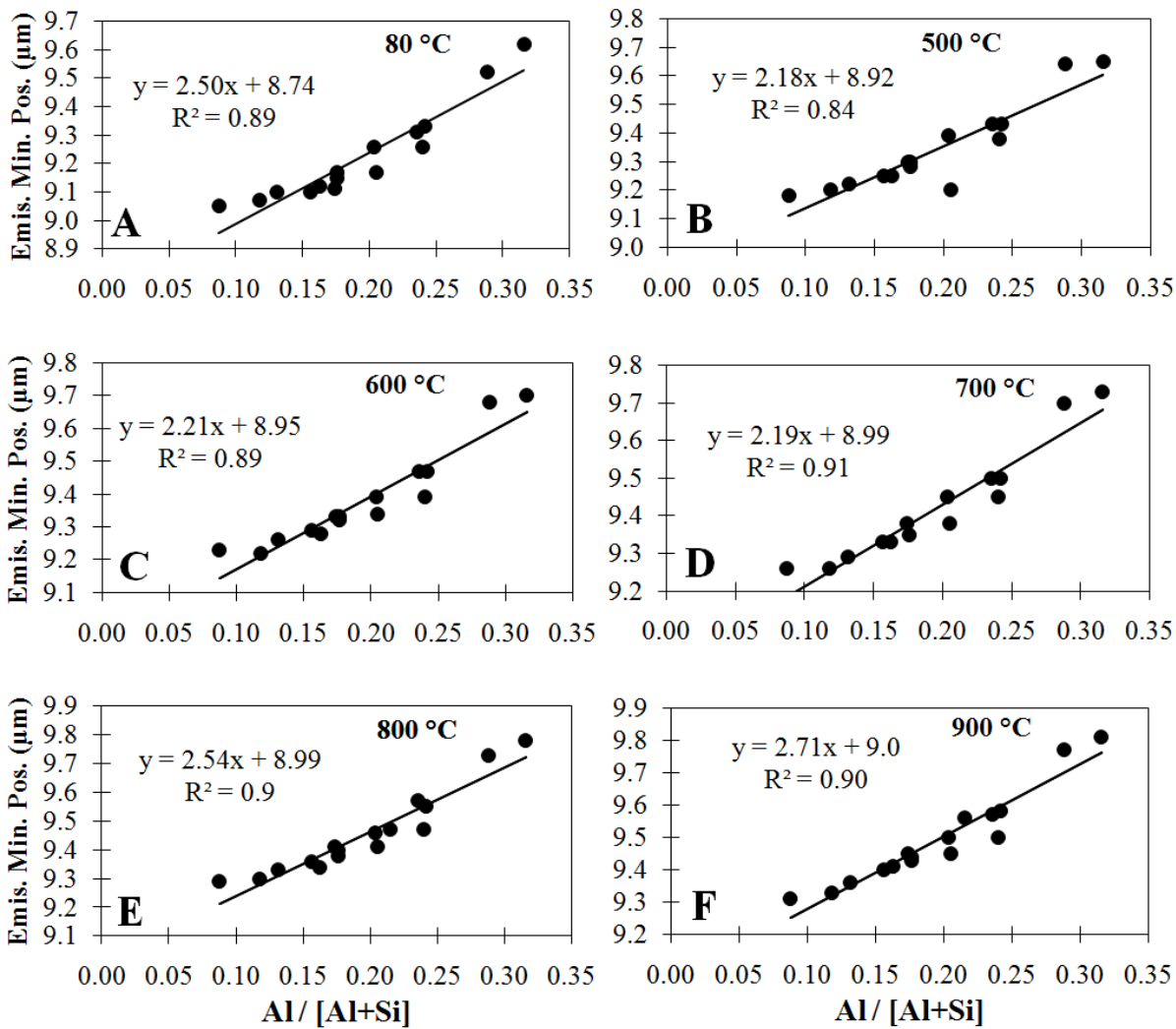


Figure 4-21 Change in emissivity minimum position with Al / [Al+Si] for all glass spectra at (A) 80 °C, (B) 500 °C, (C) 600 °C, (D) 700 °C, (E) 800 °C, and (F) 900 °C. Overall, the minimum position for each of the glasses increases slightly with increasing temperature. Al / [Al+Si] values remain the same for each temperature, as the Al / [Al+Si] of the glasses is not expected to change with increasing temperature.

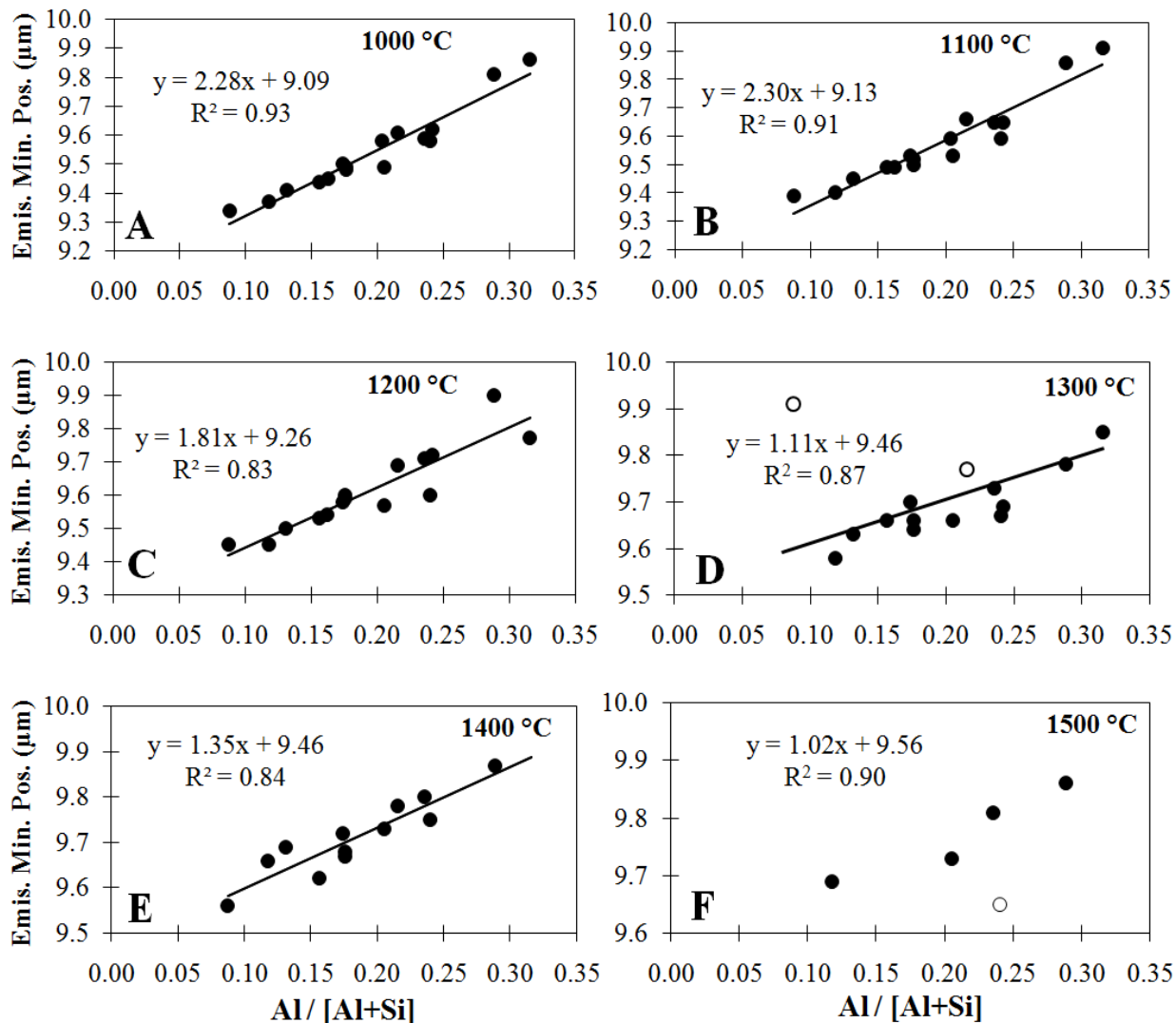


Figure 4-22 Change in emissivity minimum position with $Al / [Al+Si]$ for all glass spectra at (A) 1000 °C, (B) 1100 °C, (C) 1200 °C, (D) 1300 °C, (E) 1400 °C, and (F) 1500 °C. Open circles denote data outliers. Overall, the minimum position for each of the glasses increases slightly with increasing temperature. $Al / [Al+Si]$ values remain the same for each temperature, as the $Al / [Al+Si]$ of the glasses is not expected to change with increasing temperature.

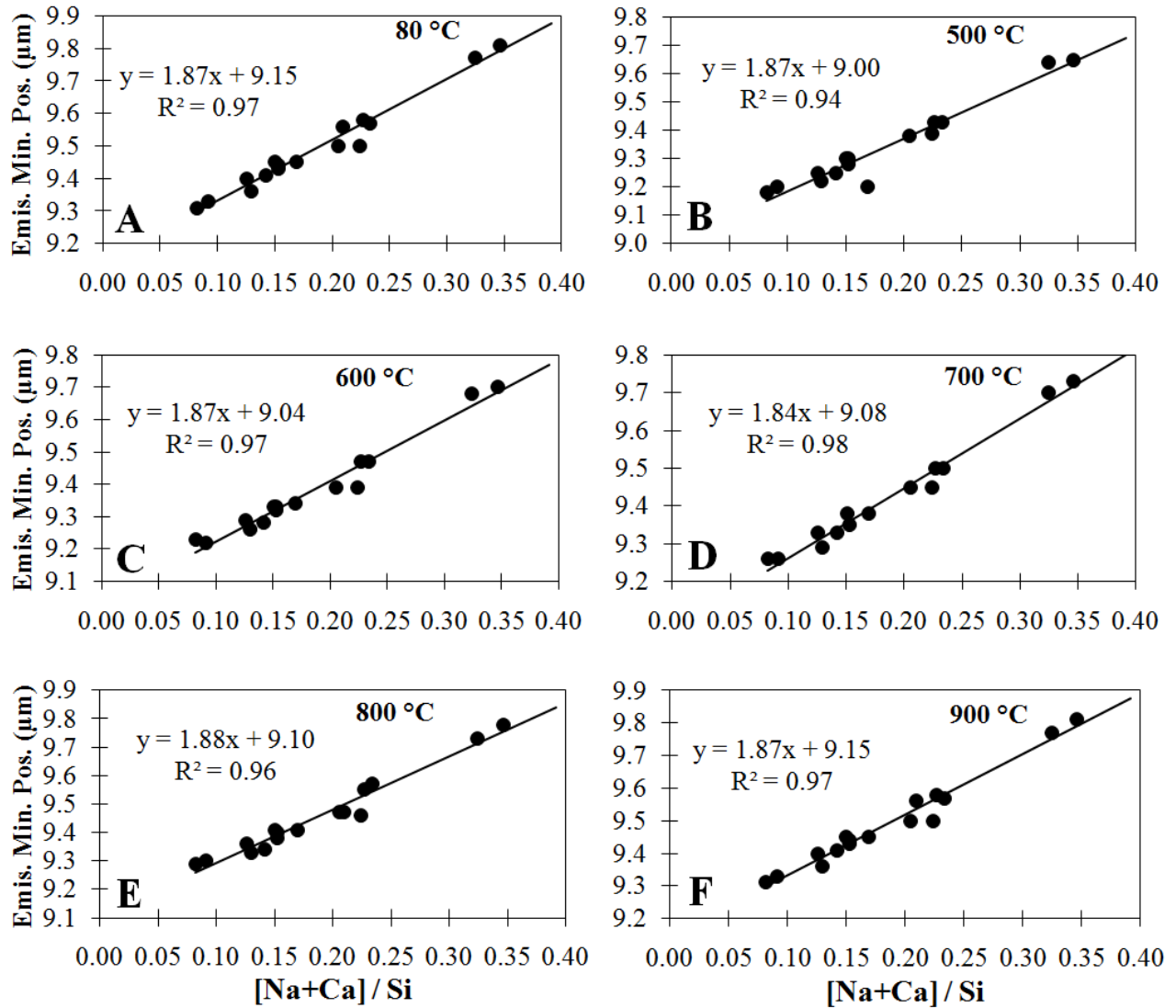


Figure 4-23 Change in emissivity minimum position with [Na+Ca] / Si for all glass spectra at (A) 80 °C, (B) 500 °C, (C) 600 °C, (D) 700 °C, (E) 800 °C, and (F) 900 °C. Overall, the minimum position for each of the glasses increases slightly with increasing temperature. [Na+Ca] / Si values remain the same for each temperature, as the [Na+Ca] / Si of the glasses is not expected to change with increasing temperature.

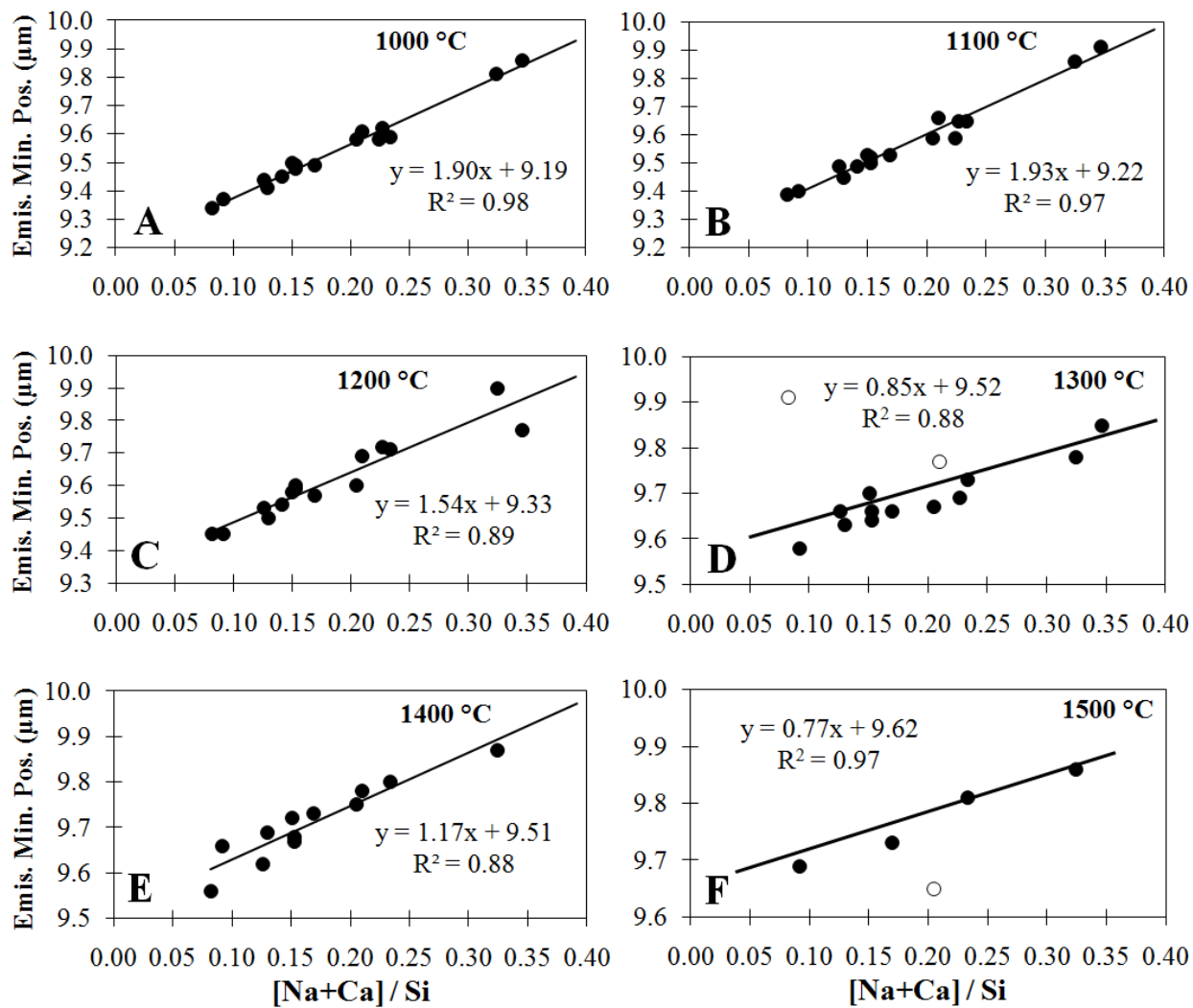


Figure 4-24 Change in emissivity minimum position with $[\text{Na}+\text{Ca}]/\text{Si}$ for all glass spectra at (A) 1000 °C, (B) 1100 °C, (C) 1200 °C, (D) 1300 °C, (E) 1400 °C, and (F) 1500 °C. Open circles denote data outliers. Overall, the minimum position for each of the glasses increases slightly with increasing temperature. $[\text{Na}+\text{Ca}]/\text{Si}$ values remain the same for each temperature, as the $[\text{Na}+\text{Ca}]/\text{Si}$ of the glasses is not expected to change with increasing temperature.

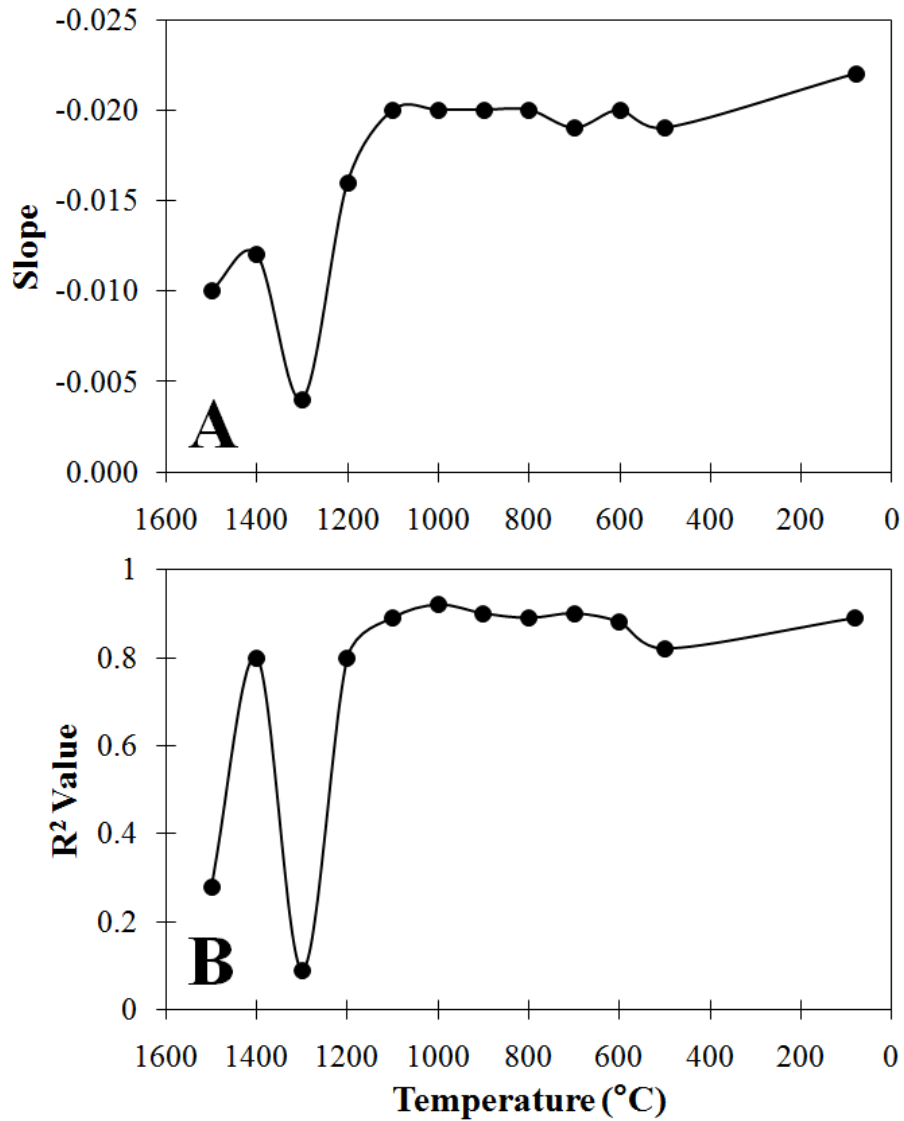


Figure 4-25 Change in (A) slope and (B) R² value with temperature for the wt. % SiO₂ vs. emissivity minimum position plots in Figures 4-19 and 4-20. Slope and R² values are variable above 1200 °C. The low point at 1300 °C is attributed to the greater degree of variability in the data at this temperature as compared to the other temperatures. The low point at 1500 °C is due to the lack of data at this temperature, as only 5 of the glasses needed to reach a temperature of 1500 °C in order to fully melt. Both slope and R² values are near-linear from 1100 °C to 80 °C.

between 1200 °C and 1500 °C. The distinct rise of both R^2 and slope between 1300 °C and 1100 °C is also consistent with the temperature range over which the inferred glass transition occurs for each of the glasses.

4.3.4 Half Width and Spectral Shape with Temperature

Spectral half-width is used to measure spectral width at 50% of the peak response. It is a widely-used tool in spectroscopy to characterize spectral shape, and changes in spectral shape with changing conditions (e.g. temperature, pressure, composition). The half width was calculated for each glass spectrum using the following method. First, the emissivity value at the half-depth of the main spectral feature was found using the following formula: $\epsilon_{\min} + (1 - \epsilon_{\min}) / 2$, where ϵ_{\min} = the emissivity minimum of the spectrum. Then the two wavelengths corresponding to the ϵ_{\min} value, λ_1 and λ_2 , were found. Subtracting λ_1 from λ_2 yielded a half-width for the main spectral feature, in microns, located at the ϵ_{\min} value. The calculation method, and the change in half-width with increasing temperature for 4 of the glasses, is shown in Figure 4-26. At lower temperatures (<1200 °C) the half-width of the spectra remains relatively constant, and variation in half-width value for a given glass is less than 0.2 μm . At temperatures exceeding 1200 °C, half-width values become much more variable. This is consistent with the variability of emissivity minimum values at the same temperatures.

4.3.5 Total Emitted Energy with Temperature

The area under the signal intensity curve for each glass at each temperature can be considered a proxy for the total emitted energy at each set point temperature. Emissivity is a dimensionless quantity; therefore the signal intensity was used in calculations, as it is directly related to emitted energy from the sample. For a given signal intensity plot, a series of vertical rectangles were drawn beneath the signal intensity curve. The area of each of these rectangles was then found by multiplying the width of the rectangle in microns ($\sim 0.2 \mu\text{m}$) by the signal intensity value at the midpoint of the rectangle. The areas of the rectangles were then added together to yield an approximation of the total area under the curve between 7 and 14 μm . The data were split into two groups around the inferred glass transition to create two separate data series. A power trend line was calculated for the data between 1100 °C and 500 °C, as these data display a change in power with increasing temperature. The trend line was then extended to include the data in the melt region ($>1200 \text{ }^\circ\text{C}$). For the purposes of this study, the units of emitted energy are in volts-microns, and are thus not absolute, as in a Planck function. However, the calculation of emitted energy in this study allows for a comparison of energy output among temperatures and among glass compositions in the absence of a true blackbody and response function for the spectrometer.

The change in emitted energy with temperature for the 7 glasses is shown in Figure 4-27. All glasses display a very similar trend in emitted energy with temperature. As the glass melts cool from their maximum temperature, emitted energy is variable; however there is an overall

slight decrease in the trend of the data. From ~ 1200 °C to 500 °C, emitted energy for all the glasses takes on an power curve ($y = x^2$) shape, which is consistent from glass to glass. This is denoted by a trend line through the data for each glass from ~1200 °C to 500 °C, all of which have a very good fit ($R^2 = 0.99$). It is important to note that this trend line is only for data between ~1200 °C to 500 °C, and does not apply to the higher temperature data. However, the high R^2 values of the trend lines, as well as their consistently good fit among all glass compositions, serve to validate the area calculation method. Data in the melt region (> 1200 °C) strays from the trend line, which corresponds with the lowering of emissivity values in this region. This verifies that the energy emitted from the glass melts differs markedly from that of the solid glasses, and that IR emission mechanisms are different above and below the T_g .

4.4 DISCUSSION

4.4.1 Calibration

The type of blackbody material utilized in deriving emissivity spectra is known to affect the overall morphology of the emission spectrum. For example use of a blackbody which has a non-unit emissivity, particularly at the Christiansen frequency, can impart errors in emission spectra (Ruff et al., 1997). An ideal blackbody has an emissivity of 1 at all wavelengths and

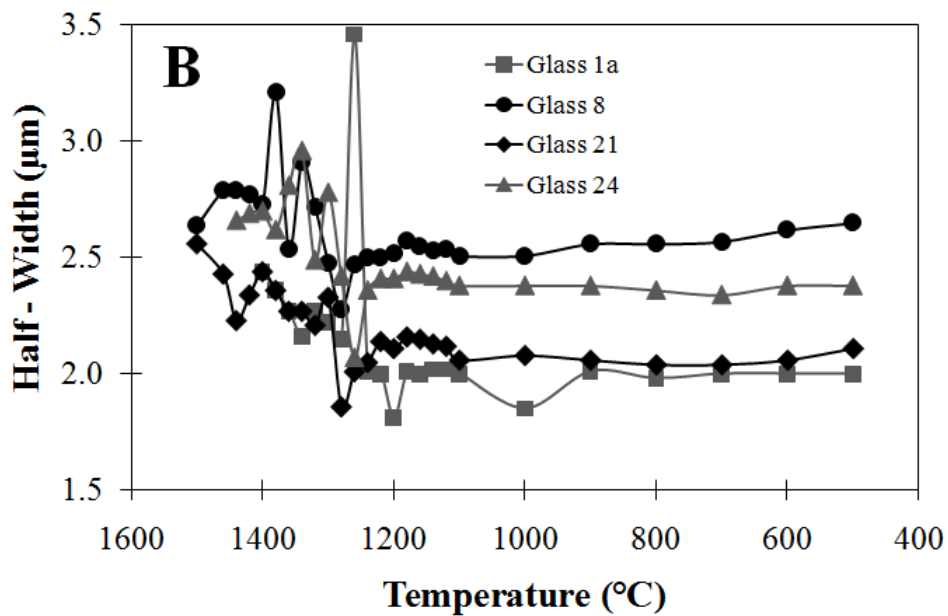
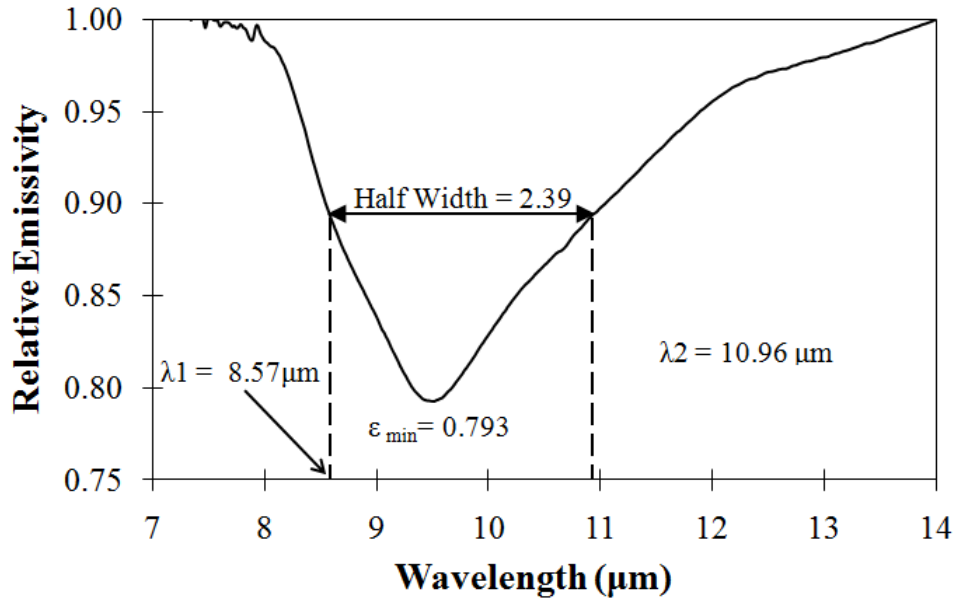


Figure 4-26 (A) Graphical representation of the half width calculation. ϵ_{\min} is the emissivity minimum value of the spectrum. λ_1 and λ_2 are the wavelengths at which the half depth falls on the spectrum. The difference between λ_1 and λ_2 is the half width of the spectrum. (B) Change in half width with increasing set point temperature for 4 of the glasses. Half width remains relatively linear at temperatures up to ~ 1200 °C. At temperatures above 1200 °C, the half width becomes much more variable with temperature. This is consistent with the variation in emissivity minimum at higher temperatures.

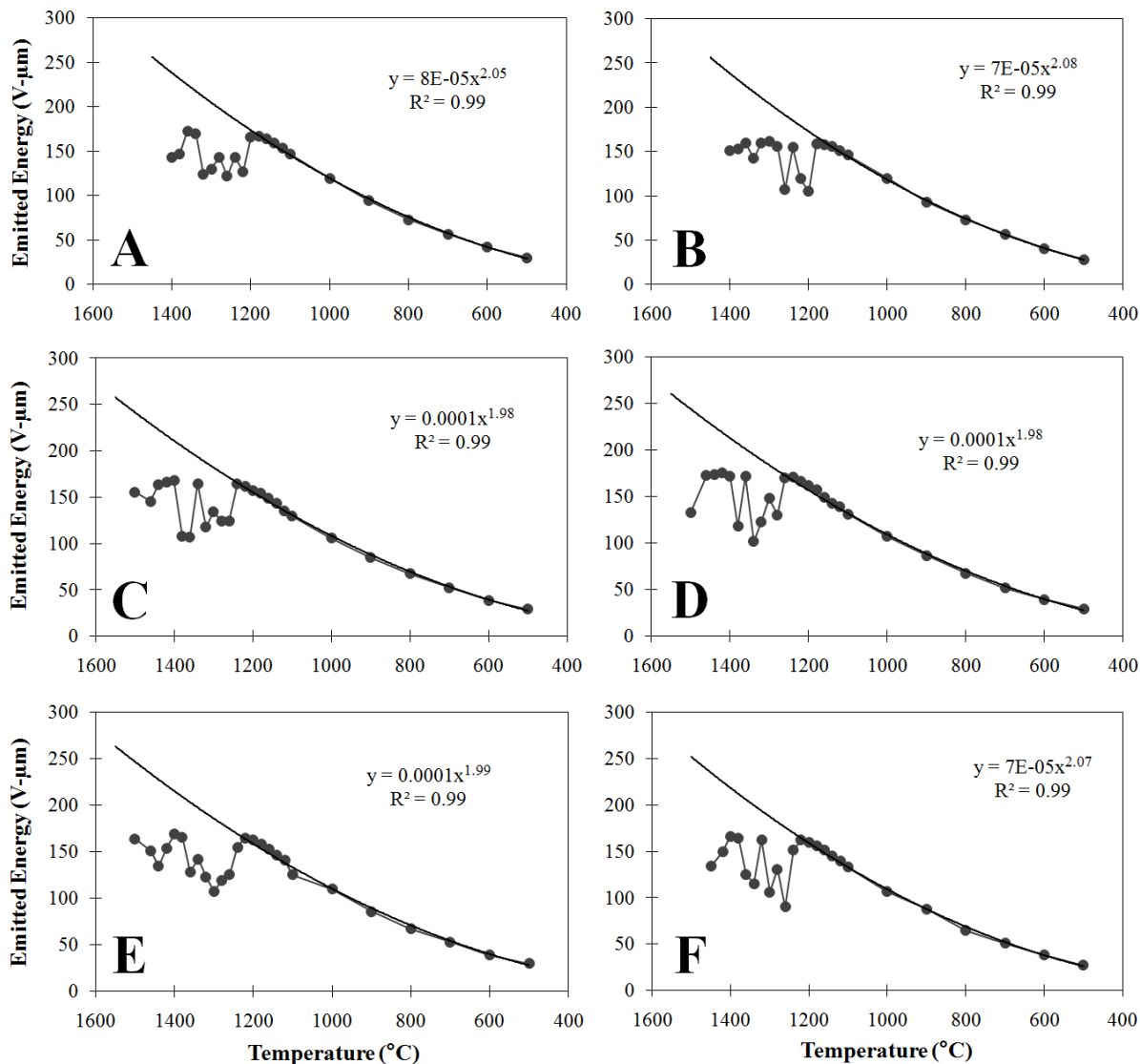


Figure 4-27 Emitted energy with decreasing temperature for (A) glass 1, (B) glass 1a, (C) glass 7, (D) glass 8, (E) glass 21, and (F) glass 24. Grey points denote the calculated emitted energy at each set point temperature. As each glass cools from its maximum temperature, the emitted energy is variable, but an overall decrease in energy occurs. From ~1200 °C to 500 °C, the emitted energy data for each glass takes on an exponential shape (thick black line), which has a consistently high R^2 value of 0.99.

temperatures. The blackbody used in the low-temperature setup closely approaches this ideal situation, and therefore absolute emission spectra can be derived. However, a similar setup could not be achieved for the micro-furnace environment due to the complexities involved in finding a material which is truly blackbody at all wavelengths within the high-temperature, oxidizing environment of the furnace.

Although the corrected ceria reference material is near-blackbody in the 7 to 14 μm range, it does undergo a significant phase change at 600 $^{\circ}\text{C}$, and at ~ 1300 $^{\circ}\text{C}$. This directly affects the signal intensity of the ceria, particularly at temperatures 1300 $^{\circ}\text{C}$ and higher, and requires that the signal intensities be corrected. High-temperature blackbodies are available, but are very expensive, and cannot be used directly within the micro-furnace to derive an accurate background spectrum of the furnace environment. For these reasons, micro-furnace spectra must currently be processed in terms of relative emissivity rather than absolute. However, relative emissivity spectra have proven very useful for studies involving thermal infrared spectroscopy, particularly those focused on spectral morphology (Gillespie et al, 1996; Li et al., 1999).

4.4.2 Relative Emissivity Spectra: 7 to 14 microns

Significant differences in spectral morphology and depth with changing temperature are evident among emission spectra of a given glass sample (Figures 4-1 to 4-7). For example, the 80 $^{\circ}\text{C}$ spectrum of each glass has a higher emissivity minimum value relative to those of spectra acquired using the micro-furnace, and in some cases the emissivity minimum position of the 80

°C spectrum is shorter than the micro-furnace spectra. Whereas micro-furnace spectra are processed into relative emissivity using corrected ceria reference spectra, all 80 °C emission spectra are derived using measurements from two true blackbodies of known temperatures. The discrepancies in emissivity minimum position and value between micro-furnace and low-temperature spectra can be attributed to the difference in emissivity processing approach.

Structural relaxation in silicates involves the breaking and remaking of primary Si-O bonds between atoms and molecules. It is this continuous structural rearrangement which allows a melt to undergo viscous flow (Moynihan, 1995). At a given temperature and pressure, a melt is in an equilibrium state. During equilibrium, the structure continually rearranges over time; however, these changes are very small, and thus the average structure of the melt can be considered constant with time. If temperature or pressure conditions change, the melt will undergo structural rearrangement at a greater scale in an attempt to once again reach equilibrium. The rate of structural relaxation will decrease with decreasing temperature, as the liquid or melt undergoes an increase in viscosity. At a given temperature, the relaxation rate will become so slow, that the structure of the melt is essentially “frozen”, and will no longer exhibit fluid behavior. This is the point at which the glass transition occurs, and the amorphous material transforms from a melt to a glass (Dingwell, 1995; Moynihan, 1995). This process occurs almost instantaneously if the melt is rapidly quenched.

The extreme variability of emissivity minimum values between the maximum temperature and ~ 1200 °C (Figures 4-8 to 4-13) could be directly related to the state of structural relaxation within the melt at a given temperature. The sample size of the melts in this study are very small (1-2 grams), and the time it takes for the melt to cool to a given set point temperature ranges from ~ 30 seconds to several minutes depending on the temperature. Given these conditions, it is likely that the melt is able to approach equilibrium at each set point temperature. However, the average structural organization of the melt is different at each temperature, and continuous small-scale changes in structure occur at a given temperature even when in equilibrium. It is feasible that this continuous relaxation at temperatures above the liquidus will affect the morphology of the emission spectrum, because spectral morphology is directly related to the structural state of the material at the time the spectrum is acquired. The most apparent effects are on the position and depth of the emissivity minimum, but the small shoulder features that appear in above-liquidus spectra of several of the glasses at ~ 11.5 and ~ 12.5 μm could also be related to structural changes associated with the melt.

Emissivity minima values and positions at temperatures below-liquidus ($< \sim 1200$ °C) decrease more systematically with decreasing temperature (Figures 4-8 to 4-13). After a melt undergoes a glass transition, and becomes a meta-stable amorphous solid, structural relaxation occurs on a much slower time scale due to the large increase in viscosity. By the time the glass reaches the amorphous solid state, relaxational modes are almost completely inactive, and vibrational modes are dominant. Therefore, spectra acquired at these lower temperatures do not reflect any large-scale changes in structural relaxation, as the glass is no longer a melt. Structural

relaxation in an amorphous material is commonly characterized in terms of experimentally measureable material properties such as entropy, enthalpy, and viscosity (Moynihan, 1995). However, study of glasses and melts using the micro-furnace has confirmed that the liquidus and T_g can also be determined in the laboratory using thermal emission spectroscopy.

4.4.3 Relative Emissivity Spectra: 14 to 20 microns

The spectral shoulder longward of 14 μm observed in ceria pellet reference spectra from 1300 °C to 1600 °C was subsequently corrected using the methods described in Chapter 3 of this work. Correction of the ceria pellet spectra was necessary in order to create a near-blackbody reference at all temperatures for use in deriving relative emissivity spectra of the glasses. Because of this correction however, all relative emissivity spectra of glasses > ~1300 °C slope upward at wavelengths > 14 μm. Since the ceria reference spectra are nearly featureless between 7 and 14 μm, and the glass spectra have a CF at 7.5 μm, all relative emissivity spectra were scaled to an emissivity of 1 at both 7.5 and 14 μm for this study (described above), thus eliminating the slope.

The appearance of the spectral shoulder at higher temperatures (Figure 4-15), and the variability of the shoulder with temperature, could be related to phase changes occurring in both the ceria and the glass samples with increasing temperature. For example, ceria (CeO₂) reacts to form Ce₂O₃ and O₂ at temperatures greater than 1000 °C, and this is accompanied by a phase change from cubic to hexagonal structure (Rao and Mishra, 2003). All of the glasses undergo a composition-dependent glass transition between 1300 °C and 1180 °C, which is characterized by

a distinct rise in emissivity minimum value as the glass cools. When a glass reaches its inferred transition temperature, the emissivity shoulder for each of the glasses also disappears, and the spectra at lower temperatures have a more consistent emissivity from 14 to 20 μm . Therefore it is possible that the T_g is not only expressed in the change in value of the emissivity minima, but also in the changes that occur at longer wavelengths.

Another possible explanation for the shoulder is the non-isothermality of both the ceria and the glass samples at temperatures above the glass transition. Observations of the furnace chamber temperature using the FLIR camera have shown that various materials within the furnace (insulation, platinum, glass sample) are at different temperatures at any given time, as they have differing thermal properties relative to one another. Furthermore, energy from surrounding furnace parts can enter the beam path directly, or reflect off the sample itself. Although sample temperature is not directly measured, it is probable that the sample undergoes cooling at the surface upon exposure to the spectrometer, and is non-isothermal itself. This is supported by FLIR measurements, which show the glass sample cooling up to ~ 20 degrees at higher temperatures, and ~ 5 degrees at lower temperatures, during the approximately 10 seconds that the furnace is opened for spectrum acquisition (Figure 3-9).

Surface emissivity spectra of the Martian surface collected by the Thermal Emission Spectrometer (TES) and the Thermal Emission Imaging System (THEMIS) instruments also show a similar distinct slope at longer wavelengths. This is attributed to an erroneous assumption of the surface temperature, by either incorrectly assuming the maximum emissivity

of the surface material, or presuming an isothermal surface where one does not exist (Bandfield, 2009). An attempt was made to model the effects of non-isothermality on the micro-furnace spectra, and determine whether the decrease in temperature of the sample in the ~10 seconds the furnace is open during sample acquisition has any effect on spectral shape. This was done by generating a variety of Planck functions at different temperatures. For example, for a set point of 900 °C, Planck functions were calculated in 20 °C increments from 850 °C to 950 °C. These curves were then mixed in various percentages (e.g. 20% 870 °C and 80% 850 °C), and divided into the micro-furnace spectrum at 900 °C to derive relative emissivity. Although some small changes in slope occurred in the relative emissivity spectra with differing mixed Planck curves, the changes were very systematic, and not as variable as the micro-furnace spectra processed using ceria. Much more variation in slope was observed with Planck-processed relative emissivity spectra that were further apart in temperature; for example, a relative emissivity spectrum derived using a 500 °C , a 650 °C , a 900 °C and a 1100 °C Planck curve had much more variability in slope relative to each other. However, this situation is unrealistic because the change in temperature in the time the micro-furnace is opened for acquisition never exceeds ~50 °C.

The underlying cause of spectral behavior longward of 14 μm cannot be definitively determined because the ceria reference spectra are not truly blackbody in all wavelength regions at all temperatures. Furthermore, it is not currently possible to calibrate the micro-furnace with an external blackbody source, nor is it possible in this study to accurately measure the occurrence

of phase changes in the ceria, quartz, and glass samples. Thus, no definitive conclusions can currently be made regarding spectral behavior above 14 μm for samples melted within the micro-furnace.

4.4.4 Heat-Up vs. Cool-Down Spectra

It is assumed that the glasses reach equilibrium at each temperature during cool-down from the maximum temperature to 500 °C. It was expected that, upon heat-up, the glass samples would also reach equilibrium at each temperature. If this condition were met, relative emissivity spectra upon heat-up would be very similar to, or the same as, the cool-down spectra at each temperature. However, heat-up spectra have different emission minimum values and positions than the cool-down spectra, and in general, the heat-up spectra are more muted at temperatures < 1200 °C (Figures 4-17 and 4-18). It can therefore be assumed that, for a given temperature, the structural state of the quenched glass upon heat-up is not the same as that of the glass upon cool-down. This is due to the fact that, while the glass is heating up and still in a solid state, relaxation time in the glass is much slower, and vibrational and relaxational modes within the structure behave differently than in a melt. Furthermore, the quenched glass is considered a true, crystal-free glass, with a “frozen” structure. The glass being allowed to slowly cool from a melted state, as opposed to being rapidly quenched, will allow for the glass to undergo relaxation on a longer time scale. Thus, the structure of a slowly-cooled solid glass will be much different than that of a rapidly quenched glass. Evidence of this difference can also be seen in the 80 °C spectra of the slowly-cooled glasses in comparison to that of the quenched glasses. For a given

glass composition, the spectrum of the slowly-cooled glass at 80 °C has a deeper emissivity minimum than the quenched glass. This deeper feature could be a function of the slowly-cooled glass having a different T_f , resulting in differences in structural relaxation. Furthermore, microlite crystallization within a slowly-cooled glass could be significant enough to deepen the main spectral feature of the glass.

4.5 CONCLUSIONS

The variation in spectral morphology with changing set point temperature has been characterized in detail for each glass in the synthetic glass suite. The emissivity minimum position and emissivity minimum value of each glass display extreme variability above the liquidus temperature, yet behave much more linearly with decreasing temperature below ~1100 °C. Additionally, glass spectra upon heat-up of the glass sample display different emissivity minimum values and positions than the cool-down spectra, and heat-up spectra are more muted at temperatures < 1200 °C. This behavior can be attributed to the specific state of structural relaxation within either the melt or the solid at a given temperature. The T_g can also be identified in each glass, as illustrated by a sharp rise in emissivity minimum near the liquidus temperature for each glass.

The appearance of a variable shoulder feature in the glass and ceria spectra longward of 14 μm is attributed to either phase changes occurring in both of these materials at approximately 1300 $^{\circ}\text{C}$, or the non-isothermality of the materials at temperatures above the glass transition. Definitive conclusions regarding the shoulder cannot currently be made, however, as it is not possible to calibrate the micro-furnace with an external blackbody source to obtain a true blackbody, nor measure the occurrence of phase changes in the ceria, quartz, and glass samples.

Overall, each of the glasses in the suite behave consistently relative to one another as they melt and cool, and significant differences in the emissivity minimum values and positions of spectra of a given glass can be seen with increasing and decreasing temperature. There are also clear differences in half width values and emitted energy between a glass in a solid state and a molten state, further verifying that the IR behavior of glasses differs below and above T_g . This study validates thermal emission spectroscopy as a tool for studying the spectral behavior of glassy melts in the laboratory. It is expected that similar changes in spectral morphology and behavior with temperature and physical state will also be observed in natural silicate glasses and melts. These data will ultimately contribute to a better understanding of the relationship between physical state and TIR spectral behavior of silicate lava domes and flows, and will improve the ability of TIR remote sensing instrumentation to map and characterize glasses and molten materials in active volcanic environments.

5.0 DERIVING SILICATE LAVA COMPOSITION FROM IMAGE AND FIELD-BASED THERMAL EMISSION SPECTRA

5.1 INTRODUCTION

Thermal emission spectroscopy has proven to be a useful and valuable technique for studying the composition and physical properties of volcanic surfaces (e.g. Walter and Salisbury, 1989; Ondrusek et al., 1993; Ramsey and Fink, 1999; Christensen et al., 2000; Byrnes et al., 2004; Ramsey and Dehn, 2004; Vaughan et al., 2005; Carter et al., 2007). The fundamental properties of Si-O and Al-O bonds within an aluminosilicate are apparent in TIR emissivity spectra (e.g. Neuville and Mysen, 1996; Dalby et al., 2006; Byrnes et al., 2007; King et al., 2008; Lee et al., 2010), and these spectral features can be utilized for the compositional mapping of active and inactive volcanic terranes. TIR data is commonly collected remotely, using spaceborne, airborne and field-based instrumentation. However, accurate determination of emissivity in the field, particularly on an active volcano, is a complex and potentially hazardous process. Thermal heterogeneities can exist, predominantly from molten and actively cooling surfaces, which complicate the derivation of emissivity data and, in turn, produce inaccurate compositional data. Furthermore, the spectral and spatial resolution of field and image-based TIR data can be much lower relative to laboratory-derived data, resulting in loss of spectral contrast and subtle spectral

features. In order to discriminate the wt. % SiO₂ composition of a volcanic surface in the field, it is important to first determine to what degree spectral and spatial degradation affects laboratory-based data, and also characterize the spectral differences between laboratory-based data and image-based data.

One of the most effective ways to determine the composition of a silicate material is to determine the half width of the emission spectrum. Methods of determining the half width include the use of Voigt functions (e.g. Langford, 1978), or Gaussian filter functions (e.g. Wertheim et al, 1974; Realmuto et al, 1995; Johnson et al, 2010). A notable example of this is the MINMAP image processing algorithm, developed by Sabine et al (1994), which fit Gaussian curves to Thermal Infrared Multispectral Scanner (TIMS) normalized emittance spectra of Sierra Nevada granitoids, based on the calculated emittance minimum value of the spectrum, in an effort to distinguish mafic and felsic compositions. These methods, although very effective and accurate, can be quite mathematically complex and are commonly employed for spectral analysis subsequent to field or image data collection. A more simplistic method of utilizing the half width to derive wt. % SiO₂ concurrently with the acquisition of field data is examined here. Half width calculations were initially performed on laboratory emission spectra of the suite of synthetic glasses. The calculation method was then applied to laboratory spectra of a group of natural glassy rocks acquired from Medicine Lake Volcano, as well emission spectra from airborne and field-based TIR imagery of the area.

5.1.1 Geology of Medicine Lake Volcano

Medicine Lake Volcano is a Quaternary shield volcano located approximately 50 kilometers E-NE of Mt. Shasta within the back-arc extensional environment eastward of the Cascade Range (Figure 5-1). Lavas from Medicine Lake volcano cover about 2000 km², with an estimated volume of 600 km³. Lavas are tholeiitic and calc-alkaline, with silica content ranging from 47% to 77%. Growth of the volcano began about 1 million years ago, following the eruption of a large volume of tholeiitic high-alumina basalt (Donnelly-Nolan, 1988). These tholeiitic basalts have continued to erupt on the flanks of the volcano (Donnelly-Nolan et al., 1990). In the Holocene, seventeen eruptive units were emplaced, all from multiple vents around the volcano. Eight of these were mafic eruptions, which occurred on the flanks of the volcano over a span of 400 years, and erupted from alignments of spatter cones, pit craters, or cinder cones. This was followed by nine late-Holocene mafic and silicic eruptions, which are all located within or near the rim of the caldera. Most of these lavas have been erupted as domes and dome chains from 30° N - trending dikes (Fink and Pollard, 1983). The main edifice of Medicine Lake volcano contains calc-alkaline lavas, dominantly of basaltic andesite and andesite compositions, whereas silicic lavas erupted from alignments of vents along the caldera rim. Donnelly-Nolan et al. (1990) have performed a detailed chemical and physical analysis of these Holocene eruptions, and petrologic analyses of Medicine Lake lavas have also been performed (Condie and Hayslip, 1975; Mertzman, 1977; Gerlach and Grove, 1982; Grove and Donnelly-Nolan, 1986).

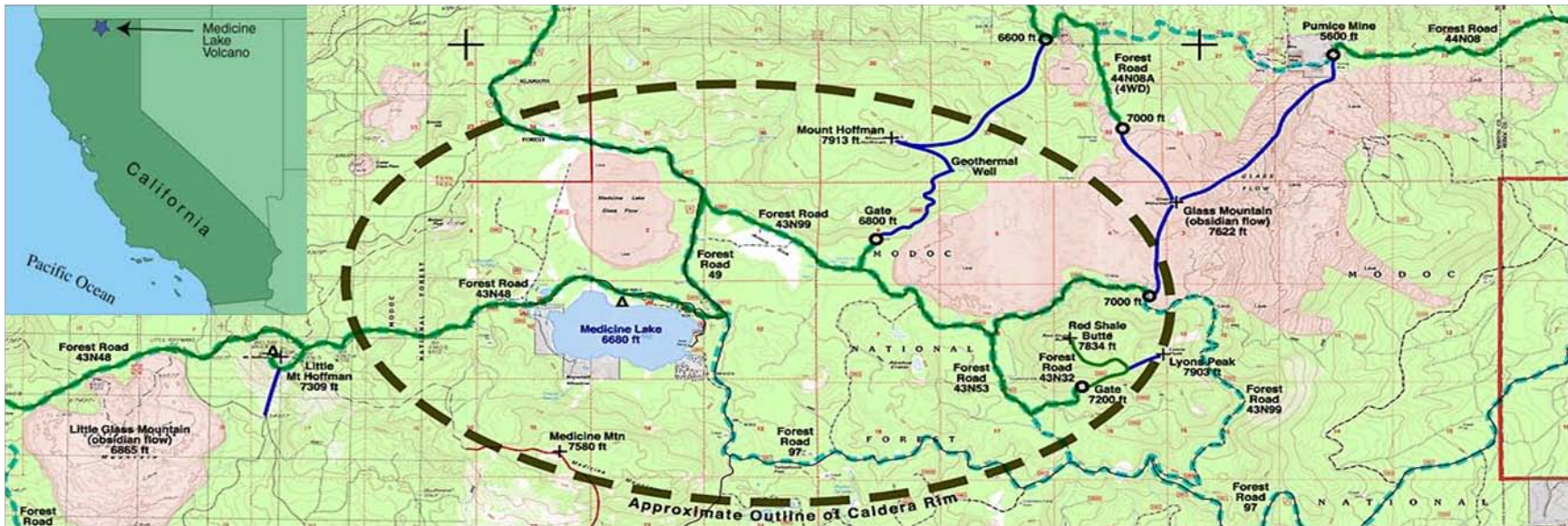


Figure 5-1 Topographic map of Glass Mountain flow and vicinity at Medicine Lake volcano. Major lava flows are shown in pink. The dotted line denotes the location of the caldera rim (Donnelly-Nolan, 1988).

Additionally, detailed geologic mapping of Medicine Lake volcano has recently been digitally compiled as a spatial database in ArcInfo GIS (Ramsey et al., 2010). Of particular interest to this study is the Glass Mountain rhyodacite flow.

5.1.2 Glass Mountain Rhyodacite Flow

Glass Mountain is an inactive, glassy rhyodacite flow located at the eastern rim of Medicine Lake Caldera (Figure 5-1). The flow has a radiocarbon date of 885 ± 40 years, making it the youngest lava at Medicine Lake volcano (Donnelly-Nolan et al., 1990). Glass Mountain is part of a thirteen-vent fissure which lies along a N 25° W trend. The coalescence of three of these vents formed Glass Mountain (Eichelberger, 1975; Heiken, 1978). Ten additional domes were emplaced at the same time as Glass Mountain (nine to the north of the flow and one to the south) and produced approximately 1 km³ of lava.

Glass Mountain and the surrounding domes were extruded following a Plinian eruption of white pumiceous airfall tephra. It has been hypothesized that prior to the tephra eruption, a shallow zoned magma body formed underlying the eastern caldera rim, with rhyolite overlying a hotter more fluid dacite (Heiken, 1978; Donnelly-Nolan, 1988; Donnelly-Nolan and Grove, 2008). The initial tephra eruption released overpressure which caused 67 wt. % SiO₂ dacite magma with basaltic andesite inclusions to rise through the rhyolite layer into the conduit and erupt. The dacite flowed down the eastern slope of Medicine Lake Volcano and separated into

two long, dark-colored lobes. The dacite eruption was followed by extrusion of lighter-colored rhyodacite, and finally a steep-sided lobe of inclusion-free 74 wt. % SiO₂ rhyolite (Anderson, 1933; Donnelly-Nolan, 1988; Donnelly-Nolan and Grove, 2008).

The compositional variability of Glass Mountain, coupled with the extensive and complex multi-scale compositional and textural mixing, makes it an ideal location for studying the spectral effects of glass composition at various spatial resolutions. The flow is well-exposed, easily accessible, and ample TIR satellite and airborne remote sensing data of the flow is available. Various TIR remote sensing studies of the domes at Medicine Lake have already been conducted. These include the study of vesicular textures using the TIMS instrument (e.g. Ondrusek et al 1993; Ramsey and Fink, 1994), characterization of the thermal emission of glassy surfaces at Medicine Lake (e.g. Ramsey et al., 1993b), and mineral, thermal and textural mapping using the Advanced Spaceborne Thermal Emission and Reflection Radiometer (ASTER) instrument (e.g. Ramsey, 1996) and the MODIS/ASTER Airborne Simulator (MASTER) (e.g. Eisinger, 2002). However, the study of lava flows using the currently available TIR remote sensing instrumentation has been limited by the relatively low spatial resolutions of these instruments. This is particularly problematic for Glass Mountain, which has extensive and complex multi-scale compositional and textural mixing. Two of the best currently available TIR instruments capable of resolving some of these small-scale features are the airborne, ten-channel MASTER instrument and the newly-designed multispectral FLIR with six TIR channels.

5.1.3 MODIS/ASTER (MASTER) Airborne Simulator

The MASTER instrument was developed to support scientific data collected by the Advanced Spaceborne Thermal Emission and Reflection Radiometer (ASTER) and Moderate Resolution Imaging Spectroradiometer (MODIS) projects. These two spaceborne instruments are located on the Terra platform, launched in 1999. The main purpose of MASTER is to underfly ASTER and MODIS, and provide a more detailed radiometric calibration for the two instruments, as well as data of a higher spatial resolution (Hook et al, 2001). MASTER is commonly flown on a Beachcraft B200 aircraft operated by Department of Energy (DOE), and also a NASA DC-8. It has 50 channels spanning the visible-near infrared (VNIR), short-wave infrared (SWIR), and TIR wavelength ranges, and can acquire imagery at a variety of altitudes and pixel sizes (Hook et al., 2001). Whereas ASTER has 5 TIR channels with a spatial resolution of 90 meters/pixel, MASTER has 10 TIR channels. The MASTER TIR image used in this study was acquired on September 14, 1999 and has a spatial resolution of 10 meters/pixel.

5.1.4 The Forward Looking Infrared Radiometer (FLIR)

The FLIR camera is a hand-held infrared camera capable of acquiring precise (0.08 °C at 30 °C) and accurate (± 2 °C) TIR radiance data at a high spatial resolution. Data products include fully radiometric JPEG images and high-speed video, both of which can be exported to a computer in real time, and subsequently analyzed with the FLIR ThermaCam software. The camera contains a 240 x 320 un-cooled microbolometer detector array, which detects energy emitted in the 7.5 to

13 μm region. FLIR cameras have gained popularity in volcanological studies over the past decade, and have been widely utilized in the research of active volcanic surfaces (e.g. Vaughn et al., 2005; Patrick et al., 2007; Carter and Ramsey, 2009, Ramsey, 2009).

The FLIR camera fore optics have been modified for use as a multi-spectral field-based TIR imager, yielding both temperature and emissivity data (Figure 5-2). This was accomplished by dividing the broadband 7.5 to 13 μm region of the FLIR into 6 individual band-passes with the use of external diffraction filters (Ramsey, 2009). Each filter is situated on a Germanium substrate and is approximately 2 mm thick and 51 mm in diameter. The wavelength centers of these filters are 8.05, 8.69, 9.32, 10.08, 10.87 and 11.53 μm . These wavelengths were chosen based on preliminary laboratory TIR spectral data of silicic glasses acquired by Lee et al. (2010) as well as overlap with the wavelength channels of both the ASTER and MASTER instruments. The use of band-pass filters with a FLIR camera is a novel approach, and provides the first field-based 6-point FLIR multispectral data of volcanic surfaces. Testing of the FLIR and filters was conducted at various lava flows at Medicine Lake volcano in August 2009, and initial results show promise for deriving accurate compositional and textural information from a broadband temperature instrument.

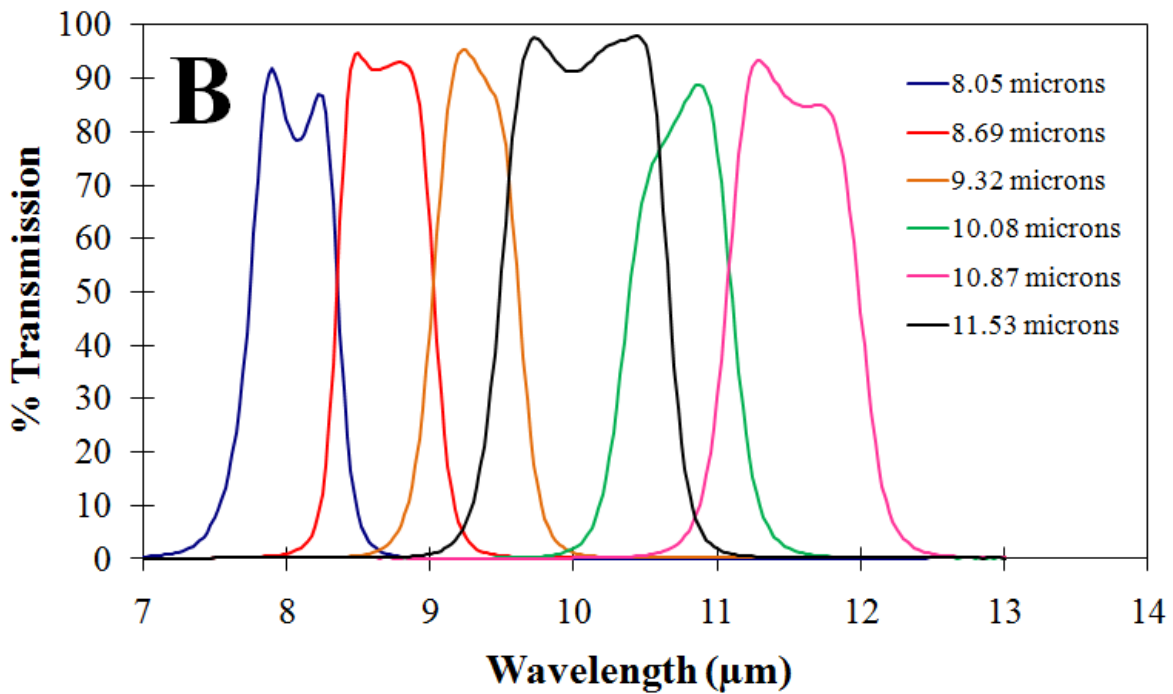


Figure 5-2 The multi-spectral field-based spectrometer. (A) FLIR thermal camera with one of the filters in the fore optics. Each filter currently fits onto the fore optics individually for image acquisition. (B) Band-passes for each of the 6 filters. The wavelength centers of the filters are 8.05, 8.69, 9.32, 10.08, 10.87 and 11.53 μm .

5.2 METHODOLOGY

Half width values were calculated for laboratory thermal emission spectra of synthetic glasses acquired at 80 °C, 500 °C, 1000 °C, and 1300 °C. These four temperatures were chosen because they are representative of the temperature span of the low-temperature setup and the micro-furnace. Half width was calculated using the method described in chapter 4, where the emissivity value at the half depth of the main spectral feature was found, and the corresponding wavelength values of the half depth were subtracted from each other to yield a half width value in microns. Half width values for all the glass samples at each temperature were then plotted against the electron microprobe-derived wt. % SiO₂ values for each glass (see Chapter 2, Table 2-1). Each laboratory spectrum was then degraded to a MASTER TIR 10-point spectrum and a FLIR 6-point spectrum, based on the band-passes for each instrument. Half width values were calculated for each of the degraded spectra and plotted against the microprobe-derived wt. % SiO₂ values.

This same process was repeated for laboratory, MASTER-degraded, and FLIR-degraded spectra of five natural samples collected at Glass Mountain. These samples are representative of the major compositions found on the lava flow. The half width value derived from each spectrum was used to calculate a wt. % SiO₂ value for each sample. This was done using the 80 °C half width vs. wt. % SiO₂ plots created for the undegraded, MASTER-degraded and FLIR-

degraded synthetic glasses (as described above). Calculated half width values from natural sample spectra were plotted on these plots and the trend line equation of the plot was used to derive a calculated wt. % SiO₂ value. The calculated wt. % SiO₂ for each sample was then compared to a range of typical wt. % SiO₂ values for the sample. This same analysis was performed on a set of fifteen 10-point spectra collected from a MASTER image of Glass Mountain, and a set of eight 6-point spectra collected from two FLIR images of two different areas on Glass Mountain. This was done in order to determine the feasibility of using the half-width calculation method for both field-based and image-based composition analysis.

5.3 RESULTS

5.3.1 Synthetic Glass Spectra

The high spectral resolution of laboratory emission spectra, coupled with the controlled environment in which they are acquired, make them ideal for initial testing of the efficacy of the half width calculation method. Laboratory emission spectra of each synthetic glass at low temperature (80 °C), as well as micro-furnace spectra acquired at 500 °C, 1000 °C, and 1300 °C, were degraded to MASTER 10-point and FLIR 6-point spectra. The degraded spectrum at each of these temperatures for one of the synthetic glasses (glass 1) is shown in Figure 5-3. Degraded spectra of the remainder of the glasses are shown in Appendix B. Because of changes

in spectral shape with temperature, the degraded spectra for both MASTER and FLIR appear different to one another. Spectral shapes are better preserved in MASTER spectra, as they are of a higher spectral resolution to FLIR.

Calculated half width values for the un-degraded spectra of all synthetic glasses at each temperature were plotted against the microprobe-derived wt. % SiO₂ measurements (Figure 5-4). A linear fit was applied to each plot, and the 80 °C, 500 °C, and 1000 °C plots show excellent R² values. However, the linear fit at 1300 °C is not as good, suggesting that calculating the half width of glasses in the melt region is potentially a more complex process. Similar plots for MASTER-degraded spectra and FLIR-degraded spectra are shown in Figures 5-5 and 5-6, respectively. MASTER-degraded spectra maintain relatively high R² values, as MASTER spectra tend to preserve more of the spectral shape. Conversely, the R² values for FLIR-degraded spectra at all temperatures are much lower relative to that of MASTER-degraded and un-degraded spectra. This confirms that half width calculations are directly affected by spectral resolution.

5.3.2 Natural Glassy Sample Spectra

Each synthetic glass was prepared from pure mineral powders, was quenched to crystal-free glass, and is a very simplistic and highly compositionally - controlled analog for dacitic and rhyolitic lavas. Natural glassy samples collected from Glass Mountain, however, are far more complex and are commonly of highly-mixed composition, variable crystallinity and variable

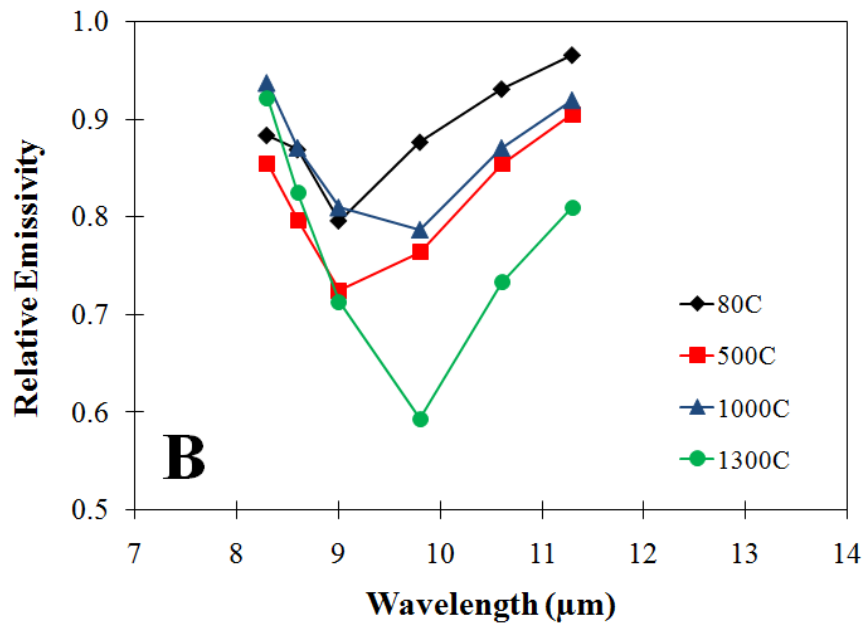
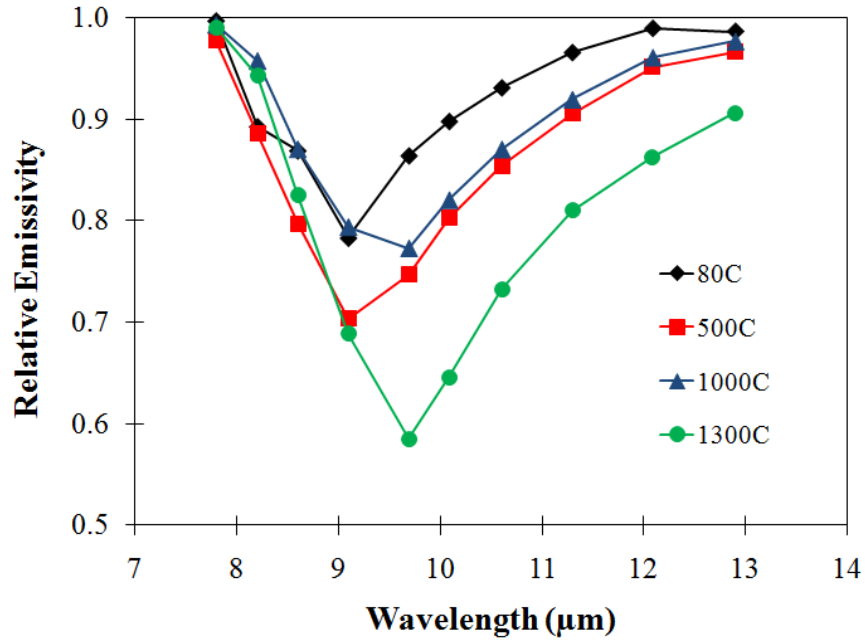


Figure 5-3 (A) MASTER-degraded emission spectra of glass 1 at 80 °C, 500 °C, 1000 °C, and 1300 °C. (B) FLIR-degraded emission spectra of glass 1 at 80 °C, 500 °C, 1000 °C, and 1300 °C.

texture. Each of these components can affect the morphology of the emission spectrum, which in turn could affect the accuracy of the half width calculation. Figures 5-7 to 5-11 show the undegraded spectrum, the MASTER-degraded spectrum, and the FLIR-degraded spectrum for five natural samples: vesicular dacite, dacite with basaltic andesite inclusions, obsidian, fine vesicular pumice (FVP), and an altered breccia.

Four of the samples, particularly the breccia sample, contain a shoulder feature at ~ 8.5 μm . The dacite with inclusions displays a prominent shoulder at ~ 10 μm . These shoulder features are expressed in the degraded spectra, and are especially well-preserved in the MASTER spectra. Half width values and wt. % SiO_2 values calculated for each undegraded natural sample spectrum were plotted on the 80 °C half-width vs. wt. % SiO_2 plot for the undegraded synthetic glass spectra (Figure 5-12A). An inverse relationship exists between calculated half width value and calculated wt. % SiO_2 , where a low half width value yields a higher calculated wt. % SiO_2 , and vice versa (Table 5.1). This leads to the calculated wt. % SiO_2 value for a given sample being either slightly higher or lower than the inferred wt. % SiO_2 composition. For example, obsidian has a half width value of 1.64 and a calculated wt. % SiO_2 value of 83.94%, whereas FVP has a half width of 2.11 and a calculated wt. % SiO_2 value of 69.70%.

A summary of calculated half width values and wt. % SiO_2 values for the MASTER-degraded natural sample spectra are shown in Figure 5-12B and Table 5-2. Calculated half width values are slightly higher than those calculated for the undegraded spectra. Thus, the calculated wt. % SiO_2 values are also somewhat larger than the inferred wt. % SiO_2 ranges. Furthermore,

the half width of the obsidian remains lower than that of the other samples. With the exception of obsidian, all half width values for the FLIR-degraded spectra are equal to or higher than that of the MASTER-degraded and un-degraded spectra (Figure 5-12C, Table 5-3). The low half width, and consequently very high calculated wt. % SiO₂, of the obsidian is particularly apparent. In contrast, the very high half width value of the breccia sample yields a much lower calculated wt. % SiO₂ value.

5.3.3 FLIR and MASTER Image Spectra

Image-based emission spectra differ markedly from laboratory-acquired spectra in that the spectral and spatial resolutions of image-based spectra are both lower. Differences in path length and pixel size, as well as atmospheric effects, can cause an overall muting of spectral features in image-based spectra, which can directly affect the calculation of the half width. Because the half width method will eventually be utilized in field-based measurements, a comparison of the half width calculation method on laboratory-based and image-based spectra is important. A series of fifteen 10-point spectra were collected from a MASTER image of Glass Mountain (Figure 5-13). Spectra are evenly distributed across the flow, and are representative of the compositional variety found at Glass Mountain. The general distribution of compositions is known from previous mapping work by Donnelly-Nolan, compositional work done by Ramsey (1996), and direct field measurements. The half-width and corresponding wt. % SiO₂ for each 10-point spectrum were calculated based on the 80 °C MASTER-degraded synthetic glass spectra plot (Figure 5-14).

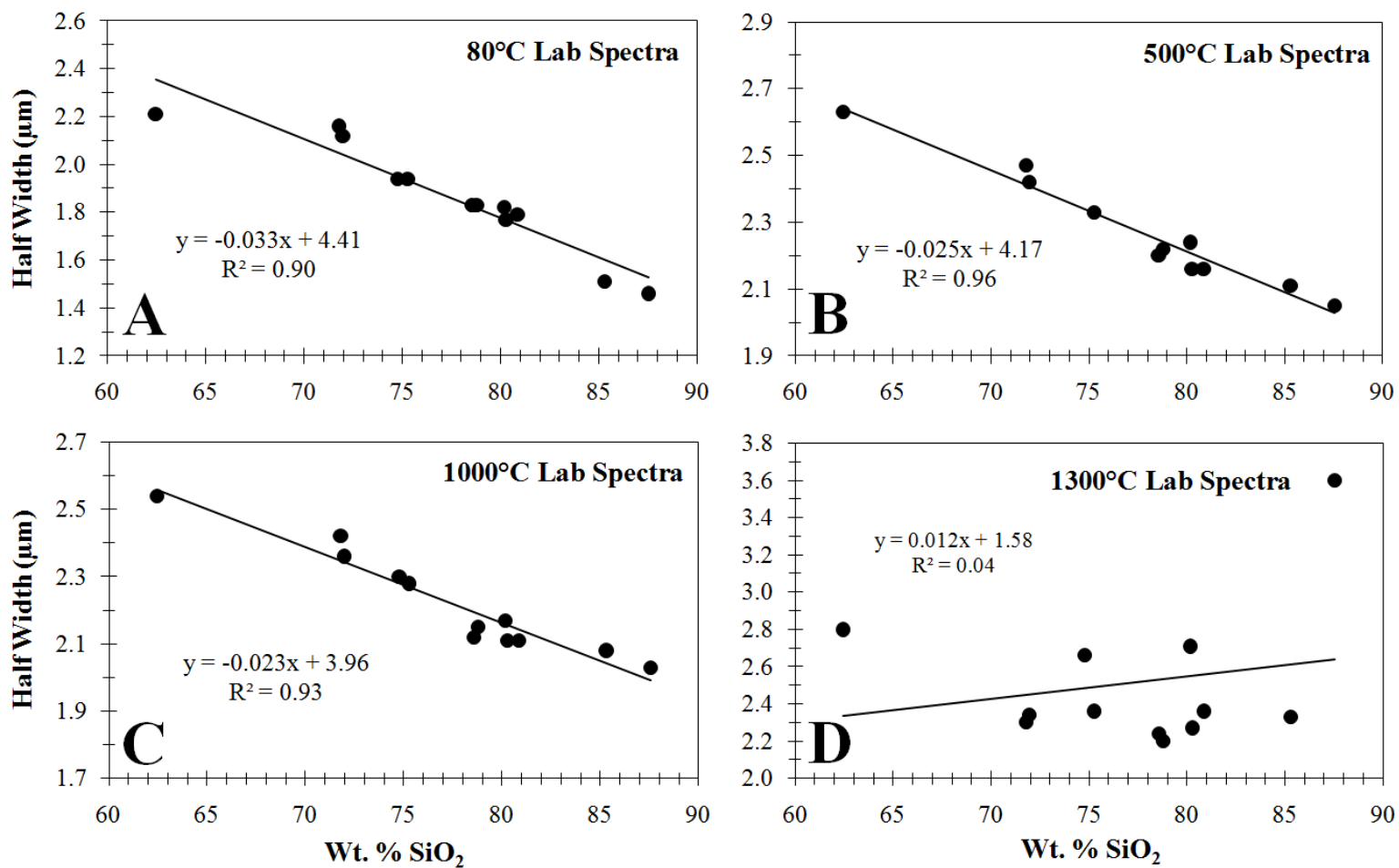


Figure 5-4 Calculated half width vs. wt. % SiO₂ for all un-degraded synthetic glass spectra at (A) 80 °C, (B) 500 °C, (C) 1000 °C, and (D) 1300 °C. Glasses at 80 °C, 500 °C, and 1000 °C show excellent fits and R² values. The fit for glasses at 1300 °C is much poorer, and suggests that calculation of the half width needs to be modified for glasses within the melt region.

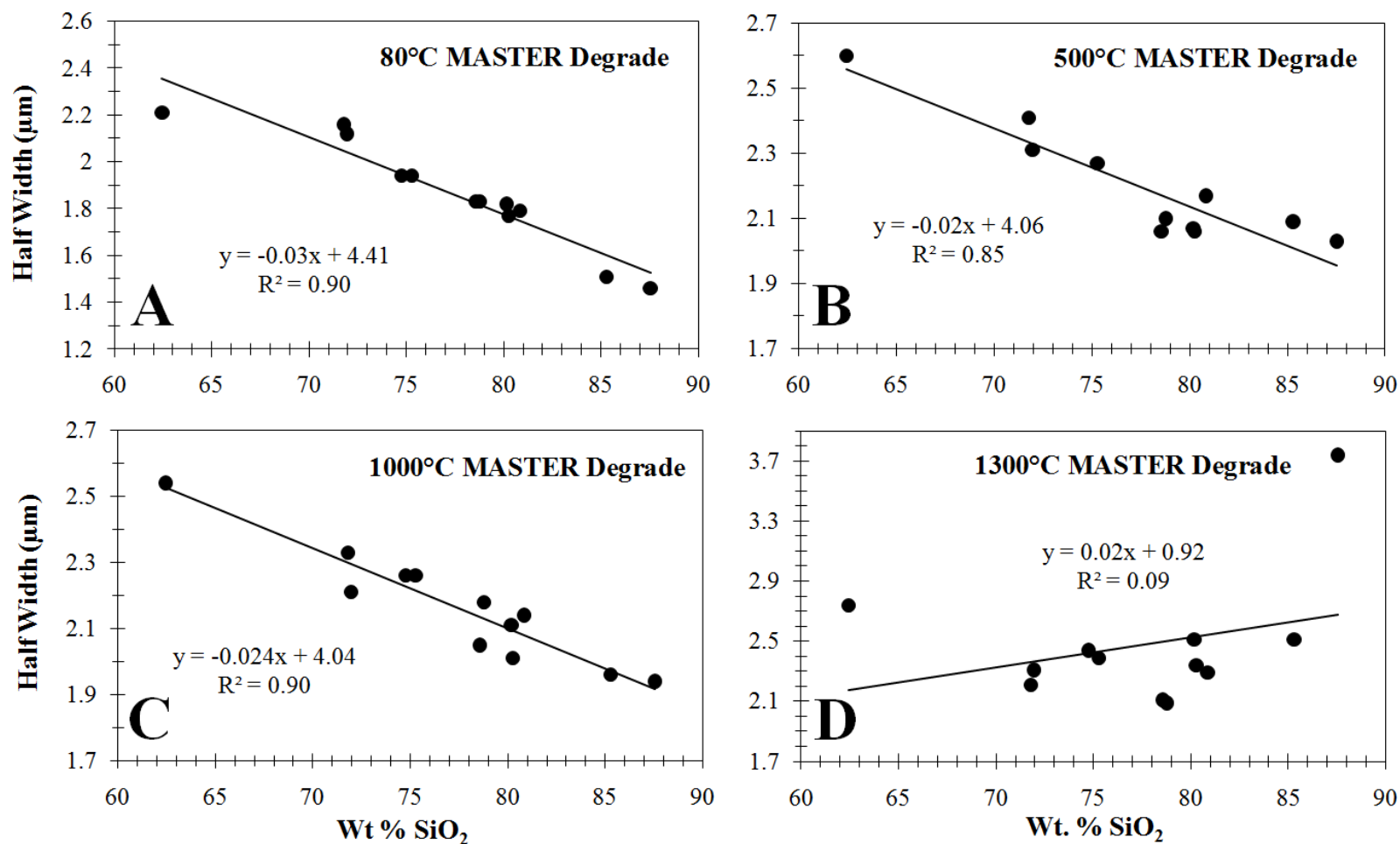


Figure 5-5 Calculated half width vs. wt. % SiO₂ for all MASTER-degraded synthetic glass spectra at (A) 80 °C, (B) 500 °C, (C) 1000 °C, and (D) 1300 °C. Glasses at 80 °C, 500 °C, and 1000 °C show good fits and R² values. The fit for glasses at 1300 °C is much poorer, and suggests that calculation of the half width needs to be modified for glasses within the melt region.

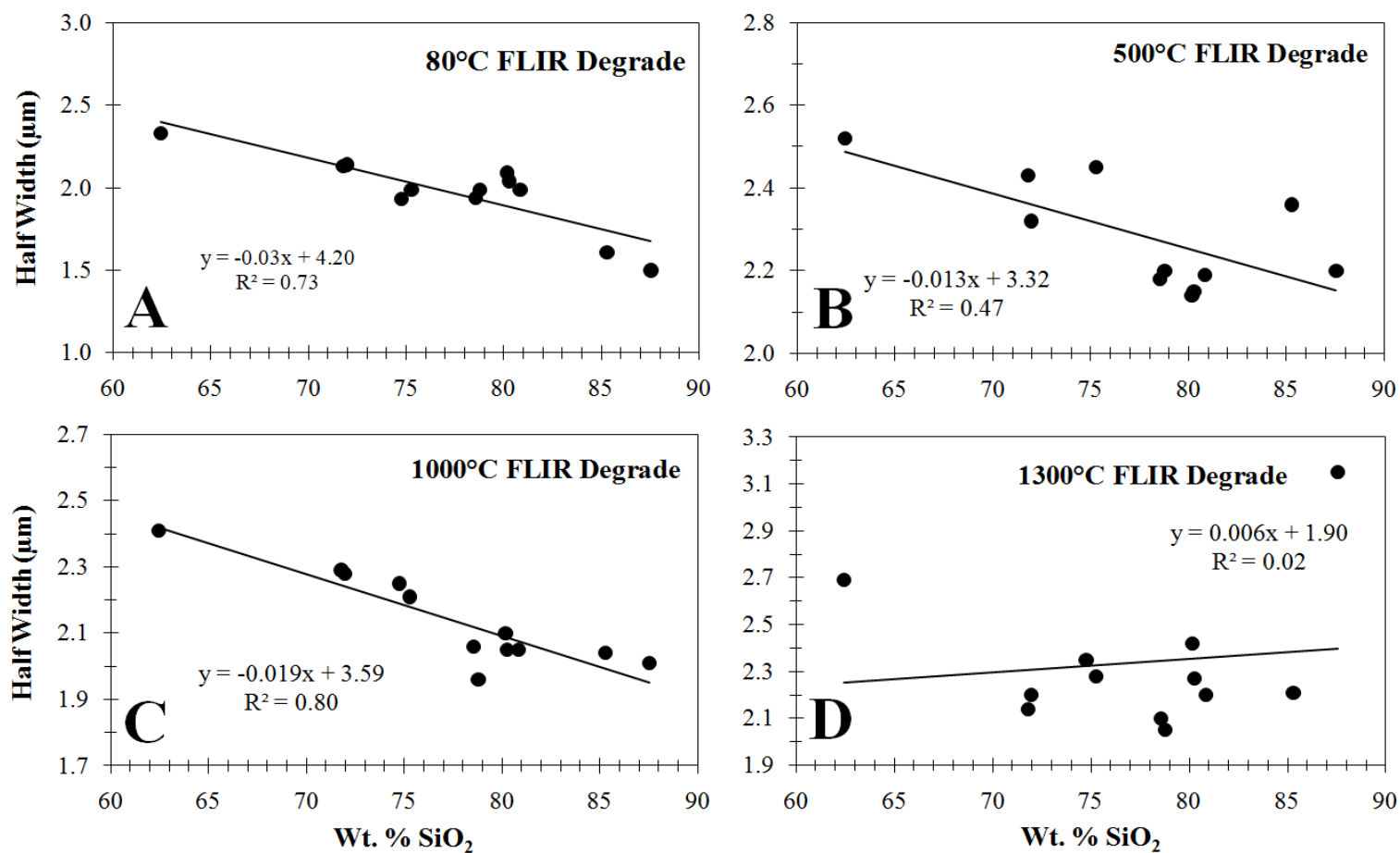


Figure 5-6 Calculated half width vs. wt. % SiO₂ for all FLIR-degraded synthetic glass spectra at (A) 80 °C, (B) 500 °C, (C) 1000 °C, and (D) 1300 °C. R² values at each temperature are poorer than that of the un-degraded and MASTER-degraded spectra. This confirms that spectral resolution is important to the accurate calculation of half width.

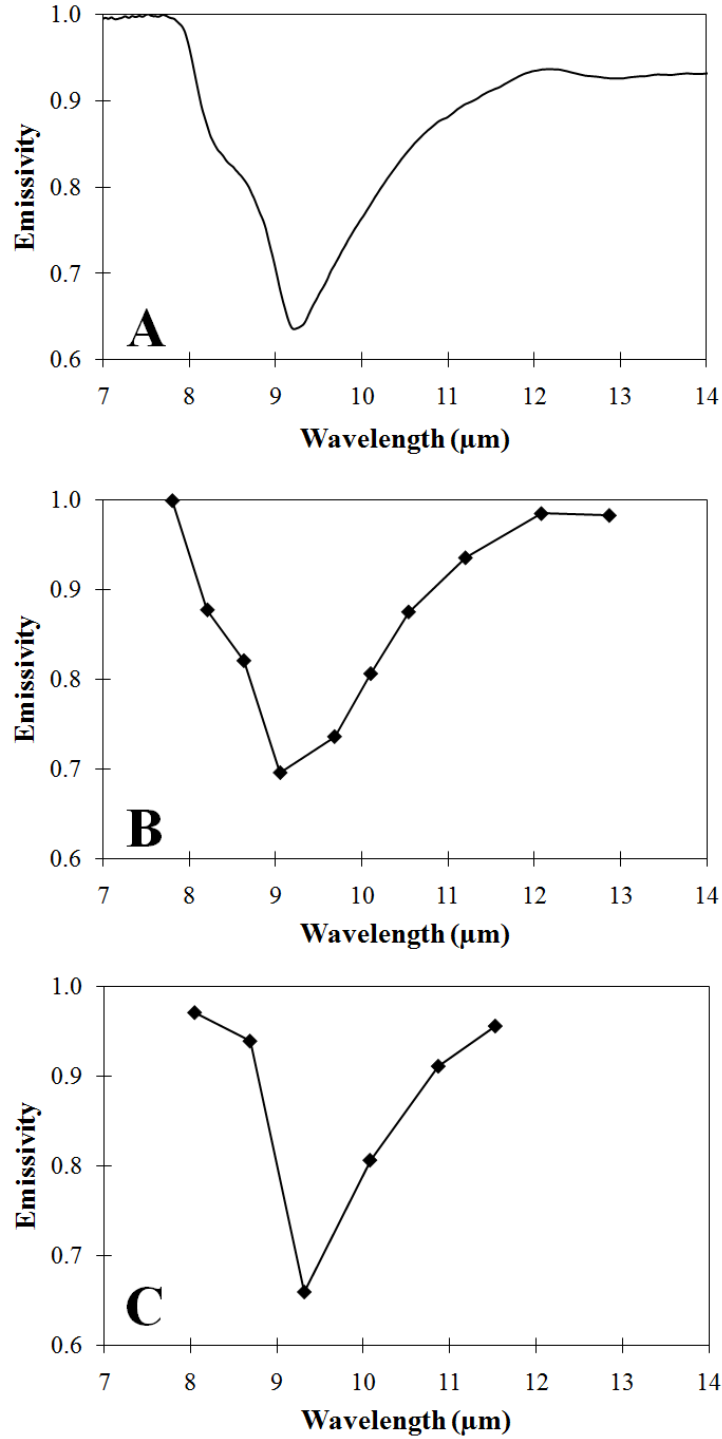


Figure 5-7 (A) Un-degraded, (B) MASTER-degraded and (C) FLIR-degraded spectra of obsidian. The spectral shoulder at ~8.5 μm is resolved in all three spectra.

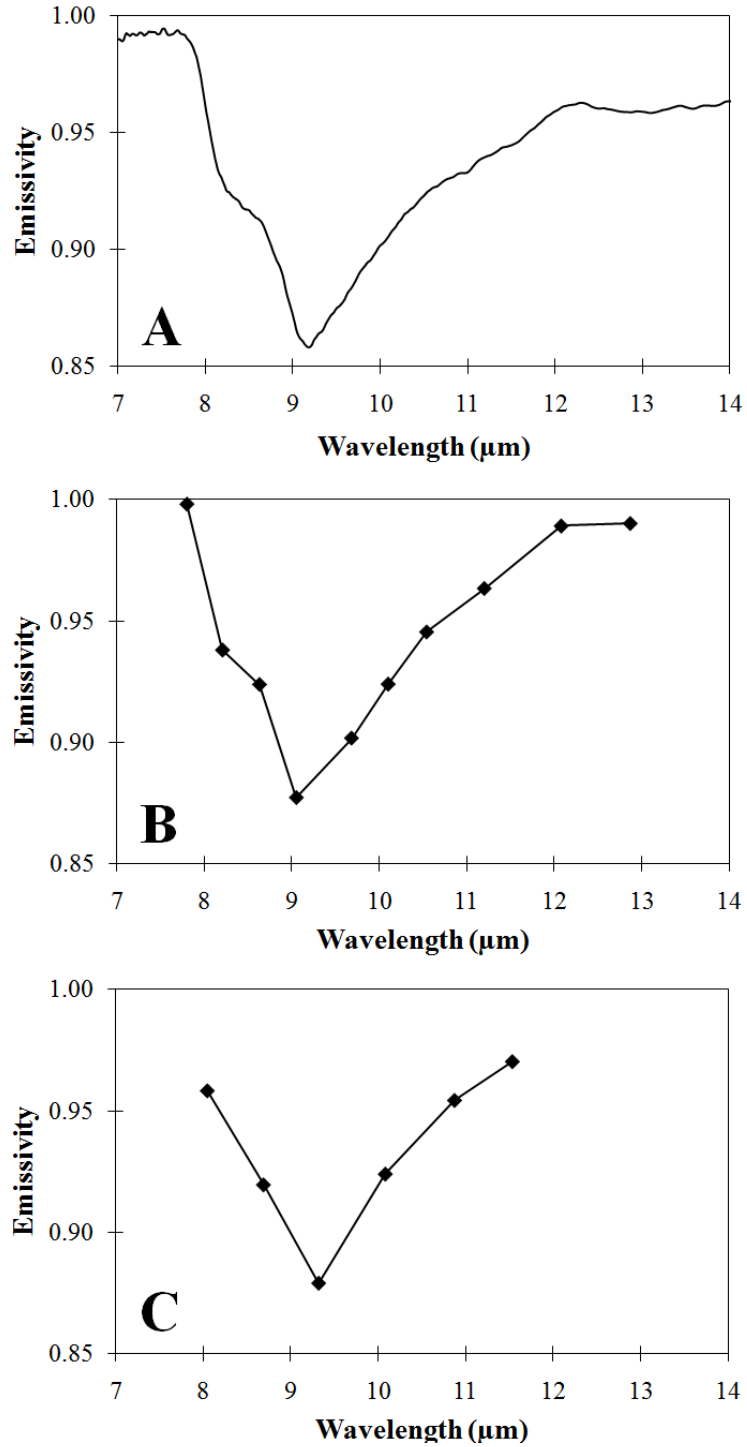


Figure 5-8 (A) Un-degraded, (B) MASTER-degraded and (C) FLIR-degraded spectra of fine vesicular pumice (FVP). The spectral shoulder at ~8.5 μm is resolved in the MASTER spectrum.

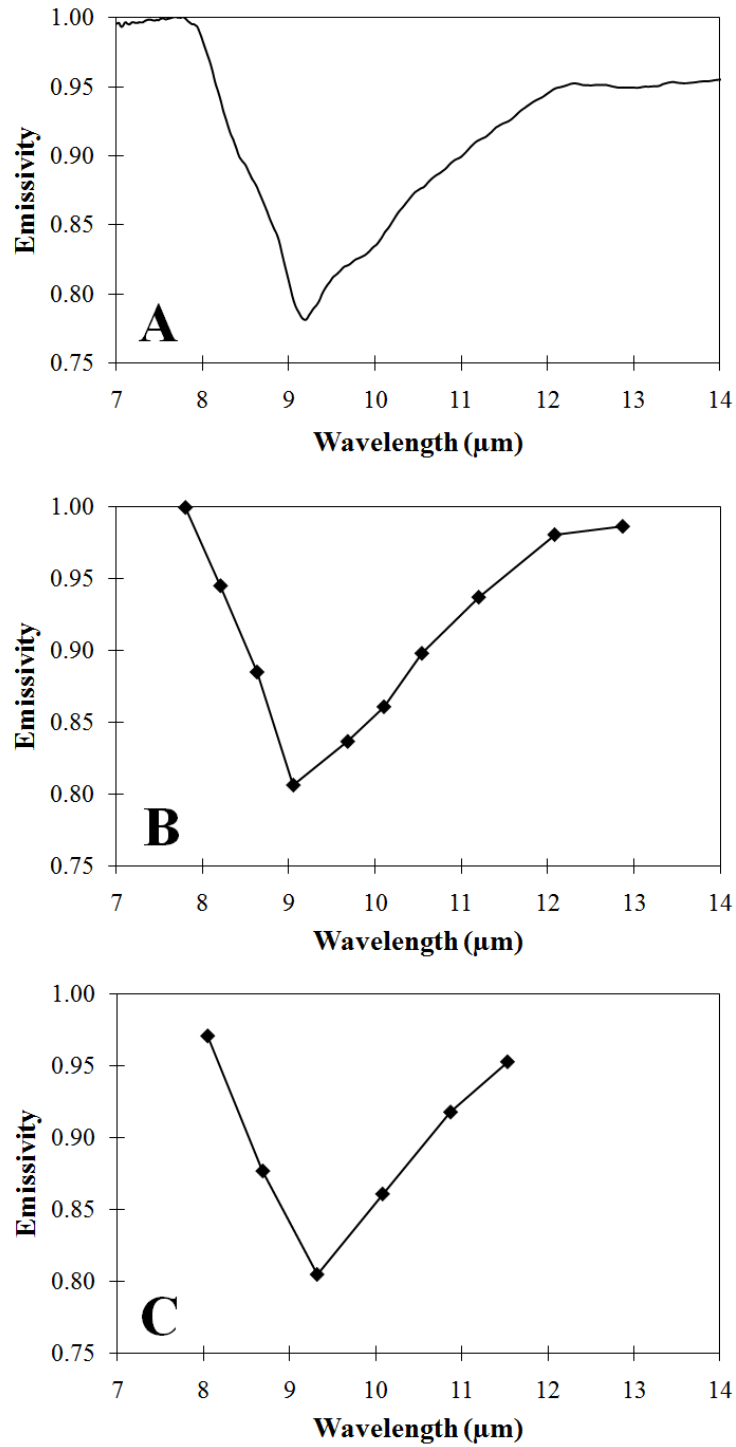


Figure 5-9 (A) Undegraded, (B) MASTER-degraded and (C) FLIR-degraded spectra of a dacite with basaltic andesite inclusions. The slight spectral feature at ~10 μm is resolved in the MASTER spectrum.

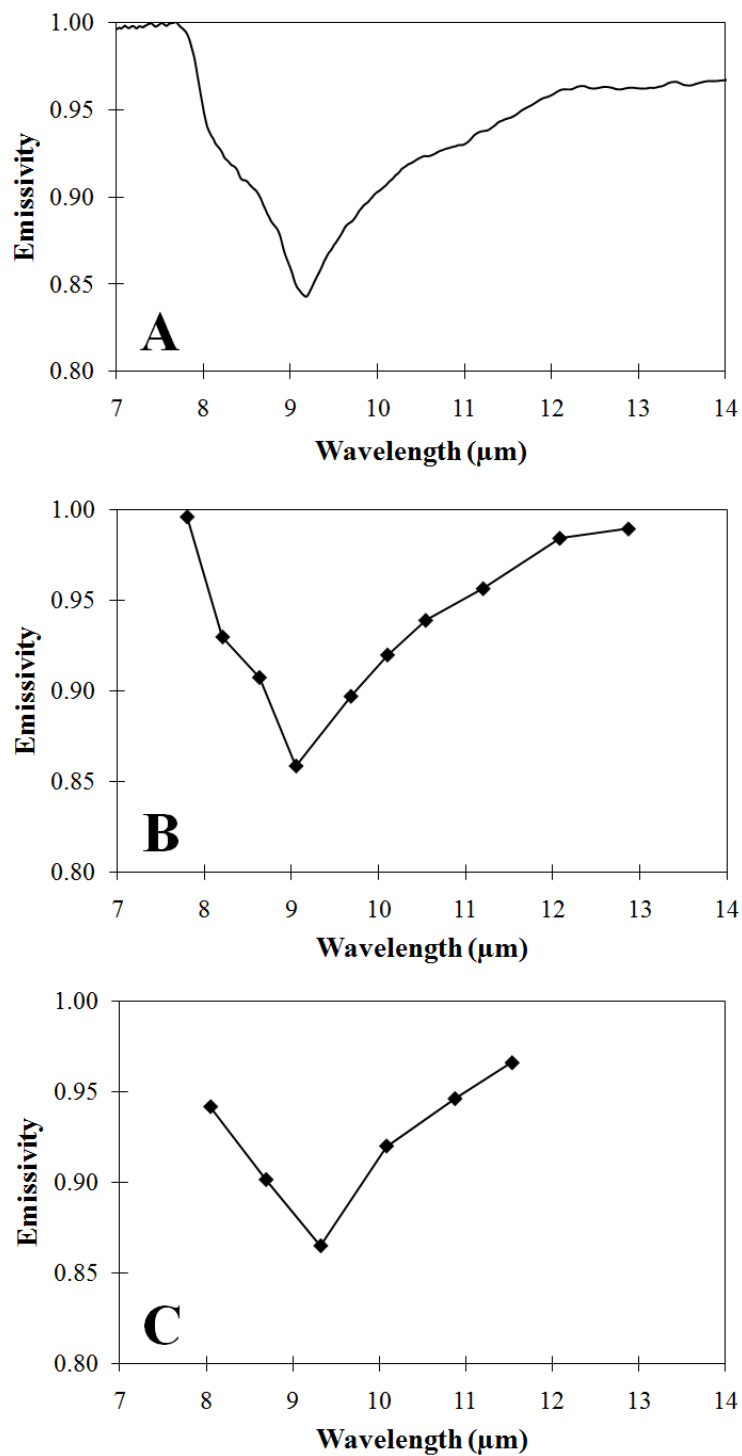


Figure 5-10 (A) Undegraded, (B) MASTER-degraded and (C) FLIR-degraded spectra of vesicular dacite. The slight spectral shoulder at $\sim 8.5 \mu\text{m}$ is resolved in the MASTER spectrum.

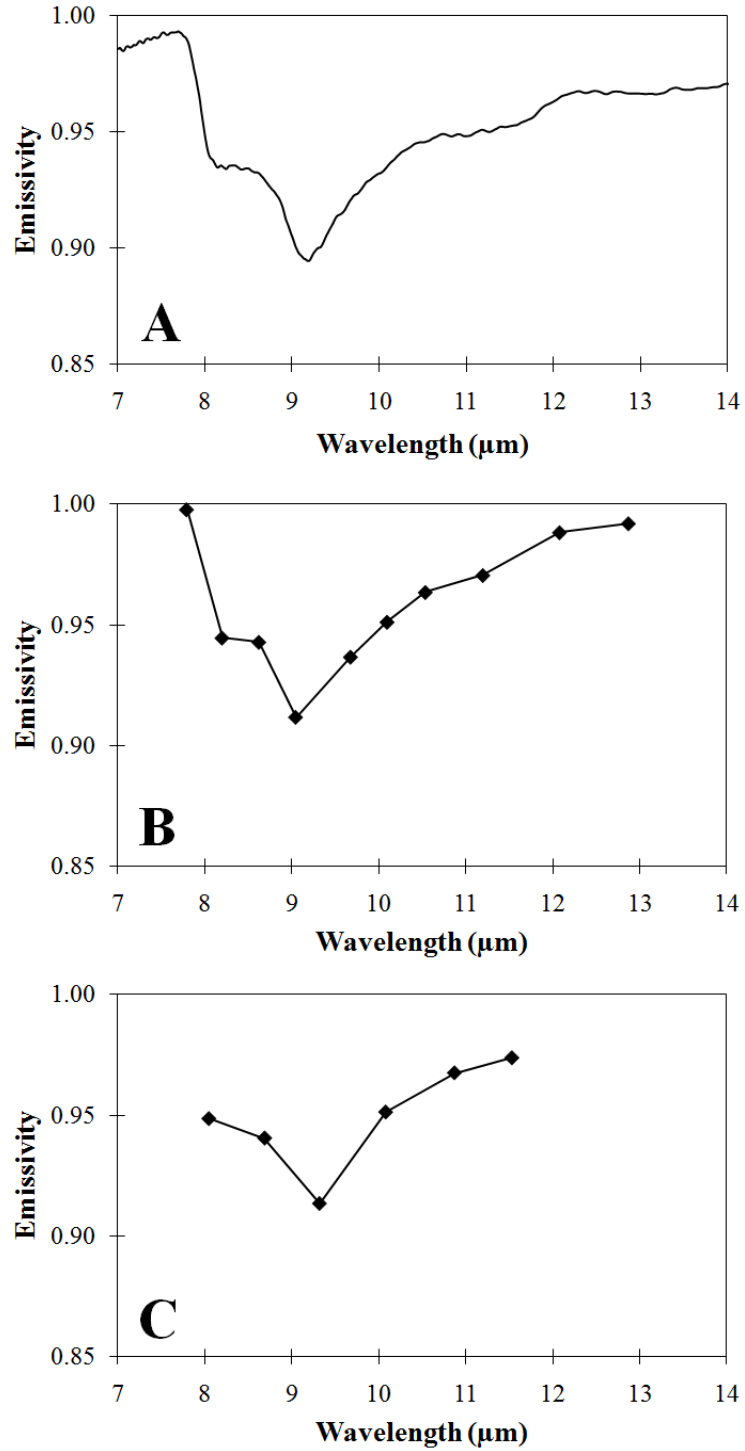


Figure 5-11 (A) Undegraded, (B) MASTER-degraded and (C) FLIR-degraded spectra of an altered breccia. The significant spectral shoulder at ~8.5 μm is resolved in both the MASTER and FLIR spectra.

Overall, the calculated half-width values are lower than that of the synthetic glass spectra. Thus, the calculated wt. % SiO₂ values are slightly higher than expected, and in most cases, do not match the inferred wt. % SiO₂ range (Table 5-4).

Two 6-band FLIR images were chosen for analysis in this study. Figure 5-15A shows a field image of an obsidian boulder located at an explosion pit westward of the rhyolite lobe (spectrum #11 on Figure 5-13). The corresponding multispectral FLIR decorrelation stretch image for this site is shown in Figure 5-15B. The half widths and wt. % SiO₂ values of the three spectra gathered from this image were calculated, and the data are summarized in Table 5-5. Half width values for these spectra are very high relative to those of MASTER and undegraded spectra. Thus, the wt. % SiO₂ values are very low, and are clearly unreasonable for obsidian. An additional field site (Figure 5-16A) and corresponding 6-point FLIR image (Figure 5-16B) display greater compositional variability. Five 6-point spectra were collected from this image, representing dacite, obsidian, and FVP. All of the half width values derived from these spectra are also very high, and display a similar inverse relationship with wt. % SiO₂ values (Table 5-6). The eight FLIR half width values are plotted on the 80 °C FLIR-degraded synthetic glass half width plot (Figure 5-17), and further illustrate the large discrepancy between the calculated and the expected wt. % SiO₂ values for dacitic and rhyolitic rocks.

5.4 DISCUSSION

The relationship between half width and wt. % SiO₂ of synthetic glass laboratory spectra is excellent at temperatures below the melt range. However, this relationship does not appear to hold true for a melted glass. This can be attributed to the wide variation observed in the emissivity minimum value and position, and the overall morphology, of melt spectra with changing temperature. The value of the emissivity minimum is a major factor in the calculation of the half width value, and subsequently the wt. % SiO₂. Further work must be done within the melt region in order to characterize the behavior of the emissivity minimum, and the half width calculation method must be modified to address the unique spectral behavior of molten samples. This includes melting and acquiring spectra of the same sample multiple times, to determine whether the spectral behavior of the melt is consistent. The prominent spectral shoulder feature that sometimes occurs at approximately 8.5 μm in many silicate spectra poses a potential problem for half width calculation. Depending on the depth of the main spectral feature, the half depth of the spectrum can sometimes lie directly on the shoulder. This is particularly problematic for MASTER and FLIR-degraded spectra, as the shoulder feature can typically show up in the degraded spectra as well. For example, the spectral shoulder of the breccia sample is particularly prominent, and shows up in both the MASTER and FLIR-degraded spectra, altering their shape by introducing a sharp bend in the spectra. This has the effect of making the emissivity minimum slightly shallower than it should be, thus affecting the calculation of the half width. This reduction in emissivity minimum with degradation is observed in all the natural

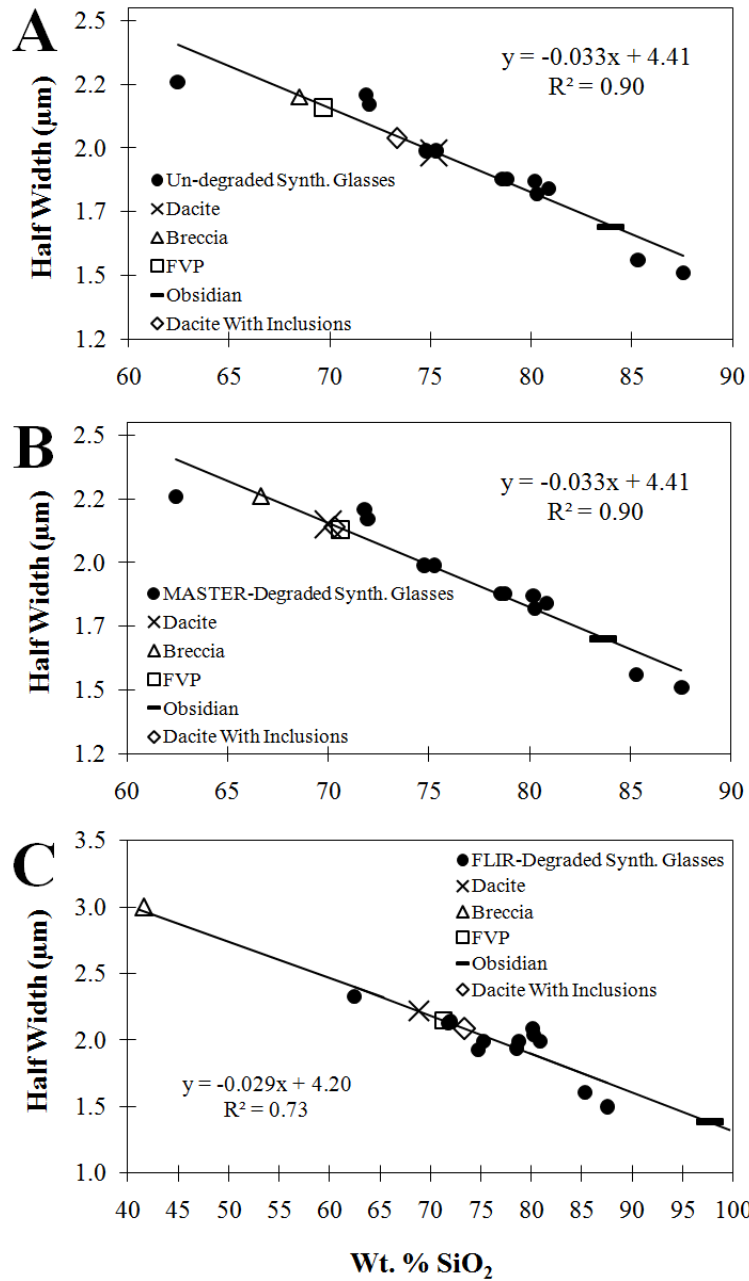


Figure 5-12 (A) Half width vs. wt. % SiO_2 plots for un-degraded synthetic glass spectra with calculated half widths and wt. % SiO_2 values for the 5 natural samples plotted on the trend line. (B) Half width vs. wt. % SiO_2 plots for MASTER-degraded synthetic glass spectra with calculated half widths and wt. % SiO_2 values for the 5 natural samples plotted on the trend line. (C) Half width vs. wt. % SiO_2 plots for FLIR-degraded synthetic glass spectra with calculated half widths and wt. % SiO_2 values for the 5 natural samples plotted on the trend line. Wt. % SiO_2 and half width values of natural samples in (A) and (B) are slightly different than the synthetic glasses. Natural samples in (C) have much different half widths and wt. % SiO_2 values than expected.

Table 5-1 Half Width and Wt. % SiO₂ for Un-degraded Natural Samples

Natural Sample Spectrum	Calculated Half Width (μm)	Calculated Wt % SiO₂	Inferred ~ Wt % SiO₂ (based on known composition)
Dacite (w/inclusions)	1.99	73.33	55-65 (Dacite)
Dacite	1.93	75.15	55-65 (Dacite)
Obsidian	1.64	83.94	65-75 (Obsidian)
FVP	2.11	69.70	65-75 (Rhyolite)
Breccia	2.15	68.48	unknown

Table 5-2 Half Width and Wt. % SiO₂ for MASTER-degraded Natural Samples

Natural Sample Spectrum	Calculated Half Width (μm)	Calculated Wt % SiO₂	Inferred ~ Wt % SiO₂ (based on known composition)
Dacite (w/inclusions)	2.09	70.30	55-65 (Dacite)
Dacite	2.10	70.00	55-65 (Dacite)
Obsidian	1.65	83.64	65-75 (Obsidian)
FVP	2.08	70.61	65-75 (Rhyolite)
Breccia	2.21	66.67	unknown

Table 5-3 Half Width and Wt. % SiO₂ for FLIR-degraded Natural Samples

Natural Sample Spectrum	Calculated Half Width (μm)	Calculated Wt % SiO₂	Inferred ~ Wt % SiO₂ (based on known composition)
Dacite (w/inclusions)	2.09	73.36	55-65 (Dacite)
Dacite	2.22	68.83	55-65 (Dacite)
Obsidian	1.39	97.75	65-75 (Obsidian)
FVP	2.15	71.26	65-75 (Rhyolite)
Breccia	3.00	41.65	unknown

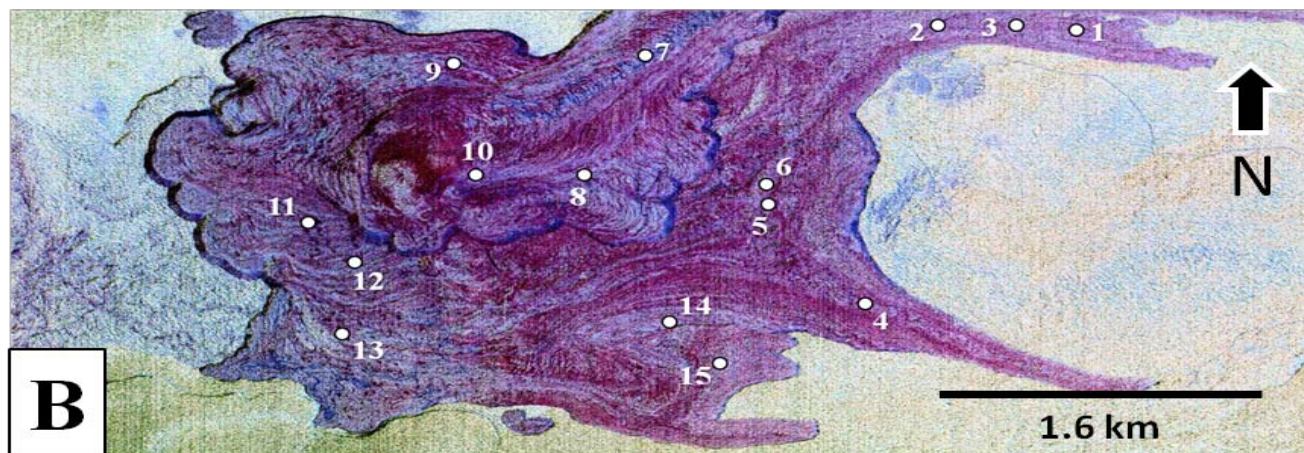


Figure 5-13 MASTER images of Glass Mountain flow, Medicine Lake Volcano. (A) Visible color image (source: Google Earth). (B) False color image. Dark and light purple colors depict the widespread compositional mixing of the flow. The image is distorted in the E-W direction due to the scanning motion of the MASTER instrument. The two long lobes to the east of the main body of the flow are 67 wt. % SiO_2 dacite, and a zone of compositionally-mixed material lies between the two lobes. The large lobe extending from the top-center of the flow to the northeast is 74 wt. % SiO_2 rhyolite. White dots denote areas where image-based emission spectra were acquired.

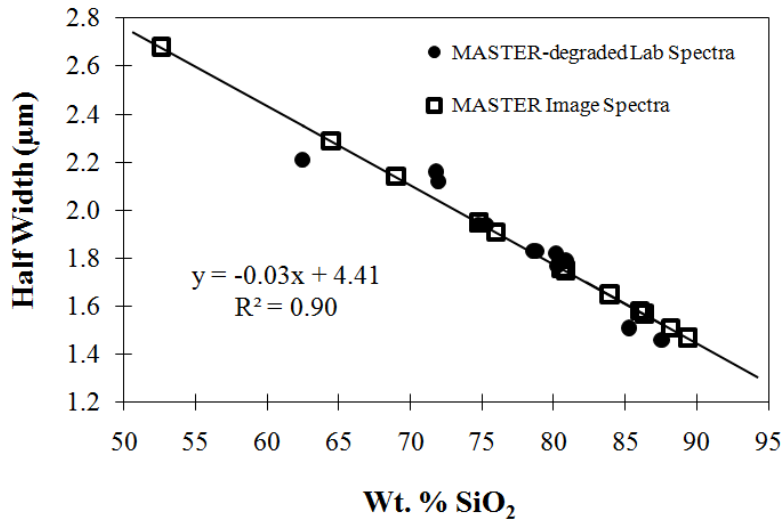


Figure 5-14 Half width vs. wt. % SiO₂ values for MASTER-degraded synthetic glass spectra, with data from MASTER image-based spectra plotted on the trend line. Half width values of the image-based spectra are within the range of the lab spectra; however, the calculated wt. % SiO₂ value for each spectrum is slightly higher than the inferred wt. % SiO₂ value for the spectrum.

sample spectra, particularly those of breccia, obsidian and FVP. A possible solution to this is to calculate the “2/3 width” of the spectrum, rather than the half width, or calculate the ratio of the half width to the “2/3 width”, in order to better define the shoulder feature in degraded spectra. Other possible methods include utilizing Gaussian curve fitting or linear unmixing, both of which can be modified for use in real-time in the field.

Synthetic glass spectra, natural sample spectra, and image-based spectral all exhibit an inverse relationship between half width and calculated wt. % SiO₂. In general, higher half width values yield lower wt. % SiO₂ values, and vice versa. Furthermore, a spectrum with a deeper spectral feature will have a lower half depth value, and thus a lower half width value. For example, obsidian has a very deep spectral feature ($\epsilon_{\min} \sim 0.63$), and a correspondingly low half

Table 5-4 Half Width and Wt. % SiO₂ values for MASTER image-based spectra

MASTER Spectrum #	Calculated Half Width (μm)	Calculated Wt. % SiO₂	Inferred ~ Wt. %SiO₂ (based on image location)
1	1.47	89.38	55-65 (Dacite Lobe)
2	2.14	69.02	55-65 (Dacite Lobe)
3	2.68	52.60	55-65 (Dacite Lobe)
4	1.51	88.16	55-65 (Dacite Lobe)
5	1.51	88.16	66-71 (Rhyodacite - Mixed)
6	1.58	86.04	66-71 (Rhyodacite - Mixed)
7	1.95	74.79	65-75 (Rhyolite)
8	1.91	76.01	65-75 (Rhyolite)
9	1.47	89.38	65-75 (Rhyolite)
10	1.65	83.91	65-75 (Rhyolite)
11	1.57	86.34	66-71 (Rhyodacite - Explosion Pit)
12	1.95	74.79	66-71 (Rhyodacite - Explosion Pit)
13	1.76	80.57	66-71 (Rhyodacite - Explosion Pit)
14	2.29	64.46	66-71 (Rhyodacite - Mixed)
15	1.75	80.87	66-71 (Rhyodacite - Mixed)

width value. This leads to a calculated wt. % SiO₂ value that is much higher than the inferred value. Laboratory-derived spectra tend to display deeper spectral features than image-based spectra. This is due primarily to the higher spectral and spatial resolutions of the laboratory, coupled with the controlled environment in which the spectra are acquired. The muted nature of the FLIR image-based spectra yield very high half width values, and consequently, very low wt. % SiO₂ values. FLIR image spectra therefore cannot be directly compared to the synthetic glass data, and a special calibration curve must be created for the FLIR camera. This can be achieved by creating 6-band images of each of the synthetic glass samples at 80 °C to derive more accurate half-width vs. wt. % SiO₂ plot for FLIR.

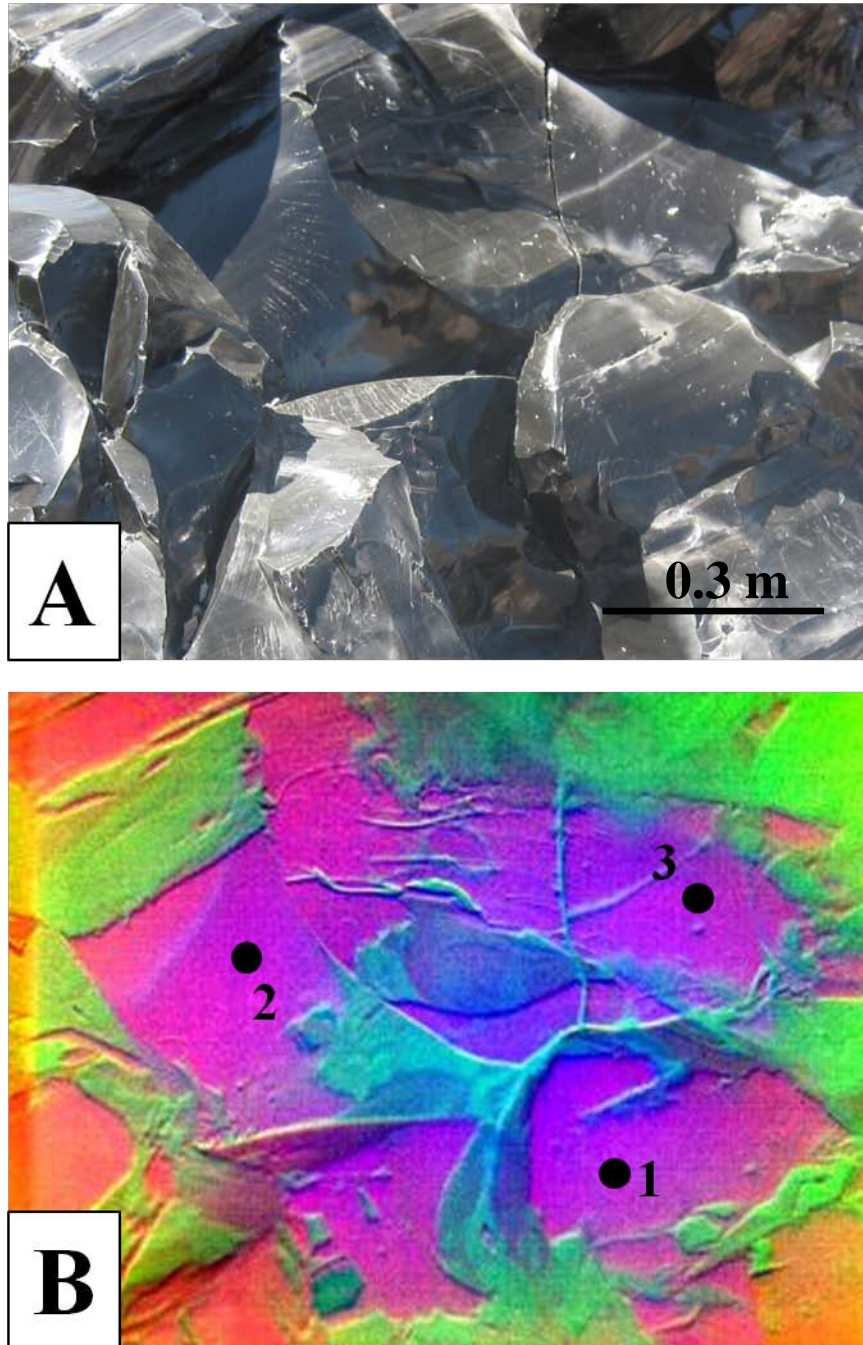


Figure 5-15 (A) Field image of an obsidian boulder ejected from an explosion pit, and (B) an RGB 6-3-1 (11.53 μm – 9.32 μm – 8.05 μm) FLIR decorrelation stretch image of the same field site. Pink and purple colors represent areas of high silica. Green and blue colors denote areas behaving as blackbody-like material. Black dots denote points at which emission spectra were acquired from the FLIR image.

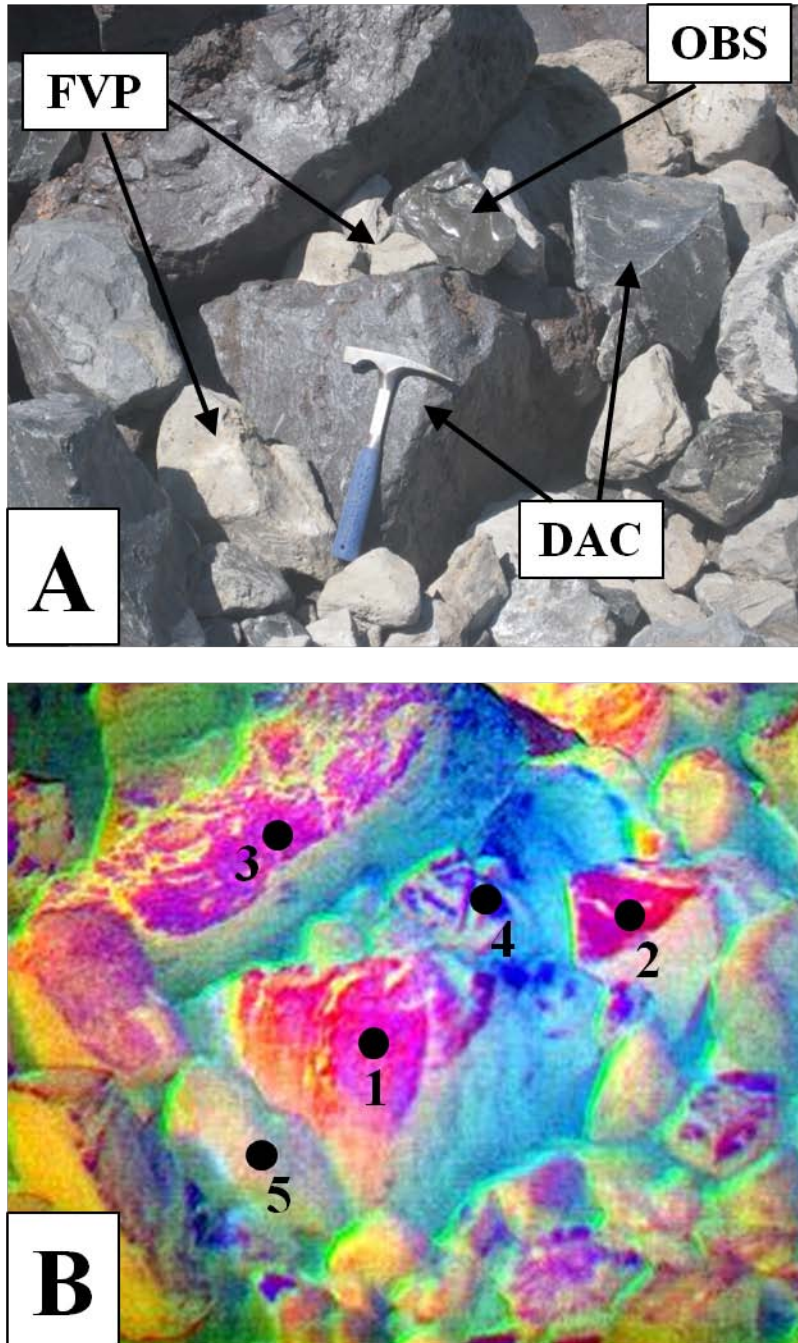


Figure 5-16 (A) Field image of a compositionally-mixed area on Glass Mountain and (B) an RGB 5-3-1 (10.87 μm – 9.32 μm – 8.05 μm)FLIR decorrelation stretch image of the same field site. Pink and purple colors represent areas of high silica. Green and blue colors denote areas behaving as blackbody-like material. Black dots denote points at which emission spectra were acquired from the FLIR image.

Table 5-5 Half Width and Wt. % SiO₂ for FLIR image-based spectra in Figure 5-13B

FLIR Spectrum #	Calculated Half Width (μm)	Calculated Wt % SiO₂	Inferred ~ Wt. % SiO₂ (based on image location)
1	3.45	25.86	65 - 75 (Obsidian)
2	3.83	12.76	66 - 75 (Obsidian)
3	4.07	4.48	67 - 75 (Obsidian)

Table 5-6 Half Width and Wt. % SiO₂ for FLIR image-based spectra in Figure 5-14B

FLIR Spectrum #	Calculated Half Width (μm)	Calculated Wt % SiO₂	Inferred ~ Wt. % SiO₂ (based on image location)
1	3.46	25.52	55 - 65 (Dacite)
2	3.46	25.52	56 - 65 (Dacite)
3	4.28	n/a	57 - 65 (Dacite)
4	3.08	38.62	67 - 75 (Obsidian)
5	4.84	n/a	67 - 75 (Fine Vesicular Pumice)

5.5 CONCLUSIONS

Given the good linear fit of the 80 °C un-degraded and MASTER-degraded synthetic glass spectra at below-melt temperatures, use of the half width to find wt. % SiO₂ from field-based spectra is promising. However, the half width calculation method must be modified in order to derive more accurate half width results for field-based data, which in turn will yield calculated wt. % SiO₂ values which more closely match actual wt. % SiO₂ compositions. This includes further investigation of the effects of emissivity minimum value and the presence of

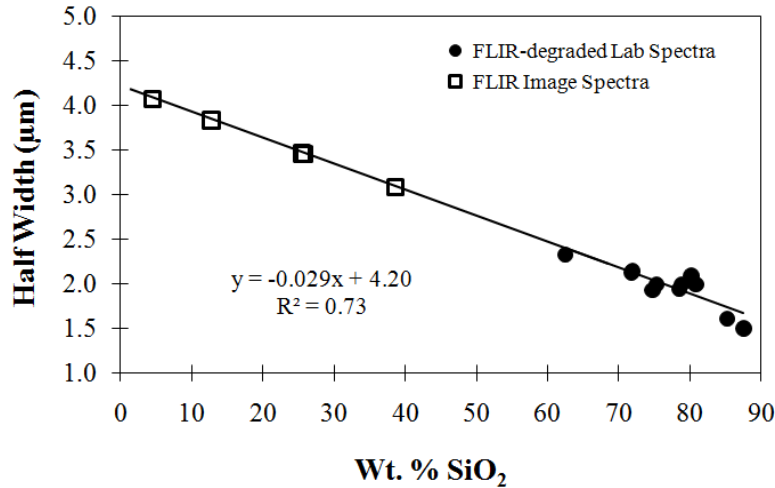


Figure 5-17 Half width vs. wt. % SiO₂ values for MASTER-degraded synthetic glass spectra, with data from MASTER image-based spectra plotted on the trend line. Half width values of the image-based spectra are within the range of the lab spectra; however, the calculated wt. % SiO₂ value for each spectrum is slightly higher than the inferred wt. % SiO₂ value for the spectrum.

spectral shoulder on the half width. Additionally, the half width values of natural sample spectra need to be directly compared to microprobe-derived wt. % SiO₂ values of samples from Glass Mountain, rather than those of synthetic glass samples. Natural samples have different cooling rates, are composed of more complex molecular structures, undergo weathering, and have more significant crystal contents than synthetic glasses. All of these factors can affect emissivity and spectral morphology, which in turn affects the correlation between half width and wt. % SiO₂.

Application of the half width method to spectra within the melt region is a more complicated process, as the emissivity minimum and width of the spectra change much more variably with increasing and decreasing temperature. More work is needed to further

characterize the spectral behavior of melts, including experiments to determine whether changes in the emissivity minimum and spectral shape with temperature are consistent each time a glass is melted. Once this is known, calibration curves can be created for each temperature, and calculated half width value of a spectrum at a given temperature can then be applied to the corresponding calibration curve. The accuracy of these calibration curves for field and image-based data of rhyolitic melts can then be tested.

There are clear differences in spectral and spatial resolution between MASTER and FLIR-degraded laboratory spectra, and spectra acquired directly from MASTER and FLIR images. Laboratory spectra are acquired over a ~2.5 cm spot size, whereas the MASTER image is 10 meters/pixel. The MASTER TIR has 10 band-passes, and the spectrometer has ~370 in this wavelength range. Even though the half width values of the MASTER image-based spectra are largely within the range of those of the MASTER-degraded laboratory spectra, the calculated wt. % SiO₂ values for MASTER image-based spectra are either slightly higher or lower than expected. The FLIR image-based spectra are even lower resolution than MASTER spectra, and the Restsrahlen feature is also more muted, leading to very high calculated half widths and correspondingly very low wt. % SiO₂ values. This further confirms that spectral resolution and the depth of the Restsrahlen feature both play a major role in the calculation, and the accuracy, of the half width of the spectrum.

Given the 10 meter pixel size of the MASTER instrument, the calculated wt. % SiO₂ will be an average over that pixel, and will encompass many different compositions. This is compounded by the fact that Glass Mountain is so intimately compositionally mixed. Therefore, wt. % SiO₂ values calculated from MASTER image-based spectra will never be quite as accurate as those of a field-based instrument with a much higher spectral and spatial resolution. Because of the lower spectral resolution of the FLIR, the half width calculations from the FLIR images are currently too high relative to the FLIR-degraded laboratory spectra, making the two incomparable. Therefore a specialized calibration curve for FLIR must be created by deriving a 6 point FLIR spectrum for each of the 80 °C synthetic glass spectra in the laboratory. Similar calibration curves can also be created for synthetic glass melts at various temperatures, and eventually for basaltic melts. These curves can then be utilized in the field to perform in-situ composition determination of silicate lavas based on the 6-point FLIR spectra. Although not as accurate for compositionally mixed flows such as Glass Mountain, a similar methodology can be applied to MASTER image-based spectra of silicate materials at various temperatures.

Accurate determination of emissivity in the field, particularly on an active volcano, is a complex and potentially hazardous process. Thermal heterogeneities, as well as changes in texture and composition, can hinder the accurate determination of emissivity and compositional information. This is compounded by the typically low spectral and spatial resolution of field and image-based TIR remote sensing data. The emissivity and spectral morphology of an active volcanic surface changes with changing composition, as well as with temperature, crystallinity,

and texture. Development of an *in-situ* field-based method for characterizing each of these variables in terms of emissivity in real-time is important, because each has a bearing on the behavior and eruptive potential of a volcano.

APPENDIX A

HIGH TEMPERATURE EMISSION SPECTRAL DATA OF SYNTHETIC GLASSES

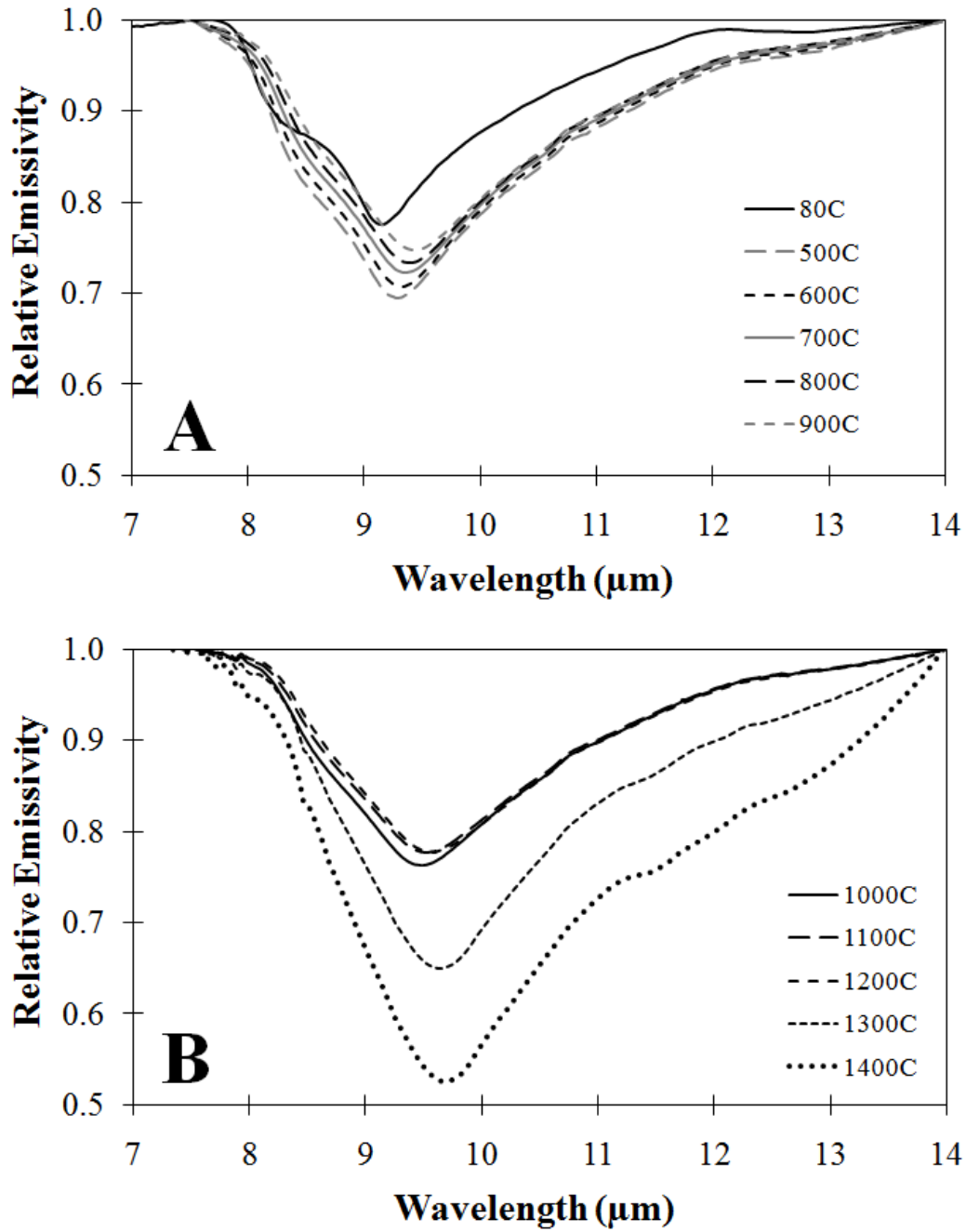


Figure A-1 Relative emissivity spectra for glass 2 from (A) 80 °C to 900 °C and (B) 1000 °C to 1400 °C.

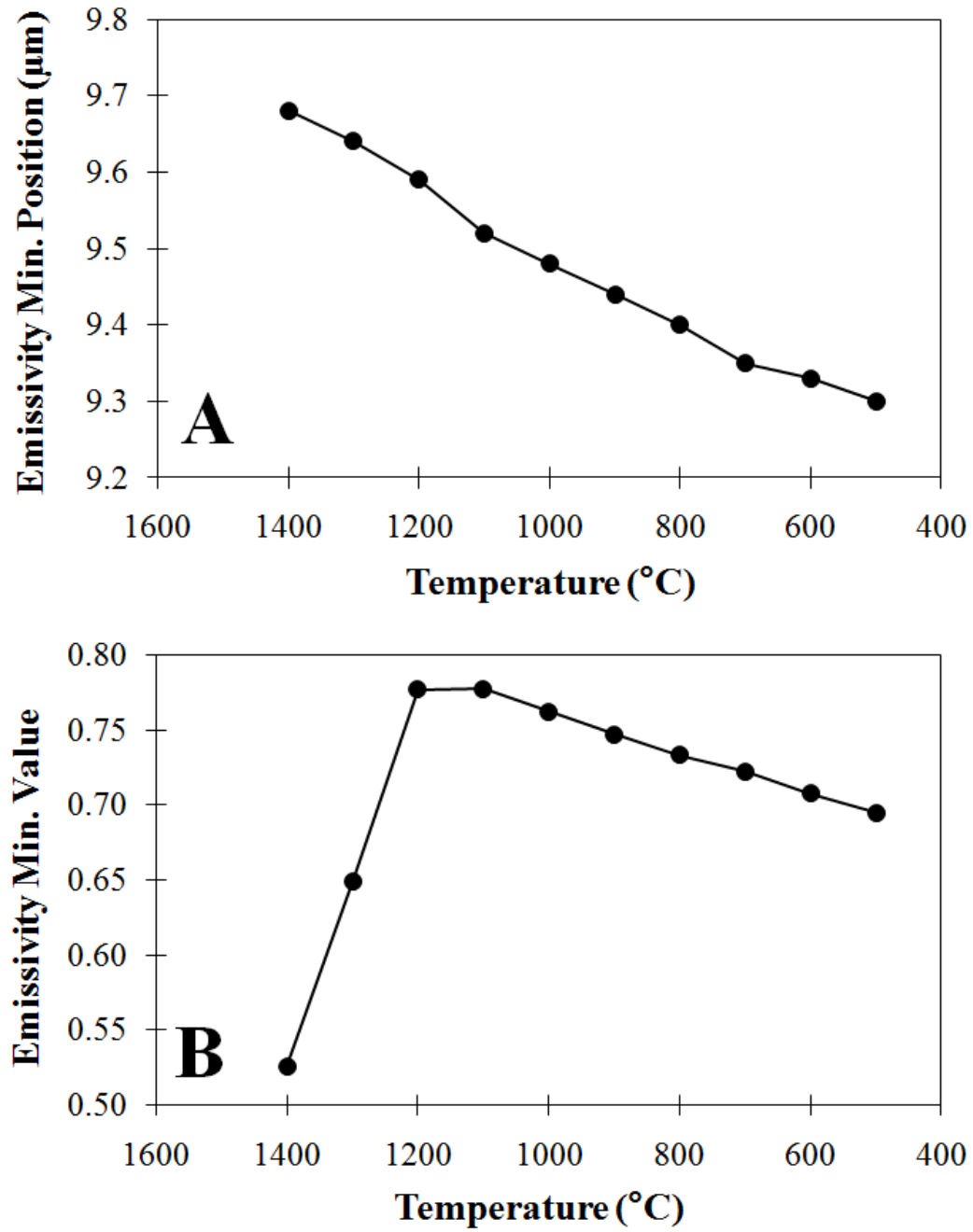


Figure A-2 Change in (A) emissivity minimum position and (B) emissivity minimum value with temperature for glass 2.

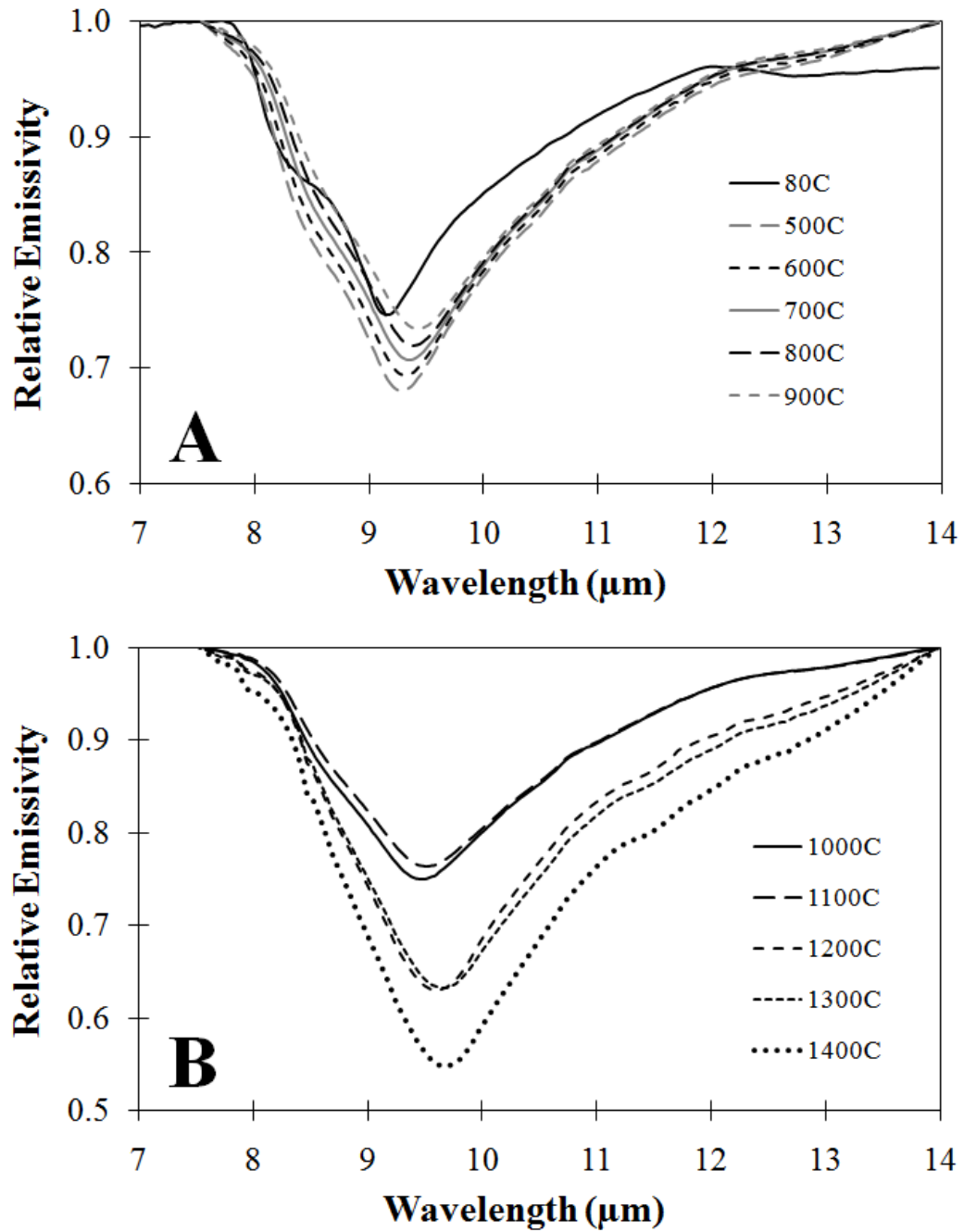


Figure A-3 Relative emissivity spectra for glass 2a from (A) 80 °C to 900 °C and (B) 1000 °C to 1400 °C.

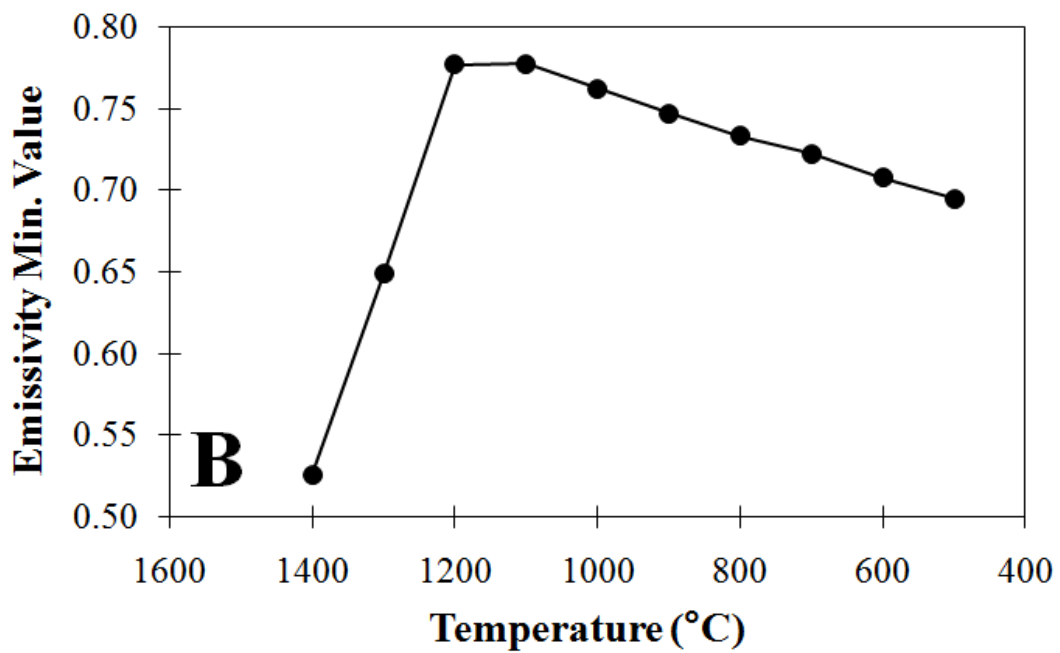
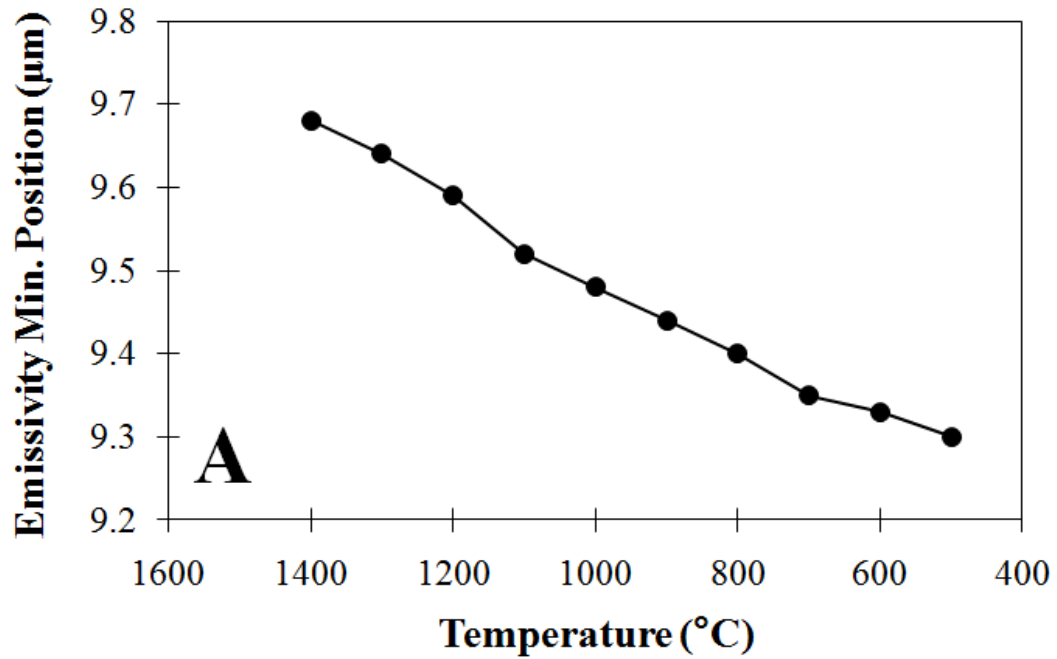


Figure A-4 Change in (A) emissivity minimum position and (B) emissivity minimum value with temperature for glass 2a.

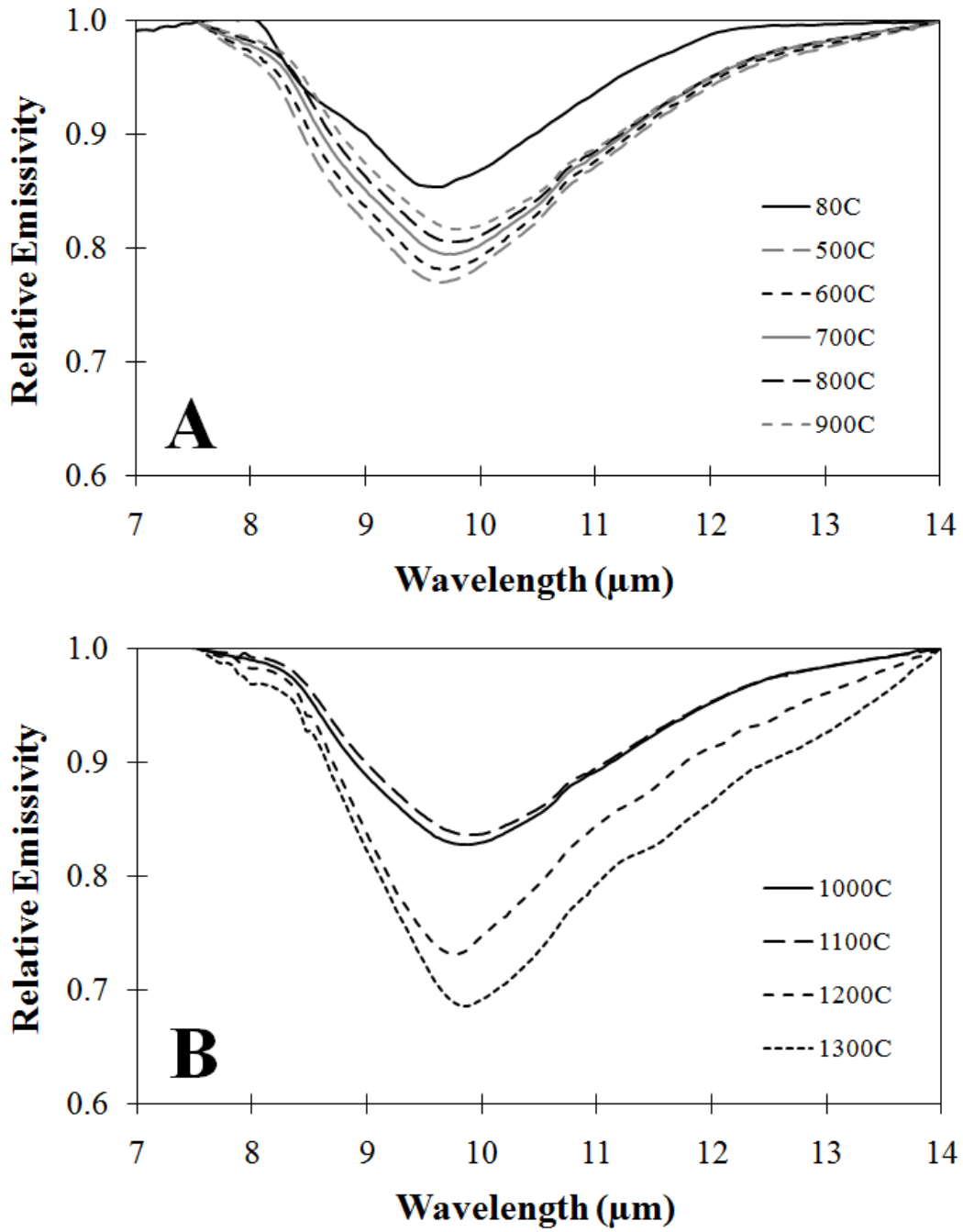


Figure A-5 Relative emissivity spectra for glass 3 from (A) 80 °C to 900 °C and (B) 1000 °C to 1300 °C.

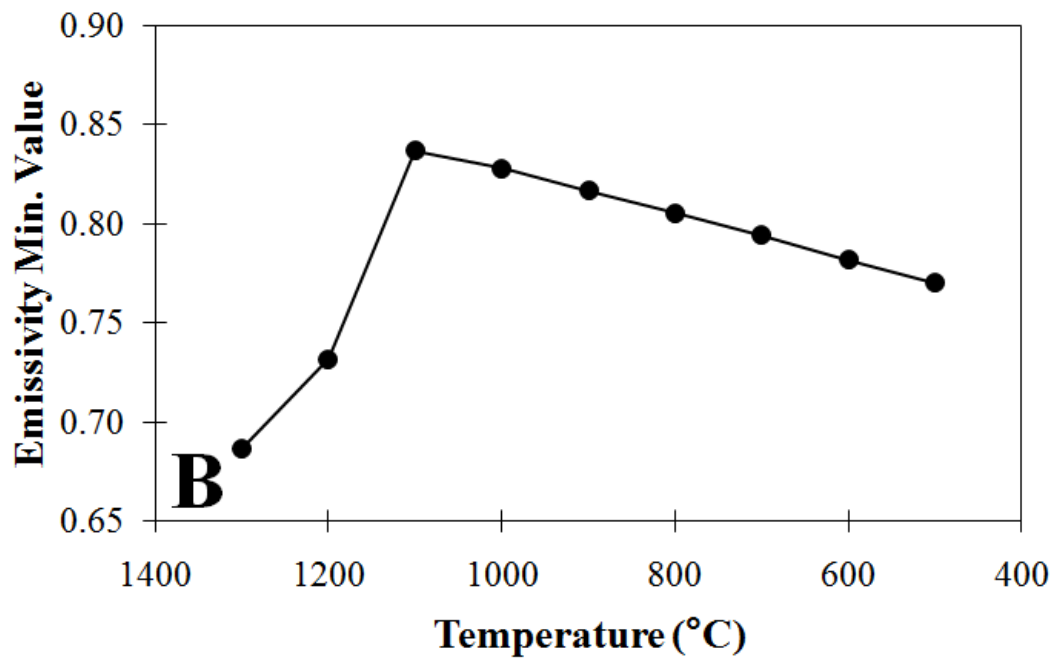
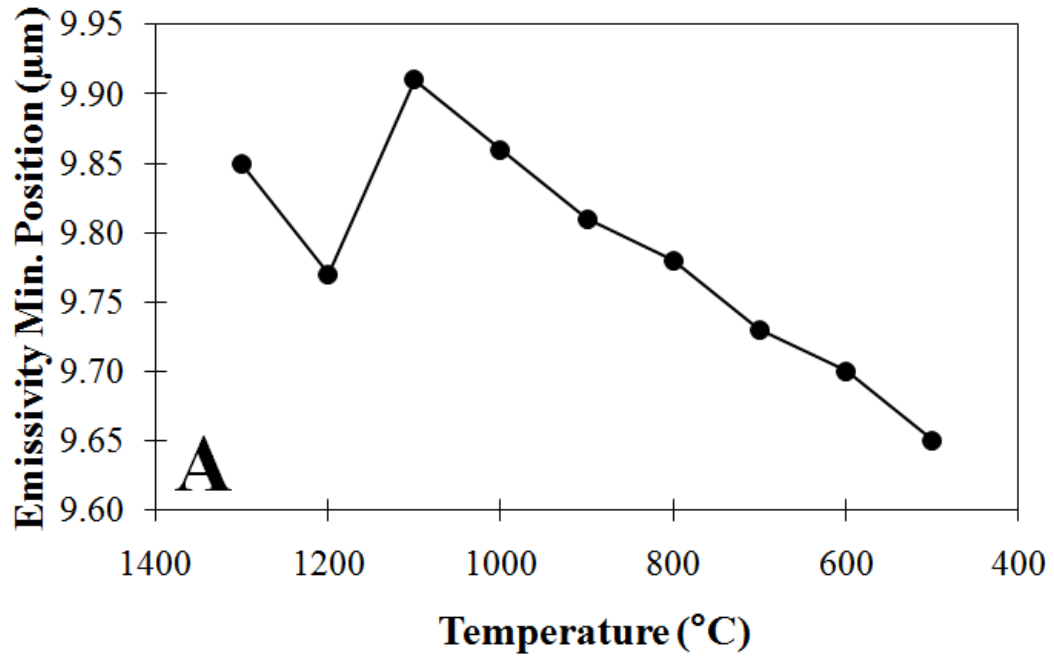


Figure A-6 Change in (A) emissivity minimum position and (B) emissivity minimum value with temperature for glass 3.

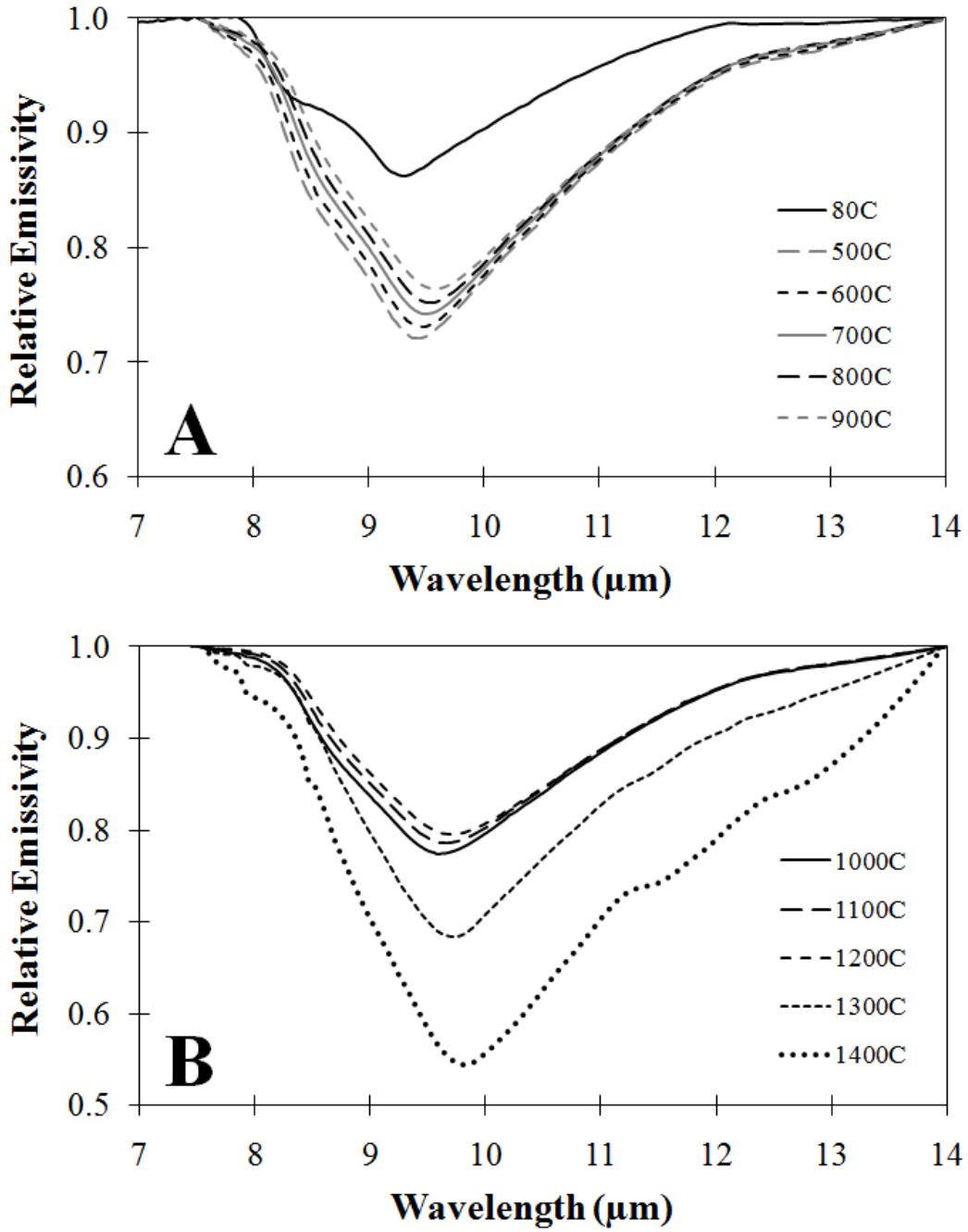


Figure A-7 Relative emissivity spectra for glass 6 from (A) 80 °C to 900 °C and (B) 1000 °C to 1400 °C.

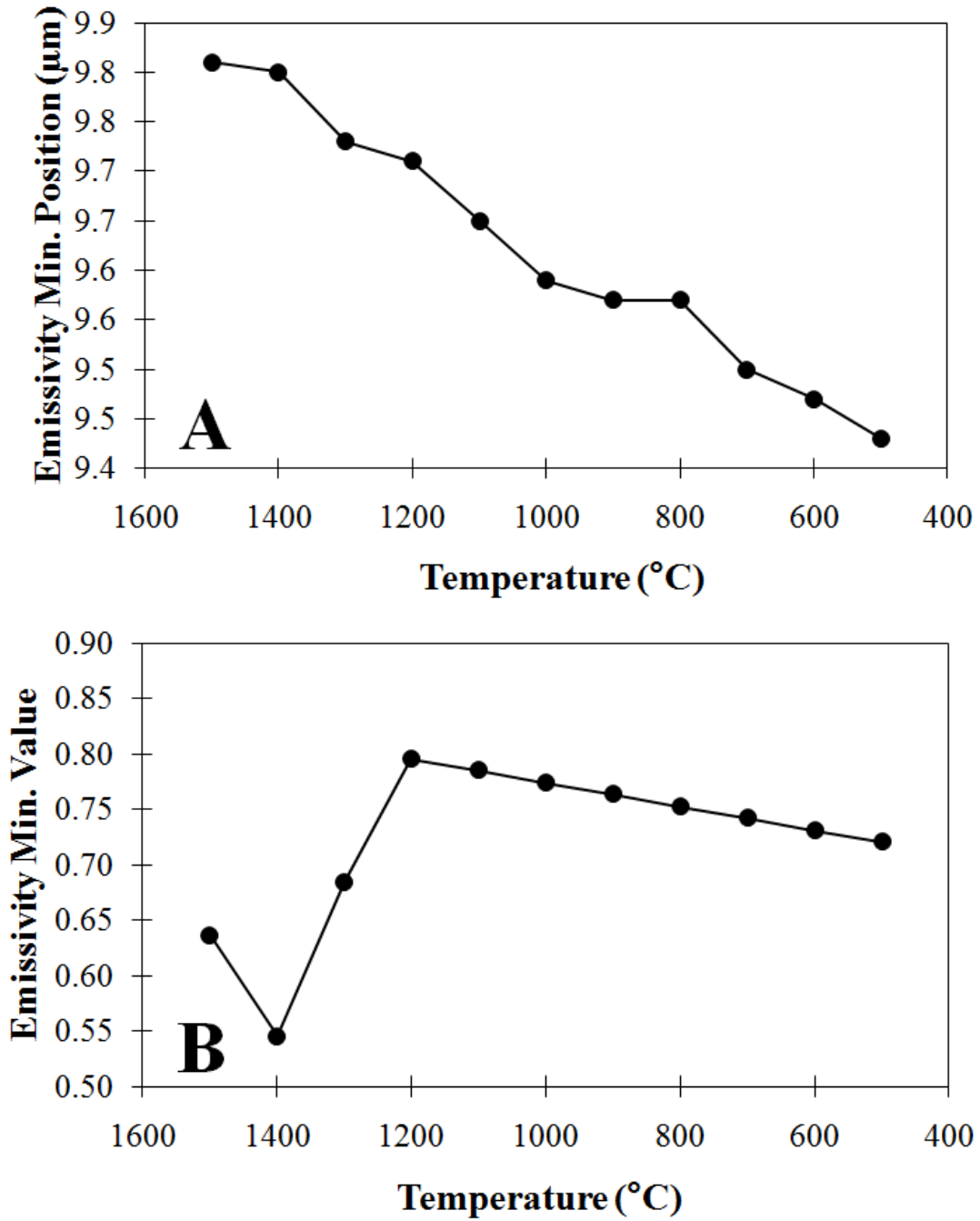


Figure A-8 Change in (A) emissivity minimum position and (B) emissivity minimum value with temperature for glass 6.

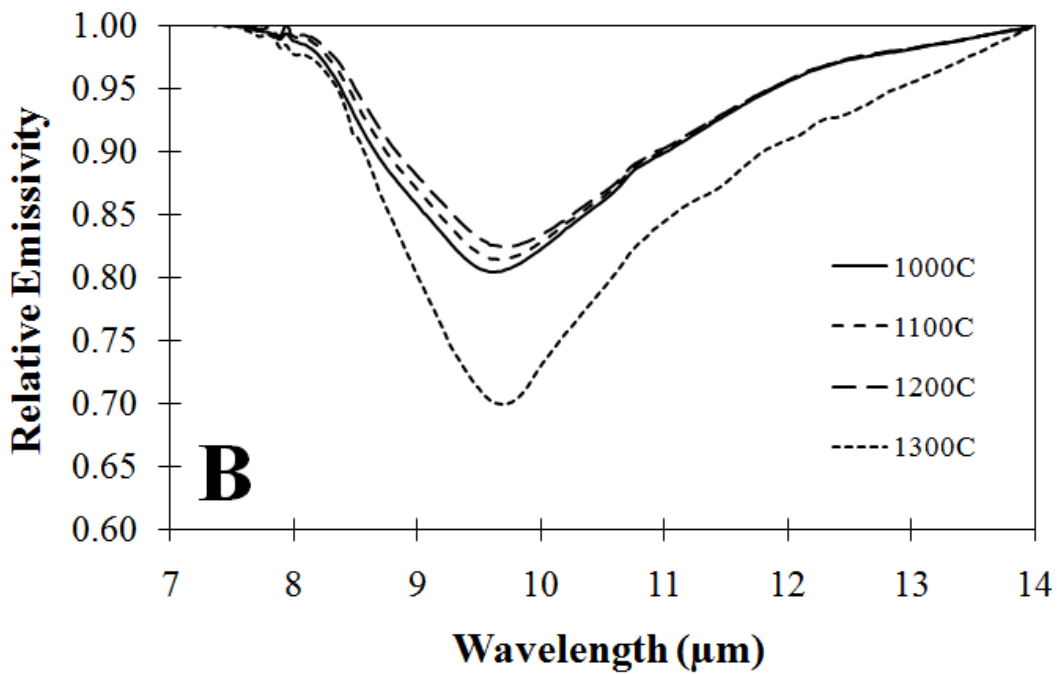
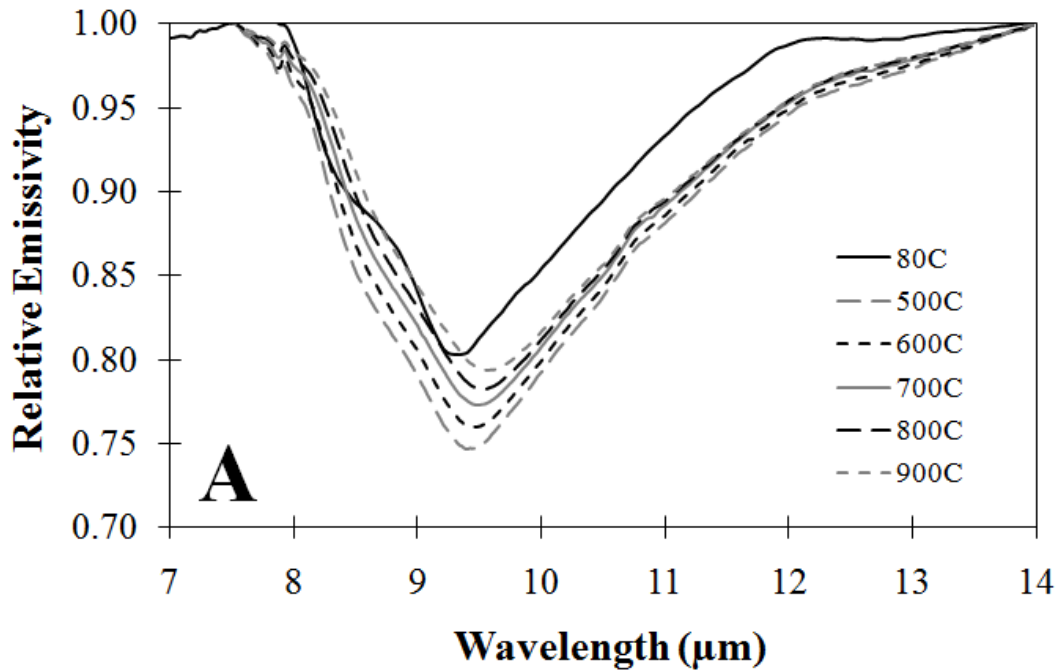


Figure A-9 Relative emissivity spectra for glass 19 from (A) 80 °C to 900 °C and (B) 1000 °C to 1300 °C.

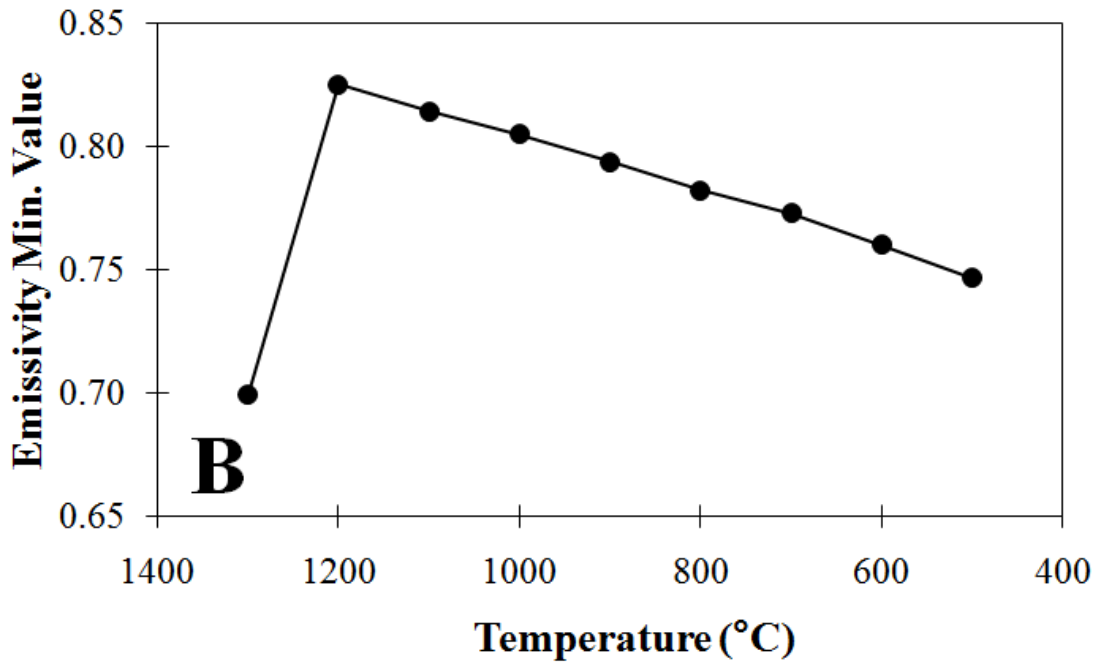
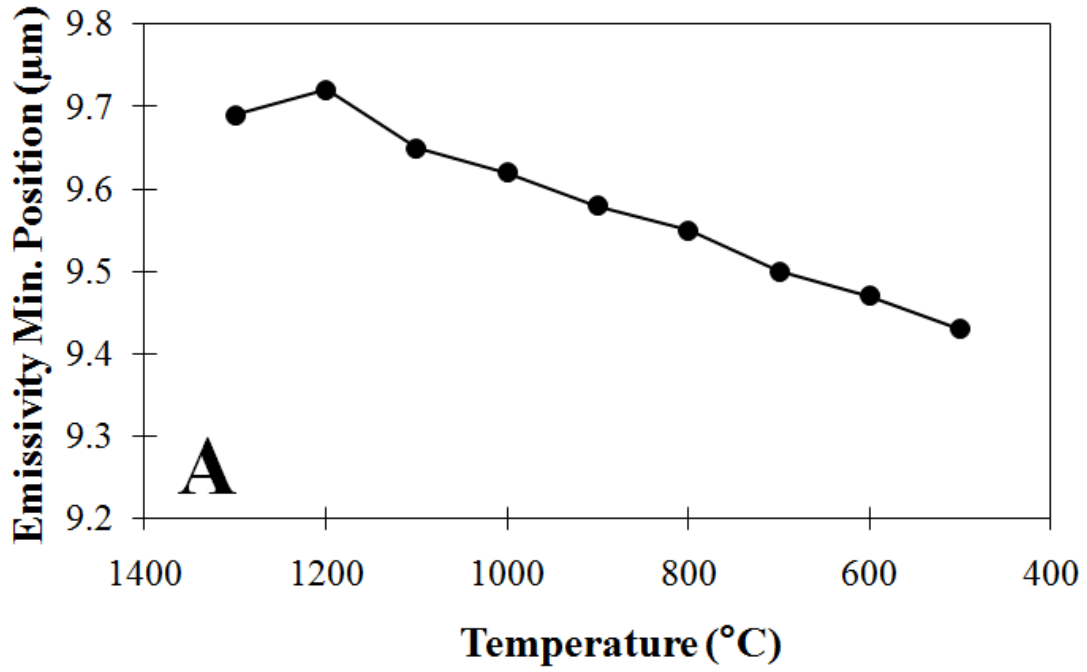


Figure A-10 Change in (A) emissivity minimum position and (B) emissivity minimum value with temperature for glass 19.

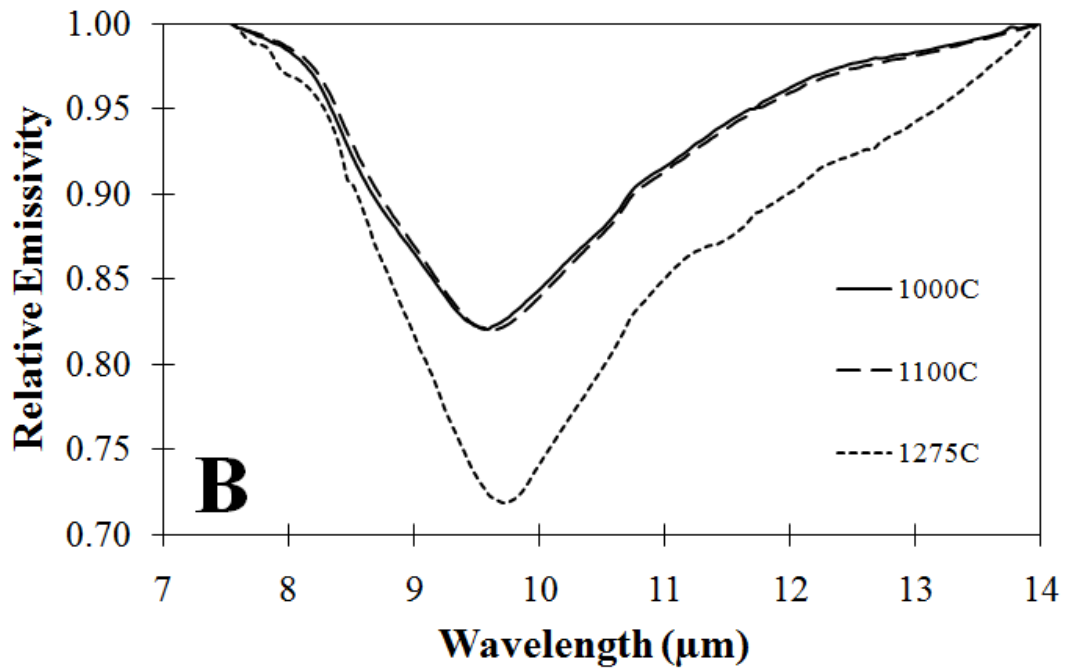
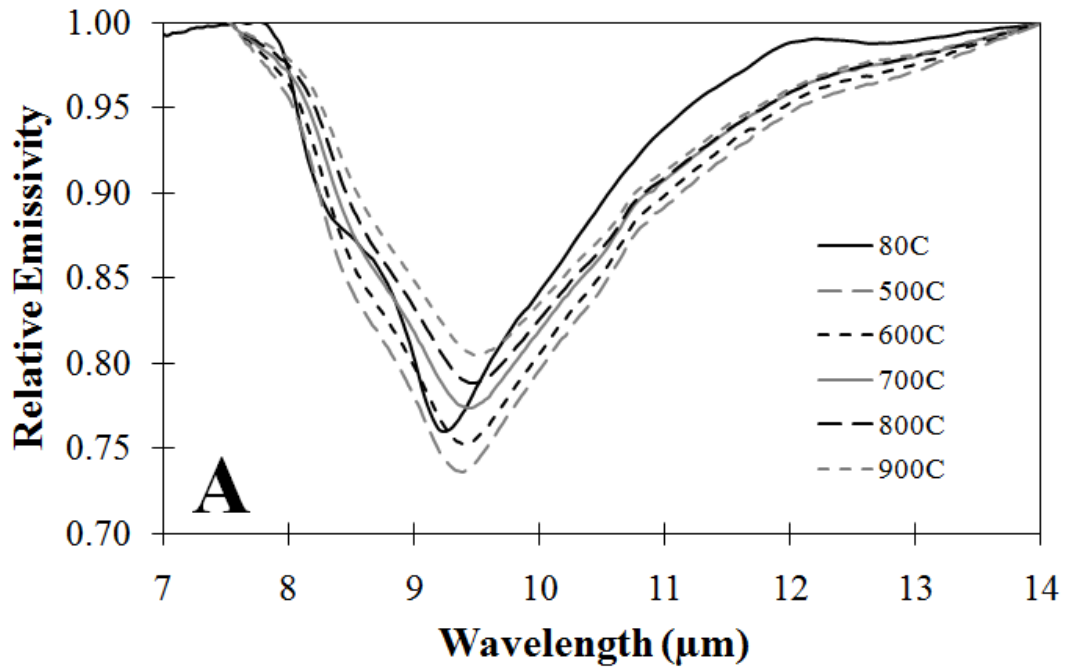


Figure A-11 Relative emissivity spectra for glass 19a from (A) 80 °C to 900 °C and (B) 1000 °C to 1275 °C.

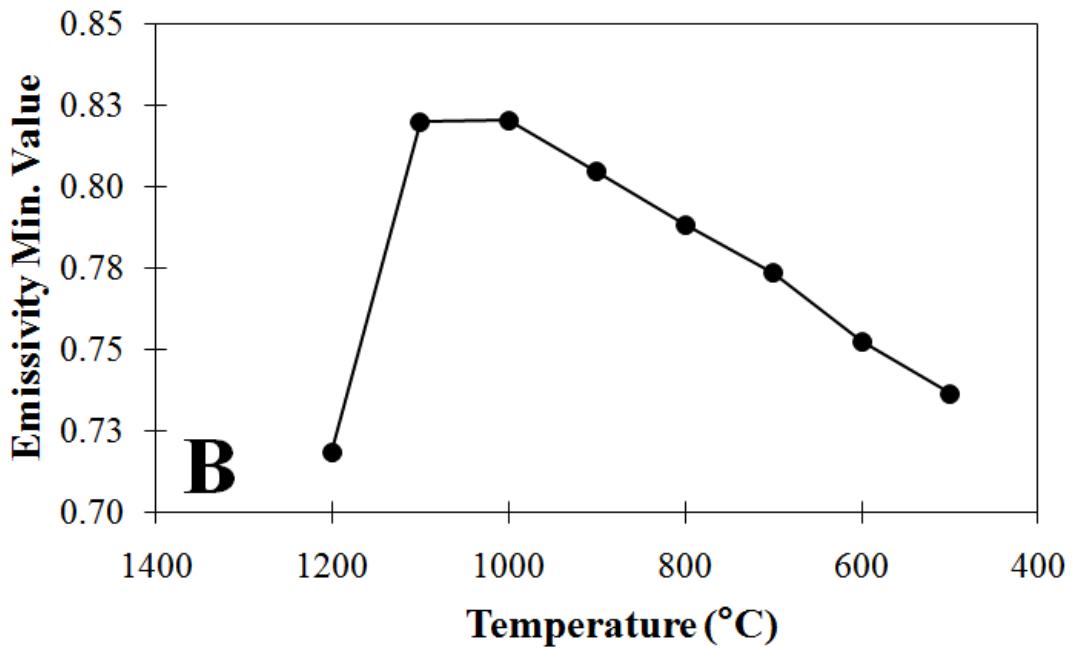
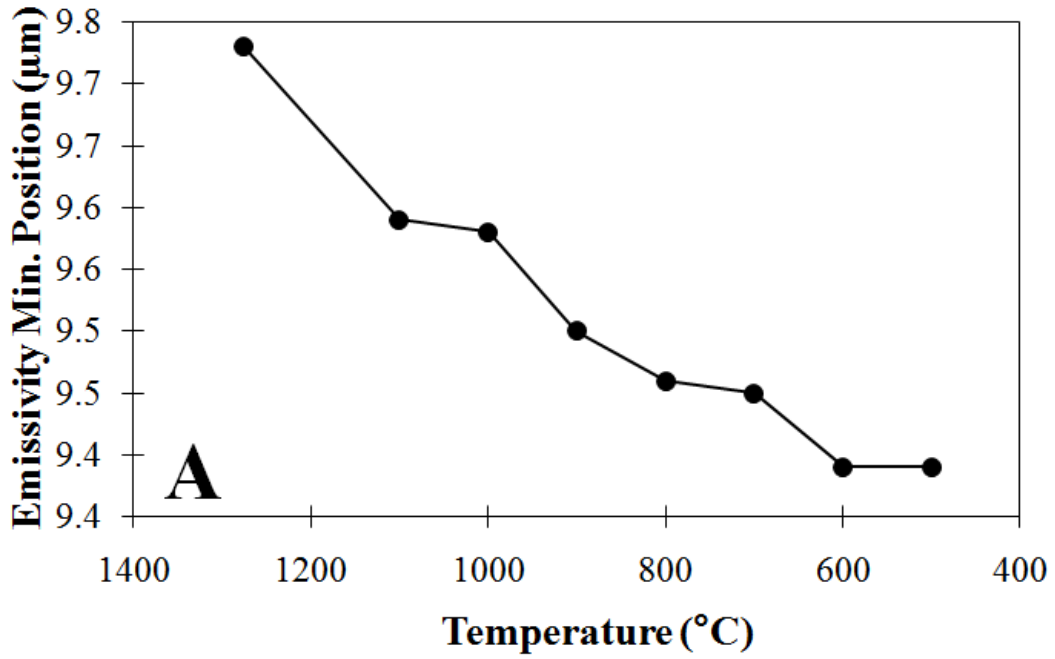


Figure A-12 Change in (A) emissivity minimum position and (B) emissivity minimum value with temperature for glass 19a.

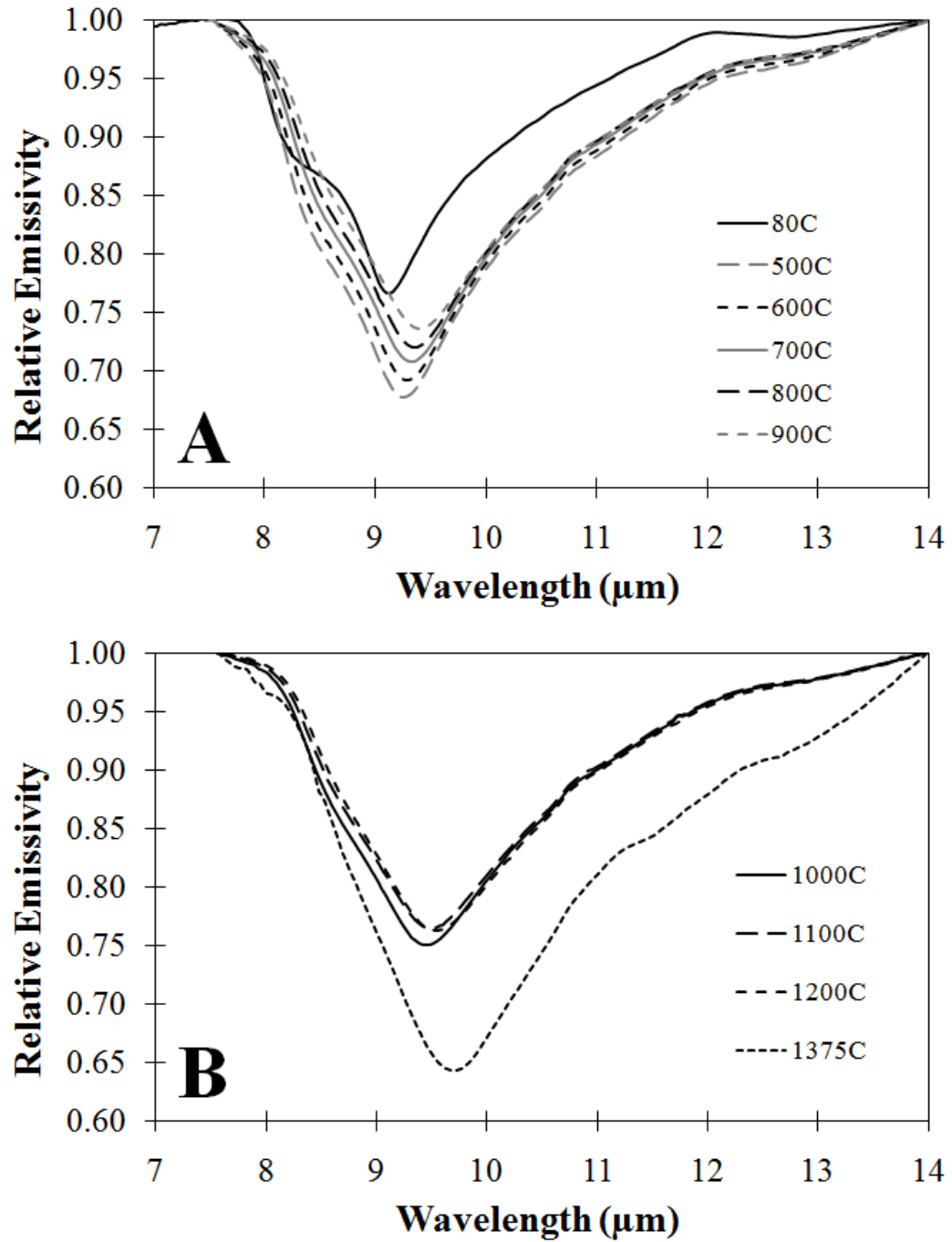


Figure A-13 Relative emissivity spectra for glass 20a from (A) 80 °C to 900 °C and (B) 1000 °C to 1375 °C.

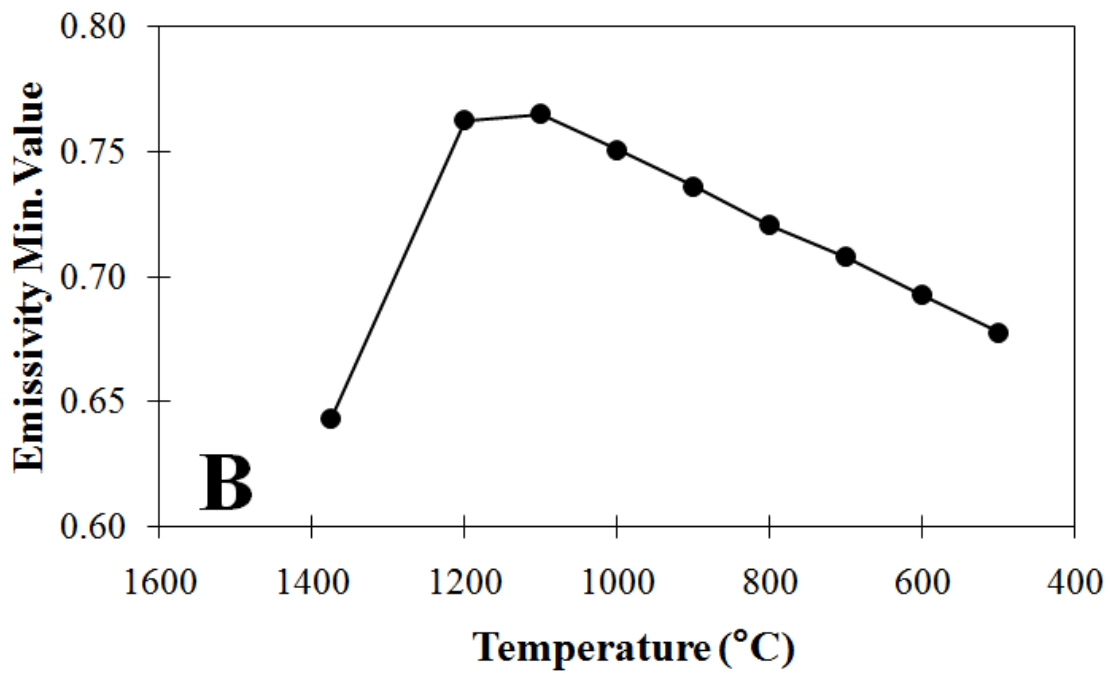
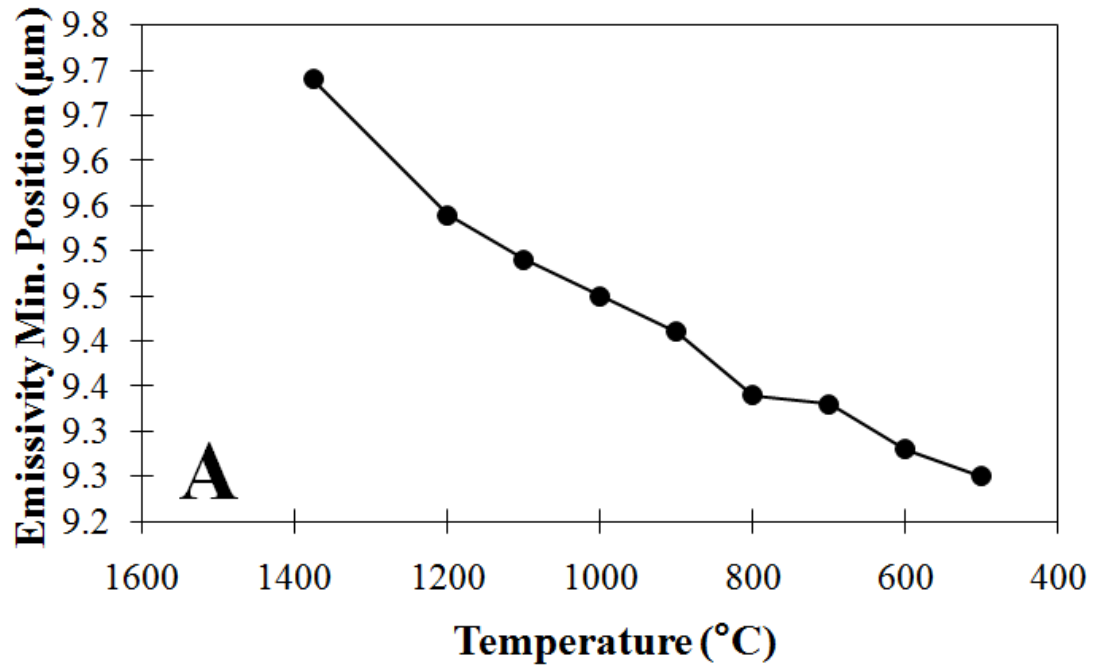


Figure A-14 Change in (A) emissivity minimum position and (B) emissivity minimum value with temperature for glass 20a.

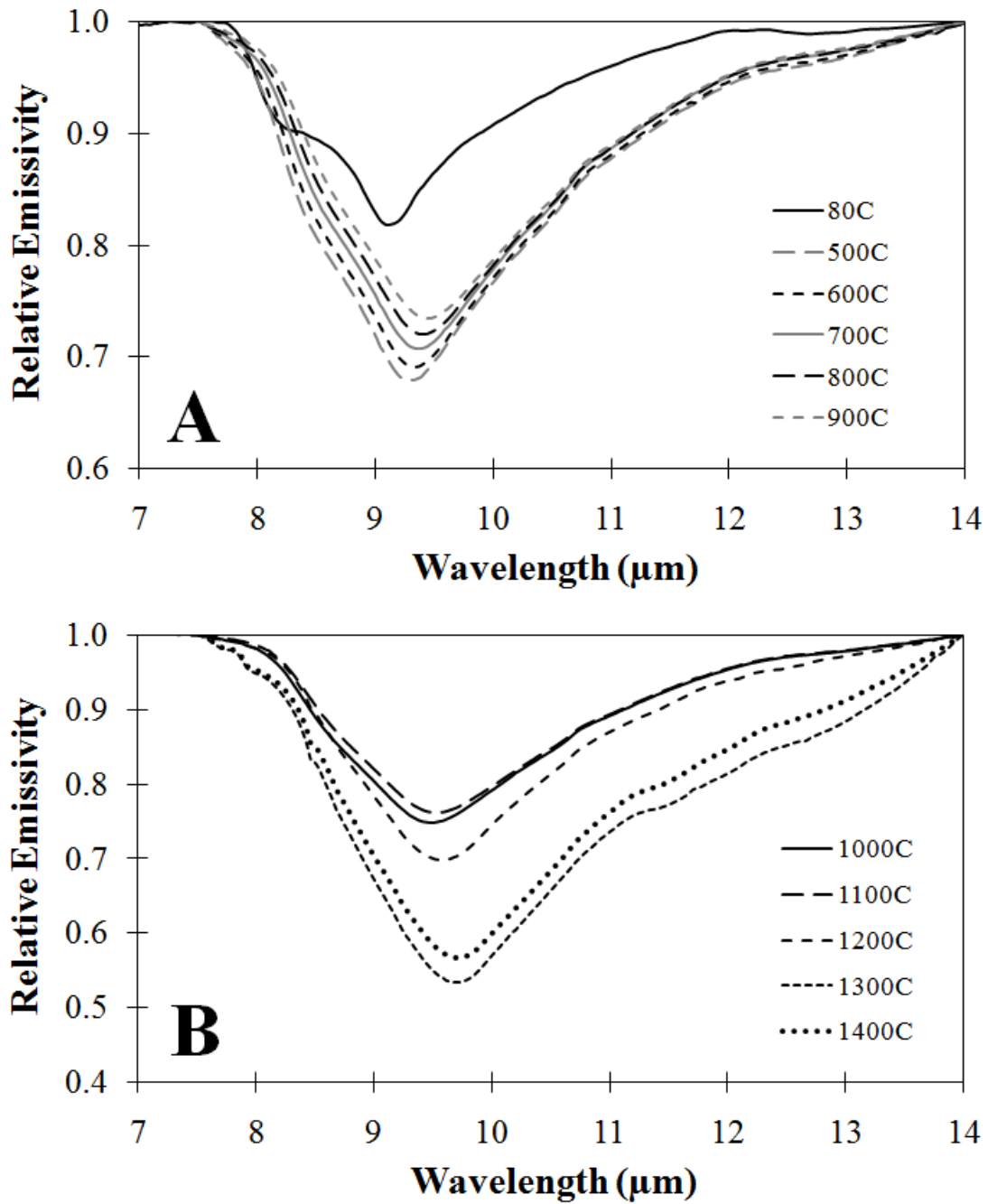


Figure A-15 Relative emissivity spectra for glass 27 from (A) 80 °C to 900 °C and (B) 1000 °C to 1400 °C.

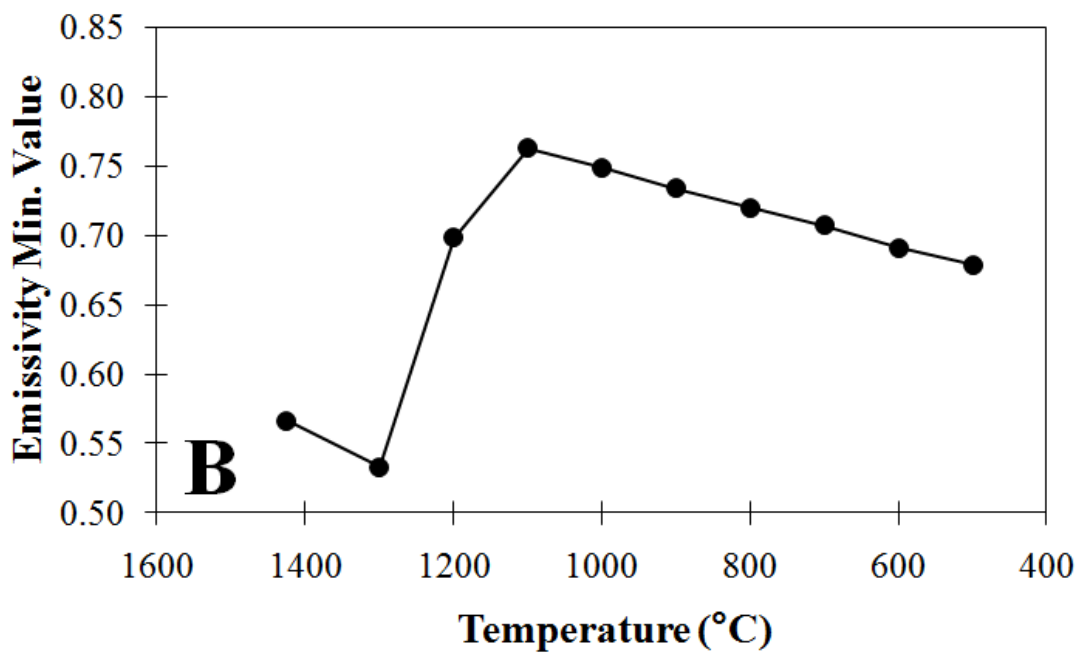
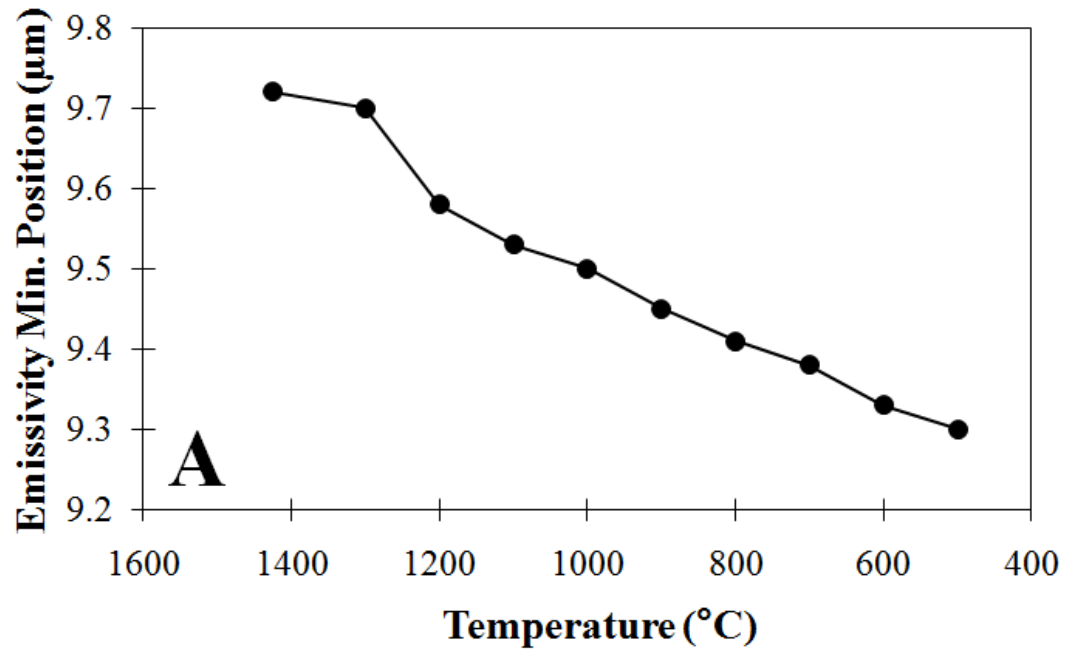


Figure A-16 Change in (A) emissivity minimum position and (B) emissivity minimum value with temperature for glass 27.

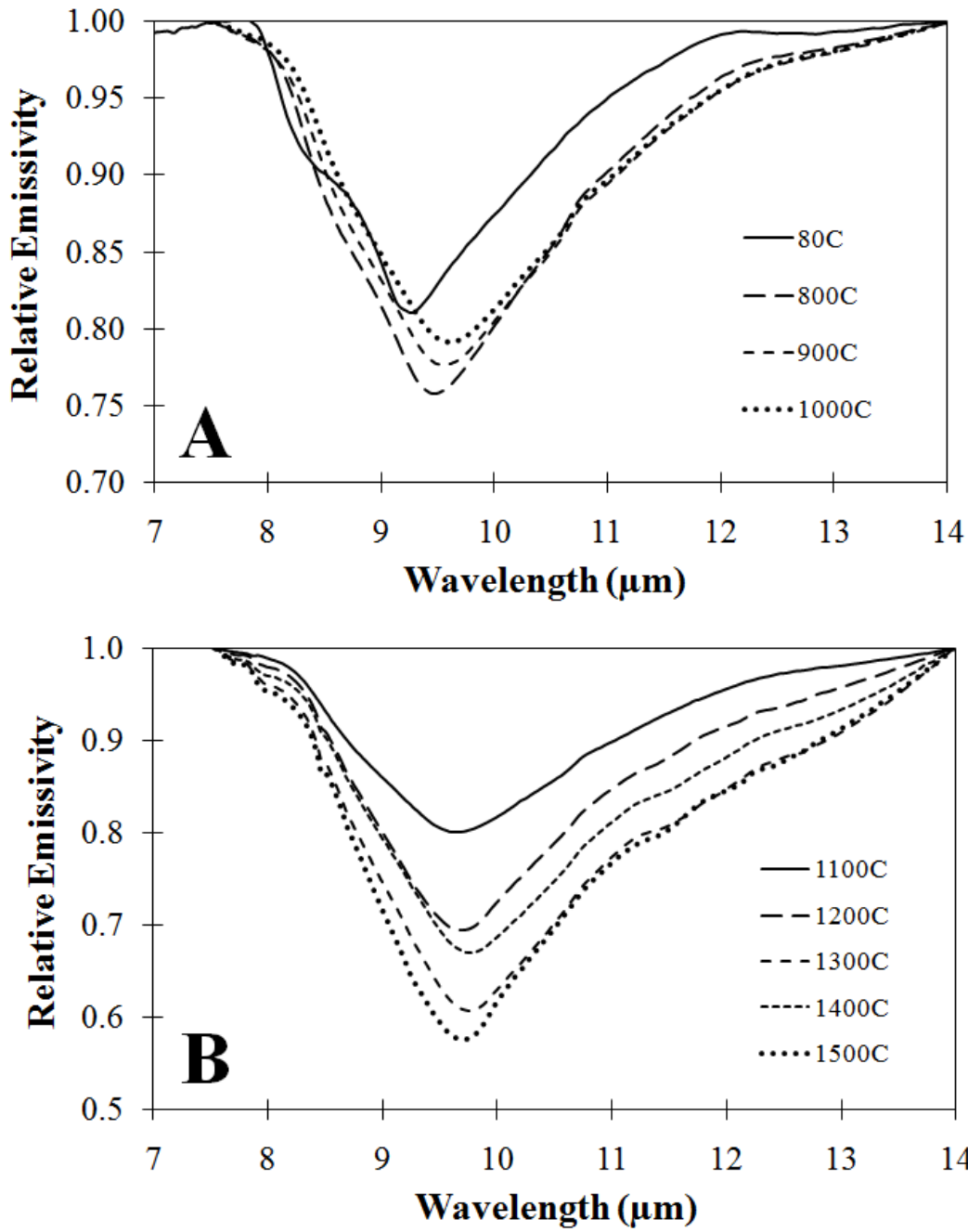


Figure A-17 Relative emissivity spectra for glass 28 from (A) 80 °C to 1000 °C and (B) 1100 °C to 1500 °C.

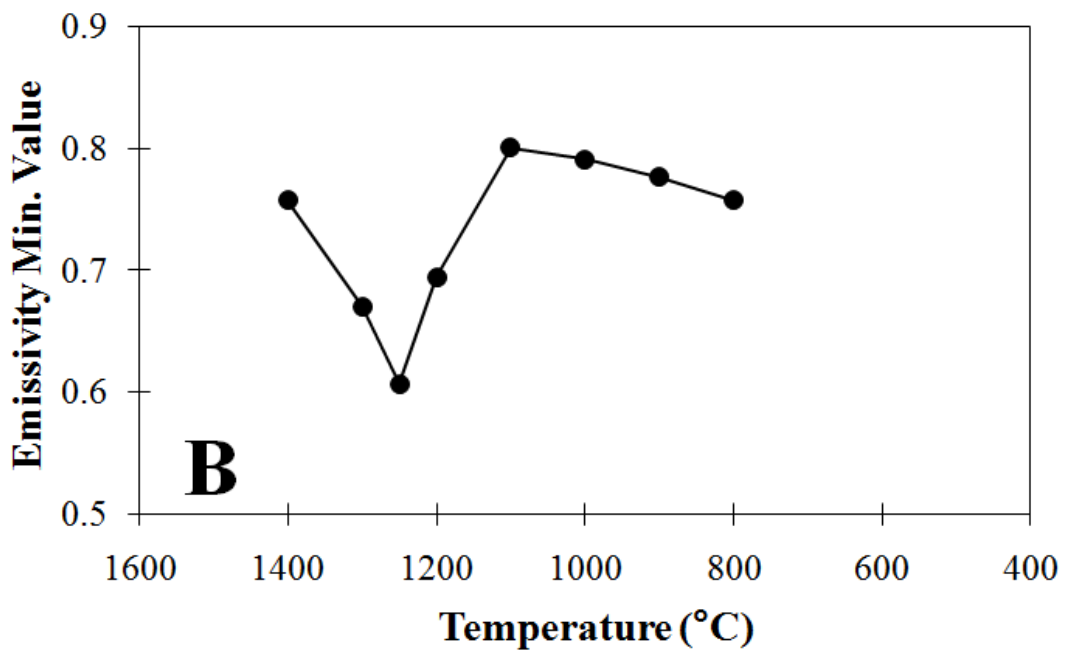
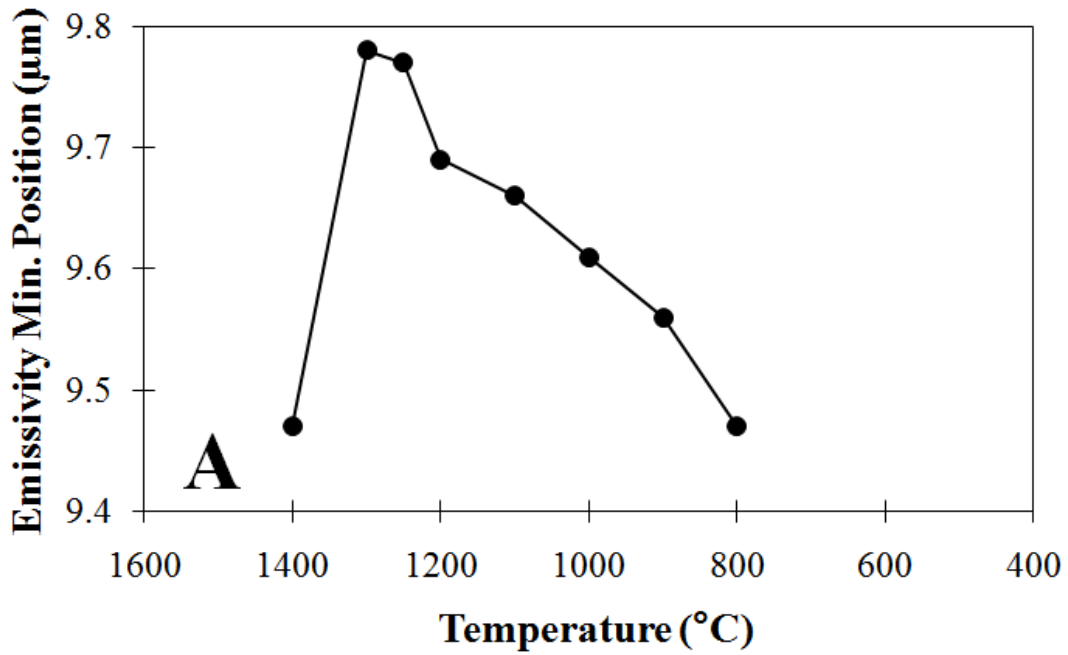


Figure A-18 Change in (A) emissivity minimum position and (B) emissivity minimum value with temperature for glass 28.

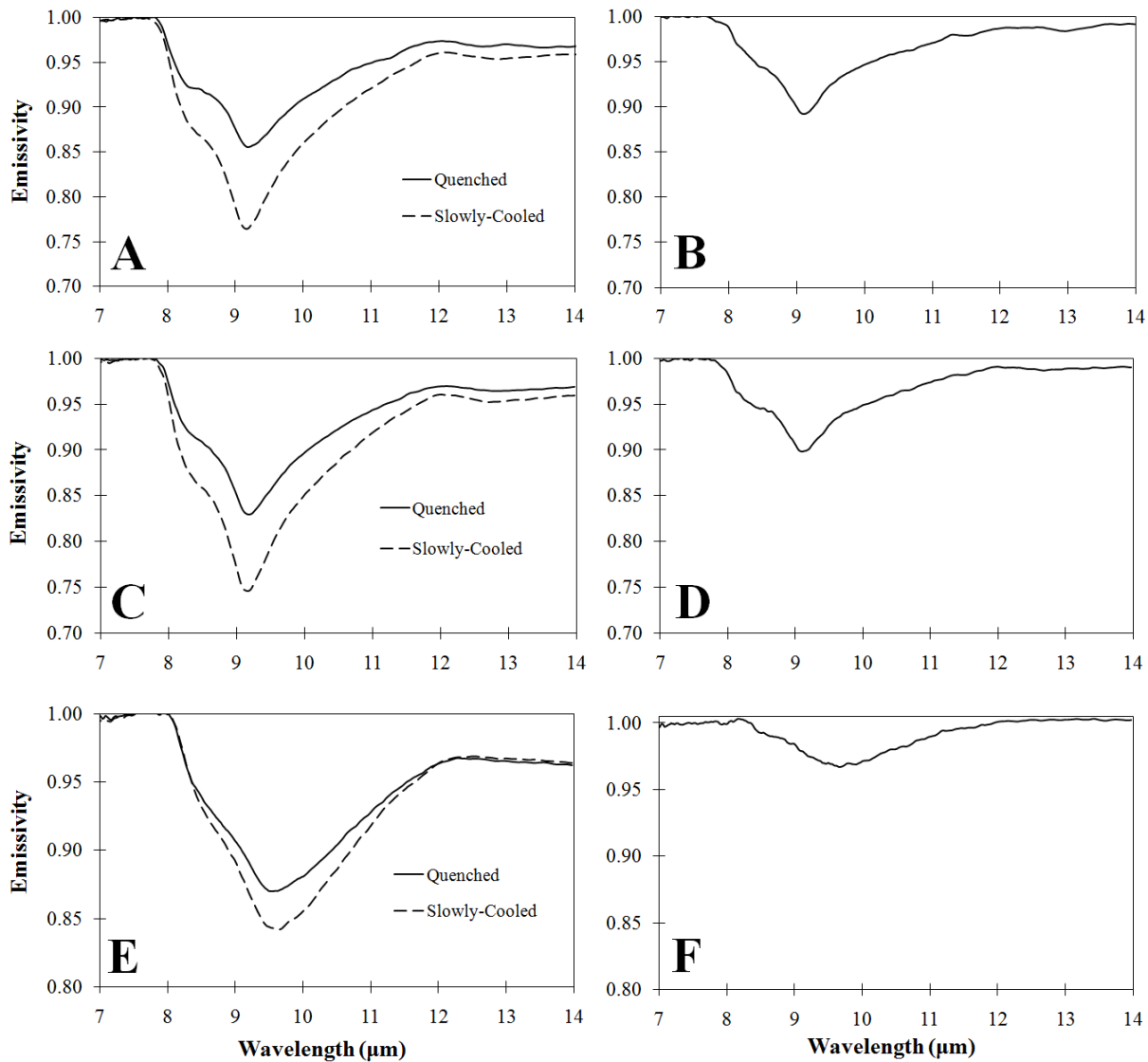


Figure A-19 Comparison of 80 °C quenched glass spectra to 80 °C slowly-cooled glass spectra for (A) glass 2, (C), glass 2a, and (E) glass 3. Slowly-cooled spectra (dotted lines) have deeper emissivity minima than their quenched counterparts (solid lines). The quenched spectrum was divided by the slowly-cooled spectrum for (B) glass 2, (D) glass 2a, and (F) glass 3. In each case, a muted spectral feature with some spectral morphology is apparent at ~9 μm.

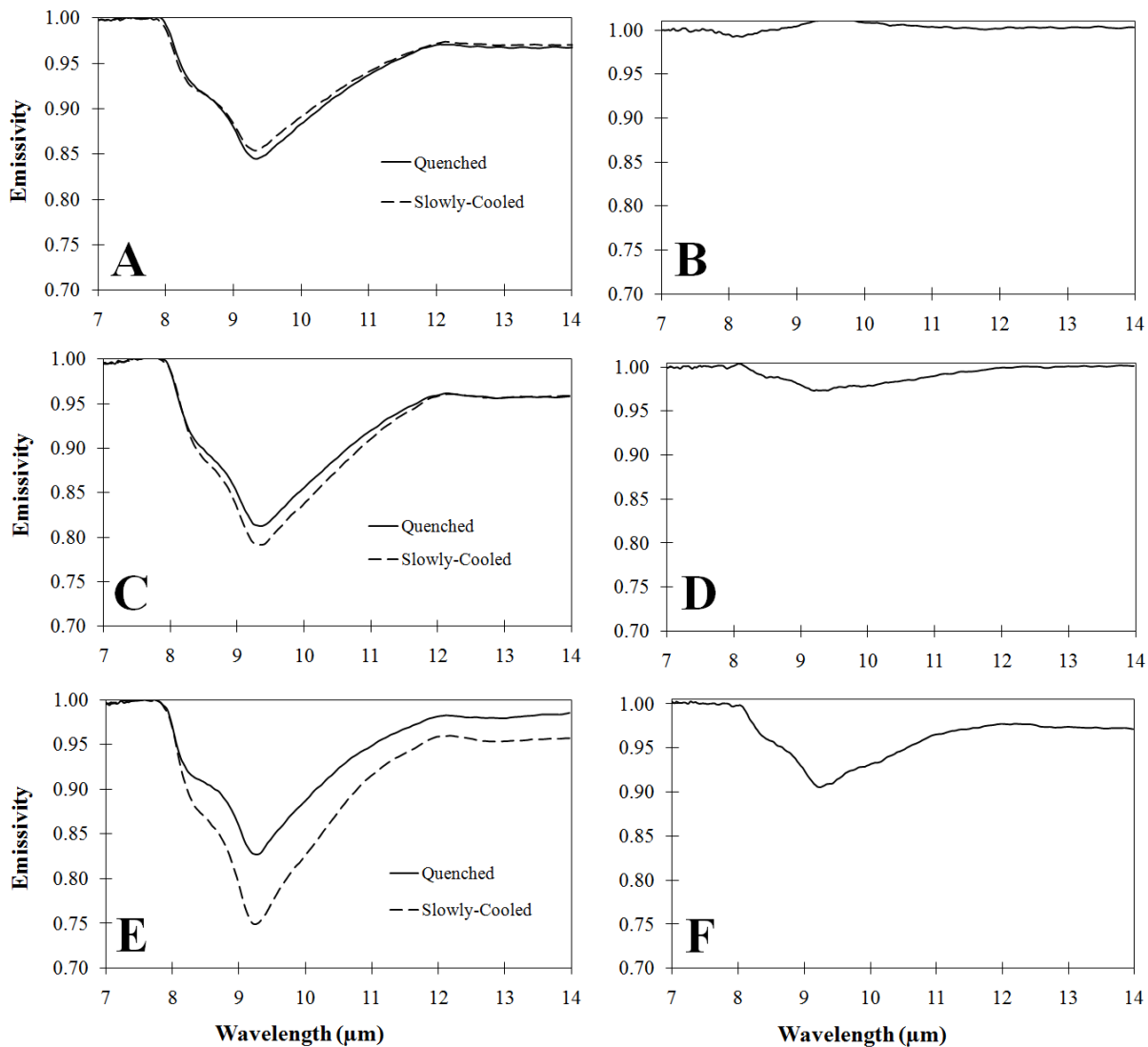


Figure A-20 Comparison of 80 °C quenched glass spectra to 80 °C slowly-cooled glass spectra for (A) glass 6, (C), glass 19, and (E) glass 19a. Slowly-cooled spectra (dotted lines) have deeper emissivity minima than their quenched counterparts (solid lines). The quenched spectrum was divided by the slowly-cooled spectrum for (B) glass 6 (D) glass 19 and (F) glass 19a. In each case, a muted spectral feature with some spectral morphology is apparent at ~9 μm.

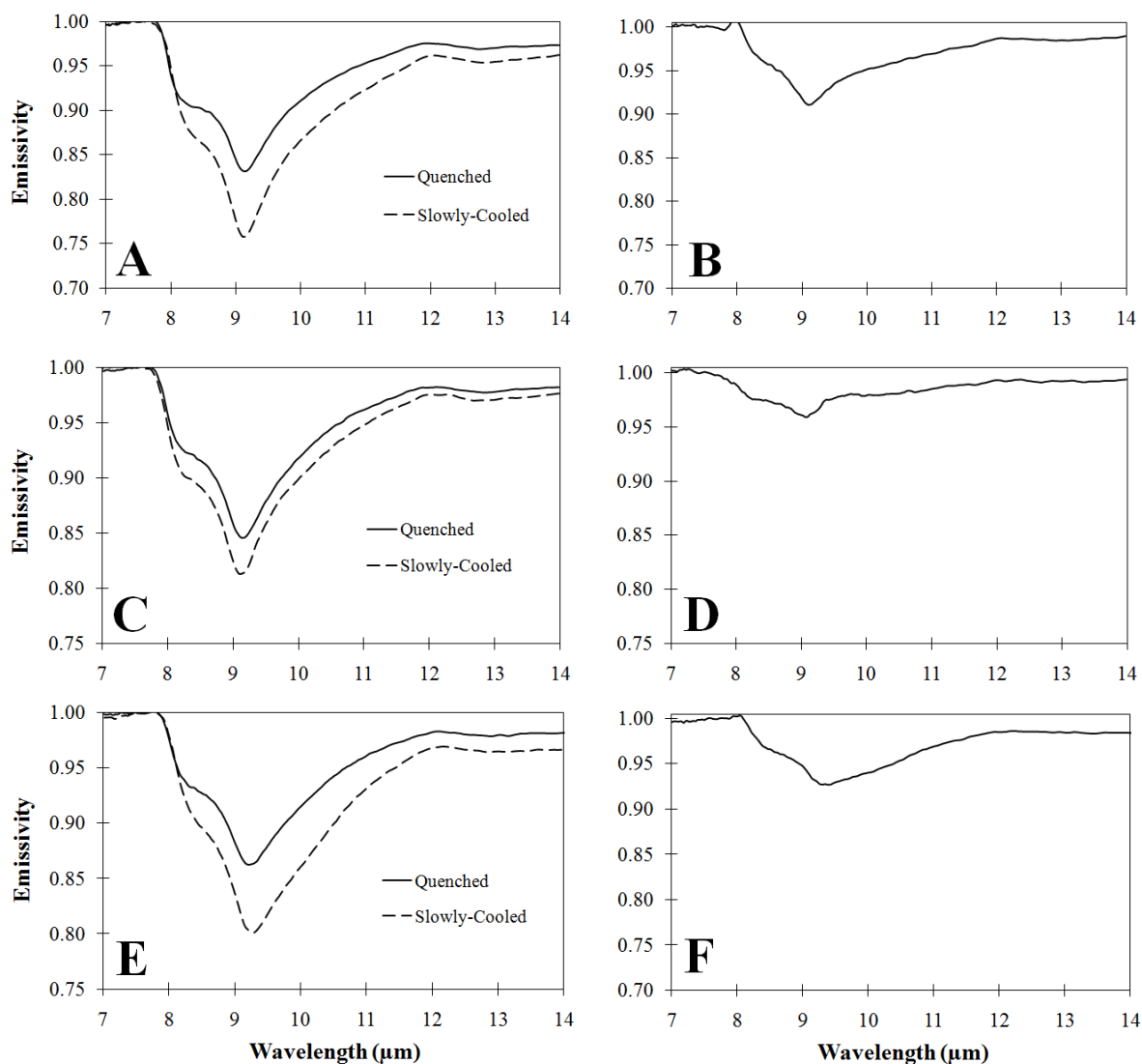


Figure A-21 Comparison of 80 °C quenched glass spectra to 80 °C slowly-cooled glass spectra for (A) glass 20a, (C), glass 27, and (E) glass 28. Slowly-cooled spectra (dotted lines) have deeper emissivity minima than their quenched counterparts (solid lines). The quenched spectrum was divided by the slowly-cooled spectrum for (B) glass 20a, (D) glass 27 and (F) glass 28. In each case, a muted spectral feature with some spectral morphology is apparent at ~9 μm.

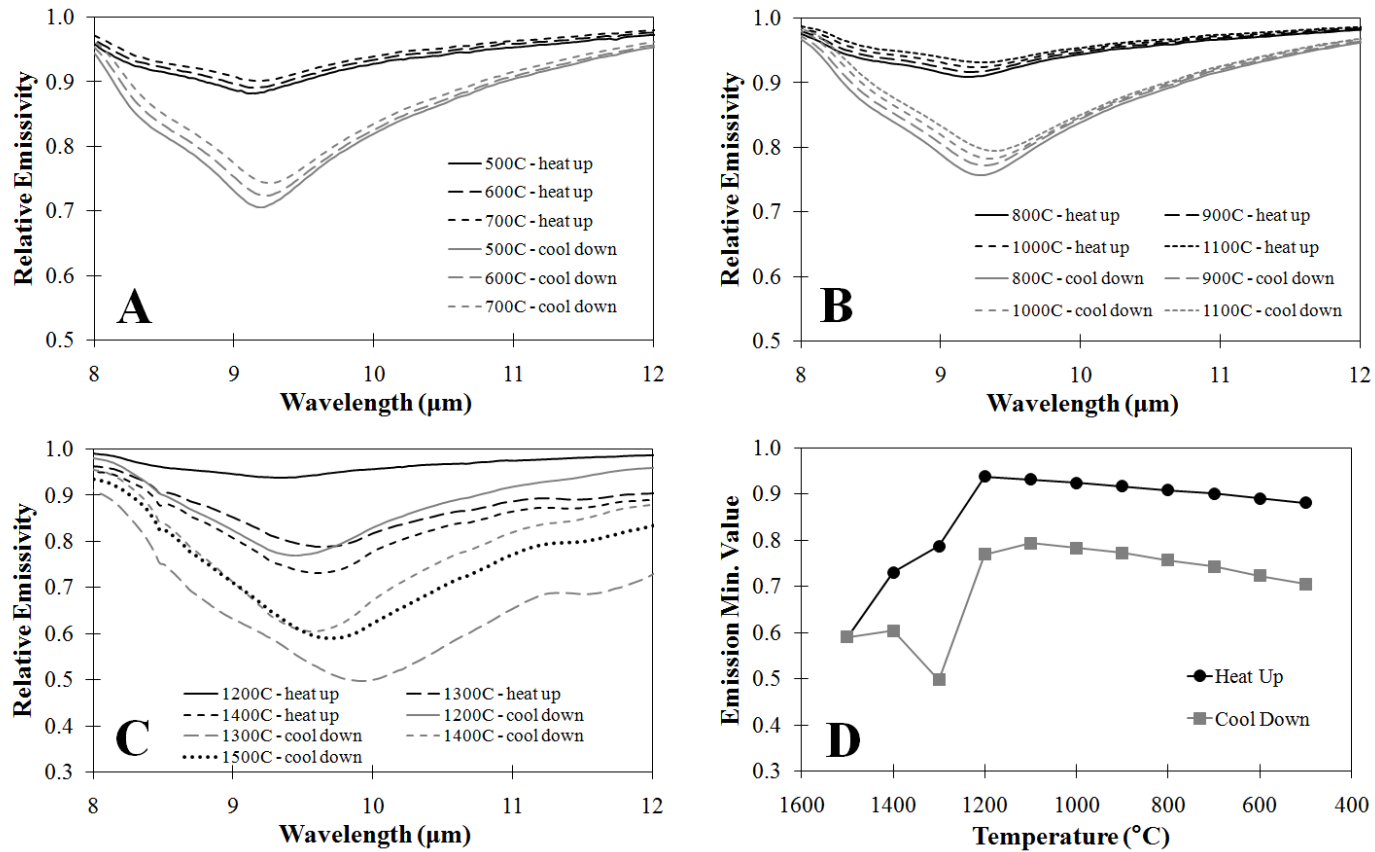


Figure A-22 Glass 21a heat-up vs. cool-down spectra from (A) 500 °C to 700 °C, (B) 800 °C to 1100 °C, and (C) 1200 °C to 1500 °C. At temperatures 1100 °C and below, the cool-down spectrum at a given temperature is more muted than the corresponding heat-up spectrum. During heat-up, the emissivity minimum values increase and emissivity minimum positions shift to longer wavelengths with increasing temperature. During cool-down, emissivity minimum values decrease and emissivity minimum positions shift to shorter wavelengths with decreasing temperature. The difference in emissivity minimum value between heat-up and cool-down spectra is shown in (D). At temperatures above 1200 °C, the emissivity minimum values of the heat-up and cool-down spectra are more variable and non-linear with temperature.

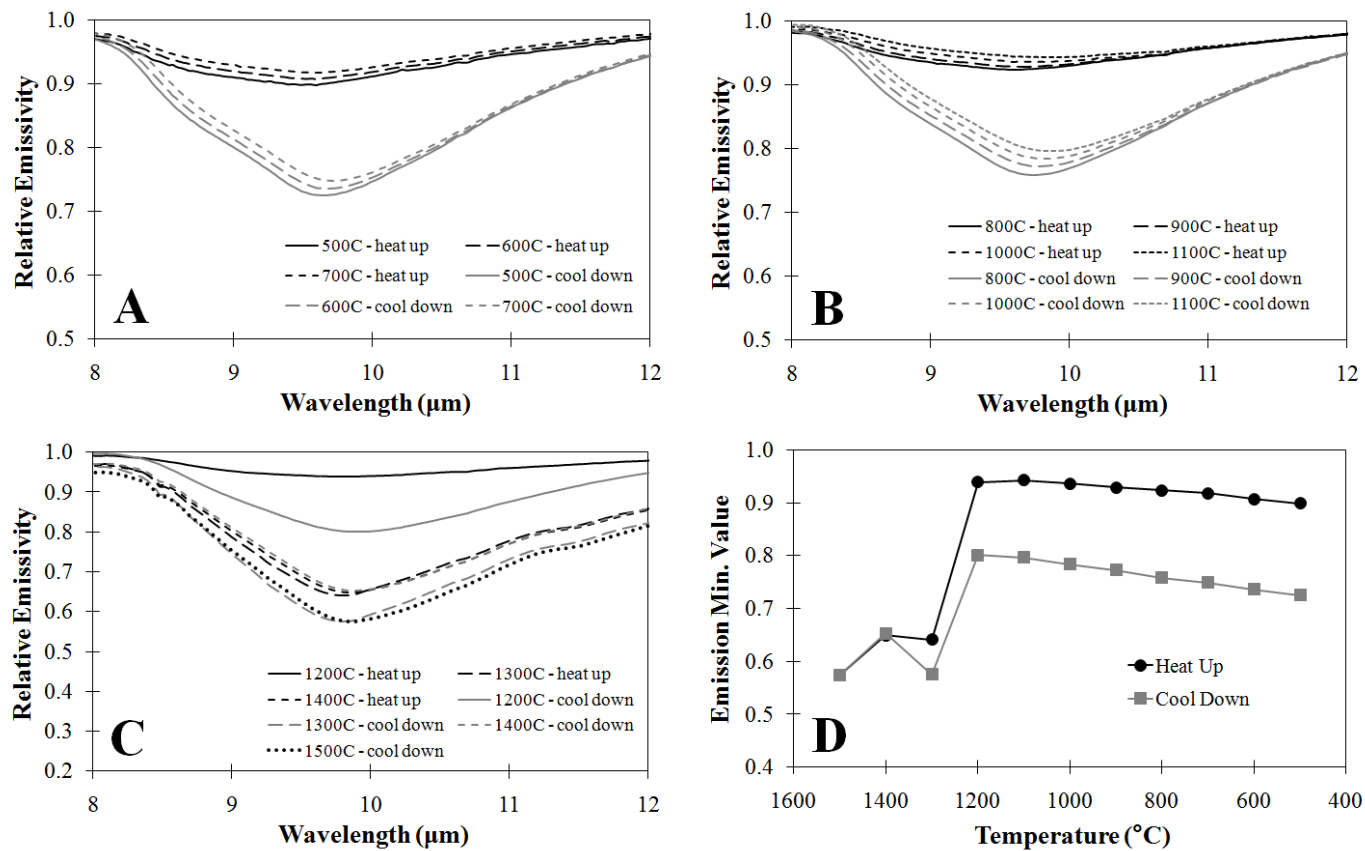


Figure A-23 Glass 24 heat-up vs. cool-down spectra from (A) 500 °C to 700 °C, (B) 800 °C to 1100 °C, and (C) 1200 °C to 1500 °C. At temperatures 1100 °C and below, the cool-down spectrum at a given temperature is more muted than the corresponding heat-up spectrum. During heat-up, the emissivity minimum values increase and emissivity minimum positions shift to longer wavelengths with increasing temperature. During cool-down, emissivity minimum values decrease and emissivity minimum positions shift to shorter wavelengths with decreasing temperature. The difference in emissivity minimum value between heat-up and cool-down spectra is shown in (D). At temperatures above 1200 °C, the emissivity minimum values of the heat-up and cool-down spectra are more variable and non-linear with temperature.

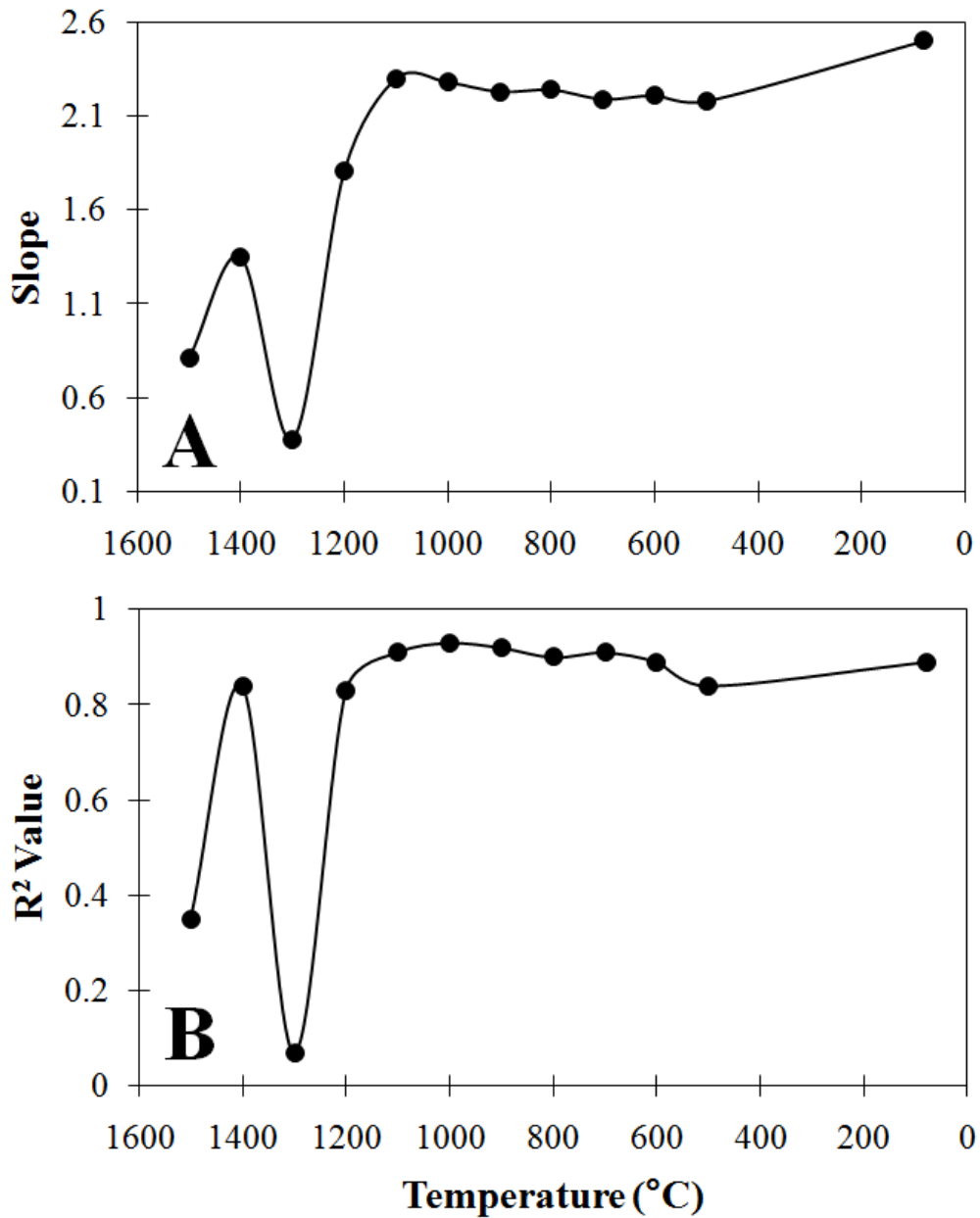


Figure A-24 Change in slope and R^2 value with temperature for the Al / [Al+Si] vs. emissivity minimum position plots in Figures 4-23 and 4-24. Slope and R^2 values are variable above 1200 °C. The low point at 1300 °C is attributed to the greater degree of variability in the data at this temperature as compared to the other temperatures. The low point at 1500 °C is due to the lack of data at this temperature, as only 5 of the glasses needed to reach a temperature of 1500 °C in order to fully melt. Both slope and R^2 values are near-linear from 1100 °C to 80 °C.

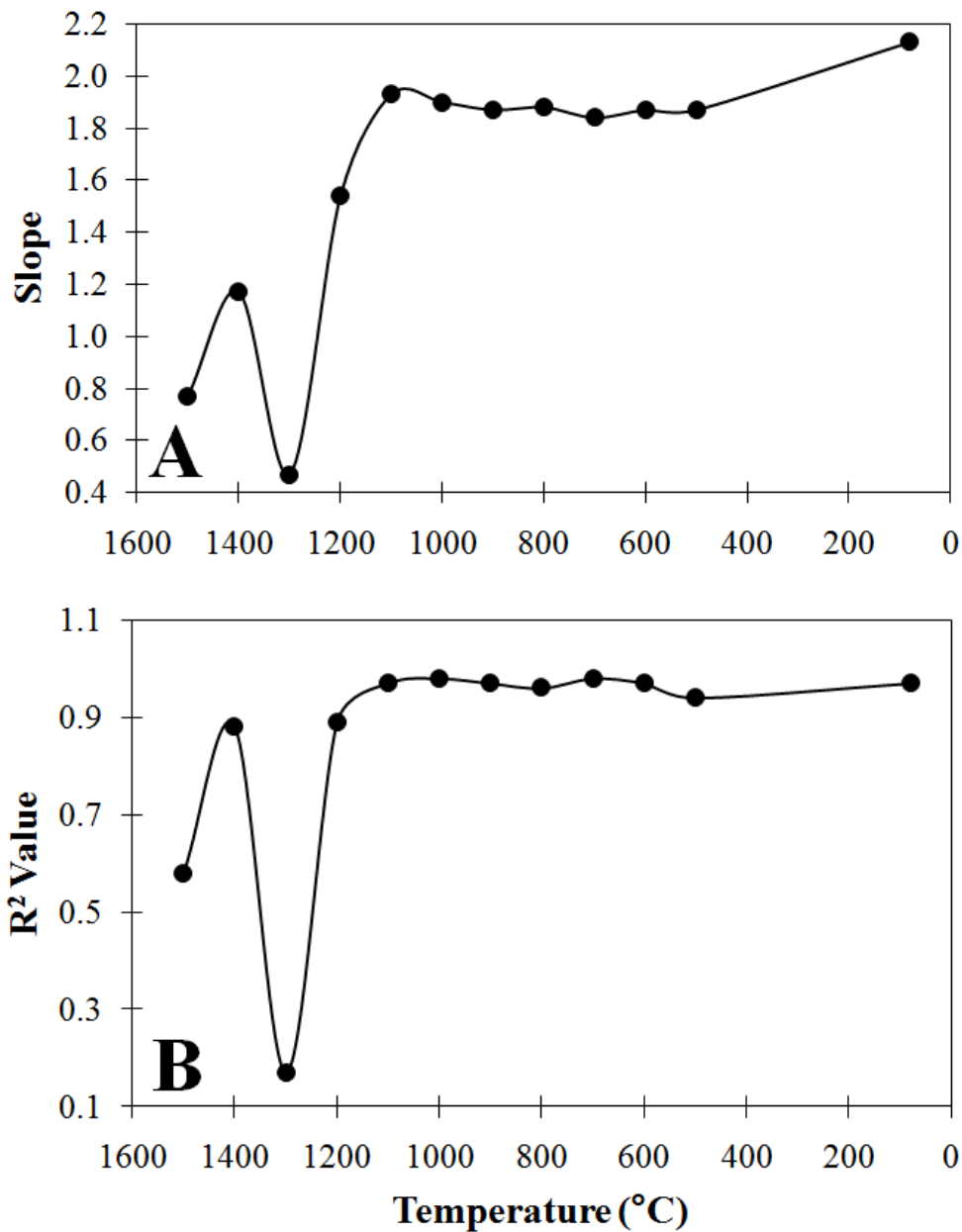


Figure A-25 Change in slope and R² value with temperature for the [Na+Ca] / Si vs. emissivity minimum position plots in Figures 4-25 and 4-26. Slope and R² values are variable above 1200 °C. The low point at 1300 °C is attributed to the greater degree of variability in the data at this temperature as compared to the other temperatures. The low point at 1500 °C is due to the lack of data at this temperature, as only 5 of the glasses needed to reach a temperature of 1500 °C in order to fully melt. Both slope and R² values are near-linear from 1100 °C to 80 °C.

APPENDIX B

MASTER- AND FLIR - DEGRADED EMISSION SPECTRA OF SYNTHETIC GLASSES

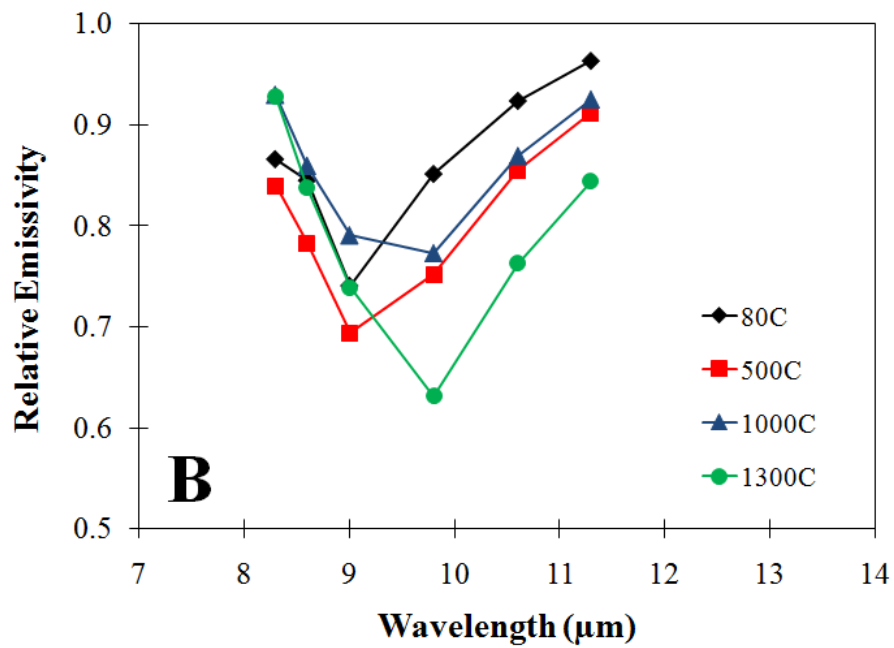
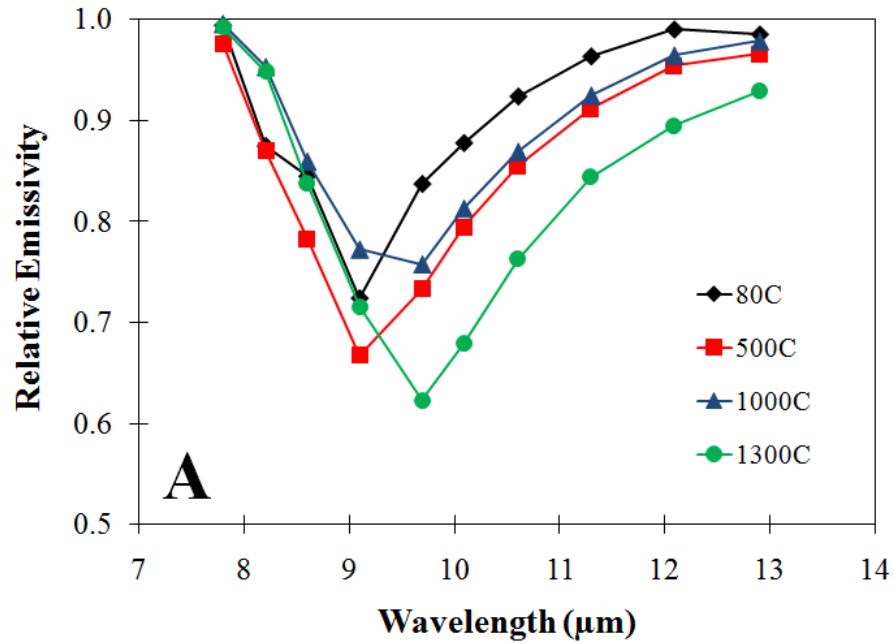


Figure B-1 (A) MASTER-degraded emission spectra of glass 1a at 80 °C, 500 °C, 1000 °C, and 1300 °C. (B) FLIR-degraded emission spectra of glass 1a at 80 °C, 500 °C, 1000 °C, and 1300 °C.

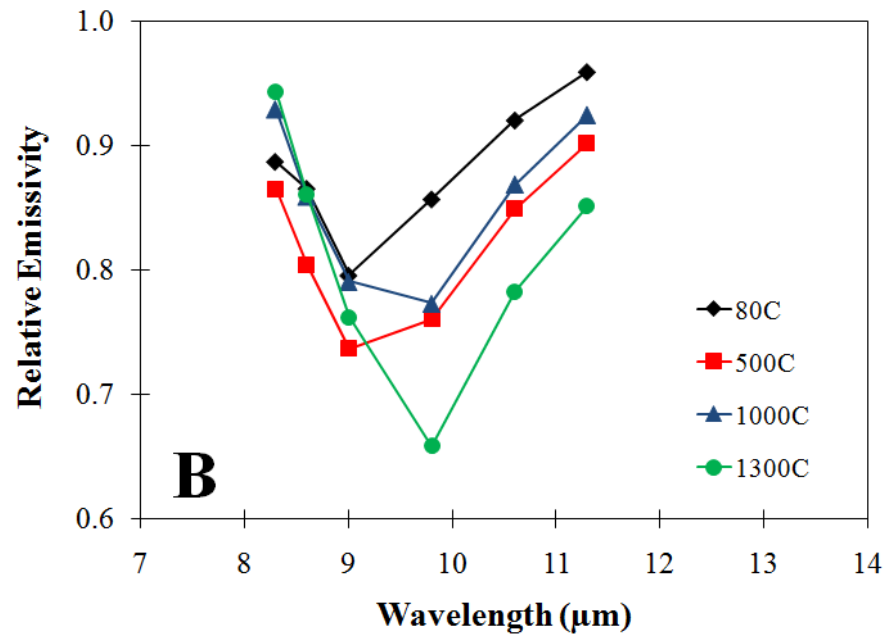
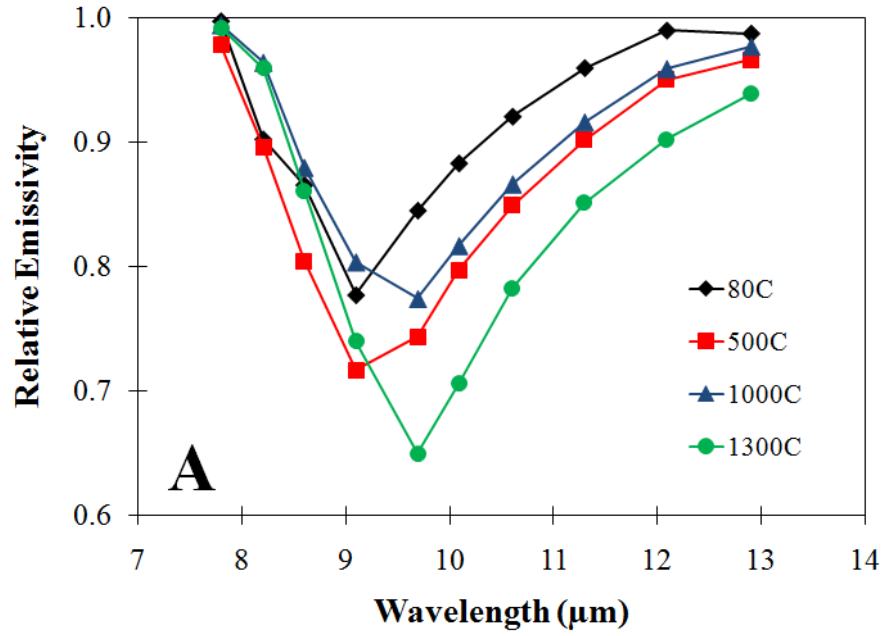


Figure B-2 (A) MASTER-degraded emission spectra of glass 2 at 80 °C, 500 °C, 1000 °C, and 1300 °C. (B) FLIR-degraded emission spectra of glass 2 at 80 °C, 500 °C, 1000 °C, and 1300 °C.

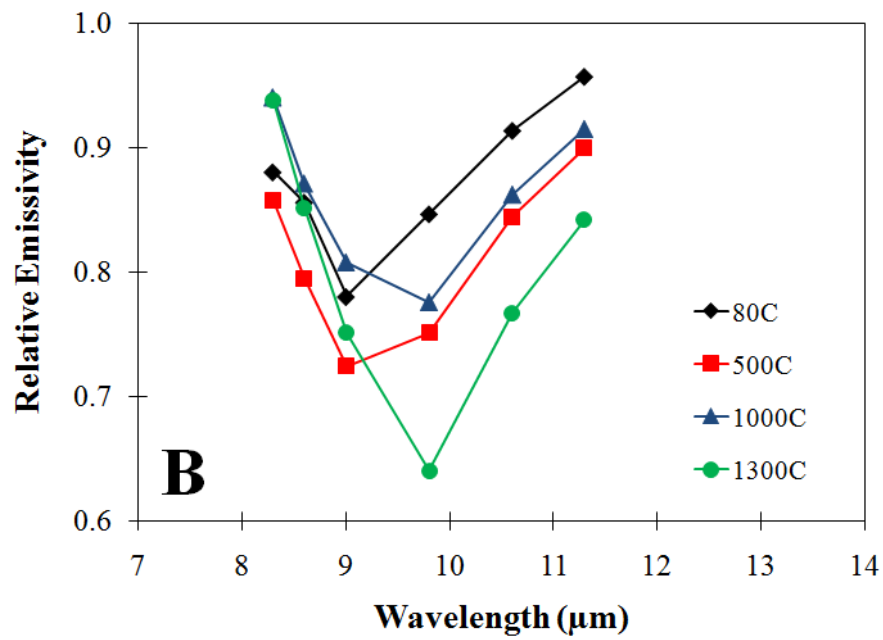
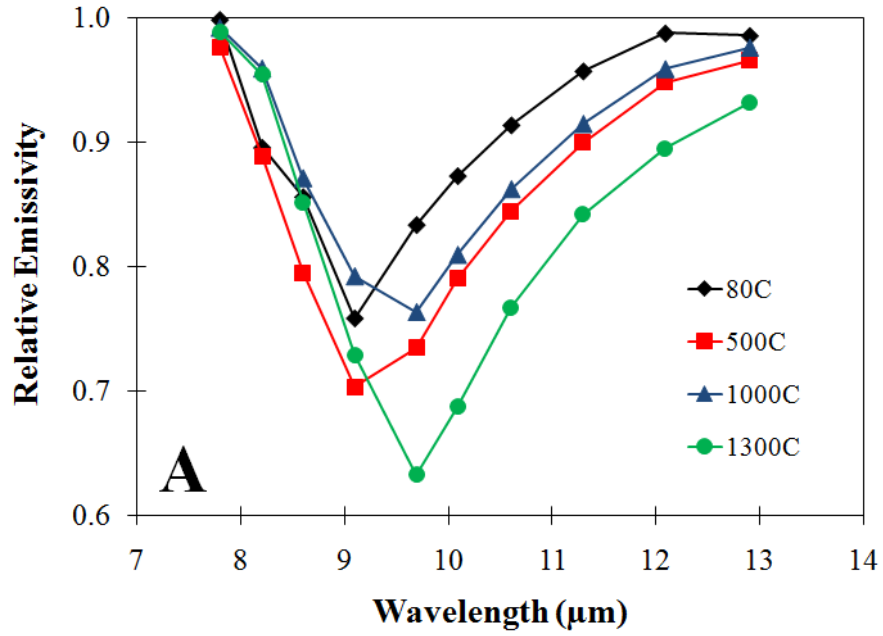


Figure B-3 (A) MASTER-degraded emission spectra of glass 2a at 80 °C, 500 °C, 1000 °C, and 1300 °C. (B) FLIR-degraded emission spectra of glass 2a at 80 °C, 500 °C, 1000 °C, and 1300 °C.

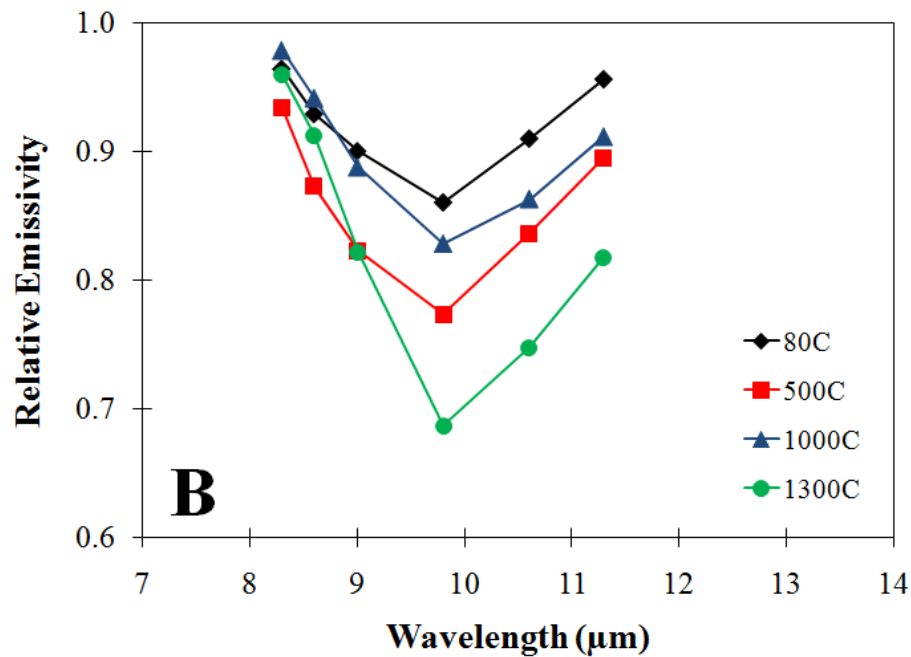
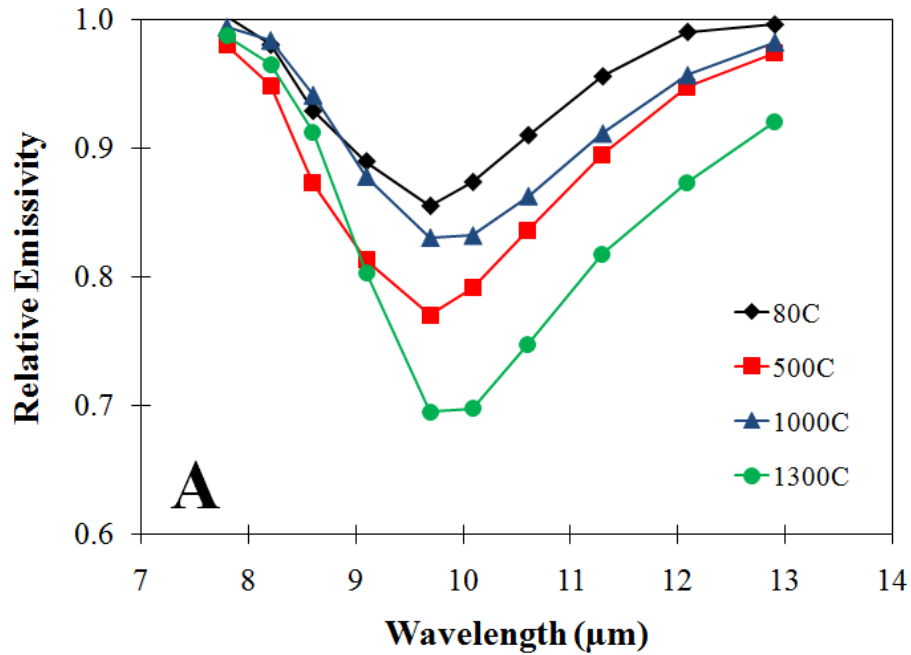


Figure B-4 (A) MASTER-degraded emission spectra of glass 3 at 80 °C, 500 °C, 1000 °C, and 1300 °C. (B) FLIR-degraded emission spectra of glass 3 at 80 °C, 500 °C, 1000 °C, and 1300 °C.

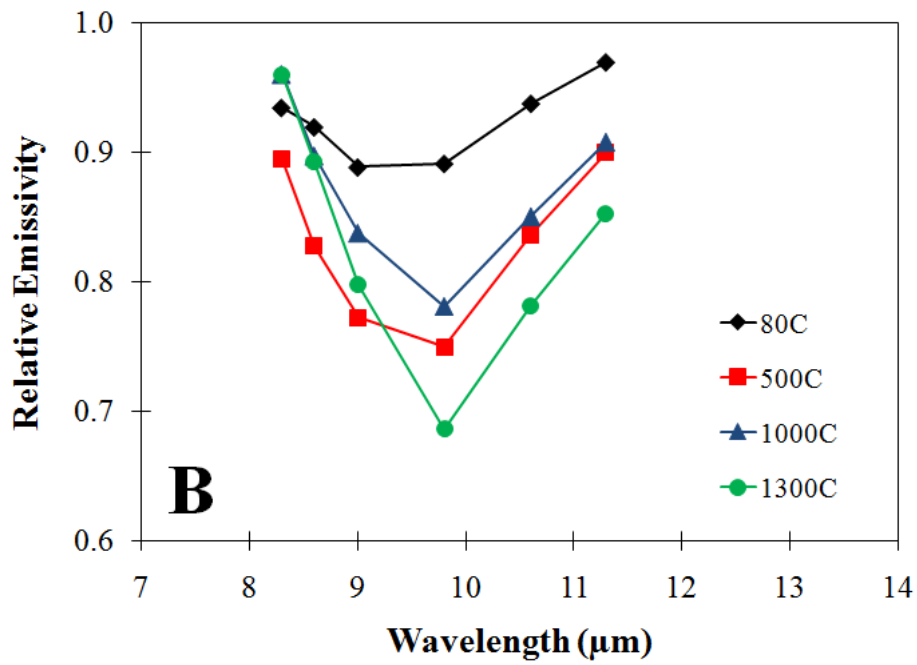
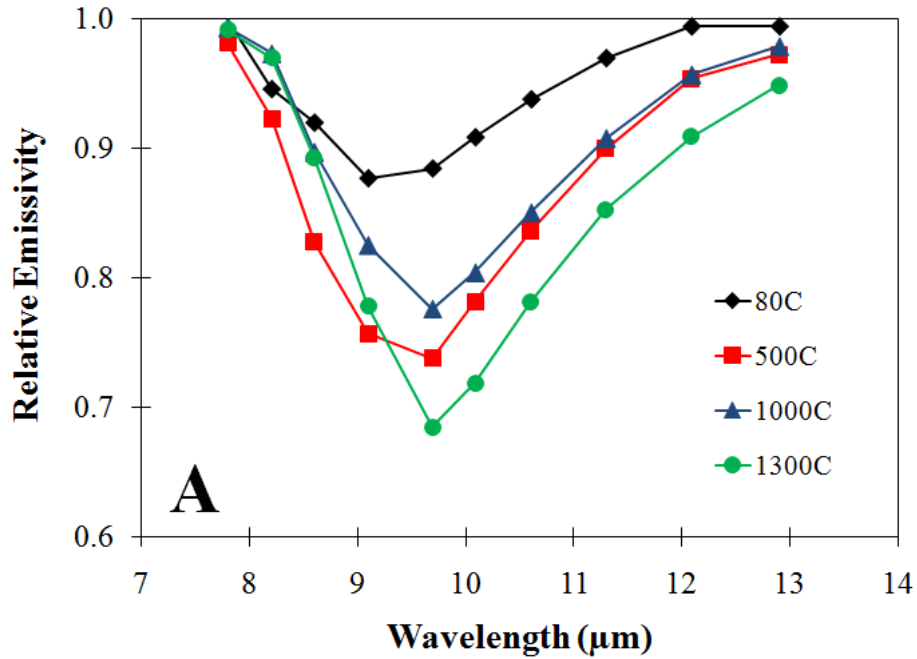


Figure B-5 (A) MASTER-degraded emission spectra of glass 6 at 80 °C, 500 °C, 1000 °C, and 1300 °C. (B) FLIR-degraded emission spectra of glass 6 at 80 °C, 500 °C, 1000 °C, and 1300 °C.

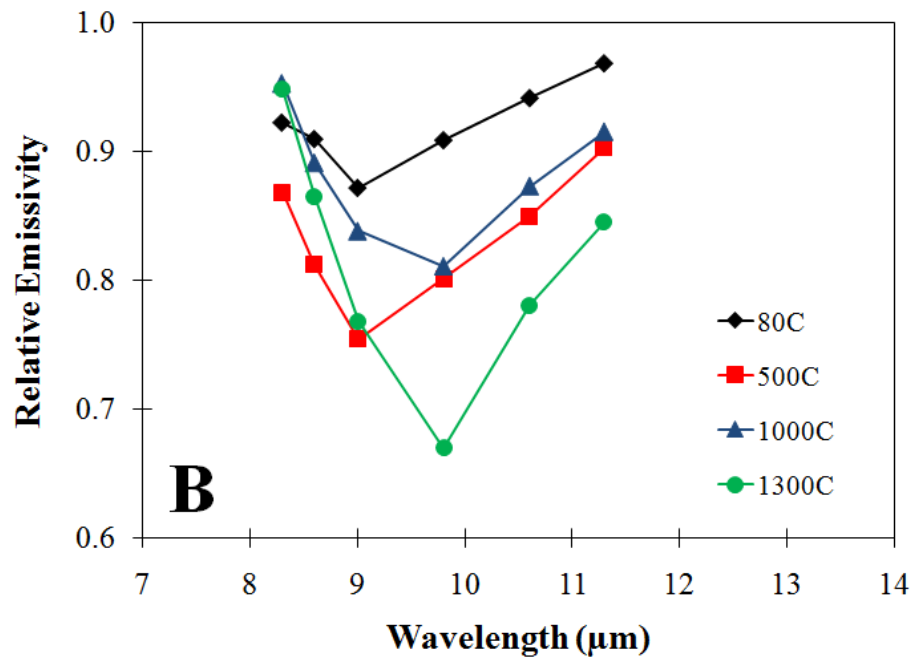
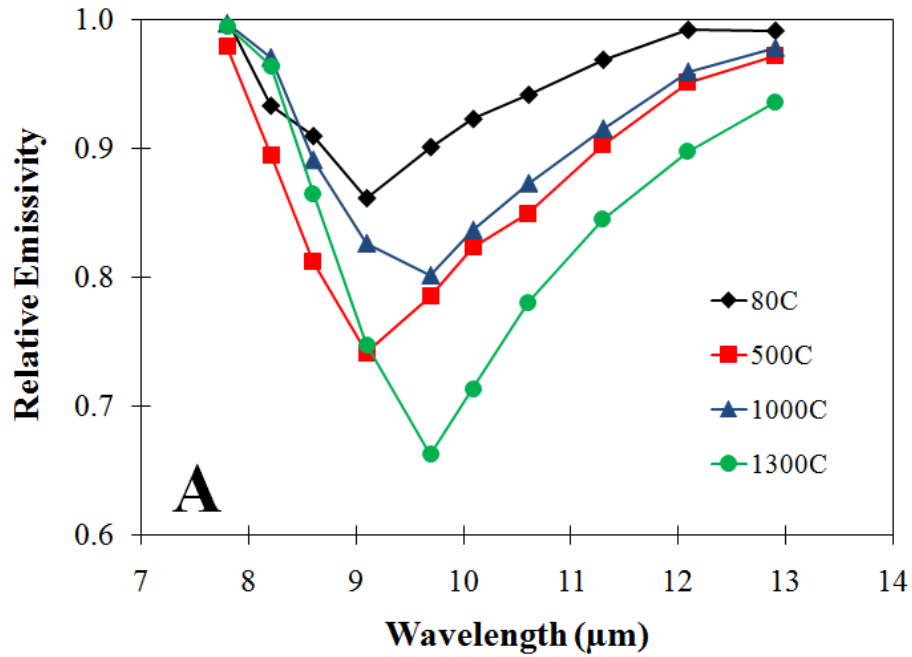


Figure B-6 (A) MASTER-degraded emission spectra of glass 7 at 80 °C, 500 °C, 1000 °C, and 1300 °C. (B) FLIR-degraded emission spectra of glass 7 at 80 °C, 500 °C, 1000 °C, and 1300 °C.

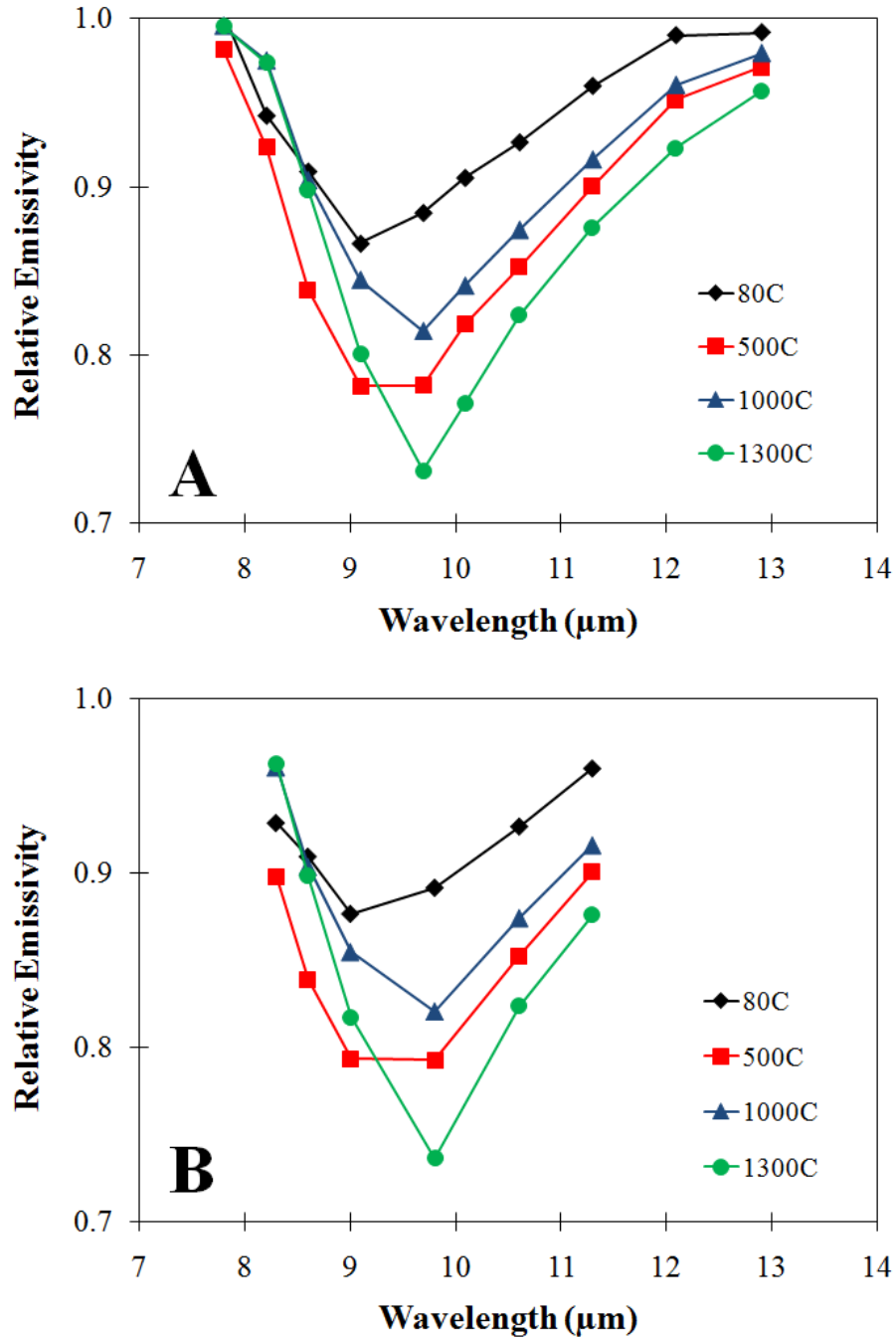


Figure B-7 (A) MASTER-degraded emission spectra of glass 8 at 80 °C, 500 °C, 1000 °C, and 1300 °C. (B) FLIR-degraded emission spectra of glass 8 at 80 °C, 500 °C, 1000 °C, and 1300 °C.

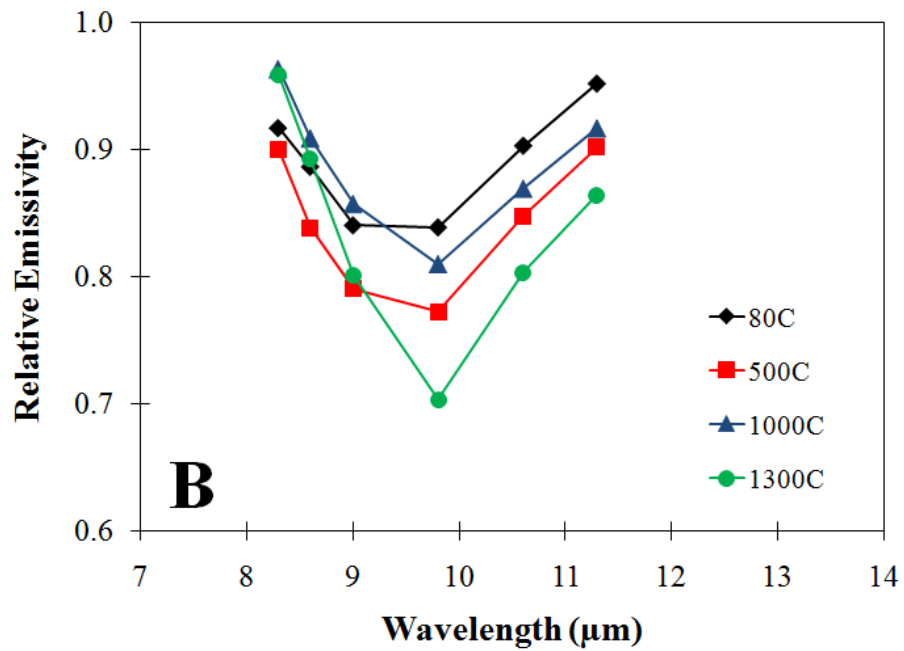
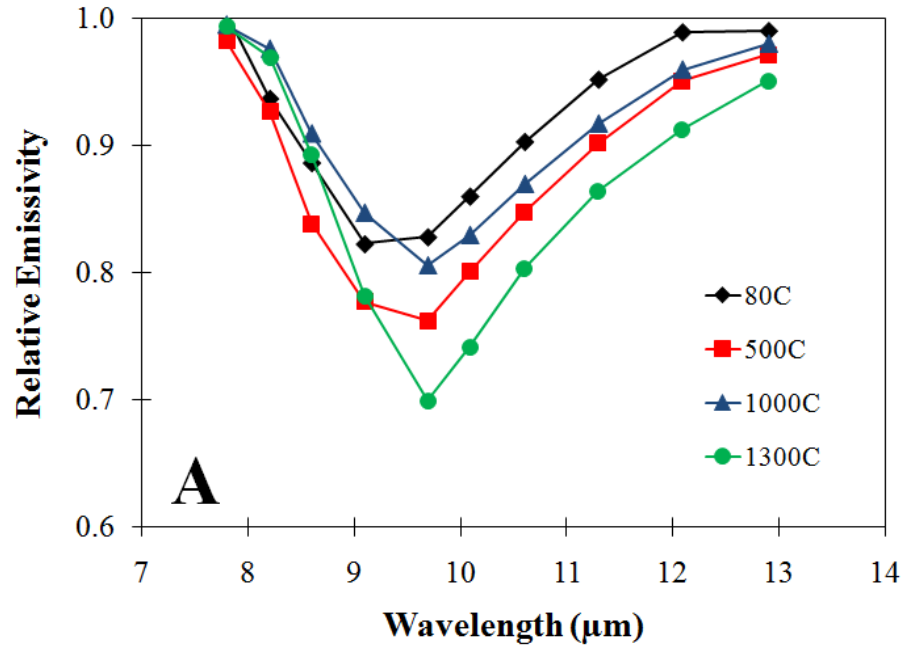


Figure B-8 (A) MASTER-degraded emission spectra of glass 19 at 80 °C, 500 °C, 1000 °C, and 1300 °C. (B) FLIR-degraded emission spectra of glass 19 at 80 °C, 500 °C, 1000 °C, and 1300 °C.

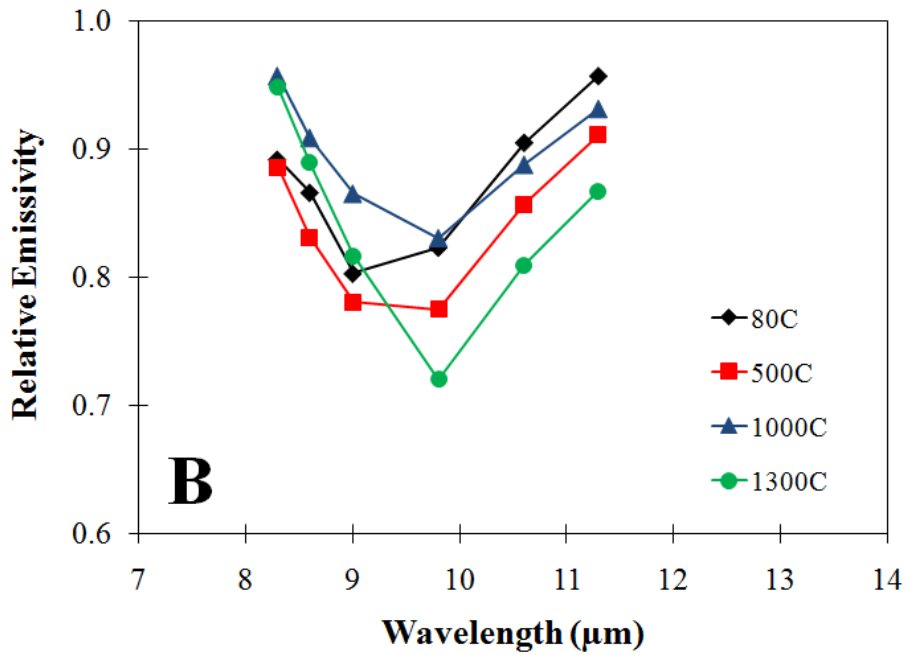
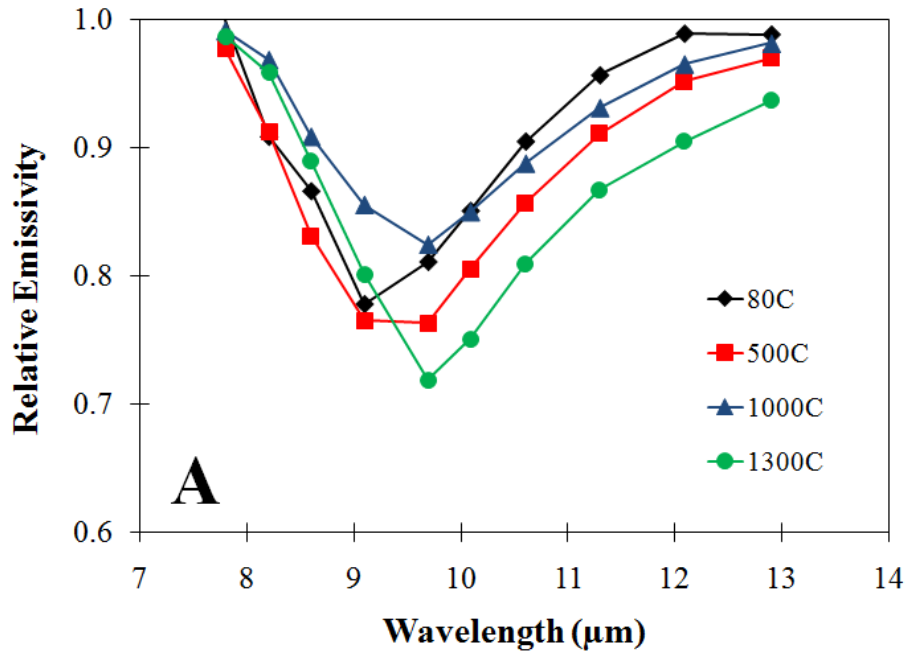


Figure B-9 (A) MASTER-degraded emission spectra of glass 19a at 80 °C, 500 °C, 1000 °C, and 1300 °C. (B) FLIR-degraded emission spectra of glass 19a at 80 °C, 500 °C, 1000 °C, and 1300 °C.

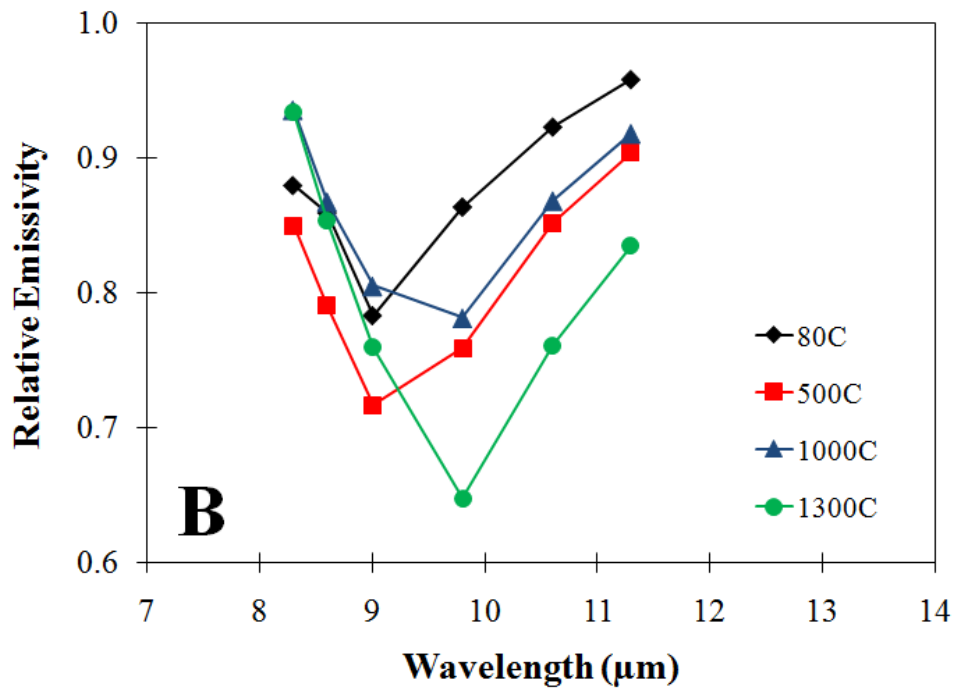
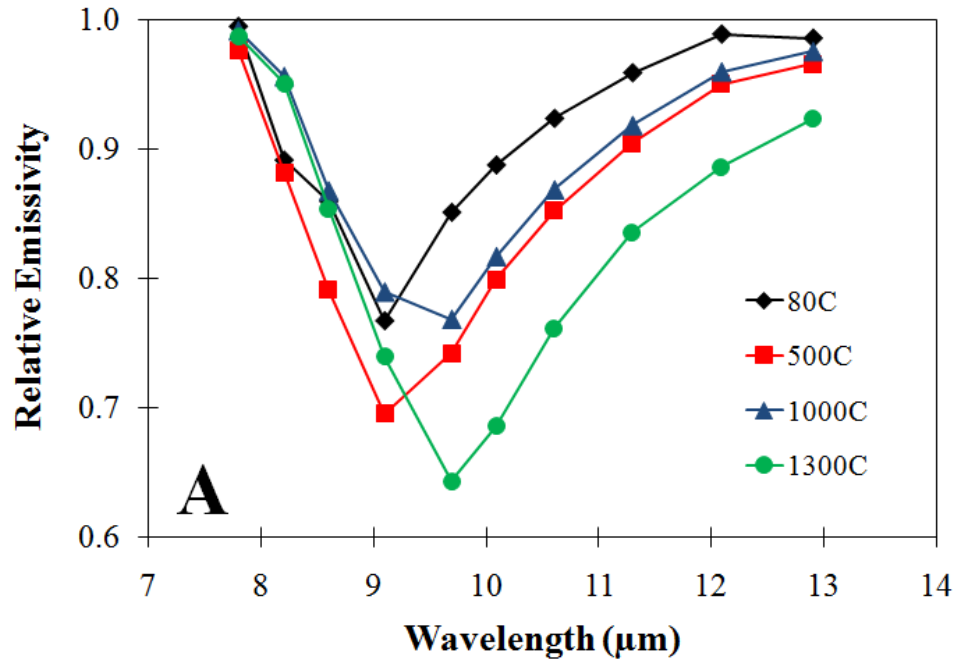


Figure B-10 (A) MASTER-degraded emission spectra of glass 20a at 80 °C, 500 °C, 1000 °C, and 1300 °C. (B) FLIR-degraded emission spectra of glass 20a at 80 °C, 500 °C, 1000 °C, and 1300 °C.

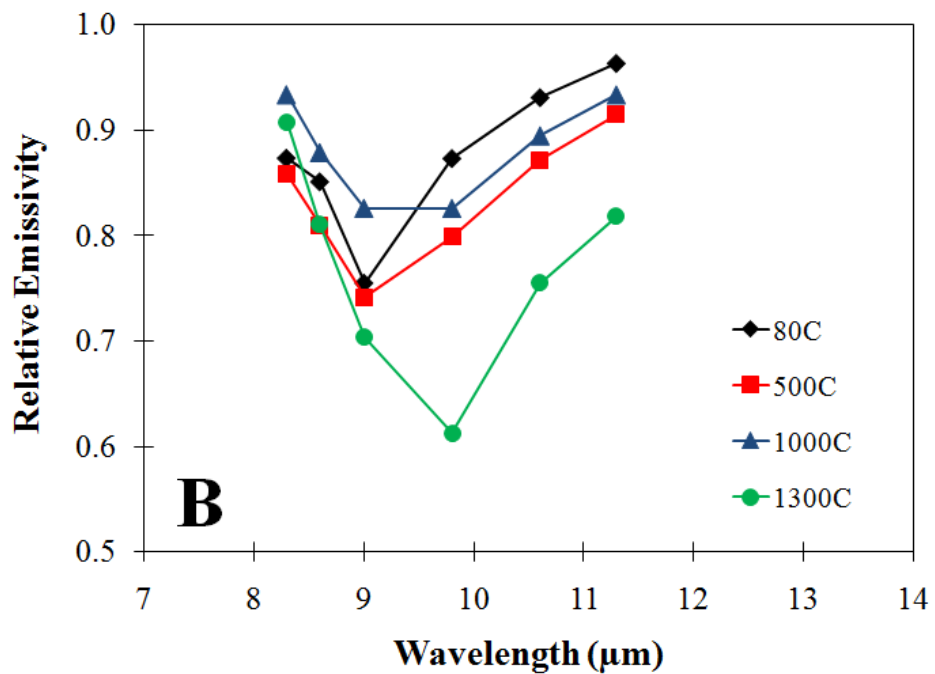
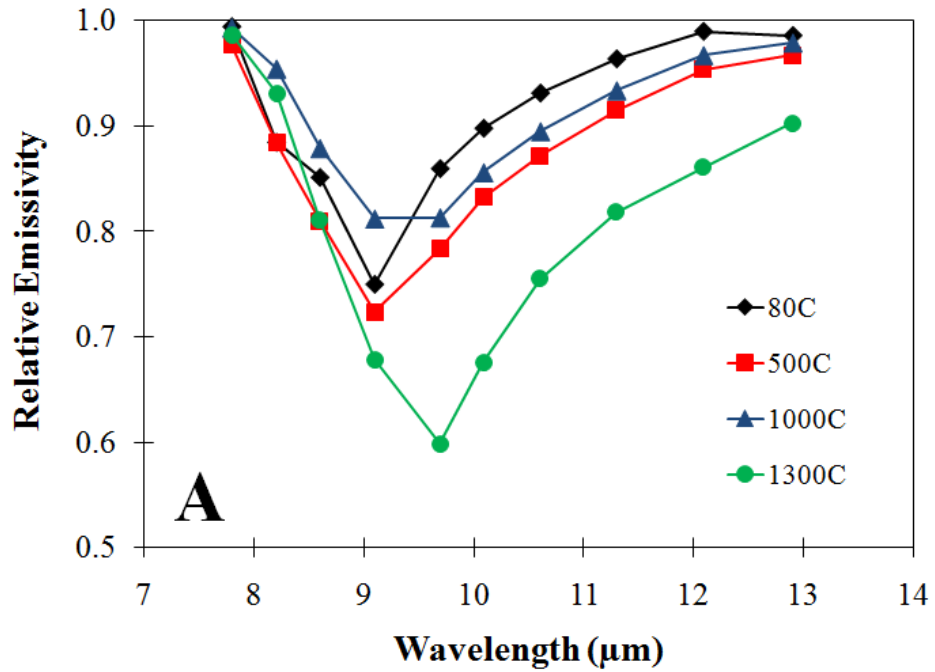


Figure B-11 (A) MASTER-degraded emission spectra of glass 21 at 80 °C, 500 °C, 1000 °C, and 1300 °C. (B) FLIR-degraded emission spectra of glass 21 at 80 °C, 500 °C, 1000 °C, and 1300 °C.

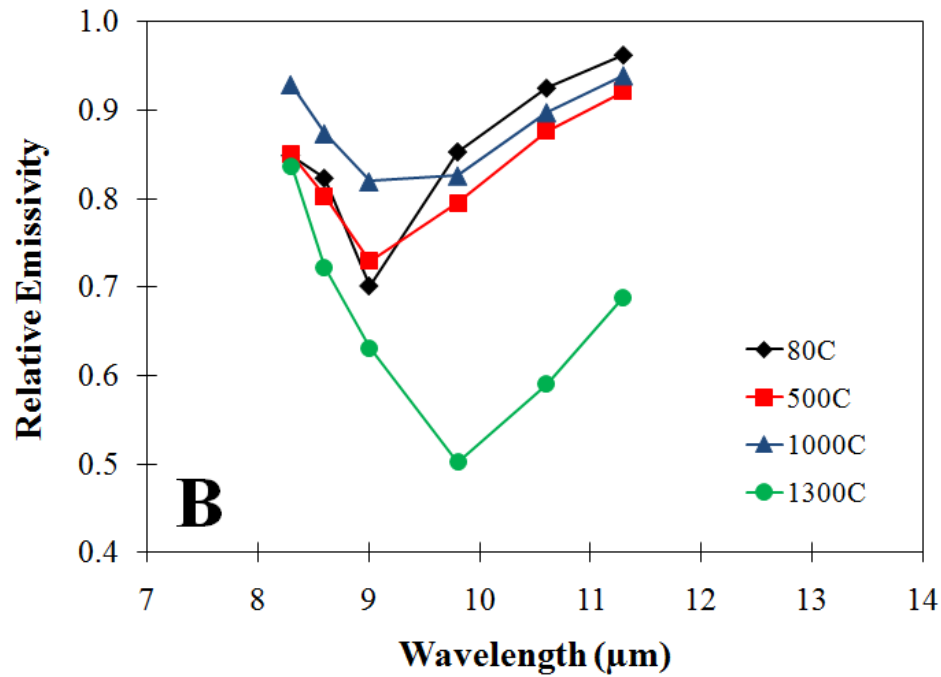
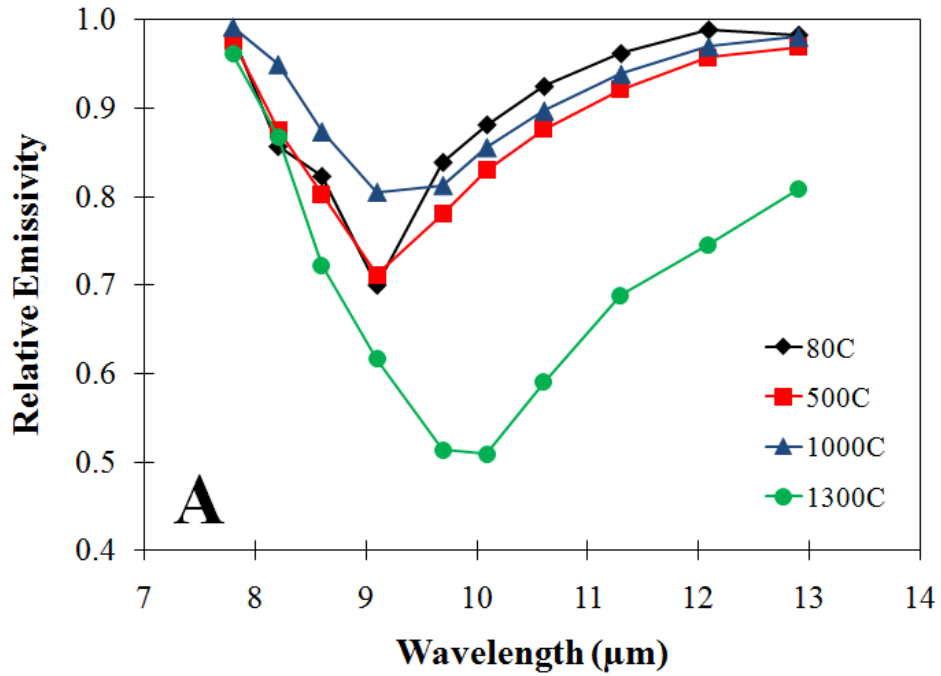


Figure B-12 (A) MASTER-degraded emission spectra of glass 21a at 80 °C, 500 °C, 1000 °C, and 1300 °C. (B) FLIR-degraded emission spectra of glass 21a at 80 °C, 500 °C, 1000 °C, and 1300 °C.

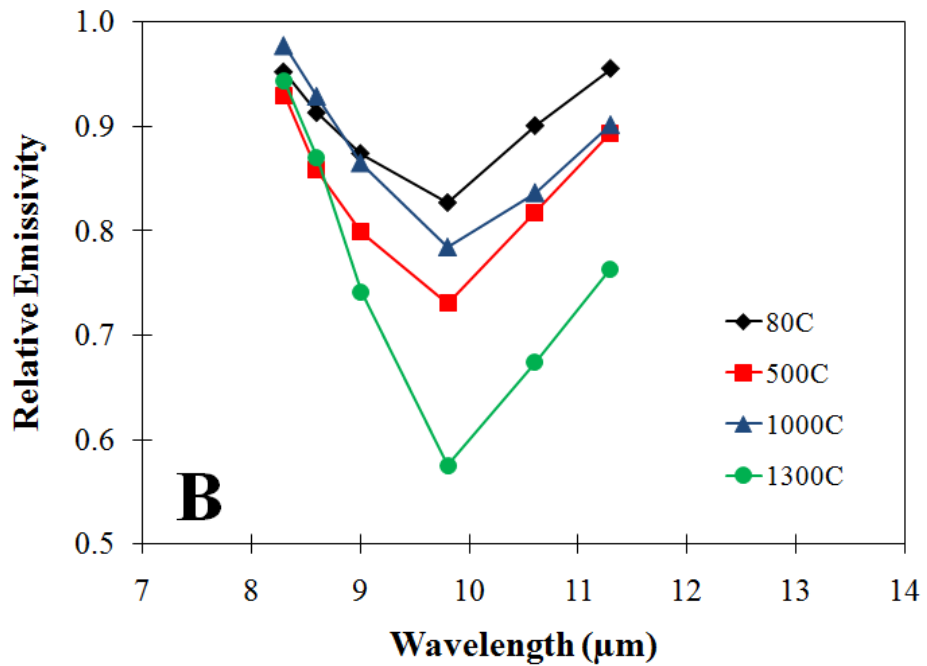
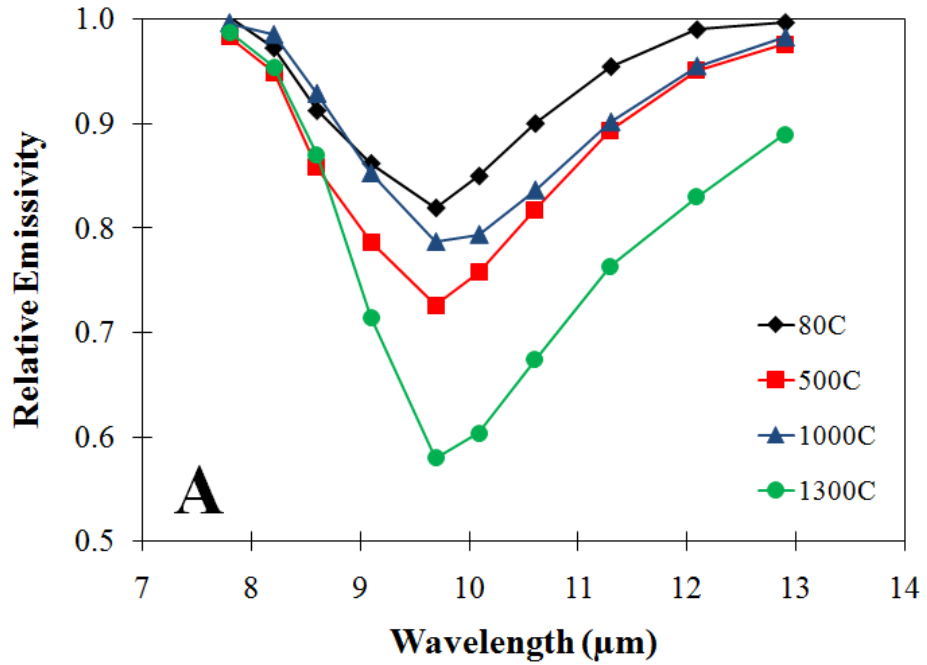


Figure B-13 (A) MASTER-degraded emission spectra of glass 24 at 80 °C, 500 °C, 1000 °C, and 1300 °C. (B) FLIR-degraded emission spectra of glass 24 at 80 °C, 500 °C, 1000 °C, and 1300 °C.

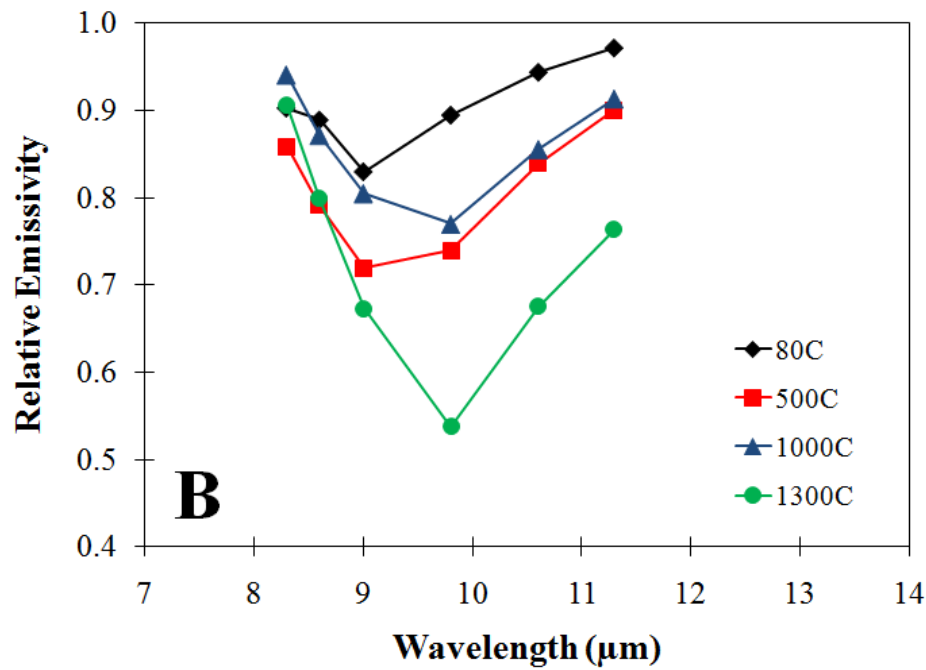
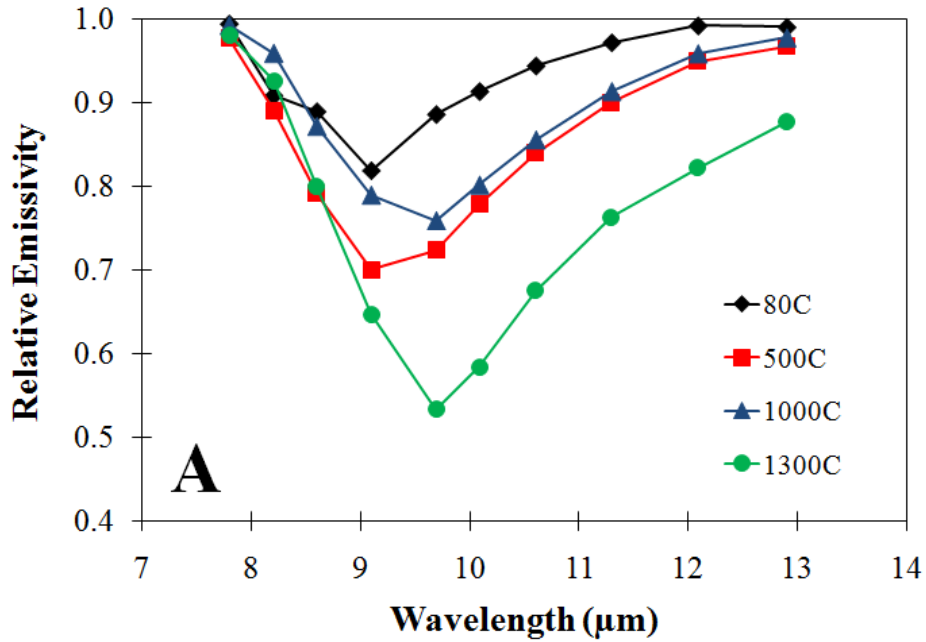


Figure B-14 (A) MASTER-degraded emission spectra of glass 27 at 80 °C, 500 °C, 1000 °C, and 1300 °C. (B) FLIR-degraded emission spectra of glass 27 at 80 °C, 500 °C, 1000 °C, and 1300 °C.

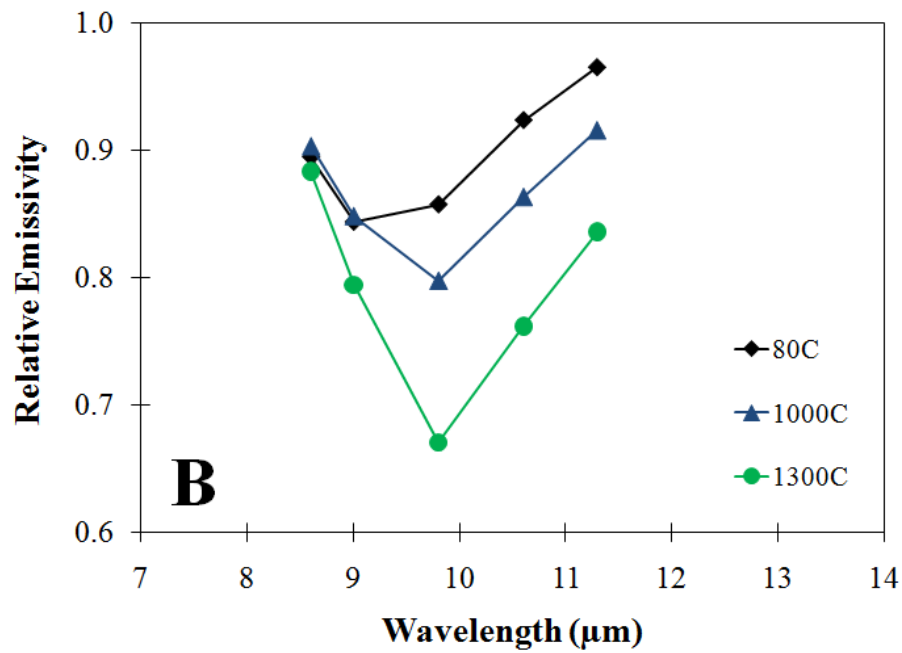
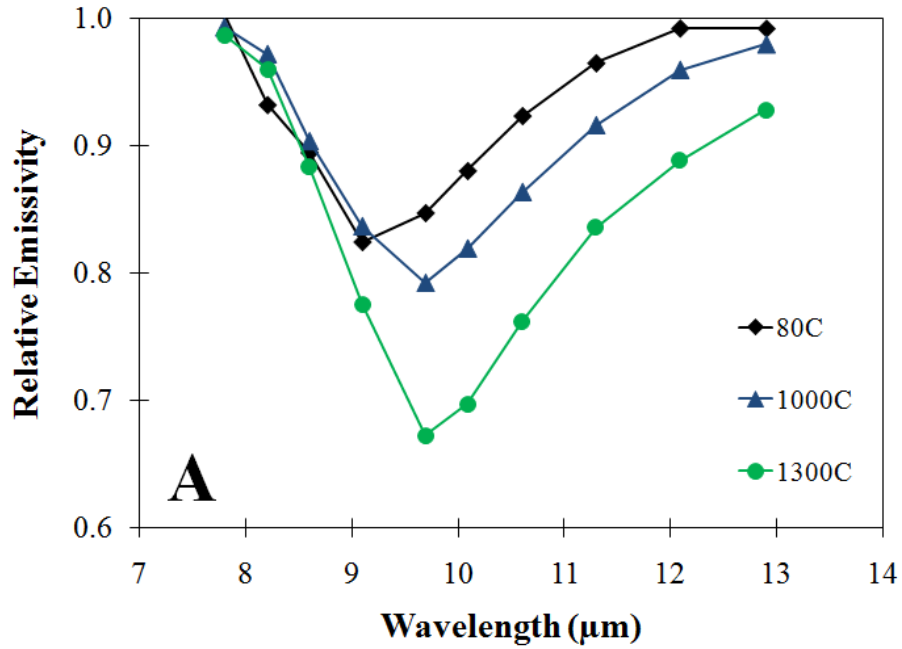


Figure B-15 (A) MASTER-degraded emission spectra of glass 28 at 80 °C, 500 °C, 1000 °C, and 1300 °C. (B) FLIR-degraded emission spectra of glass 28 at 80 °C, 500 °C, 1000 °C, and 1300 °C.

BIBLIOGRAPHY

- Abtahi, A.A., Kahle, A.B., Abbott, E.A., Gillespie, A.R., Sabol, D., Yamada, G., and Pieri, D. (2002), Emissivity changes in basalt cooling after eruption from Pu'u 'O'o, Kilauea, Hawaii, *Amer. Geophys. Union Eos Trans.*, abstract V71A-1263.
- Agarwal, A., and Tomozawa, M. (1997), Correlation of silica glass properties with the infrared spectra, *J. Non Cryst. Solids*, 209, 166-174.
- Anderson, C.A. (1933) Volcanic history of glass mountain, northern California. *American Journal of Science*, XXVI, 485-506.
- Angeli, F., Delaye, J-M., Charpentier, T., Petit, J-C., Ghaleb, D. and Faucon, P. (2000), Influence of glass chemical composition on the Na-O bond distance: a ^{23}Na 3Q-MAS NMR and molecular dynamics study, *J. Non Cryst. Solids*, 276, 132-144.
- Bandfield, J.L. (2009), Effects of surface roughness and greybody emissivity on Martian thermal infrared spectra, *Icarus*, doi:10.1016/j.icarus.2009.03.031.
- Bell, R. J., Bird, N.F., and Dean, P. (1968), The vibrational spectra of vitreous silica, germania, and beryllium fluoride, *J. Phys. Chem. (Proc. Phys. Soc.)*, 1, 299-303.
- Brown, C.M., Naber, R.H., Tilford, S. G., and Ginter, M.L. (1973), High temperature furnace system for vacuum ultraviolet spectroscopic studies, *Applied Optics IP*, 12, 1858.
- Byrnes, J. M., Ramsey, M.S. and Crown, D.A. (2004), Surface unit characterization of the Mauna Ulu flow field, Kilauea volcano, Hawaii, using integrated field and remote sensing analyses, *J. Volcanol. Geotherm. Res.*, 135, 169-193.
- Byrnes, J. M., King, P.L., Ramsey, M.S., and Lee, R.J. (2005), Synthesis and analysis of silicate glasses: applications to remote sensing of volcanic surface units on Earth and Mars, *Lunar Planet. Sci. [CD ROM]*, XXXVI, abstract 2089.
- Byrnes, J. M., King, P.L., Ramsey, M.S., and Lee, R.J. (2007), Thermal infrared reflectance and emission spectroscopy of quartzofeldspathic glasses, *Geophys. Res. Lett.*, 34, L01306, doi:10.1029/2006GL027893.

- Carter, A. J., Ramsey, M.S. and Belousov, A.B. (2007), Recent crater formation at Bezymianny Volcano lava dome: Significant changes observed in satellite and field data, *Bull. Volc.*, 69, 811-815, doi: 10.1007/s00445-007-0113-x.
- Carter, A.J., Ramsey, M.S., Durant, A.J., Skilling, I.P., Wolfe, A.L. (2009), Micron scale roughness of volcanic surfaces from thermal infrared spectroscopy and scanning electron microscopy, *J. Geophys. Res.*, 114, B02213, doi:10.1029/2008JB005632.
- Carter, A.J. and Ramsey, M.S. (2009), ASTER-and field-based observations at Bezymianny Volcano: Focus on the 11 May 2007 pyroclastic flow deposit, *Rem. Sens. Environ.*, 113, 2412-2151.
- Christensen, P. R., Bandfield, J.L., Smith, M.D., Hamilton, V.E., and Clark, R.N. (2000), Identification of a basaltic component on the Martian surface from Thermal Emission Spectrometer data, *J. Geophys. Res.*, 105(E4), 9609-9622.
- Clark, R. N. (1999), Chapter 1: Spectroscopy of Rocks and Minerals, and Principles of Spectroscopy, in *Manual of Remote Sensing, Volume 3, Remote Sensing for the Earth Sciences*, edited by A.N. Rencz, pp. 3-58, John Wiley and Sons, New York.
- Condie, K.C. and Hayslip, D.L. (1975), Young bimodal volcanism at Medicine Lake volcanic center, northern California, *Geochim. Cosmochim. Acta*, 39, 1165-1178.
- Crisp, J., Kahle, A.B., and Abbott, E.A. (1990), Thermal infrared spectral character of Hawaiian basaltic glasses, *J. Geophys. Res.*, 95(B13), 21657-21669.
- Dalby, K. N., and King, P.L. (2006), A new approach to determine and quantify structural units in silicate glasses using micro Fourier-Transform Infrared spectroscopy, *Am. Mineral.*, 91, 1783-1793, doi: 10.2138/am.2006.2075.
- Dalby, K.N., Dufresne, C.D.M, King, P.L., Byrnes, J.M., Lee, R.J. and Ramsey M.S. (2006), Characterization of glasses using infrared spectroscopy, *Geochim. Cosmochim. Acta Suppl.*, 70(18), 125.
- Dalby, K.N. (2007) Structure of Silicate Glasses: An FTIR and XPS Study, Ph.D. Dissertation, University of Western Ontario, London ON.
- Dalby, K. N., Dufresne, C. D. M., Lee, R. J., and King, P. L. Effect of aluminosilicate glass composition on thermal infrared spectra, in prep.
- Daniel I., Gillet, P.H., McMillan P.F., Richet P. (1995) An in-situ high temperature study of stable and meta-stable CaAl₂Si₂₀ 8 polymorphs, *Mineral Mag*, 59, 25-34.
- De Maeyer, E.A.P., Verbeeck, R.M.H and Vercruyse, C.W.J. (2002), Infrared spectrometric study of acid-degradable glasses, *J. Dent. Res.*, 81, 552-555.

- Dingwell, D.B. (1995), Relaxation in Silicate Melts: Some Applications, in Structure, Dynamics and Properties of Silicate Melts, *Min. Soc. Am. Rev. Mineral.*, vol. 33, edited by J. F. Stebbins et al., pp. 21-63, Min. Soc. Am., Blacksburg, VA.
- Domine, F. and Piriou, B. (1983), Study of sodium silicate melt and glass by infrared reflectance spectroscopy, *J. Non-crystal. Solids*, 5, 125-130.
- Donnelly-Nolan, J.M. (1988), A magmatic model of Medicine Lake volcano, California. *J. Geophys. Res.*, 93, 4412-4420.
- Donnelly-Nolan, J.M., Champion, D.E., Miller, C.D., Grove, T.L., Trimble, D.A. (1990), Post-11,000-year volcanism at Medicine Lake Volcano, Cascade Range, California, *J. Geophys. Res.* 95, 19693–19704.
- Donnelly-Nolan, J.M. and Grove, T.L. (2008), The late Holocene compositionally zoned Glass Mountain eruption at Medicine Lake volcano, California, *American Geophysical Union, Fall Meeting 2008*, abstract #V21C-2121.
- Dowty, E. (1987), Vibrational interactions of tetrahedral in silicate glasses and crystals: 1. Calculations on ideal silicate-aluminate-germanate structural units, *Phys. Chem. Mineral.*, 14, 80-93.
- Dufresne, C.D.M., King, P.L, Darby Dyar, M. and Dalby, K.N. (2009), Effect of SiO₂, total FeO, Fe³⁺/Fe²⁺, and alkali elements in basaltic glasses on mid-infrared spectra, *Am. Mineral.*, 94, 1580-1590.
- Eichelberger, J.C. (1975), Origin of andesite and dacite: Evidence of mixing at Glass Mountain in California and at other circum-Pacific volcanoes, *Geol. Soc. Am. Bull.*, 86, 1381-1391.
- Eisinger, C. (2002) Characterizing the composition of silicic lavas using infrared remote sensing. MS Thesis, Arizona State University, Tempe, 67 pp.
- Farges, F. and Brown, Jr., G.E. (1996), An empirical model for the anharmonic analysis of high-temperature XAFS spectra of oxide compounds with applications to the coordination environment of Ni in NiO, γ -Ni₂SiO₄ and Ni-bearing Na-disilicate glass and melt, *Chem. Geol.*, 128, 93–106.
- Farnan I. and Stebbins J.F. (1990), High-temperature 298i NMR investigation of solid and molten silicates. *J. Am. Chem. Soc.*, 112, 32-39.
- Fink, J.H. and Pollard, D.D (1983), Structural evidence for dikes beneath silicic domes, Medicine Lake Highland volcano, California, *Geology*, 11, 458-461.
- Fink, J.H., and Anderson, S.W. (2000), Lava Domes and Coulees, in *Encyclopedia of Volcanoes*, edited by H. Sigurdsson et al., Academic Press, San Diego, CA, 307- 319.

- Gerlach, D.C. and Grove, T.L. (1982), Petrology of Medicine Lake volcanics: Characterization of endmembers of magma mixing, *Contrib. Mineral. Petrol.*, 80, 147-159.
- Gervais, F. and Piriou, B. (1975), Temperature dependence of transverse and longitudinal optic modes in the α and β phases of quartz, *Phys. Rev. Lett.*, 11, 3944-3950. DOI: 10.1103/PhysRevB.11.3944
- Gillespie, A.R., Rokugawa, S., Hook, S., Matsunaga, T., and Kahle, A.B. (1996), Temperature/emissivity separation algorithm theoretical basis document, version 2.3, Jet Propulsion Laboratory, Pasadena, CA
<http://asterweb.jpl.nasa.gov/asterhome/atbd/ATBD-AST-03.doc>
- Gruener, G., Odier, P., De Sousa Meneses, D., Florian, P., and Richet, P. (2001), Bulk and local dynamics in glass-forming liquids: a viscosity, electrical conductivity, and NMR study of aluminosilicate melts, *Physical Review B*, 64, 24206.
- Grove, J. and Jellyman, P.E. (1955), The infrared transmission of glass in the range room temperature to 1400C, *J. Soc. Glass Technol.* 39, 3.
- Grove, T.L. and Donnelly-Nolan, J.M. (1986), The evolution of young silicic lavas at Medicine Lake Volcano, California: Implications for the origin of compositional gaps in calc-alkaline series lavas, *Contrib. Mineral. Petrol.*, 92, 281-302.
- Guillot, B. and N. Sator (2007), A computer simulation study of natural silicate melts. Part I: Low pressure properties, *Geochim. Cosmochim. Acta*, 71, 1249-1265.
- Hall, A. (1996), *Igneous Petrology* (2nd ed.), Longman Group Limited, Essex, England.
- Hapke, B. (1993), *Theory of Reflectance and Emittance Spectroscopy*, 455 pp., Cambridge Univ. Press, New York.
- Heaney, P. J. (1994), Structure and chemistry of the low-pressure silica polymorphs in: *Reviews in Mineralogy*, Vol.29 Silica - Physical behavior, geochemistry and materials applications. Mineralogical Society of America, Washington, D.C.
- Heiken, G. (1978), Plinian-type eruption at the Medicine Lake Highland, California, and the nature of the underlying magma, *J. Volcanol. Geotherm. Res.*, 4, 375-402.
- Helgason, H., Gunnlaugsson, P., Jonsson, K. and Steinthorsson, S. (1994), High temperature Mossbauer spectroscopy of titanomagnetite and maghemite in basalts, *Hyperfine Interactions*, 91, 595-599.
- Henderson, G.S. (2005), The structure of silicate melts: a glass perspective, *Can. Mineral.*, 43, 1921-1958.

- Henderson, G.S., Calas, G. and Stebbins, J.F. (2006), The structure of silicate glasses and melts, *Elements*, 2, 269-273.
- Hibbard, M.J. (1995), *Petrography to Petrogenesis*, 587pp, Prentice Hall, Englewood Cliffs, New Jersey.
- Hook, S.J. Myers, J.J., Thome, K.J., Fitzgerald, M. and Kahle, A.B. (2001), The MODIS/ASTER airborne simulator (MASTER) – a new instrument for earth science studies, *Remote. Sens. Environ.*, 76, 93-102.
- Ildfonse, P., Cabaret, D., Saintavit, P.H., Calas, G., Flanck, A.-M., and Lagarde, P. (1998), Aluminum X-ray absorption near edge structure in model compounds and Earth's surface minerals, *Phys. Chem. Minerals*, 25, 112–121.
- Jensen, J.R. *Remote Sensing of the Environment: An Earth Resource Perspective*. 2nd Ed. Prentice Hall, New Jersey, 2007.
- Johnson, J.R., Horz, F., and Staid, M.I. (2003), Thermal infrared spectroscopy and modeling of experimentally shocked plagioclase feldspars, *Am. Mineral.*, 88, 1575-1582.
- Johnson, J.R., Staid, M.I., Titus, T.N., and Becker, K. (2006), Shocked plagioclase signatures in Thermal Emission Spectrometer data of Mars, *Icarus*, 180(1), 60-74.
- Johnson, W.R., Hook, S.J., Mouroulis, P., Wilson, D.W., Gunapala, S.D., Hill, C.J., Realmuto, V., Mumolo, J.M., Eng, B.T. (2010), Field Calibration of a broadband compact thermal infrared spectrometer for earth science, *IEEE Conf.*, Paper # 1360.
- Kahle, A.B., Gillespie, A.R., Abbott, E.A., Abrams, M.J., Walker, R.E., Hoover, G., and Lockwood, J.P. (1988), Relative dating of Hawaiian lava flows using multispectral thermal infrared images: A new tool for geologic mapping of young volcanic terranes, *J. Geophys. Res.*, 93, 15239-15251.
- King, P.L., Ramsey, M.S., McMillan, P.F., and Swayze, G. (2004), Laboratory Fourier transform infrared spectroscopy methods for geologic samples, in *Infrared Spectroscopy in Geochemistry, Exploration Geochemistry, and Remote Sensing*, Mineral. Assoc. of Can. Short Course Ser., vol. 33, edited by P. L. King et al., pp. 57-91, Mineral. Assoc. of Can., Ottawa.
- King, P.L., Dufresne, C.D.M, and Dalby, K.N. (2008), Effect of SiO₂, total FeO, Fe²⁺/Fe³⁺ and alkalis in glasses on thermal infrared spectra, *Lunar Planet. Sci. [CD ROM]*, XXXIX, abstract 2256.

- King, P.L., Lee, R.J., Ramsey, M.S., McCutcheon, W.A., Schofield, C.M.D., and Shearer, C.K. (2011), Using Thermal Infrared Spectroscopy of Glasses to Unravel Composition and Thermal History – A New Thermometer for Lunar Glass Beads?, *Lunar Planet. Sci.*, Abstract 2069.
- Kirkpatrick R.J. (1988), MAS NMR spectroscopy of minerals and glasses. In: Hawthorne F.C. (ed.) *Spectroscopic Methods in Mineralogy and Geochemistry. Rev Mineral*, 18, 341-403
- Korb, A.R., Salisbury, J.W. and D'Aria, D.M. (1999), Thermal-infrared remote sensing and Kirchhoff's law 2. Field measurement,, *J. Geophys. Res.*, 104(B7), 15339–15350.
- Langford, J.I. (1978), A rapid method for analyzing the breadths of diffraction and spectral lines using the Voigt function, *J. Appl. Cryst.*, 11 10-14 doi:10.1107/S0021889878012601
- Le Chatelier, H. (1889), Sur la dilatation du quartz, *Comptes Rendus*, 108, 1046.
- Lee, R.J., King, P.L., and Ramsey, M.S. (2010), Spectral analysis of synthetic quartzofeldspathic glasses using laboratory thermal infrared spectroscopy, *J. Geophys. Res.*, 115, B06202, doi:10.1029/2009JB006672.
- Li, Z-L, Becker, F., Stoll, M.P., and Zhengming, W. (1999), Evaluation of Six Methods for Extracting Relative Emissivity Spectra from Thermal Infrared Images, *Rem. Sens. Environ.*, 69, 197-214
- Lyon, R.J.P. (1965), Analysis of rocks by spectral infrared emission (8 to 25 microns), *Econ. Geol.*, 60, 715-736.
- Magnien, V., Neuville, D.R., Cormier, L., Mysen, B.O., Briois, V., Belin, S., Pinet, O., and Richet, P. (2004), Kinetics of iron oxidation in silicate melts: a preliminary XANES study, *Chem. Geol.*, 213, 253–263.
- Magnien, V., Neuville, D.R., Cormier, L., Roux, J., Hazemann, J.-L., Pinet, O., and Richet, P. (2006), Kinetics of iron redox reactions in silicate liquids: a high-temperature X-ray absorption and Raman spectroscopy study, *Journal of Nuclear Materials*, 352, 190–195.
- McMillan, P. (1984), Structural studies of silicate glasses and melts - applications and limitations of Raman spectroscopy, *Am. Mineral.*, 69, 622-644.
- McMillan, P.F., and Hoffmeister, A. (1988), Infrared and Raman Spectroscopy, *Rev. Mineral. Geochem.*, 18(1), 99-159.
- McMillan, P.F., Wolf, G.H., and Poe, B.T. (1992), Vibrational spectroscopy of silicate liquids and glasses, *Chem. Geol.*, 96, 351-366.

- McMillan, P.F., Poe, B.T., Gillet, P., and Reynard, B. (1994), A study of SiO₂ glasses and supercooled liquid to 1950 K via high-temperature Raman spectroscopy, *Geochim. Cosmochim. Acta*, 58, 3653-3664.
- McMillan, P.F., and Wolf, G.H. (1995), Vibrational spectroscopy of silicate liquids, in Structure, Dynamics and Properties of Silicate Melts, Min. Soc. Am. Rev. Mineral., vol. 33, edited by J. F. Stebbins et al., pp. 247-315, Min. Soc. Am., Blacksburg, VA.
- McMillan, P.F., Grzechnik, A. and Chotalla, H. (1998), Structural characterization of SiO₂±CsAlO₂ and SiO₂±RbAlO₂ glasses, *J. Non-Crystal. Solids*, 226, 239-248.
- Mertzman, S.A. Jr. (1977), The petrology and chemistry of the Medicine Lake volcano, California, *Contrib. Mineral. Petrol.*, 62, 221-247.
- Minitti, M.E., Mustard, J.F., and Rutherford, M.J. (2002), Effects of glass content and oxidation on the spectra of SNC-like basalts: Applications to Mars remote sensing, *J. Geophys. Res.*, 107, 5030, doi:10.1029/2001JE001518.
- Minitti, M.E., Wyatt, M.B. and Hamilton, V.E. (2006), Investigating the role of compositionally-diverse glasses in interpreting Martian chemistry and mineralogy as viewed by TES, *Eos Trans. AGU*, 87(52), Fall Meet. Suppl., Abstract P23C-0067.
- Minitti, M.E., Weitz, C.M, Lane, M.D. and Bishop, J.L. (2007), Morphology, chemistry, and spectral properties of Hawaiian rock coatings and implications for Mars, *J. Geophys. Res.*, 112, E05015, doi:10.1029/2006JE002839.
- Minitti, M.E. and Hamilton, V.E. (2010), Searching for basaltic to intermediate igneous glasses in Martian surface materials, *Lunar. Planet. Sci.*, Abstract 1533.
- Moersch, J.E., and Christensen, P.R. (1995), Thermal emission from particulate surfaces: A comparison of scattering models with measured spectra, *J. Geophys. Res.*, 100, 7465-7477.
- Moynihan, C.T. (1995), Structural Relaxation and the Glass Transition, in Structure, Dynamics and Properties of Silicate Melts, Min. Soc. Am. Rev. Mineral., vol. 33, edited by J. F. Stebbins et al., pp. 1-18, Min. Soc. Am., Blacksburg, VA.
- Mysen, B.O., Virgo, D., and Scarfe, C.M. (1980a), Relations between the anionic structure and viscosity of silicate melts – a Raman spectroscopic study, *Am. Mineral.*, 65, 690-710.
- Mysen, B.O., Virgo, D., and Kushiro, L. (1981b), The structural role of aluminum in silicate melts - a Raman spectroscopic study at 1 atmosphere, *Am. Mineral.*, 66, 678-701.

- Mysen, B. O., Virgo, D., and Seifert, F.A. (1982a), The structure of silicate melts: implications for chemical and physical properties of natural magma, *Reviews of Geophysics and Space Physics*, 20, 353-383.
- Mysen B.O. (1988), *Structure and Properties of Silicate Melts*. Elsevier.
- Mysen B.O. (1990), Role of Al in depolymerized, peralkaline aluminosilicate melts in the systems $\text{Li}_2\text{O}-\text{Al}_2\text{O}_3-\text{SiO}_2$, $\text{Na}^*\text{O}-\text{Al}_2\text{O}_3-\text{SiO}_2$ and $\text{K}_2\text{O}-\text{Al}_2\text{O}_3-\text{SiO}_2$, *Amer. Mineral.* 75, 120-134.
- Mysen B.O. and Frantz J.D. (1992), Raman spectroscopy of silicate melts at magmatic temperatures: $\text{Na}_2\text{O}-\text{SiO}_2$, $\text{K}_2\text{O}-\text{SiO}_2$ and $\text{Li}_2\text{O}-\text{SiO}_2$ binary compositions in the temperature range 25 1475 ~ C, *Chem. Geol.*, 96, 321-332.
- Mysen B. O. and Frantz J.D. (1993), Structure and properties of alkali silicate melts at magmatic Temperatures, *Eur. J. Mineral.*, 5, 393- 407.
- Neuvill, D.R., and Mysen, B.O. (1996), Role of aluminum in the silicate network: In situ, high-temperature study of glasses and melts on the join $\text{SiO}_2-\text{NaAlO}_2$, *Geochim. Cosmochim. Acta*, 60, 1727-1737.
- Neuvill, D.R., Cormier, L. and Massiot, D. (2004), Al environment in tectosilicate and peraluminous glasses: A ^{27}Al MQ-MAS NMR, Raman, and XANES investigation, *Geochim. Cosmochim. Acta*, 68, 5071-5079.
- Neuvill, D.R., Cormier, L., Flank, A.-M., Briois, V., and Massiot, D. (2004a), Al speciation and Ca environment in calcium aluminosilicate glasses and crystals by Al and Ca K-edge X-ray absorption spectroscopy, *Chem. Geol.*, 213, 153–163.
- Neuvill, D.R., Cormier, L., and Massiot, D. (2004b), Al environment in tectosilicate and peraluminous glasses: a ^{27}Al MQ-MAS NMR, Raman, and EXAFS investigation, *Geochim. Cosmochim. Acta*, 68, 5071–5079.
- Neuvill, D.R., L. Cormier, and D. Massiot (2006), Al coordination and speciation in calcium aluminosilicate glasses: effects of composition determined by ^{27}Al MQ-MAS NMR and Raman spectroscopy, *Chem. Geol.*, 229, 173-185.
- Neuvill, D.R., Cormier, L., de Ligny, D., Roux, J., Flank, A-M., and Lagarde, P. (2008), Environments around Al, Si, and Ca in aluminate and aluminosilicate melts by X-ray absorption spectroscopy at high temperature, *Am. Mineral.*, 93, 228-234 DOI: 10.2138/am.2008.2646
- Nicodemus, F.E. (1965), Directional reflectance and emissivity of an opaque surface, *Appl. Opt.*, 4, 767-773.

- Ondrusek, J., Christensen, P.R. and Fink, J.H. (1993), Mapping the distribution of vesicular textures on silicic lavas using the Thermal Infrared Multispectral Scanner, *J. Geophys. Res.*, *98*, 15903-15908.
- Patrick, M.R., Harris, A.J.L., Ripepe, M., Dehn, J., Rothery, D.A., and Calvari, S. (2007), Strombolian explosive styles and source conditions: Insights from thermal (FLIR) video, *Bull. Volcanol.*, *69*, 769-784 DOI: 10.1007/s00445-006-0107-0.
- Poe, B.T., McMillan, P.F., Angell, C.A., and Sato, R.K. (1992), Al and Si coordination in SiO₂-Al₂O₃ glasses and liquids: a study by NMR and IR spectroscopy and MD simulations, *Chem. Geol.*, *96*, 333-349.
- Poe, B.T., McMillan, P.F., Cote, B., Massiot, D., and Coutures, J.P (1992b), SiO₂-Al₂O₃ liquids: in-situ study by high temperature ²⁷Al NMR spectroscopy and molecular dynamics simulations, *J. Phys. Chem.*, *96*, 8220-8224.
- Poe, B.T., McMillan, P.F., Coté, B., Massiot, D., and Coutures, J.P. (1993), Magnesium and calcium aluminate liquids: In situ high temperature ²⁷Al NMR spectroscopy, *Science*, *259*, 786-788.
- Poe, B.T., McMillan, P.F., Coté, B., Masiot, D., and Coutures, J.P. (1994), Structure and dynamics in calcium aluminate liquids: high-temperature ²⁷Al NMR and Raman spectroscopy, *J. Amer. Ceramic Soc.*, *77*, 1832-1838.
- Poe, B.T., Romano, C., Zotov, N., Cibin, G., and Marcelli, A. (2001), Compression mechanisms in aluminosilicate melts: Raman and XANES spectroscopy of glasses quenched from pressures up to 10 GPa, *Chem. Geol.*, *174*, 21-31.
- Ramsey, M.S., Fink, J.H., and Christensen, P.R. (1993b), Thermal emission analysis of mineral glasses: Application to remote sensing studies of Holocene silicic lava flows, *Abstr. of the IAVCEI Gen. Assembly*, *89*.
- Ramsey, M.S. and Fink, J.H. (1994), Remote monitoring of volcanic domes: Detection of chemical, textural, and thermal heterogeneities, *Eos Trans. AGU abstract*, *75*, 716.
- Ramsey, M.S. (1996), Quantitative analysis of geological surfaces: A deconvolution algorithm for midinfrared remote sensing data, Ph.D. dissertation, Ariz. State Univ., Tempe, AZ, 276 pp.
- Ramsey, M. S., and Christensen, P.R. (1998), Mineral abundance determination: Quantitative deconvolution of thermal emission spectra, *J. Geophys. Res.*, *103*, 577-596.
- Ramsey, M. S., and Fink, J.H. (1999), Estimating silicic lava vesicularity with thermal remote sensing: A new technique for volcanic mapping and monitoring, *Bull. Volc.*, *61*, 32-39.

- Ramsey, M. S. (2004), Quantitative geological surface processes extracted from infrared spectroscopy and remote sensing, in *Infrared Spectroscopy in Geochemistry, Exploration Geochemistry, and Remote Sensing*, Mineral. Assoc. of Can. Short Course Ser., vol. 33, edited by P. L. King et al., pp. 197-213, Mineral. Assoc. of Can., Ottawa.
- Ramsey, M. S. and Dehn J. (2004), Spaceborne observations of the 2000 Bezymianny, Kamchatka eruption: the integration of high-resolution ASTER data into near real-time monitoring using AVHRR, *J. Volcanol. Geotherm. Res.*, 135, 127-146.
- Ramsey, M.S. and Wessels, R.L. (2007), Monitoring changing eruption styles of Kilauea Volcano over the summer of 2007 with spaceborne infrared data, *Eos Trans. AGU*, 88(52): *Fall Meet. Suppl.*, Abstract V51H-07.
- Ramsey, M.S. (2009), What more have we learned from thermal infrared remote sensing of active volcanoes other than they are hot?, *Eos Trans. AGU*, 90(52), *Fall Meet. Suppl.*, Abst. V24B-01.
- Ramsey, D.W., Donnelly-Nolan, J.M., and Felger, T.J. (2010), Digital geologic map database of Medicine Lake Volcano, northern California, *AGU Fall Mtg Abstract* #V11C-2290.
- Rao, G.R. and Mishra, B.G. (2003), Structural, redox, and catalytic chemistry of ceria based materials, *Bulletin of the Catalysis Society of India*, 2, 122-134.
- Realmuto, V.J., Hon, K., Kahle, A.B., Abbott, E.A. and Pieri, D.C. (1992), Multispectral thermal infrared mapping of the 1 October 1988 Kupaianaha flow field, Kilauea Volcano, Hawaii, *Bull. Volc.*, 55, 33-44.
- Realmuto, V.J., Hajek, P., Sinha, M.P., and Chrien, T.G. (1995), The 1994 laboratory calibration of TIMS, in *Summaries of the Fifth Annual Airborne Earth Science Workshop*, vol.2, V.J. Realmuto (ed.), JPL Publ. 95-1, 25-28.
- Richet, P., Gillet, P., Pierre, A., Bouhifd, A., Daniel, I., and Fiquet, G. (1993), Raman spectroscopy, X-ray diffraction, and phase relationship determinations with a versatile heating cell for measurements up to 3600 K (or 2700 K in air), *J. Applied Phys.*, 74, 5451-5456.
- Ruff, S.W., Christensen, P.R, Barbera, P.W. and Anderson, D.L. (1997), Quantitative thermal emission spectroscopy of minerals: A laboratory technique for measurement and calibration, *J. Geophys. Res.*, 102, 14899-14913.
- Rybicki, G. and Lightman, A.P. (1979), *Radiative Processes in Astrophysics*. New York: Wiley-Interscience, p. 25.

- Sabine, C., Realmuto, V.J. and Taranik, J.V. (1994), Quantitative estimation of granitoid composition from thermal infrared multispectral scanner (TIMS) data, Desolation Wilderness, northern Sierra Nevada, California, *J. Geophys. Res.*, 99(B3), 4261–4271, doi:10.1029/93JB03127.
- Salisbury, J.W., Walter, L.S., Vergo, N. and D’Aria, D.M. (1991), Infrared (2.1-25 um) Spectra of Minerals, 267 pp., Johns Hopkins Univ. Press, Baltimore, MD.
- Salisbury, J.W. and Wald, A. (1992), The role of volume scattering in reducing spectral contrast of Reststrahlen bands in spectra of powdered minerals, *Icarus*, 96, 121-128.
- Schairer, J. (1957), Melting relations of the common rock-forming oxides, *J. Am. Ceram. Soc.*, 40, 215-235.
- Seifert, F.A, Mysen, B.O., Virgo, D. (1981), Structural similarity between glasses and melts relevant to petrological processes, *Geochim. Cosmochim. Acta*, 45, 1879-1884.
- Seifert, F., Mysen, B.O., and Virgo, D. (1982), Three-dimensional network structure of quenched melts (glass) in the system $\text{SiO}_2\text{-NaAlO}_2$, $\text{SiO}_2\text{-CaAl}_2\text{O}_4$ and $\text{SiO}_2\text{-MgAl}_2\text{O}_4$, *Am. Min.*, 67, 696–717.
- Spearing, D.R., Farnan, I., and Stebbins, J.F. (1992), Dynamics of the alpha- beta phase transitions in quartz and cristobalite as observed by in-situ high temperature ^{29}Si and ^{17}O NMR, *Phys. Chem. Minerals* 19, 307-321.
- Stebbins J.F. (1988b), Effects of temperature and composition on silicate glass structure and dynamics: Si-29 NMR results, *J. Non-Cryst. Solids*, 106, 359-369.
- Stebbins J.F., Farnan I. and Xue X. (1992), The structure and dynamics of alkali silicate liquids: a view from NMR spectroscopy, *Chem. Geol.*, 96, 371-385.
- Stebbins, J.F. and Farnan, I. (1992), Effects of high temperature on silicate liquid structure; a multinuclear NMR study, *Science*, 255, 586–589.
- Stebbins, J.F. (1995), Dynamics and structure of silicate and oxide melts: nuclear magnetic resonance studies, in Structure, Dynamics and Properties of Silicate Melts, Min. Soc. Am. Rev. Mineral., vol. 33, edited by J. F. Stebbins et al., pp. 191-246, Min. Soc. Am., Blacksburg, VA.
- Stebbins, J.F. and Xu, Z. (1997), NMR evidence for excess non-bridging O atoms in an aluminosilicate glass, *Nature*, 390, 60–62.
- Sweet, J.R., and White, W.B. (1969), Study of sodium silicate glasses and liquids by infrared reflectance spectroscopy, *Phys. Chem. Glasses*, 10, 246-251.

- Tomozawa, M., Hong, J.W. and Ryu, S.R. (2005), Infrared (IR) investigation of the structural changes of silica glasses with fictive temperature, *J. Non-Cryst. Solids*, *351*, 1054-1060.
- Vaughan, R.G., Wessels, R. and Ramsey, M.S. (2005), Monitoring renewed volcanic activity at Mount St. Helens with high-resolution thermal infrared data: ASTER, MASTER and FLIR, *Eos Trans. AGU*, *86*(52), Fall Meet. Suppl., Abstract V53D-1603.
- Walter, L.S., and Salisbury, J.W. (1989), Spectral characterization of igneous rocks in the 8 to 12 um region, *J. Geophys. Res.*, *94*, 9203-9213.
- Wertheim, G.K., Butler, M.A., West, K.W., Buchanan, D.N.E. (1974), Determination of the Gaussian and Lorentzian content of experimental line shapes, *Review of Scientific Instruments*, *45*, 1369-1371.
- Woodruff, R. and Ramelow, G (1968), Atomic absorption spectroscopy with a high-temperature furnace. *Spectrochimica Acta*, *23b*, 685-671.
- Wright, S.P. and Ramsey, M.S. (2006), Thermal infrared data analyses of Meteor Crater, Arizona: Implications for Mars spaceborne data from the Thermal Emission Imaging System, *J. Geophys. Res.*, *111*(E8), doi:10.1029/2005JE002472.
- Wyatt, M.B., Hamilton, V.E., McSween Jr., H.Y. and Christensen, P.R. (2001), Analysis of terrestrial and Martian volcanic compositions using thermal emission spectroscopy: I. Determination of mineralogy, chemistry, and classification strategies, *J. Geophys. Res.*, *106*, 14711-14732.